Medical Radiology · Diagnostic Imaging
Series Editors: H.-U. Kauczor · H. Hricak · M. Knauth

Elke Hattingen
Ulrich Pilatus *Editors*

Brain Tumor Imaging

Springer

Medical Radiology

Diagnostic Imaging

For further volumes:
http://www.springer.com/series/4354

Elke Hattingen • Ulrich Pilatus
Editors

Brain Tumor Imaging

Springer

Editors
Elke Hattingen
Neuroradiology, Department of Radiology,
University Hospital Bonn
Bonn, Germany

Ulrich Pilatus
Neuroradiology, Goethe University
Hospital Frankfurt
Frankfurt/Main
Germany

ISSN 0942-5373 ISSN 2197-4187 (electronic)
Medical Radiology
ISBN 978-3-642-45039-6 ISBN 978-3-642-45040-2 (eBook)
DOI 10.1007/978-3-642-45040-2

Library of Congress Control Number: 2015949175

Springer Heidelberg New York Dordrecht London

Printed on acid-free paper

Springer-Verlag GmbH Berlin Heidelberg is part of Springer Science+Business Media (www.springer.com)

Contents

Contributors

O. Bähr Neurooncology, University Cancer Center, Goethe University Hospital, Frankfurt, Frankfurt/Main, Germany

N. Galldiks Neuroscience and Medicine, Forschungszentrum Jülich, Jülich, Germany

Neurology, University of Cologne, Cologne, Germany

I. Goetz Radiation Oncology, University Medical Center Freiburg, Freiburg, Germany

A. L. Grosu Radiation Oncology, University Medical Center Freiburg, Freiburg, Germany

E. Hattingen Neuroradiology, Department of Radiology, University Hospital Bonn, Bonn, Germany

H. Lanfermann Diagnostic and Interventional Neuroradiology, Hannover Medical School, Hannover, Germany

K. J. Langen Neuroscience and Medicine, Forschungszentrum Jülich, Jülich, Germany

Nuclear Medicine, RWTH Aachen University Hospital, Aachen, Germany

U. Nöth Brain Imaging Center (BIC), Goethe University Frankfurt, Frankfurt/Main, Germany

U. Pilatus Neuroradiology, Goethe University Hospital Frankfurt, Frankfurt/Main, Germany

C. Preibisch Neuroradiology, Klinikum Rechts der Isar, TU Munich, Munich, Germany

P. Raab Diagnostic and Interventional Neuroradiology, Hannover Medical School, Hannover, Germany

J. P. Steinbach Neurooncology, University Cancer Center, Goethe University Hospital Frankfurt, Frankfurt/Main, Germany

W. Stummer Neurosurgery, University Hospital Münster, Münster, Germany

V. Toth Neuroradiology, Klinikum Rechts der Isar, TU Munich, Munich, Germany

M. Warmuth-Metz Neuroradiology, University Hospital of Würzburg, Würzburg, Germany

M. Weller Neurology, University Hospital Zurich, Zurich, Switzerland

J. Wölfer Neurosurgery, University Hospital Münster, Münster, Germany

C. Zimmer Neuroradiology, Klinikum Rechts der Isar, TU Munich, Munich, Germany

Brain Tumor Imaging

Oliver Bähr, Joachim P. Steinbach, and Michael Weller

Contents

Abstract

The variety of brain tumors with different histology, localization, age distribution, and prognosis might be confusing. The WHO Classification of Tumours of the Central Nervous system (2007) includes more than 100 different entities (Louis et al. 2007). The comparison of primary brain and CNS tumors by site and by histology facilitates a first insight (Ostrom et al. 2014). Moreover, this reflects the incidence rates of specific brain tumors. Besides metastatic tumors of the CNS, meningeal tumors and glioma account for more than 60 % of all primary brain tumors. Regarding malignant tumors, gliomas even represent 80 % of all primary brain tumors. From 45 years of age and older, meningioma is the most frequent and glioblastoma the second most frequent brain tumor. In children and adolescents, pilocytic astrocytoma and embryonal tumors are more relevant (Ostrom et al. 2014).

1 Introduction

1.1 Overview

The variety of brain tumors with different histology, localization, age distribution, and prognosis might be confusing. The WHO Classification of Tumours of the Central Nervous system (2007) includes more than 100 different entities (Louis et al. 2007). The comparison of primary brain and CNS tumors by site and by histology facilitates a first insight (Ostrom et al. 2014). Moreover, this reflects the incidence rates of specific brain tumors. Besides metastatic tumors of the CNS, meningeal tumors and glioma account for more than 60 % of all primary brain tumors. Regarding malignant tumors, gliomas even represent 80 % of all primary brain tumors. From 45 years of age and older, meningioma is the most frequent and glioblastoma the second most frequent brain tumor. In children and adolescents, pilocytic astrocytoma and embryonal tumors are more relevant (Ostrom et al. 2014).

O. Bähr (✉) • J.P. Steinbach
Dr. Senckenberg Institute of Neurooncology, University Cancer Center, Goethe University Hospital, Frankfurt, Germany
e-mail: oliver.baehr@med.uni-frankfurt.de; joachim.steinbach@med.uni-frankfurt.de

M. Weller
Department of Neurology, University Hospital Zurich, Zurich, Switzerland

E. Hattingen, U. Pilatus (eds.), *Brain Tumor Imaging*,
Med Radiol Radiat Oncol (2016)
DOI 10.1007/174_2016_1072, © Springer Berlin Heidelberg

Taken together, this illustrates that gliomas besides brain metastases are the most challenging entities in adult neurooncology.

Another important point is the differentiation of extra- and intracerebral localization of brain tumors. This usually allows an early distinction between meningiomas and gliomas or brain metastasis. As the clinical management differs substantially, this radiological differentiation is important. Small meningiomas in uncomplicated locations might not need an early histological diagnosis and can be followed by MRI scans. On the other hand, gliomas or brain metastasis usually need an immediate histological diagnosis. Further, the early radiological differentiation between gliomas, metastasis, and lymphomas is equally essential as the clinical management differs. For primary CNS lymphomas, steroids should be avoided before histological diagnostics and have traditionally been preferred over resection (Weller et al. 2012a). If brain metastases are suspected, systemic diagnostics are essential, and brain surgery may not always be necessary.

The current WHO classification from 2007 tries to indicate the prognosis of primary brain tumors by grading tumors from I° (benign) to IV° (malignant) primarily based on morphology (Louis et al. 2007). However, it is clear that the progress in molecular analyses will profoundly alter and refine this classification. In the future, prognostic and predictive markers and profiles will have practical importance for the vast majority of patients. Accordingly, a number of established molecular markers will be integrated in the upcoming WHO classification (Louis et al. 2014; Weller et al. 2012b, 2013; Wick et al. 2014).

In this chapter, we will focus on glioma, lymphoma, and brain metastasis.

2 Clinical Management

As the location of brain tumors is variable, the clinical presentation can be heterogeneous. Neurological or neuropsychological deficits, epileptic seizures, and symptoms of increased intracranial pressure are guiding symptoms. Symptomatic treatment includes, but is not limited to, anticonvulsive drugs for symptomatic epilepsy and dexamethasone for the treatment of symptomatic peritumoral edema (Soffietti et al. 2010; Weller et al. 2012c, 2014).

After medical history taking and the neurological examination, MRI of the brain with contrast-enhancing agent is the most important diagnostic procedure. Lumbar puncture to allow the evaluation of the cerebrospinal fluid (CSF) can be helpful in primary CNS lymphoma where tumor cells or tumor-specific molecular alterations can be detected in CSF or in germ cell tumors where elevated amounts of AFP or β-HCG can be found. In almost all other cases, the diagnosis should be confirmed via a stereotactic biopsy or, when appropriate, via resection. Despite all innovative imaging, the procurement of tumor tissue has gained particular relevance in the era of molecular diagnostic (Weller et al. 2014).

Nonetheless, innovative imaging has gained a lot of attention in the last decade. Before confirmation of the diagnosis via tissue analysis, MR spectroscopy, MR perfusion, and positron emission tomography (PET) imaging can be helpful for specific topics (Suchorska et al. 2014, 2015). Spectroscopy and perfusion can be helpful to distinguish between neoplastic lesions and other possible diagnoses. Some of the most important differential diagnoses are infectious or inflammatory causes and postischemic lesions. Moreover, metabolic imaging might show “hot spots” inside a tumor mass that can be targeted by stereotactic biopsy, thereby increasing the chance to get the most accurate diagnosis (Hermann et al. 2008). PET imaging using amino acid tracers also supports the diagnostic workup or can guide stereotactic biopsy to hot spots.

After the diagnosis has been confirmed pathologically, these innovative imaging modalities can be even more valuable. In particular, they may be useful for planning of radiotherapy (Revannasiddaiah et al. 2014). The irradiated field can be tailored to include areas with elevated PET tracer uptake, and radiation dose may be increased at hot spots seen on MR spectroscopy/perfusion or on amino acid PET.

Even more established in clinical practice is the use of innovative imaging for the monitoring during therapy and follow-up. MRI and PET can both be useful to distinguish between progressive tumor and pseudoprogression (Hutterer et al. 2014).

Functional MRI and fiber tracking using diffusion tensor imaging (DTI) might help to identify eloquent areas and improve results of surgery. Intraoperative brain mapping and awake surgery can be of further benefit. This may help to increase the extent of resection and improve progression-free survival (PFS) and overall survival (OS) while reducing perioperative morbidity.

3 Glial Tumors

3.1 Focal Glial and Glioneuronal Tumors Versus Diffuse Gliomas

Compared to focal glial tumors like pilocytic astrocytomas of the WHO grade I, grade II gliomas show diffuse infiltrative growth patterns and a propensity to evolve into grade III or grade IV gliomas. Therefore, and in contrast to pilocytic astrocytomas, a surgical cure is not possible in these (Louis et al. 2007).

Like pilocytic astrocytomas, glioneuronal tumors like dysembryoplastic neuroepithelial tumors (DNET) or ganglioglioma show a benign course. If clinically necessary, these glioneuronal tumors can usually be resected completely.

3.2 Low-Grade Versus High-Grade Gliomas

Neuropathological analyses of diffuse astrocytomas (WHO grade II) reveal well-differentiated fibrillary or gemistocytic neoplastic astrocytes on a loosely structured and often microcystic tumor matrix. Cellularity is only moderately increased. There is no mitotic activity, and proliferation rate determined by Ki-67/MIB-1 labeling index is usually below 4 % (Louis et al. 2007).

Histopathology of anaplastic astrocytomas shows the same features as those for diffuse astrocytoma. In addition, anaplastic astrocytoma shows increased cellularity, distinct nuclear atypia, and mitotic activity. Proliferation rate ranges from 5 to 10 %, but might overlap with low-grade gliomas and glioblastomas. Microvascular proliferation and necrosis are still absent (Louis et al. 2007).

Glioblastomas show a remarkable regional heterogeneity with anaplastic, poorly differentiated pleomorphic astrocytic tumor cells. Nuclear atypia is common, and mitotic activity is high. Proliferation rates range between 10 and 20 %, again with high regional heterogeneity. Microvascular proliferation and/or necrosis is essential for the diagnosis of glioblastoma (Louis et al. 2007).

Regarding prognosis, the WHO classification has obvious limitations. First, oligodendroglial tumors, anaplastic or not, have a similar clinical course that is superior to that of astrocytoma of the corresponding WHO grade. Molecular markers like 1p/19q deletions, IDH1/2 mutations, and MGMT promotor methylation are of prognostic value as they define subgroups of favorable survival. In addition, they are of predictive value and necessary for therapy decisions. It is now clear that true oligodendroglial tumors are characterized by 1p/19q codeletions and uniformly carry IDH1/2 mutations (Weller et al. 2012b, 2013; Reuss et al. 2015).

Moreover, anaplastic gliomas with favorable clinical and molecular markers can show superior survival compared to low-grade gliomas with unfavorable markers. On the other hand, anaplastic glioma with unfavorable constellation can have a prognosis inferior to that of patients with glioblastoma and favorable markers. This elucidates that molecular markers should be incorporated into an upcoming WHO classification (Louis et al. 2014; Reuss et al. 2015; Hartmann et al. 2010).

3.3 Astrocytomas Versus Oligodendroglial Tumors

In contrast to astrocytomas (see above), oligodendroglial tumor cells are monomorphic cells that show uniform round nuclei and perinuclear halos on paraffin sections ("honeycomb"). Microcalcifications, mucoid/cystic degenerations, and a dense network of branching capillaries (chicken wire) are frequently observed. Again, the presence of microvascular proliferation or necrosis is not compatible with the diagnosis of a low-grade glioma (Louis et al. 2007).

Compared to the corresponding low-grade gliomas, mitotic activity, microvascular proliferation, and areas of necrosis are frequent in anaplastic oligodendroglial tumors. A diagnosis of so-called mixed oligoastrocytoma has been established for tumors with both morphological features of oligodendroglioma and astrocytoma (Louis et al. 2007). However, the definition of oligoastrocytoma, low grade or anaplastic, is under heavy debate, and molecular markers are likely to lead to the omission of this diagnosis (Louis et al. 2007).

The mentioned calcifications in histology of oligodendroglial tumors are relevant for clinical management as they often can be detected on CT and MRI scans.

As shown by the NOA-04 trial, anaplastic oligodendroglioma and anaplastic oligoastrocytoma display a favorable outcome compared to anaplastic astrocytoma (Wick et al. 2009). This is also true for low-grade gliomas. As response rates to radiotherapy or chemotherapy in oligodendroglial tumors are higher than in astrocytic tumors, the avoidance of perioperative morbidity has even higher importance.

3.4 Low-Grade Glioma (WHO Grade II)

The absence of neurological symptoms and the presence of younger age or oligodendroglial histology are favorable clinical prognostic factors (Pignatti et al. 2002). However, even when short-term MRI scans (e.g., 3 months) suggest stable tumor size, all low-grade gliomas constantly grow in the long run (Mandonnet et al. 2003). Consequently, adjuvant treatment will be necessary at a certain time point in the course of the disease for all patients. Resection improves seizure control and may reduce the risk of malignant transformation (Soffietti et al. 2010).

3.4.1 Diffuse Astrocytoma (WHO Grade II)

After gross total resection, adjuvant treatment can be postponed at least in patients younger than 40 years of age with no neurological symptoms and a favorable location of the tumor (Pignatti et al. 2002). Regarding all other patients, there is an ongoing debate on which patients to treat and on the best time point of treatment. Radiotherapy prolongs PFS but not OS (van den Bent et al. 2005). Therefore, the EORTC defined five prognostic factors useful to identify low-risk and high-risk patients, the latter being treated with early radiotherapy (Pignatti et al. 2002). Prognostic favorable factors are age < 40 years, largest tumor diameter < 6 cm, tumor not crossing the midline, oligodendroglial or oligoastrocytic histology, and absence of a neurological deficit. Patients with two or fewer unfavorable factors are low-risk patients where therapy might be postponed unless their tumor is located in eloquent brain areas or patients suffer from untreatable epilepsy. Patients with three or more risk factors have dismal prognosis and might be treated immediately unless gross total resection was possible. In these cases, therapy might still be postponed. Chemotherapy also has activity in diffuse astrocytoma (Pace et al. 2003; Quinn et al. 2003; Brada et al. 2003). It is well established for patients who progressed after initial radiotherapy and can be an alternative as initial treatment in some patients. PCV (procarbazine, CCNU, and vincristine) and temozolomide seem to be comparable regarding efficacy with a better toxicity profile for temozolomide.

Recently, the updated results of the RTOG 9802 trial have been presented, although not published in detail yet (Shaw et al. 2012). This trial compared 54 Gy of radiotherapy with 54 Gy of radiotherapy followed by adjuvant chemotherapy with six cycles of PCV. In this regimen, procarbazine, CCNU, and vincristine are combined to a 6-week cycle. This trial included high-risk patients with low-grade glioma > 40 years of age and/or less than total resection. Median OS increased from 7.8 to 13.3 years in the combination therapy group although, interestingly, 77 % of the patients that progressed after radiotherapy had received salvage chemotherapy. A detailed analysis on histology subtypes and especially on molecular markers is lacking.

Whether these rather low-threshold criteria to define high-risk patients will translate to everyday practice is under debate. Further, it remains unanswered whether PCV alone would be equivalent and whether temozolomide could safely replace PCV in combination with radiotherapy. Therefore, many centers recommend the combination of radiotherapy and PCV.

3.4.2 Oligodendroglioma and Oligoastrocytoma (WHO Grade II)

After resection or diagnostic biopsy, the considerations for adjuvant treatment are similar to those for astrocytomas. The prognostic factors defined by the EORTC and mentioned above also apply to oligodendroglioma and oligoastrocytoma. As oligodendroglial tumors more often respond to chemotherapy, this is a more common choice for initial treatment in many centers (van den Bent et al. 1998, 2003). Nonetheless, the emerging standard of care is radiotherapy followed by chemotherapy with PCV according to the RTOG 9802 trial (Shaw et al. 2012).

3.5 Anaplastic Glioma (WHO Grade III)

In contrast to low-grade gliomas, adjuvant treatment is mandatory for patients with anaplastic glioma. The limitations of the current WHO classification are obvious in these tumors as mentioned above. Molecular markers have already entered diagnostic workup and therapeutic decision making (Weller et al. 2014).

3.5.1 Anaplastic Astrocytoma (WHO Grade III)

For adjuvant treatment, radiotherapy (60 Gy) was traditionally applied. According to the results of the NOA-04 trial, primary chemotherapy with temozolomide or with PCV seems to be equivalent regarding PFS and OS (Wick et al. 2009). Many brain tumor centers treat patients with anaplastic astrocytomas with radiochemotherapy according to the EORTC NCIC protocol with concomitant temozolomide and six cycles of adjuvant temozolomide. While reasonable, the evidence for this approach is limited and might be provided by the CATNON trial (EORTC 26053–22054). In this ongoing trial, the addition of temozolomide to first-line radiotherapy of anaplastic gliomas without 1p/19q deletion (mostly anaplastic astrocytoma) will be evaluated. In a 2 × 2 design, this study compares radiotherapy alone with radiotherapy plus concomitant temozolomide, radiotherapy plus adjuvant temozolomide, and radiotherapy plus concomitant and adjuvant temozolomide.

In the recurrent situation, treatment is less firmly established, and randomized controlled trials are rare. Second surgery might be an option if possible. Further treatment will depend on first-line treatment. Patients that progress after radiotherapy will be treated with either temozolomide chemotherapy or nitrosourea-based chemotherapy. If first-line treatment consisted of chemotherapy, radiotherapy is an option. Depending on availability, bevacizumab is often applied at progression after radiotherapy and alkylating chemotherapy, with modest PFS rates at 6 months (Weller et al. 2014).

3.5.2 Anaplastic Oligodendroglioma and Oligoastrocytoma

Radiotherapy has long been the standard of care in anaplastic oligodendroglioma and anaplastic oligoastrocytoma. However, these tumors not just frequently respond to radiotherapy, but also to chemotherapy. Especially in tumors with loss of 1p and 19q (LOH 1p/19q), PCV chemotherapy shows response rates of up to 100 % (Cairncross et al. 1994; Buckner et al. 2003). The NOA-04 trial showed that radiotherapy, PCV chemotherapy, and temozolomide are comparable in first-line treatment (Wick et al. 2009). Therefore, many centers recommended temozolomide as first-line therapy in the past, as it shows a superior tolerability profile compared to PCV. The sequence of therapeutic options (RT, PCV, TMZ) was the main focus in this trial.

In 2013, the long-term results of two large randomized controlled trials were published. Both the RTOG 9402 and the EORTC 26951 trial evaluated the combination of radiotherapy and PCV chemotherapy compared to radiotherapy alone in patients with anaplastic oligodendroglioma or oligoastrocytoma (Cairncross et al. 2006; van den Bent et al. 2006). Only after a follow-up of 6 years it became obvious that patients with LOH 1p/19q showed a dramatic benefit in OS when treated with radiotherapy and PCV (Cairncross et al. 2013; van den Bent et al. 2013). Hence, the 1p/19q status is not just prognostic but also predictive, requiring the testing for this marker before treatment planning. As for low-grade glioma, it remains unclear whether PCV alone would achieve similar results and whether temozolomide could safely replace PCV.

3.5.3 Gliomatosis Cerebri

Gliomatosis cerebri is a rare and controversial diagnosis and might be revised in future WHO classifications. This tumor cannot be defined by the neuropathologist alone. The diagnosis requires a combination of glioma histology and the radiological involvement of at least three cerebral lobes (Louis et al. 2007).

As this entity is the prototype of an infiltrative tumor, surgical resection is usually no option, and stereotactic biopsy leads to the diagnosis.

Histological features and prognosis are highly variable since any glioma histology together with radiology can lead to the diagnosis. Usually, all patients receive treatment after diagnosis.

Large randomized trials for adjuvant treatment are lacking. Radiotherapy, PCV, and temozolomide are active treatments (Herrlinger 2012; Sanson et al. 2004). Due to the diffuse growth, radiotherapy usually results in whole brain radiotherapy and is therefore frequently postponed. Instead, chemotherapy is frequently recommended for first-line treatment. The NOA-05 trial is one of the few prospective trials on chemotherapy in gliomatosis cerebri (Glas et al. 2011). Chemotherapy with PC (procarbazine + CCNU) resulted in prolonged tumor control in some patients in this trial, and the median OS was only 30 months.

3.6 Glioblastoma (WHO Grade IV)

Glioblastoma is the most frequent malignant primary brain tumor. Several studies suggest that the extent of resection is relevant for prognosis, although class I evidence is still lacking (Sanai et al. 2011; Kreth et al. 2013). Surgery using 3D navigation systems and intraoperative monitoring is standard in most centers. With 5-ALA-guided resection and intraoperative MRI, two techniques to improve extent of resection have been evaluated in a randomized controlled setting (Senft et al. 2011; Stummer et al. 2006). Both studies showed an increase of patients with gross total resection and superior survival. Awake surgery is done by some centers but cannot be regarded as a standard for patients with glioblastoma.

The current standard of care was defined in 2005 with the results of the EORTC 26981–22981 NCIC CE.3 (Stupp et al. 2005, 2009). This trial compared radiotherapy, the former standard of care, with radiotherapy plus concomitant and adjuvant chemotherapy with temozolomide. Median OS was prolonged from 12.1 to 14.6 months. Two-year survival rate increased from 10.4 to 26.5 %. In addition, a companion paper reported on the predictive value of the MGMT promoter methylation status (Hegi et al. 2005). The benefit of the addition of temozolomide was far lower when the MGMT promotor was not methylated. Patients with a methylated MGMT promotor showed a median OS of 15.3 months when they received radiotherapy alone and 21.7 months after combined treatment. Importantly, the majority of patients had alkylating agent chemotherapy at progression, diluting the survival benefit afforded by temozolomide in the experimental arm. When the MGMT promotor was unmethylated, median OS reached 11.8 and 12.7 months for radiotherapy alone and combined treatment, respectively. This benefit in patients with unmethylated MGMT promotor was small but still significant. Therefore, and because of missing alternatives as well as a certain amount of uncertainty regarding the procedures for testing the MGMT promotor, most patients are treated with a combined radiochemotherapy irrespective of the MGMT promotor status (Weller et al. 2014).

In elderly patients with glioblastoma, the MGMT status is more relevant. The NOA-08 trial randomized patients older than 65 years between radiotherapy alone and temozolomide alone (Wick et al. 2012). For the whole cohort, there was no significant difference in PFS and OS, suggesting that temozolomide is equally active in these patients. When analyzing the subgroups of patients with methylated and unmethylated MGMT promotor, however, significant and clinically relevant differences were observed. In patients with methylated MGMT promotor temozolomide resulted in an event-free survival (EFS) of 8.4 months compared to 4.6 months for radiotherapy. In contrast, in patients with unmethylated MGMT promotor, temozolomide showed an EFS of 3.3 months and radiotherapy of 4.6 months. Similar results were observed in the Nordic trial (Malmstrom et al. 2012). As a result of these studies, treatment planning in older patients depends on MGMT status (Wick et al. 2014; Weller et al. 2012b, 2014). Patients with methylated MGMT promotor should receive temozolomide, either alone or in combination with radiotherapy for patients with a good clinical status. Radiotherapy alone is not sufficient for these patients. When the MGMT promotor is unmethylated, radiotherapy is the therapy of choice. Temozolomide seems to have no or only minimal efficacy in these patients.

In the recurrent situation, no formal standard is established. If possible, second surgery and second radiotherapy are regularly applied even if evidence for efficacy is low (Fogh et al. 2010; Grosu et al. 2005). Regarding chemotherapy, nitrosourea-based protocols and temozolomide are frequently used and approved by authorities (Batchelor et al. 2013; Wick et al. 2010; Perry et al. 2010; Norden et al. 2013). The antiangiogenic drug bevacizumab has resulted in unprecedented response rates and promising PFS times in patients with recurrent glioblastoma in the BRAIN trial (Friedman et al. 2009). As large randomized and controlled trials are missing, the influence on OS is unclear. Nonetheless, the FDA approved bevacizumab for the treatment of recurrent glioblastoma in 2009. The European authorities have refused approval in the same year.

A small but randomized phase II study (BELOB trial) conducted in the Netherlands compared CCNU ($n=46$) with bevacizumab ($n=50$) and the combination of both ($n=52$) in patient with recurrent glioblastoma (Taal et al. 2014). The combination of bevacizumab and CCNU resulted in a median OS of 12 months whereas CCNU and bevacizumab alone only reached 8 months, respectively. A large randomized controlled phase III trial comparing CCNU with CCNU plus bevacizumab has just finished recruitment, and results are expected in late 2015.

Regarding the use of bevacizumab in first-line treatment, two randomized controlled trials showed 4 months benefit for PFS but no benefit for OS (Chinot et al. 2014; Gilbert et al. 2014). Therefore, bevacizumab has no role in first-line therapy.

As antiangiogenic agents often abrogate contrast enhancement and edema of glioblastoma, this might in part explain the discrepancy between effects on PFS and OS. Furthermore, even T2-weighted MRI sequences are influenced by bevacizumab (Hattingen et al. 2013). This emphasizes the need for innovative imaging for the follow-up of patients on antiangiogenic therapy (Hutterer et al. 2014).

4 Primary CNS Lymphomas

Primary CNS lymphomas are malignant lymphomas, usually B-cell lymphomas, arising in the CNS without lymphoma manifestations outside the nervous system (Louis et al. 2007). This is a rare entity with a much higher incidence in AIDS patients. With the introduction of highly active antiretroviral therapy (HAART), the occurrence in AIDS patients has markedly dropped.

Primary CNS lymphomas typically involve the supratentorial brain parenchyma, but can also occur in the spinal cord and the posterior fossa. In rare cases, lymphoma cells can be found in the cerebrospinal fluid (CSF). Ocular disease can be detected in up to 15 % of all cases. Some primary CNS lymphomas show a perivascular growth pattern and thereby result in atypical MRI findings. In less than 10 %, occult systemic lymphomas are present.

This possible dissemination defines the diagnostic workup (Korfel & Schlegel 2013). Besides cerebral MRI, at least systemic staging with computed tomography, CSF analysis (if safely possible) and ophthalmologic examination are recommended. For the clinical management, it is essential to early consider a possible diagnosis of CNS lymphoma. Steroids, as often applied for symptomatic therapy in patients with malignant glioma or brain metastases, must be avoided in lymphoma patients before histological diagnosis. Steroids are cytotoxic to lymphoma cells and can thereby impede a clear histological diagnosis.

Diagnosis is still commonly made via stereotactic biopsy, although the best contemporary evidence indicates a benefit from open surgical resection at least with unifocal disease (Weller et al. 2012a). The therapy usually consists of high-dose methotrexate chemotherapy for all patients who can tolerate it (Korfel & Schlegel 2013). The monoclonal CD20 antibody rituximab and dexamethasone are frequently combined with chemotherapy. High-dose chemotherapy followed by autologous stem-cell transplantation can be considered in younger patients (Illerhaus et al. 2006). Intrathecal/intraventricular chemotherapy is part of some protocols (Pels et al. 2003). Whole brain radiotherapy is active in primary CNC lymphomas but is associated with delayed neurotoxicity (Doolittle et al. 2013). Therefore, radiotherapy should be reserved for patients who cannot receive chemotherapy or in the recurrent setting (Korfel et al. 2015; Thiel et al. 2010).

5 Metastatic Tumors of the CNS

Brain metastases are approximately five times more frequent than primary brain tumors, and 25 % of all patients dying because of malignancies show metastatic involvement of the brain in autopsies (Louis et al. 2007). The frequency of underlying cancer entities depends on their respective incidence and tropism for CNS. Non-small cell lung cancer (NSCLC) accounts for 50 % of all patients with brain metastasis, followed by breast cancer (~15 %), melanoma (~10 %), and renal cancer (~10 %) (Ostrom et al. 2014). In general, the prognosis for patients with metastatic tumors of the CNS is unfavorable. The incidence of brain metastasis is increasing due to improved systemic therapies with sometimes limited CNS activity (Ahluwalia et al. 2014).

The clinical presentation does not differ from primary brain tumors, and in cases of single metastasis, MRI scans might also be similar to a malignant glioma. When numerous tumors are visible on MRI, the diagnosis is usually easy with infectious diseases being the relevant differential diagnosis.

All therapeutic considerations regarding brain metastases must account for the systemic situation of the underlying cancer entity (Ahluwalia et al. 2014). Neurosurgical resections can be considered in patients with solitary or singular brain metastases and lesions causing mass effects or neurological symptoms (Patchell et al. 1990). Stereotactic radiosurgery is an active alternative to surgery and is typically applied in patients with up to five small metastases (<3 cm) (Aoyama et al. 2006; Kocher et al. 2011). The maximum number of metastases that can be treated with radiosurgery has increased during the last years (Yamamoto et al. 2014; Hunter et al. 2012). When neurosurgery and focal radiotherapy are not possible, whole brain radiotherapy (WBRT) is an active option. WBRT prolongs PFS but not OS and is associated with a relevant cognitive decline in some patients (Chang et al. 2009; Aoyama et al. 2007). Therefore, WBRT can be postponed in patients where all brain metastases can be sufficiently treated with a local treatment modality (surgery or radiosurgery). Systemic chemotherapy is frequently applied according to the underlying cancer type (Ahluwalia et al. 2014). Usually, systemic chemotherapy does not render one of the aforementioned brain-directed therapies unnecessary. This might be different for some targeted therapies like BRAF inhibitors for malignant melanoma (Ahluwalia et al. 2014).

In general, the number and efficacy of therapeutic options are often limited, and therefore, the intensification of preclinical and clinical research in this rather neglected field is warranted.

References

Ahluwalia MS, Vogelbaum MV, Chao ST, Mehta MM (2014) Brain metastasis and treatment. F1000Prime Rep 6:114

Aoyama H, Shirato H, Tago M, Nakagawa K, Toyoda T, Hatano K, Kenjyo M, Oya N, Hirota S, Shioura H, Kunieda E, Inomata T, Hayakawa K, Katoh N, Kobashi G (2006) Stereotactic radiosurgery plus whole-brain radiation therapy vs stereotactic radiosurgery alone for treatment of brain metastases: a randomized controlled trial. JAMA 295(21):2483–2491

Aoyama H, Tago M, Kato N, Toyoda T, Kenjyo M, Hirota S, Shioura H, Inomata T, Kunieda E, Hayakawa K, Nakagawa K, Kobashi G, Shirato H (2007) Neurocognitive function of patients with brain metastasis who received either whole brain radiotherapy plus stereotactic radiosurgery or radiosurgery alone. Int J Radiat Oncol Biol Phys 68(5):1388–1395

Batchelor TT, Mulholland P, Neyns B, Nabors LB, Campone M, Wick A, Mason W, Mikkelsen T, Phuphanich S, Ashby LS, Degroot J, Gattamaneni R, Cher L, Rosenthal M, Payer F, Jurgensmeier JM et al (2013) Phase III randomized trial comparing the efficacy of cediranib as monotherapy, and in combination with lomustine, versus lomustine alone in patients with recurrent glioblastoma. J Clin Oncol 31(26):3212–3218

Brada M, Viviers L, Abson C, Hines F, Britton J, Ashley S, Sardell S, Traish D, Gonsalves A, Wilkins P, Westbury C (2003) Phase II study of primary temozolomide chemotherapy in patients with WHO grade II gliomas. Ann Oncol 14(12):1715–1721

Buckner JC, Gesme D Jr, O'Fallon JR, Hammack JE, Stafford S, Brown PD, Hawkins R, Scheithauer BW, Erickson BJ, Levitt R, Shaw EG, Jenkins R (2003) Phase II trial of procarbazine, lomustine, and vincristine as initial therapy for patients with low-grade oligodendroglioma or oligoastrocytoma: efficacy and associations with chromosomal abnormalities. J Clin Oncol 21(2):251–255

Cairncross G, Macdonald D, Ludwin S, Lee D, Cascino T, Buckner J, Fulton D, Dropcho E, Stewart D, Schold C Jr et al (1994) Chemotherapy for anaplastic oligodendroglioma. National Cancer Institute of Canada Clinical Trials Group. J Clin Oncol 12(10): 2013–2021

Cairncross G, Berkey B, Shaw E, Jenkins R, Scheithauer B, Brachman D, Buckner J, Fink K, Souhami L, Laperierre N, Mehta M, Curran W (2006) Phase III trial of chemotherapy plus radiotherapy compared with radiotherapy alone for pure and mixed anaplastic oligodendroglioma: Intergroup Radiation Therapy Oncology Group Trial 9402. J Clin Oncol 24(18):2707–2714

Cairncross G, Wang M, Shaw E, Jenkins R, Brachman D, Buckner J, Fink K, Souhami L, Laperriere N, Curran W, Mehta M (2013) Phase III trial of chemoradiotherapy for anaplastic oligodendroglioma: long-term results of RTOG 9402. J Clin Oncol 31(3):337–343

Chang EL, Wefel JS, Hess KR, Allen PK, Lang FF, Kornguth DG, Arbuckle RB, Swint JM, Shiu AS, Maor MH, Meyers CA (2009) Neurocognition in patients with brain metastases treated with radiosurgery or radiosurgery plus whole-brain irradiation: a randomised controlled trial. Lancet Oncol 10(11):1037–1044

Chinot OL, Wick W, Mason W, Henriksson R, Saran F, Nishikawa R, Carpentier AF, Hoang-Xuan K, Kavan P, Cernea D, Brandes AA, Hilton M, Abrey L, Cloughesy T (2014) Bevacizumab plus radiotherapy-temozolomide for newly diagnosed glioblastoma. N Engl J Med 370(8):709–722

Doolittle ND, Korfel A, Lubow MA, Schorb E, Schlegel U, Rogowski S, Fu R, Dosa E, Illerhaus G, Kraemer DF, Muldoon LL, Calabrese P, Hedrick N, Tyson RM, Jahnke K, Maron LM et al (2013) Long-term cognitive function, neuroimaging, and quality of life in primary CNS lymphoma. Neurology 81(1):84–92

Fogh SE, Andrews DW, Glass J, Curran W, Glass C, Champ C, Evans JJ, Hyslop T, Pequignot E, Downes B, Comber E, Maltenfort M, Dicker AP, Werner-Wasik M (2010) Hypofractionated stereotactic radiation therapy: an effective therapy for recurrent high-grade gliomas. J Clin Oncol 28(18):3048–3053

Friedman HS, Prados MD, Wen PY, Mikkelsen T, Schiff D, Abrey LE, Yung WK, Paleologos N, Nicholas MK, Jensen R, Vredenburgh J, Huang J, Zheng M, Cloughesy T (2009) Bevacizumab alone and in combination with irinotecan in recurrent glioblastoma. J Clin Oncol 27(28):4733–4740

Gilbert MR, Dignam JJ, Armstrong TS, Wefel JS, Blumenthal DT, Vogelbaum MA, Colman H, Chakravarti A, Pugh S, Won M, Jeraj R, Brown PD, Jaeckle KA, Schiff D, Stieber VW, Brachman DG et al (2014) A randomized trial of bevacizumab for newly diagnosed glioblastoma. N Engl J Med 370(8):699–708

Glas M, Bähr O, Felsberg J, Rasch K, Wiewrodt D, Schabet M, Simon M, Urbach H, Steinbach JP, Rieger J, Fimmers R, Bamberg M, Nagele T, Reifenberger G, Weller M, Herrlinger U (2011) NOA-05 phase 2 trial of procarbazine and lomustine therapy in gliomatosis cerebri. Ann Neurol 70(3):445–453

Grosu AL, Weber WA, Franz M, Stark S, Piert M, Thamm R, Gumprecht H, Schwaiger M, Molls M, Nieder C (2005) Reirradiation of recurrent high-grade gliomas using amino acid PET (SPECT)/CT/MRI image fusion to determine gross tumor volume for stereotactic fractionated radiotherapy. Int J Radiat Oncol Biol Phys 63(2):511–519

Hartmann C, Hentschel B, Wick W, Capper D, Felsberg J, Simon M, Westphal M, Schackert G, Meyermann R, Pietsch T, Reifenberger G, Weller M, Loeffler M, von Deimling A (2010) Patients with IDH1 wild type anaplastic astrocytomas exhibit worse prognosis than IDH1-mutated glioblastomas, and IDH1 mutation status accounts for the unfavorable prognostic effect of higher age: implications for classification of gliomas. Acta Neuropathol 120(6): 707–718

Hattingen E, Jurcoane A, Daneshvar K, Pilatus U, Mittelbronn M, Steinbach JP, Bähr O (2013) Quantitative T2 mapping of recurrent glioblastoma under bevacizumab improves monitoring for non-enhancing

tumor progression and predicts overall survival. Neuro Oncol 15(10):1395–1404
Hegi ME, Diserens AC, Gorlia T, Hamou MF, de Tribolet N, Weller M, Kros JM, Hainfellner JA, Mason W, Mariani L, Bromberg JE, Hau P, Mirimanoff RO, Cairncross JG, Janzer RC, Stupp R (2005) MGMT gene silencing and benefit from temozolomide in glioblastoma. N Engl J Med 352(10):997–1003
Hermann EJ, Hattingen E, Krauss JK, Marquardt G, Pilatus U, Franz K, Setzer M, Gasser T, Tews DS, Zanella FE, Seifert V, Lanfermann H (2008) Stereotactic biopsy in gliomas guided by 3-tesla 1H-chemical-shift imaging of choline. Stereotact Funct Neurosurg 86(5):300–307
Herrlinger U (2012) Gliomatosis cerebri. Handb Clin Neurol 105: 507–515
Hunter GK, Suh JH, Reuther AM, Vogelbaum MA, Barnett GH, Angelov L, Weil RJ, Neyman G, Chao ST (2012) Treatment of five or more brain metastases with stereotactic radiosurgery. Int J Radiat Oncol Biol Phys 83(5):1394–1398
Hutterer M, Hattingen E, Palm C, Proescholdt MA and Hau P (2014) Current standards and new concepts in MRI and PET response assessment of antiangiogenic therapies in high-grade glioma patients. Neuro Oncol 1–16, doi:10.1093/neuonc/nou322
Illerhaus G, Marks R, Ihorst G, Guttenberger R, Ostertag C, Derigs G, Frickhofen N, Feuerhake F, Volk B, Finke J (2006) High-dose chemotherapy with autologous stem-cell transplantation and hyperfractionated radiotherapy as first-line treatment of primary CNS lymphoma. J Clin Oncol 24(24):3865–3870
Kocher M, Soffietti R, Abacioglu U, Villa S, Fauchon F, Baumert BG, Fariselli L, Tzuk-Shina T, Kortmann RD, Carrie C, Ben Hassel M, Kouri M, Valeinis E, van den Berge D, Collette S, Collette L et al (2011) Adjuvant whole-brain radiotherapy versus observation after radiosurgery or surgical resection of one to three cerebral metastases: results of the EORTC 22952–26001 study. J Clin Oncol 29(2):134–141
Korfel A, Schlegel U (2013) Diagnosis and treatment of primary CNS lymphoma. Nat Rev Neurol 9(6):317–327
Korfel A, Thiel E, Martus P, Mohle R, Griesinger F, Rauch M, Roth A, Hertenstein B, Fischer T, Hundsberger T, Mergenthaler HG, Junghanss C, Birnbaum T, Fischer L, Jahnke K, Herrlinger U, et al (2015) Randomized phase III study of whole-brain radiotherapy for primary CNS lymphoma. Neurology 84(12):1242–1248
Kreth FW, Thon N, Simon M, Westphal M, Schackert G, Nikkhah G, Hentschel B, Reifenberger G, Pietsch T, Weller M, Tonn JC (2013) Gross total but not incomplete resection of glioblastoma prolongs survival in the era of radiochemotherapy. Ann Oncol 24(12):3117–3123
Louis DN, Ohgaki H, Wiestler OD, Cavenee WK, Burger PC, Jouvet A, Scheithauer BW, Kleihues P (2007) The 2007 WHO classification of tumours of the central nervous system. Acta Neuropathol 114(2): 97–109
Louis DN, Perry A, Burger P, Ellison DW, Reifenberger G, von Deimling A, Aldape K, Brat D, Collins VP, Eberhart C, Figarella-Branger D, Fuller GN, Giangaspero F, Giannini C, Hawkins C, Kleihues P et al (2014) International Society of Neuropathology–Haarlem consensus guidelines for nervous system tumor classification and grading. Brain Pathol 24(5):429–435
Malmstrom A, Gronberg BH, Marosi C, Stupp R, Frappaz D, Schultz H, Abacioglu U, Tavelin B, Lhermitte B, Hegi ME, Rosell J, Henriksson R (2012) Temozolomide versus standard 6-week radiotherapy versus hypofractionated radiotherapy in patients older than 60 years with glioblastoma: the Nordic randomised, phase 3 trial. Lancet Oncol 13(9):916–926
Mandonnet E, Delattre JY, Tanguy ML, Swanson KR, Carpentier AF, Duffau H, Cornu P, Van Effenterre R, Alvord EC Jr, Capelle L (2003) Continuous growth of mean tumor diameter in a subset of grade II gliomas. Ann Neurol 53(4):524–528
Norden AD, Lesser GJ, Drappatz J, Ligon KL, Hammond SN, Lee EQ, Reardon DR, Fadul CE, Plotkin SR, Batchelor TT, Zhu JJ, Beroukhim R, Muzikansky A, Doherty L, Lafrankie D, Smith K et al (2013) Phase 2 study of dose-intense temozolomide in recurrent glioblastoma. Neuro Oncol 15(7):930–935
Ostrom QT, Gittleman H, Liao P, Rouse C, Chen Y, Dowling J, Wolinsky Y, Kruchko C, Barnholtz-Sloan J (2014) CBTRUS statistical report: primary brain and central nervous system tumors diagnosed in the United States in 2007–2011. Neuro Oncol 16(Suppl 4):iv1–iv63
Pace A, Vidiri A, Galie E, Carosi M, Telera S, Cianciulli AM, Canalini P, Giannarelli D, Jandolo B, Carapella CM (2003) Temozolomide chemotherapy for progressive low-grade glioma: clinical benefits and radiological response. Ann Oncol 14(12):1722–1726
Patchell RA, Tibbs PA, Walsh JW, Dempsey RJ, Maruyama Y, Kryscio RJ, Markesbery WR, Macdonald JS, Young B (1990) A randomized trial of surgery in the treatment of single metastases to the brain. N Engl J Med 322(8):494–500
Pels H, Schmidt-Wolf IG, Glasmacher A, Schulz H, Engert A, Diehl V, Zellner A, Schackert G, Reichmann H, Kroschinsky F, Vogt-Schaden M, Egerer G, Bode U, Schaller C, Deckert M, Fimmers R et al (2003) Primary central nervous system lymphoma: results of a pilot and phase II study of systemic and intraventricular chemotherapy with deferred radiotherapy. J Clin Oncol 21(24):4489–4495
Perry JR, Belanger K, Mason WP, Fulton D, Kavan P, Easaw J, Shields C, Kirby S, Macdonald DR, Eisenstat DD, Thiessen B, Forsyth P, Pouliot JF (2010) Phase II trial of continuous dose-intense temozolomide in recurrent malignant glioma: RESCUE study. J Clin Oncol 28(12):2051–2057
Pignatti F, van den Bent M, Curran D, Debruyne C, Sylvester R, Therasse P, Afra D, Cornu P, Bolla M, Vecht C, Karim AB (2002) Prognostic factors for survival in adult patients with cerebral low-grade glioma. J Clin Oncol 20(8):2076–2084
Quinn JA, Reardon DA, Friedman AH, Rich JN, Sampson JH, Provenzale JM, McLendon RE, Gururangan S, Bigner DD, Herndon JE 2nd, Avgeropoulos N, Finlay J, Tourt-Uhlig S, Affronti ML, Evans B, Stafford-Fox V et al (2003) Phase II trial of temozolomide in patients with progressive low-grade glioma. J Clin Oncol 21(4):646–651
Reuss DE, Sahm F, Schrimpf D, Wiestler B, Capper D, Koelsche C, Schweizer L, Korshunov A, Jones DT, Hovestadt V, Mittelbronn M, Schittenhelm J, Herold-Mende C, Unterberg A, Platten M, Weller M et al (2015) ATRX and IDH1-R132H immunohistochemistry with subsequent copy number analysis and IDH sequencing as a basis for an "integrated" diagnostic approach for adult astrocytoma, oligodendroglioma and glioblastoma. Acta Neuropathol 129(1):133–146
Revannasiddaiah S, Susheela SP, Kallur KG (2014) Integration of methionine-PET into the radiotherapy planning process for high grade glioma: prospects against non-central and central failures. Radiother Oncol 113(2):296
Sanai N, Polley MY, McDermott MW, Parsa AT, Berger MS (2011) An extent of resection threshold for newly diagnosed glioblastomas. J Neurosurg 115(1):3–8
Sanson M, Cartalat-Carel S, Taillibert S, Napolitano M, Djafari L, Cougnard J, Gervais H, Laigle F, Carpentier A, Mokhtari K, Taillandier L, Chinot O, Duffau H, Honnorat J, Hoang-Xuan K, Delattre JY (2004) Initial chemotherapy in gliomatosis cerebri. Neurology 63(2):270–275
Senft C, Bink A, Franz K, Vatter H, Gasser T, Seifert V (2011) Intraoperative MRI guidance and extent of resection in glioma surgery: a randomised, controlled trial. Lancet Oncol 12(11):997–1003
Shaw EG, Wang M, Coons SW, Brachman DG, Buckner JC, Stelzer KJ, Barger GR, Brown PD, Gilbert MR, Mehta MP (2012) Randomized trial of radiation therapy plus procarbazine, lomustine, and vincristine chemotherapy for supratentorial adult low-grade glioma: initial results of RTOG 9802. J Clin Oncol 30(25):3065–3070
Soffietti R, Baumert BG, Bello L, von Deimling A, Duffau H, Frenay M, Grisold W, Grant R, Graus F, Hoang-Xuan K, Klein M, Melin B, Rees J, Siegal T, Smits A, Stupp R et al (2010) Guidelines on management of low-grade gliomas: report of an EFNS-EANO Task Force. Eur J Neurol 17(9):1124–1133

Stummer W, Pichlmeier U, Meinel T, Wiestler OD, Zanella F, Reulen HJ (2006) Fluorescence-guided surgery with 5-aminolevulinic acid for resection of malignant glioma: a randomised controlled multicentre phase III trial. Lancet Oncol 7(5):392–401

Stupp R, Mason WP, van den Bent MJ, Weller M, Fisher B, Taphoorn MJ, Belanger K, Brandes AA, Marosi C, Bogdahn U, Curschmann J, Janzer RC, Ludwin SK, Gorlia T, Allgeier A, Lacombe D et al (2005) Radiotherapy plus concomitant and adjuvant temozolomide for glioblastoma. N Engl J Med 352(10):987–996

Stupp R, Hegi ME, Mason WP, van den Bent MJ, Taphoorn MJ, Janzer RC, Ludwin SK, Allgeier A, Fisher B, Belanger K, Hau P, Brandes AA, Gijtenbeek J, Marosi C, Vecht CJ, Mokhtari K et al (2009) Effects of radiotherapy with concomitant and adjuvant temozolomide versus radiotherapy alone on survival in glioblastoma in a randomised phase III study: 5-year analysis of the EORTC-NCIC trial. Lancet Oncol 10(5):459–466

Suchorska B, Tonn JC, Jansen NL (2014) PET imaging for brain tumor diagnostics. Curr Opin Neurol 27(6):683–688

Suchorska B, Jansen NL, Linn J, Kretzschmar H, Janssen H, Eigenbrod S, Simon M, Popperl G, Kreth FW, la Fougere C, Weller M, Tonn JC (2015) Biological tumor volume in 18FET-PET before radiochemotherapy correlates with survival in GBM. Neurology 84(7):710–719

Taal W, Oosterkamp HM, Walenkamp AM, Dubbink HJ, Beerepoot LV, Hanse MC, Buter J, Honkoop AH, Boerman D, de Vos FY, Dinjens WN, Enting RH, Taphoorn MJ, van den Berkmortel FW, Jansen RL, Brandsma D et al (2014) Single-agent bevacizumab or lomustine versus a combination of bevacizumab plus lomustine in patients with recurrent glioblastoma (BELOB trial): a randomised controlled phase 2 trial. Lancet Oncol 15(9):943–953

Thiel E, Korfel A, Martus P, Kanz L, Griesinger F, Rauch M, Roth A, Hertenstein B, von Toll T, Hundsberger T, Mergenthaler HG, Leithauser M, Birnbaum T, Fischer L, Jahnke K, Herrlinger U et al (2010) High-dose methotrexate with or without whole brain radiotherapy for primary CNS lymphoma (G-PCNSL-SG-1): a phase 3, randomised, non-inferiority trial. Lancet Oncol 11(11):1036–1047

van den Bent MJ, Kros JM, Heimans JJ, Pronk LC, van Groeningen CJ, Krouwer HG, Taphoorn MJ, Zonnenberg BA, Tijssen CC, Twijnstra A, Punt CJ, Boogerd W (1998) Response rate and prognostic factors of recurrent oligodendroglioma treated with procarbazine, CCNU, and vincristine chemotherapy. Dutch Neuro-oncology Group. Neurology 51(4):1140–1145

van den Bent MJ, Taphoorn MJ, Brandes AA, Menten J, Stupp R, Frenay M, Chinot O, Kros JM, van der Rijt CC, Vecht Ch J, Allgeier A, Gorlia T (2003) Phase II study of first-line chemotherapy with temozolomide in recurrent oligodendroglial tumors: the European Organization for Research and Treatment of Cancer Brain Tumor Group Study 26971. J Clin Oncol 21(13):2525–2528

van den Bent MJ, Afra D, de Witte O, Ben Hassel M, Schraub S, Hoang-Xuan K, Malmstrom PO, Collette L, Pierart M, Mirimanoff R, Karim AB (2005) Long-term efficacy of early versus delayed radiotherapy for low-grade astrocytoma and oligodendroglioma in adults: the EORTC 22845 randomised trial. Lancet 366(9490):985–990

van den Bent MJ, Carpentier AF, Brandes AA, Sanson M, Taphoorn MJ, Bernsen HJ, Frenay M, Tijssen CC, Grisold W, Sipos L, Haaxma-Reiche H, Kros JM, van Kouwenhoven MC, Vecht CJ, Allgeier A, Lacombe D et al (2006) Adjuvant procarbazine, lomustine, and vincristine improves progression-free survival but not overall survival in newly diagnosed anaplastic oligodendrogliomas and oligoastrocytomas: a randomized European Organisation for Research and Treatment of Cancer phase III trial. J Clin Oncol 24(18):2715–2722

van den Bent MJ, Brandes AA, Taphoorn MJ, Kros JM, Kouwenhoven MC, Delattre JY, Bernsen HJ, Frenay M, Tijssen CC, Grisold W, Sipos L, Enting RH, French PJ, Dinjens WN, Vecht CJ, Allgeier A et al (2013) Adjuvant procarbazine, lomustine, and vincristine chemotherapy in newly diagnosed anaplastic oligodendroglioma: long-term follow-up of EORTC brain tumor group study 26951. J Clin Oncol 31(3):344–350

Weller M, Martus P, Roth P, Thiel E, Korfel A (2012a) Surgery for primary CNS lymphoma? Challenging a paradigm. Neuro Oncol 14(12):1481–1484

Weller M, Stupp R, Hegi ME, van den Bent M, Tonn JC, Sanson M, Wick W, Reifenberger G (2012b) Personalized care in neuro-oncology coming of age: why we need MGMT and 1p/19q testing for malignant glioma patients in clinical practice. Neuro Oncol 14(Suppl 4):iv100–iv108

Weller M, Stupp R, Wick W (2012c) Epilepsy meets cancer: when, why, and what to do about it? Lancet Oncol 13(9):e375–e382

Weller M, Pfister SM, Wick W, Hegi ME, Reifenberger G, Stupp R (2013) Molecular neuro-oncology in clinical practice: a new horizon. Lancet Oncol 14(9):e370–e379

Weller M, van den Bent M, Hopkins K, Tonn JC, Stupp R, Falini A, Cohen-Jonathan-Moyal E, Frappaz D, Henriksson R, Balana C, Chinot O, Ram Z, Reifenberger G, Soffietti R, Wick W (2014) EANO guideline for the diagnosis and treatment of anaplastic gliomas and glioblastoma. Lancet Oncol 15(9):e395–e403

Wick W, Hartmann C, Engel C, Stoffels M, Felsberg J, Stockhammer F, Sabel MC, Koeppen S, Ketter R, Meyermann R, Rapp M, Meisner C, Kortmann RD, Pietsch T, Wiestler OD, Ernemann U et al (2009) NOA-04 randomized phase III trial of sequential radiochemotherapy of anaplastic glioma with procarbazine, lomustine, and vincristine or temozolomide. J Clin Oncol 27(35):5874–5880

Wick W, Puduvalli VK, Chamberlain MC, van den Bent MJ, Carpentier AF, Cher LM, Mason W, Weller M, Hong S, Musib L, Liepa AM, Thornton DE, Fine HA (2010) Phase III study of enzastaurin compared with lomustine in the treatment of recurrent intracranial glioblastoma. J Clin Oncol 28(7):1168–1174

Wick W, Platten M, Meisner C, Felsberg J, Tabatabai G, Simon M, Nikkhah G, Papsdorf K, Steinbach JP, Sabel M, Combs SE, Vesper J, Braun C, Meixensberger J, Ketter R, Mayer-Steinacker R et al (2012) Temozolomide chemotherapy alone versus radiotherapy alone for malignant astrocytoma in the elderly: the NOA-08 randomised, phase 3 trial. Lancet Oncol 13(7):707–715

Wick W, Weller M, van den Bent M, Sanson M, Weiler M, von Deimling A, Plass C, Hegi M, Platten M, Reifenberger G (2014) MGMT testing–the challenges for biomarker-based glioma treatment. Nat Rev Neurol 10(7):372–385

Yamamoto M, Serizawa T, Shuto T, Akabane A, Higuchi Y, Kawagishi J, Yamanaka K, Sato Y, Jokura H, Yomo S, Nagano O, Kenai H, Moriki A, Suzuki S, Kida Y, Iwai Y et al (2014) Stereotactic radiosurgery for patients with multiple brain metastases (JLGK0901): a multi-institutional prospective observational study. Lancet Oncol 15(4):387–395

MR Imaging of Brain Tumors

Elke Hattingen and Monika Warmuth-Metz

Contents

Abstract

This chapter gives an overview of important radiological aspects in brain tumor imaging. It was not our aim to deal with the wide differential diagnosis of brain tumors, and this chapter should not replace a neuroradiological textbook. Instead, it addresses important radiological and neurological aspects which should be known by the radiologist reporting brain tumors. In general, age is one of the most important criterion to distinguish different brain neoplasms, since the differential diagnosis differ considerably between ages. Therefore, the chapter is divided into childhood and adulthood brain tumors. Further, important pitfalls in brain tumor diagnosis are treated especially concerning non-neoplastic brain lesions and post-treatment changes. The localization of brain tumors in relation to functional brain areas is another important issue which has to be reported by the neuroradiologist, since preservation of important brain function is the ultimate goal and determines the treatment modality. Therefore, this chapter gives some help to localize a tumor with respect to the functional primary motor and language areas.

Abbreviations

MRI	Magnetic resonance imaging
CT	Computed tomography
CNS	Central nervous system
SE	Spin echo
FLAIR	Fluid-Attenuated Inversion Recovery
PD	Proton density
i.v.	intravenous
fMRI	Functional MRI
DWI	Diffusion-weighted imaging
ADC	Apparent diffusion coefficient
DTI	Diffusion tensor imaging
SWI	Susceptibility-weighted imaging
PNET	Primitive neuroepithelial tumor
DNET	Dysembryoplastic neuroepithelial tumor

E. Hattingen (✉)
Neuroradiology, University Hospital of Goethe University Frankfurt, Schleusenweg 2-16, 60528, Frankfurt
e-mail: Elke.Hattingen@kgu.de

M. Warmuth-Metz
Neuroradiology, University Hospital of Würzburg, Josef-Schneider-Str. 2, 97080, Würzburg

E. Hattingen, U. Pilatus (eds.), *Brain Tumor Imaging*,
Medical Radiology. Diagnostic Imaging,
DOI: 10.1007/174_2016_936,

Table 1 Image protocol for brain tumor

	Slice thickness/gab	Weighting	Details	Important features
Axial	5 mm/0–0.5 mm	T2WI	T2-TSE	Cortical ribbon sign, infiltration of insula, basal ganglia
Axial	5 mm/0–0.5 mm	T1WI before/after administration of contrast agent	SE preferred, without fat suppression, without MT pulses, same sequence ∓ contrast	Consider T1-hyperintensities
Coronal or sagittal	5 mm/0–0.5 mm	T1WI after administration of contrast agent	SE preferred, should not be replaced by 3D sequences	Depicts late enhancement when acquired after axial sequence
Axial	5 mm/0–0.5 mm (FLAIR with gab)	FLAIR or PD (long TR)	Optional 3D FLAIR	
Axial	5–6 mm/0.5–1 mm	DWI	Calculate ADC	Low ADC: postsurgical infarcts, cell density, abscess, antiangiogenic therapy
Axial		T2*WI	SWI before/after administration of contrast agent	(micro) Hemorrhages, blooming veins, tumor vessels
Second plane	Depends on the localization of the tumor	T2WI or T1WI	Choose the sequence which best depicts the tumor	Follow-up examinations should include exact the same sequence
3D post CM		Avoid inversion pulses (MPRAGE)	Does not replace second plane	Measure enhancement in 3 planes

MPR Multiplanar reformatting
PPL Posterior pituitary lobe
WI Weighted imaging

1 Introduction

Magnetic resonance imaging is clearly the method of choice for the imaging of CNS diseases. Computed tomography is an alternative in case of emergency or MRI contraindications. For radiotherapy planning, the physical properties of CT are essential (Stephenson and Wiley 1995). Still, it is the only method for a reliable depiction of calcification, which might have a diagnostic potential in some tumor entities especially in pediatric tumors and low-grade gliomas (Zulfiqar et al. 2012; Tsuda et al. 1997). The signal intensities on MRI and density values on CT allow a limited diagnosis of the histology of the tumor. Invasive angiography or conventional radiography is useful only in rare exceptions.

There are no standardized MR imaging protocols for brain tumors, so that the protocols given here are considered as proposals (Table 1). However, more and more patients with brain tumors, especially children (see Sect. 3), are included in treatment trials which have their own imaging protocols. For the European SIOPE (Europeenne International de la Société Societe International d'Oncologie Pédiatrique) brain tumor trials, an agreement of all reference (neuro)radiologists has been found. The following advice is based on this consensus.

Additional to the standard spin echo (SE) sequences, an increasing number of various sequences have become available. However, the imaging characteristics on these sequences and thus the size and morphology of tumors might vary artificially. The key to a correct evaluation of study patients in a comparable way is to keep standardized imaging sequences during follow-up. A standard imaging protocol should contain T2 and FLAIR or proton density sequences. They should be combined with T1-weighted sequences before and after intravenous administration of contrast agent.

2 Brain Tumors in Adults

2.1 Questions to the Radiologist

For each space-occupying lesion, inflammatory or vascular disease should be considered before a real neoplasm is diagnosed. Especially subacute hemorrhage, venous infarction, arteriovenous malformations, large demyelinating diseases, or necrotic infections may look like a real neoplastic tumor. Patient's history, neurological symptoms, and patient's age are mandatory information to provide the correct diagnosis. Further, there are some imaging features which may specify the entity of a lesion. These features include diffusion restriction of T2-hyperintense lesions (Fig. 1), capsular and target-like structures of the margin, and the halo sign of the marginal zone

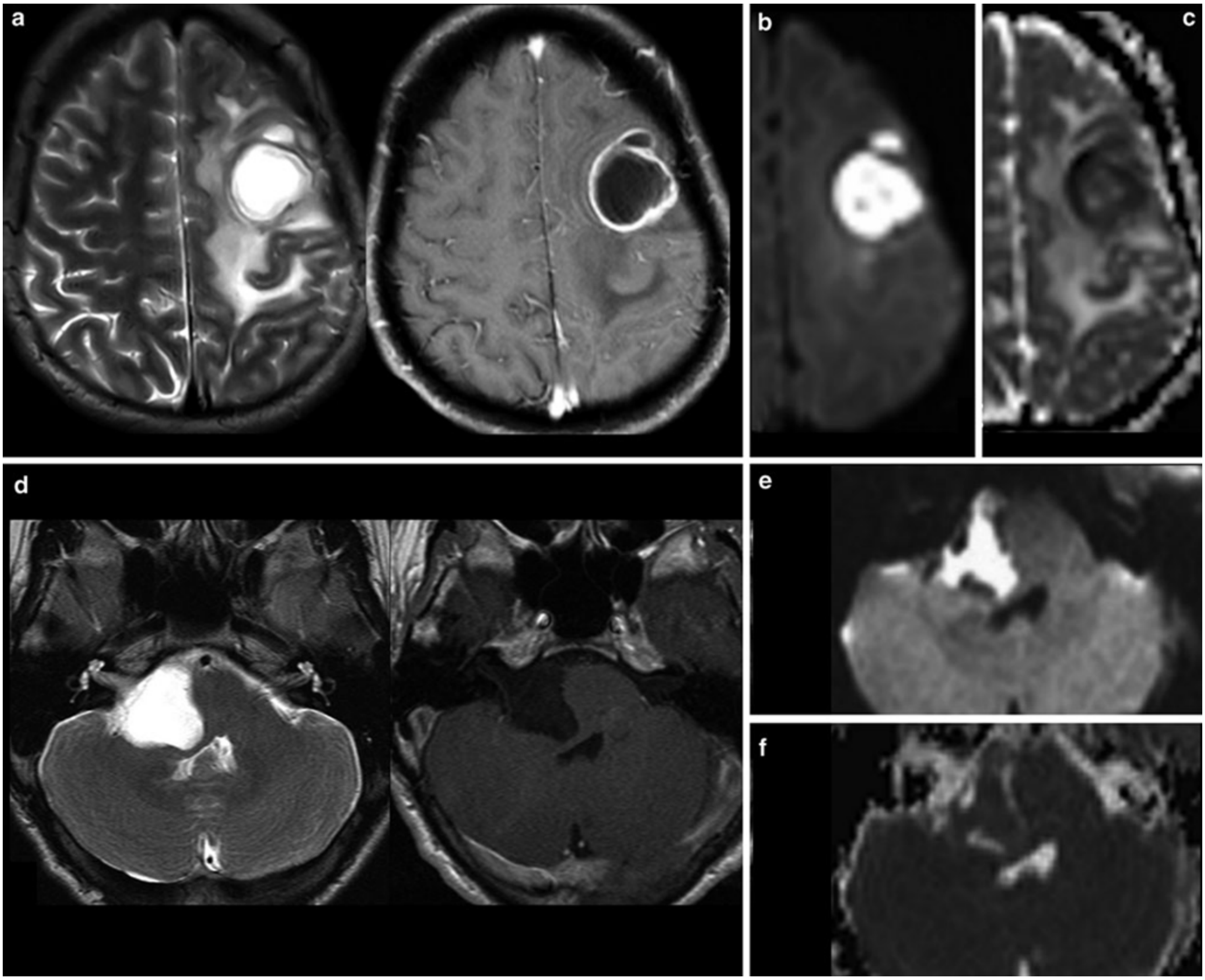

Fig. 1 Very hyperintense DWI lesions with corresponding lower ADC values. Ring-enhancing lesion with edema in patient with lung cancer (**a**). Very high DWI signal (**b**) with lower ADC values (**c**) were highly suspicious for an abscess, which was confirmed by stereotactic puncture. Also note the hypointense signal of the capsule in T2WI (**a**). The hyperintense and nonenhancing lesion in the pontocerebellar angle (**d**) shows high DWI signal (**e**) with lower ADC values (**f**). These features are almost pathognomonic for epidermoids differentiating them from arachnoid cysts and cystic schwannomas

(Fig. 2). Veins should be screened for thrombosis and arteries for any other pathology (e.g., aneurysm, malformations). Beside hemorrhage, T2*WI and especially thin-sliced susceptibility-weighted imaging (SWI) depict the "blooming" of any collection of blood either in hemorrhages and micro bleeds, cavernomas, or in vascular thromboses (Tong et al. 2008) (Fig. 3). The skull base, orbit, and viscerocranium should be screened for tumors and inflammatory diseases as they may secondarily infiltrate into the brain (Fig. 4). Especially in younger patients, the eyes and skin should also be inspected for malformations and hamartia indicating neurocutaneous diseases (Kandt 2003).

First Question: Tumor or Tumor-Like Lesion?

The most important question regarding the tumor entity is the differentiation between intracerebral (also named intra-axial) and extracerebral (extra-axial) localization. Extracerebral tumors are mostly benign neoplasms like meningiomas and schwannomas, whereas intracerebral tumors are malignant in the majority of cases, especially in older patients. Extracerebral tumors are rare in younger patients; thus neurocutaneous syndromes, previous radiation therapy, or metastases (e.g., neuroblastomas) should be considered.

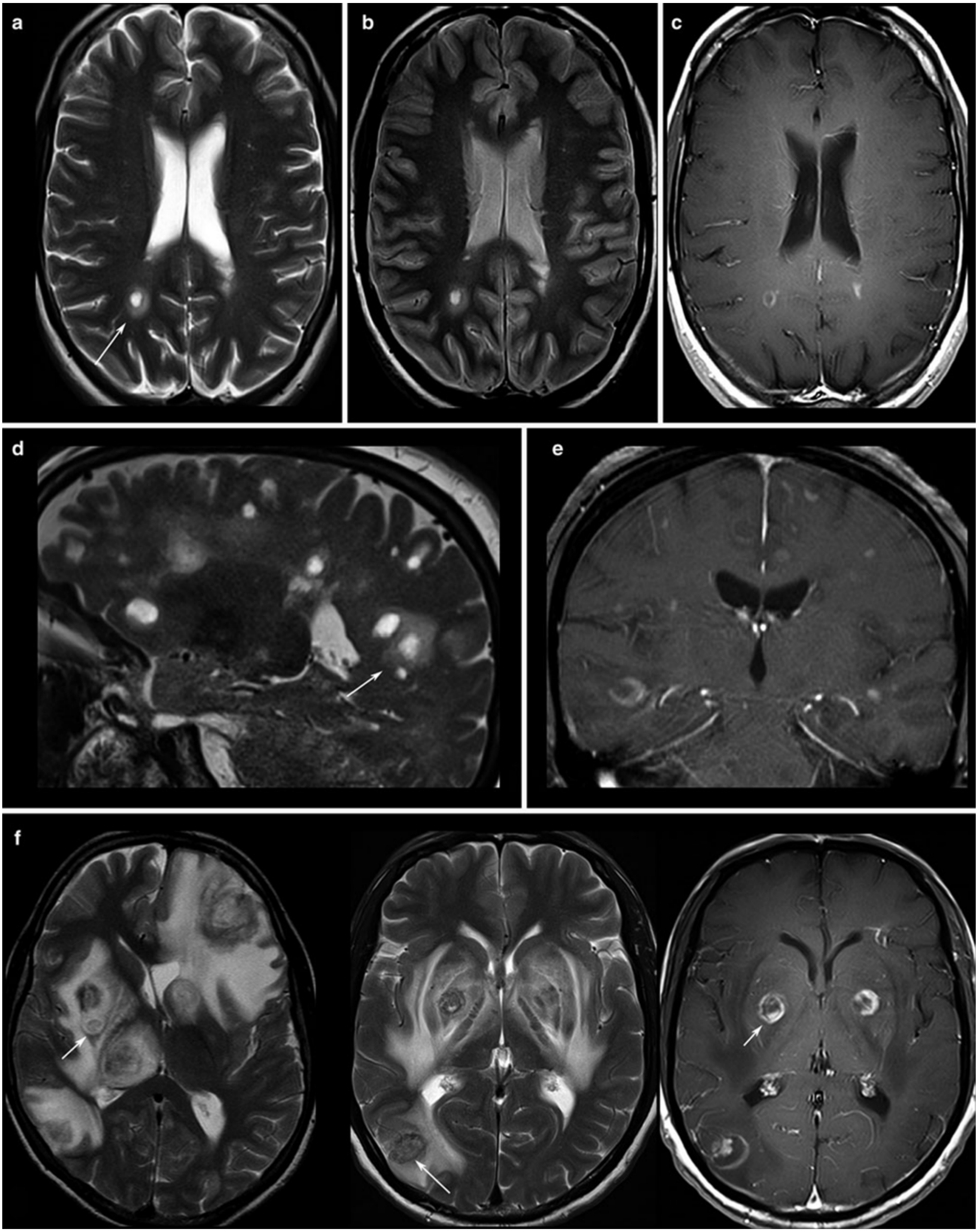

Fig. 2 Patients with multiple sclerosis, the T2WI (**a**, **d**) and proton density WI (**b**) show the typical "halo" surrounding the lesion (*arrows*). T1WI depicts round, patchy, (**c**) or crescent-shaped (**e**) enhancements which are typical for demyelinating lesions. (**f**) Toxoplasmosis reveal target phenomena in some of the lesions (*arrows*) which are typically located in the basal ganglia and in the subcortical region

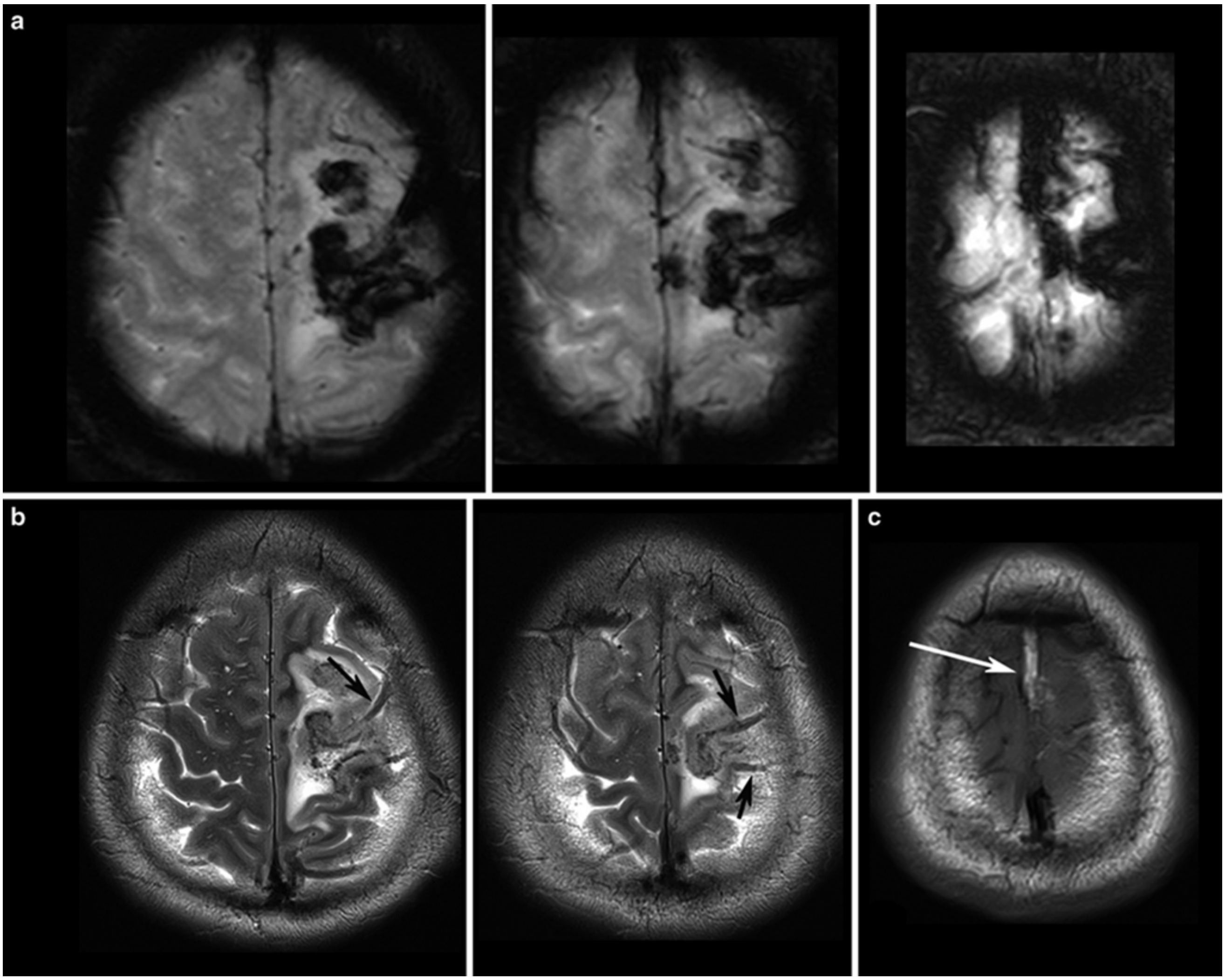

Fig. 3 T2*WI (**a**) shows the blooming of the thrombosis in the cortical veins (*arrows* in **b**) and in the superior sagittal sinus which is hyperintense in the T1WI (*arrows* in **c**) due to methemoglobin

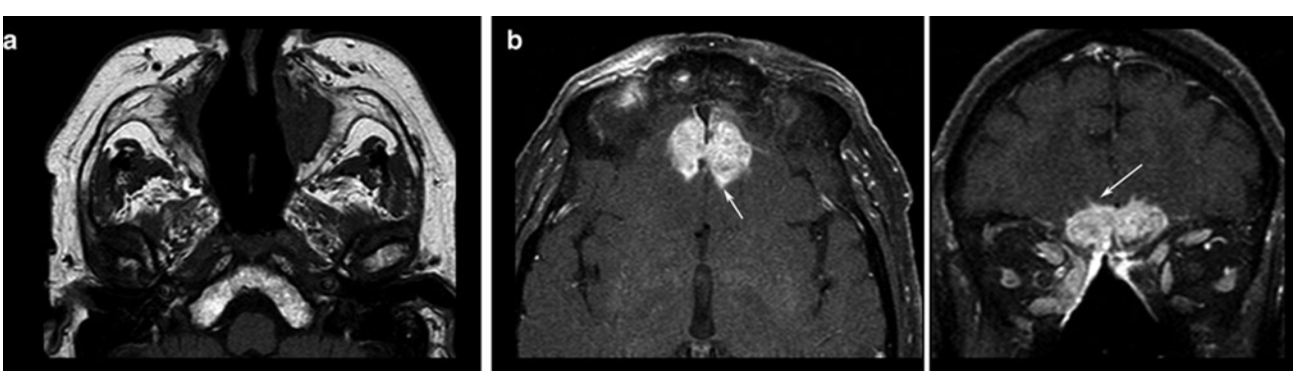

Fig. 4 T1WI spin echo sequence shows the destruction of bony cortico-steroid medication. Patient had Wegener granulomatosis of the structures in the nasal cavity (**a**) and hyperostosis resulting from the infiltrates of the frontal skull base (**b**), developing intracranial tumor masses chronical infection. Also note the hypertrophic subcutaneous fat due to with small intracerebral infiltration (*arrows*, surgically confirmed)

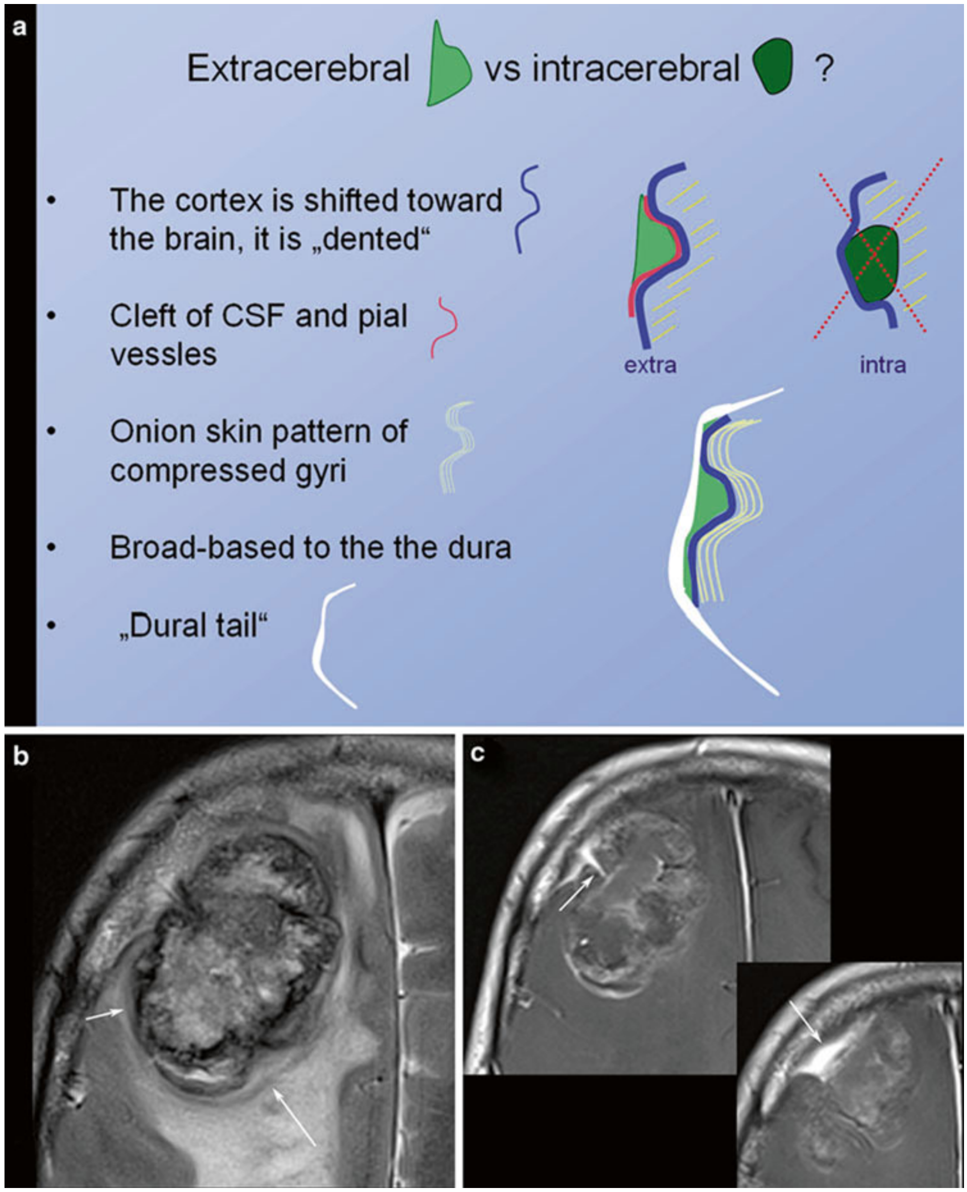

Fig. 5 Schematic illustration of extracerebral versus intracerebral tumors is shown in (**a**). In meningiomas with irregular enhancement and marked intracerebral edema, (**b**) the extracerebral location might be difficult to evaluate. However, broad and sometimes umbilicated basis to the thickened dura (*arrow* in **c**) and the shifted cortex (*arrow* in **b**) may help to correctly diagnose extracerebral tumor

Second Question: Intracerebral (Intra-axial) or Extracerebral (Extra-axial)?

Signs indicating an extracerebral tumor are illustrated in Fig. 5.

The next question addresses the number of tumors. Singular large intracerebral tumors are mostly glial tumors; otherwise metastases should be suspected.

Finally, the possibility of a cerebral lymphoma should be considered. Corticosteroids should be withheld if a lymphoma is a differential diagnosis based on the imaging findings until a stereotactic needle biopsy has been performed (Fig. 6). Lympholytic activity of corticosteroids makes the histopathological diagnosis more difficult or even impossible. Therefore, radiologists should be familiar with imaging features of this tumor entity (Bühring et al. 2001).

Third Question: Is Cerebral Lymphoma Possible?

2.2 Tumor Localization

The description of tumor localization should consider two aspects: the precise anatomical localization and the spatial relation to functional representations of motor and language skills. Anatomical designation not only means the lobe and gyrus but also the relationship to white and gray matter

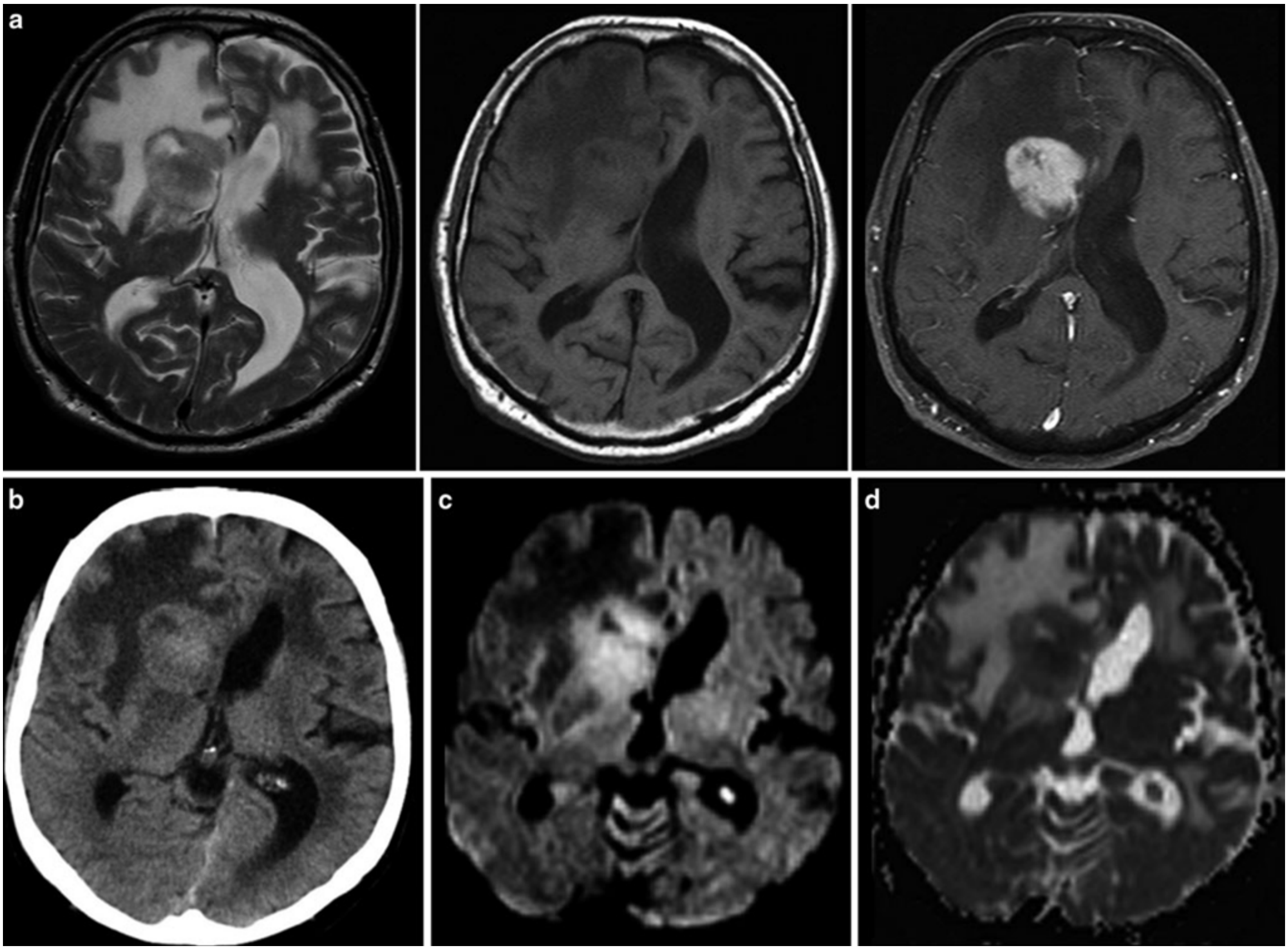

Fig. 6 Typical primary CNS lymphoma (PCNSL) showing features of a tumor with dense-packed tumor cells. The tumor is almost isointense to the gray matter in T2WI and T1WI (**a**) and enhances contrast agent with a patchy appearance. On CCT the tumor is isodense to gray matter (**b**). *DWI signal is bright due to the narrowed extracellular space* (**c**) *and corresponding ADC values are low* (**d**)

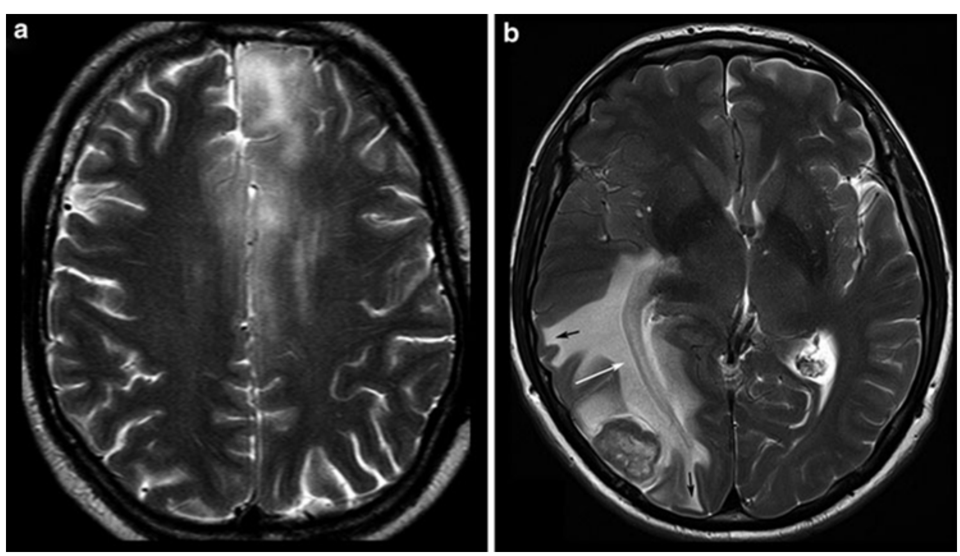

Fig. 7 Diffuse infiltrating gliomas often infiltrate the cortical *gray* matter (left and also right frontal lobe in **a**), resulting in a swelling and blurring *gray-white* matter interface ("ribbon sign"). In contrast, vasogenic edema (**b**) respects the *gray-white* matter interface and white matter tracts, extends finger-like into the gyri (*black arrows*), and demasks the optic radiation (*white arrow*)

Table 2 Cerebral anatomy with respect to brain function

	Spatial resolution	Distortions and signal loss	Tumor related dislocation			
Sectional MRI	+	GE >> SE	Anatomical distortions in large tumors (edema)	White matter tracts mostly invisible	Anatomical interindividual variances	Variance between function and anatomy
3D MRI	++	Due to GE	Anatomical distortions in large tumors (edema)	White matter tracts mostly invisible	Anatomical interindividual variances	Variance between function and anatomy
Surface reformatting	++	Minimal		White matter not depicted	Contorted proportions	
fMRI	Reduced	Skull base, blood products, metal, mineral	False-negative or positive activations	Discrepancy between vascular response and neuronal activity	Task dependent activation depicts only part of language function	Needs intact neurovascular coupling
DTI	Reduced	Skull base, blood products, metal, mineral				
Tractography	Reduced	See DTI	May assume tract damage		Different methodologies	Significantly affected by the method

structures. The infiltration of the cortical ribbon (cortical ribbon sign) and thickening of the corpus callosum are typical features of infiltrative glial tumors which help to differentiate them from vasogenic edema (Fig. 7).

The primary motor, sensory, auditory, and visual cortices are assigned at the brain surface. However, surface relief may be difficult to recognize in sectional images and anatomy might be distorted by the tumors. The identification of surface anatomy is easier with interactive observation of 3D objects. Further, planar reformatting of the brain surface helps to delineate the central sulcus which marks the perirolandic region with the primary sensorimotor cortex (Table 2) (Figs. 8 and 9).

However, this direct allocation of anatomy to function and vice versa is only true for primary cortical areas: the variance increases with the complexity of brain function. One of the most investigated functions is the language since neurosurgeons have the primary goal of preserving the language during tumor resection. Another critical issue is to protect important white matter tracts. To achieve these goals, functional MRI (fMRI) and tractography are well-established components of presurgical imaging (Fig. 10). MR tractography virtually dissects functionally critical white matter tracts, such as the corticospinal tract and the arcuate fascicle (Fig. 11), enabling the neurosurgeon to plan the surgical approach which best preserves the tract during resection. However, uncritical and inexpertly handling of these methods bears the imminent danger of misinterpretations (Jellison et al. 2004).

Therefore, the main indication and the undoubted strength of fMRI and DTI is the presurgical planning. Functional language MRI can localize language dominant hemisphere (Ruff et al. 2008; Roux et al. 2003; Kim et al. 2009; Spreer et al. 2002) (Fig. 11). However, surgical resection of tumors in the language areas of the dominant hemispheres still requires awake craniotomy and direct brain mapping to prevent postsurgical aphasia (Kim et al. 2009). Tractography may depict the relation between tumor and white matter tract, but it should not determine the extent of resection during surgery.

2.3 Tumor Malignancy

The imaging criteria of malignancy include blurring tumor margins, tumor edema, necroses, and contrast enhancement. However, these signs of malignancy are not as reliable as they allow the definite categorization into low- and high-grade tumors. Diffuse gliomas infiltrate the brain tissue by definition. Therefore, they mainly do not have sharp margins. In contrast, metastases and also highly malignant PNETs often have sharply delineated margins between tumor and edema (Fig. 12). Low-grade neuroepithelial glioneuronal tumors like gangliogliomas and DNETs may be associated with cortical dysplasia which may blur anatomical structures. Further, especially gangliogliomas may show areas of contrast enhancement (Fig. 13). Necroses are difficult to differentiate from tumor cysts; in both, the

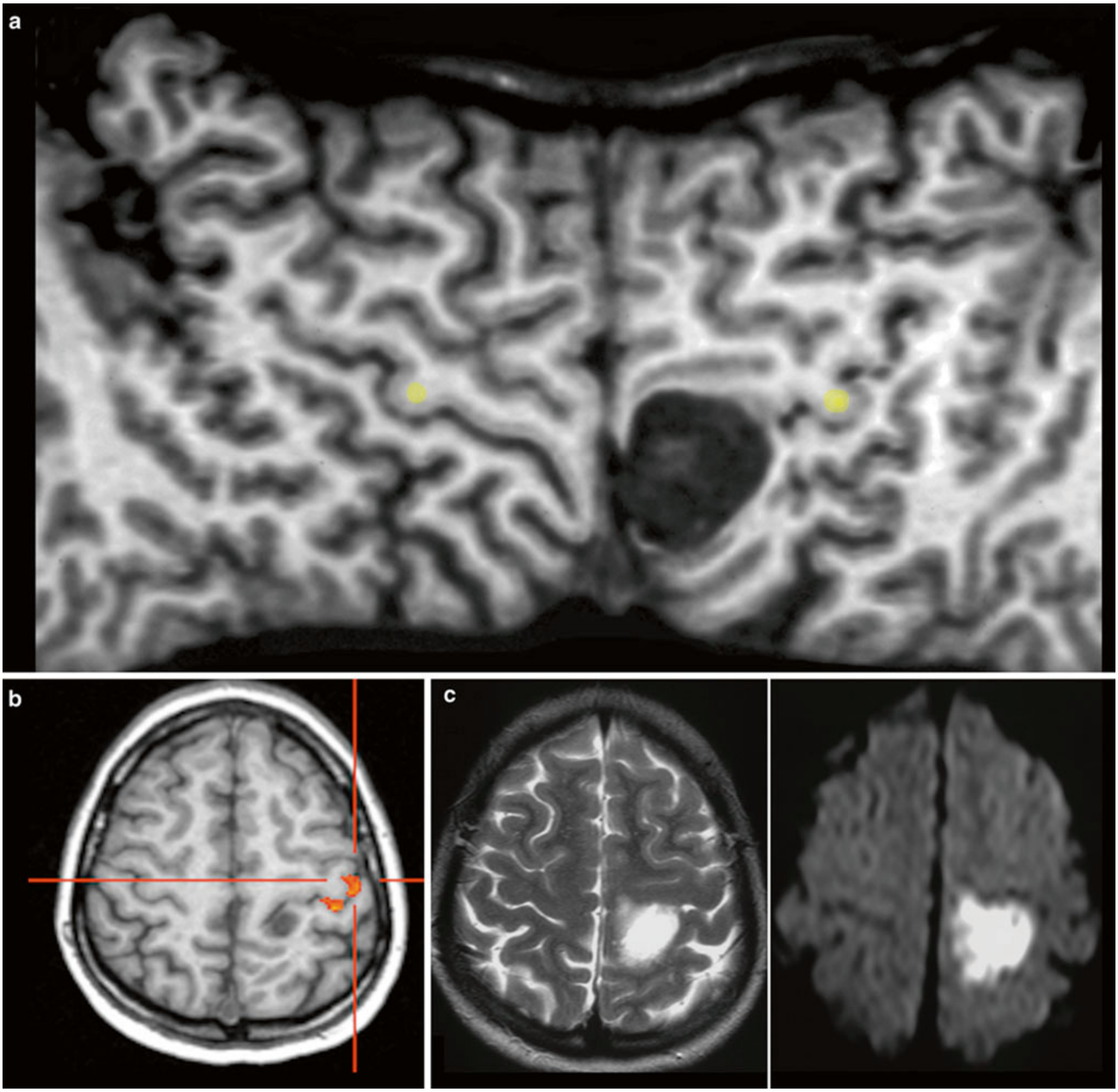

Fig. 8 The surface-reformatted image (**a**) shows both hemispheres from the interhemispheric fissure to the Sylvian fissure, displaying the entire central sulcus. The space-occupying lesion is located in the post-central gyrus, shifting the precentral sulcus forward. The fMRI *with motor activation of the hand* (**b**) *and intraoperative monitoring confirmed this localization. It was an epidermoid with characteristic very hyperintense signal in T2WI* (**c**) *and very high signal on DWI* (*see also Fig.* 1)

margins may enhance. However, cysts enhance linearly in contrast to the often partially nodular enhancement at the margins of tumor necroses.

Malignant gliomas generate tumor vessels with impaired blood-brain barrier. The higher vascular permeability causes extravasal accumulation of contrast agent with consecutive signal increase on T1WI. Therefore, contrast enhancement is one important hallmark of tumor malignancy. Considering that most of the WHO grade I astrocytomas and a larger amount of grade II oligodendroglioma (White et al. 2005) may also enhance due to higher vasculature, this sign of malignancy has a limited value (Fig. 14). On the other side, about 30 % of high-grade WHO III astrocytomas do not enhance contrast agent (Scott et al. 2002; Muragaki et al. 2008; Chaichana et al. 2009) (Fig. 15).

Although the histopathological WHO classification still is the gold standard to categorize tumor entity and their malignancy, the molecular genetic profile of a brain tumor

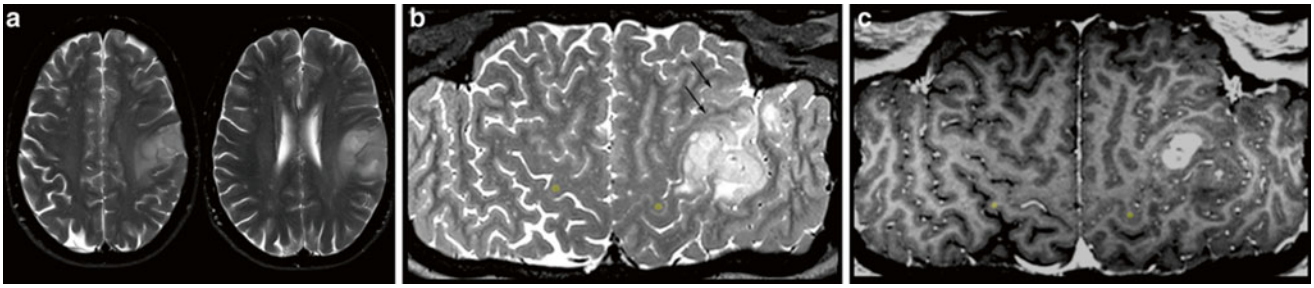

Fig. 9 Exact location of this perirolandic glioma is difficult to define in axial slices (**a**). The surface-reformatted image depicts the precentral gyrus in whole length, showing the hand knob of the motor hand area (*yellow dots* in **b** and **c**). The tumor including its enhancing part is located in the postcentral region, but T2-weighted reformatted image (**b**) clearly shows infiltration into the precentral gyrus and the inferior frontal gyrus (*arrows*)

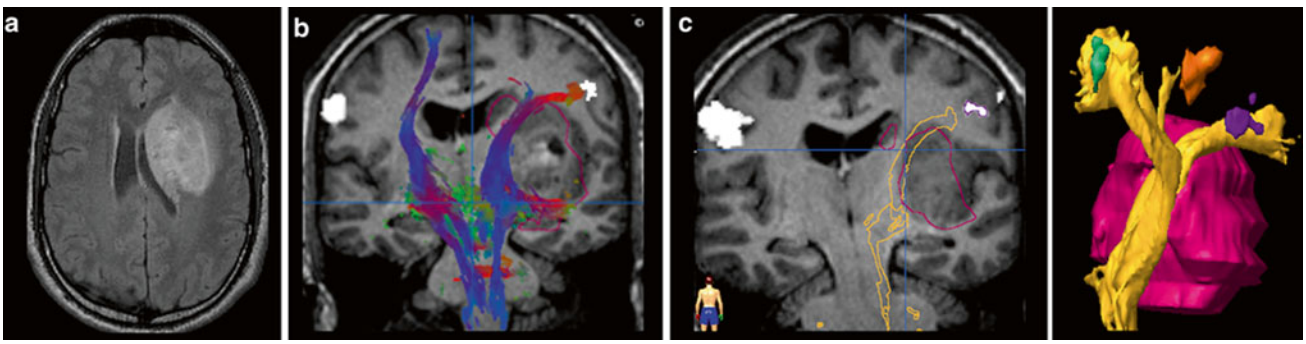

Fig. 10 Presurgical DTI and fMRI in brain tumors. FLAIR shows a tumor located in the basal ganglia in a patient with latent hemiparesis (**a**). Tractography was performed with BrainLab® using the functional areas of the tongue, hand, and foot in the motor cortex (*white spots*) as seed region and the cerebral peduncle as target region. In (**b**) the corticospinal tract is shown with different color-coded tracking fibers. In (**c**) preoperative virtually dissected corticospinal tract was transformed in a three-dimensional object which can be integrated into a standard neuronavigation system, allowing for intraoperative visualization of the tracts

becomes more and more important for tumor diagnosis. Up to date, there are only few studies investigating imaging features of brain tumors with different molecular profiles (Aghi et al. 2005; Eoli et al. 2007; Diehn et al. 2008). Considering that these profiles determine the metabolism of the tumor, MR spectroscopy and metabolic imaging with PET should be the methods of choice to recognize molecular pattern ("PET Imaging of Brain Tumors").

2.4 Tumor Monitoring

Monitoring treatment effects on brain tumors becomes more and more complex. In conventional MR imaging, contrast enhancement is the hallmark of tumor growth. However, this imaging feature is more than ambiguous regarding tumor monitoring. On the one side, endothelial cells are sensitive to radiation and chemotherapy and—most often associated with temozolomide treatment—therapy-induced changes may yield a blood-brain barrier damage with contrast enhancement and mass effect of the treated brain tissue (Fig. 16). Neuro-oncologists introduced the term "pseudoprogression" defining an increased (>25 % in diameter) or new enhancement of irradiated tissue usually detected within 3 months of radiation that subsequently abates without further treatment. This phenomenon is observed in approximately 20–30 % of patients treated with today's standard therapy for glioblastomas (Brandsma et al. 2008). On the other side, new antiangiogenic treatments normalize the blood-brain barrier damage and thus reduce the contrast enhancement independent from real antineoplastic effects, which is named "pseudoresponse" (Figs. 17 and 18). Being familiar with the imaging features of infiltrative brain tumors may however help to recognize nonenhancing tumors (Fig. 18). Neuro-oncologists are aware of these diagnostic challenges and addressed these problems in their new response criteria for malignant gliomas (Wen et al. 2010).

Figure 19 illustrates these response criteria (RANO) (Wen et al. 2010).

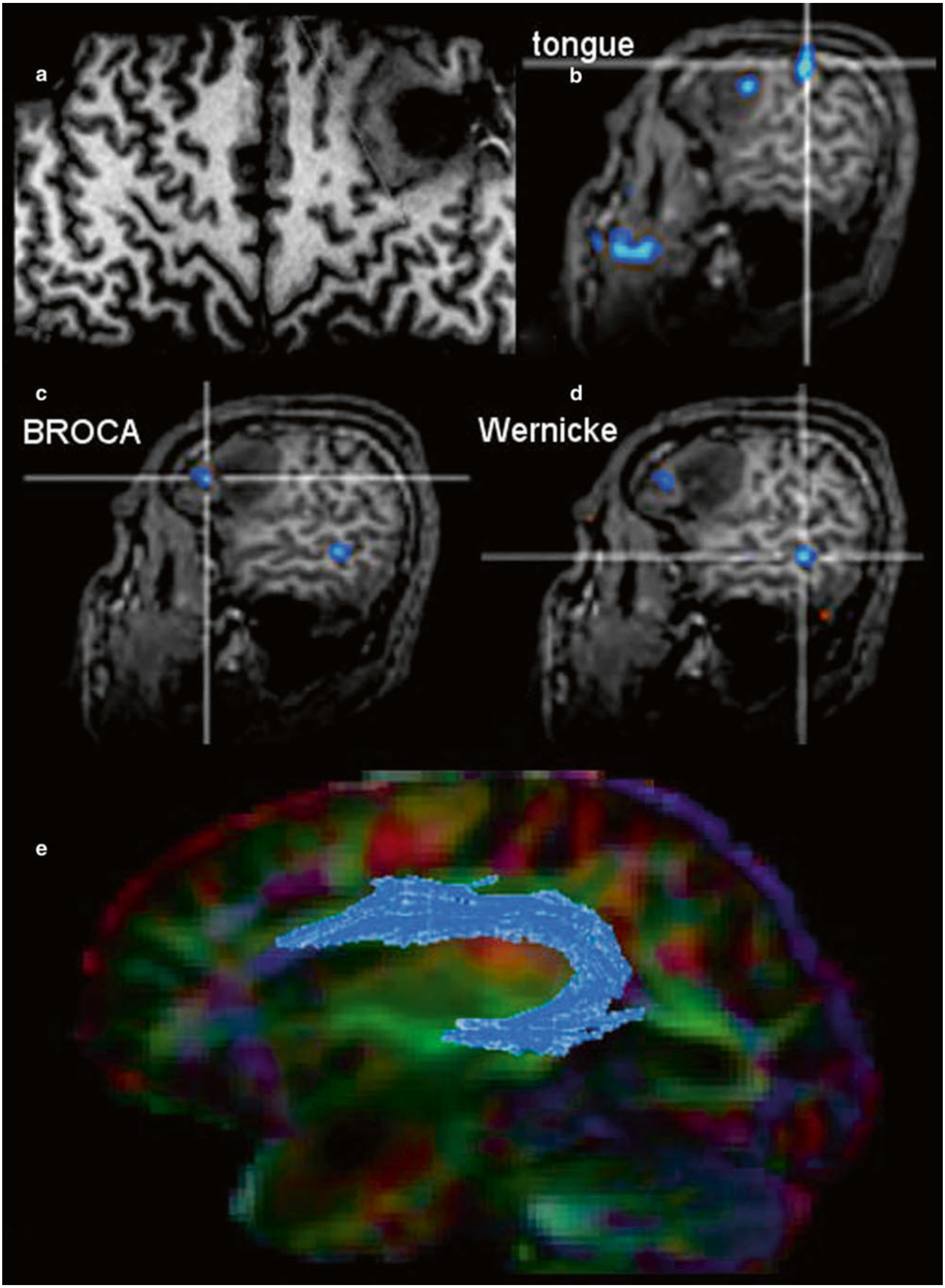
a
tongue
b
c
BROCA
d
Wernicke
e

Fig. 11 The surface-reformatted image shows a glioma in the inferior frontal lobe (**a**). The motor function of the tongue was located behind the tumor, but one activation area was found inside the tumor (**b**). Patient had a seizure with reversible aphasia. FMRI was performed using verbal subtest of the German Wilde Intelligence Test: The patient is required to find a pair of synonyms out of a set of five words presented simultaneously (Spreer et al. 2002). The frontal language activation area (**c**) and the temporal language area (**d**) are both located in the tumor-bearing left hemisphere, which was defined as dominant for language (also confirmed by word generation test). In (**e**) fiber tracking of the arcuate fascicule (blue) projected on the color-direction map is demonstrated in a patient with a tumor near the temporal pole

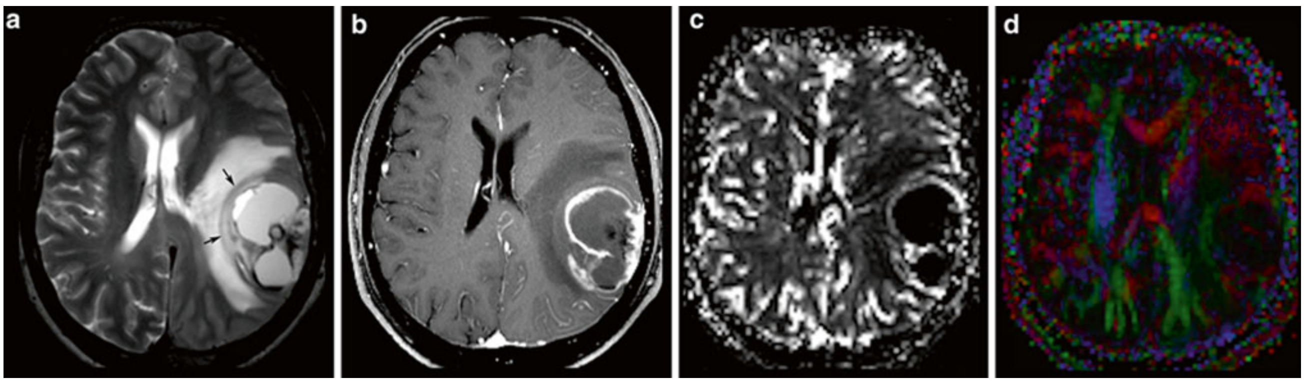

Fig. 12 A large cystic-necrotic tumor abuts the brain surface and is surrounded by huge edema. Margins of the tumor are shapely delineated (*arrows* in **a**). The contrast-enhancing rim, which also involves the brain surface (**b**), shows moderate increase of cerebral blood volume of the tumor margins (**c**), which does not extend into the surrounding brain tissue (which is often seen in glioblastomas). The color-coded FA map (color-direction map) shows that the corticospinal tract (blue area in the right hemisphere) is involved by the edema. The blue indicates diffusion along the inferior/superior axis (**d**)

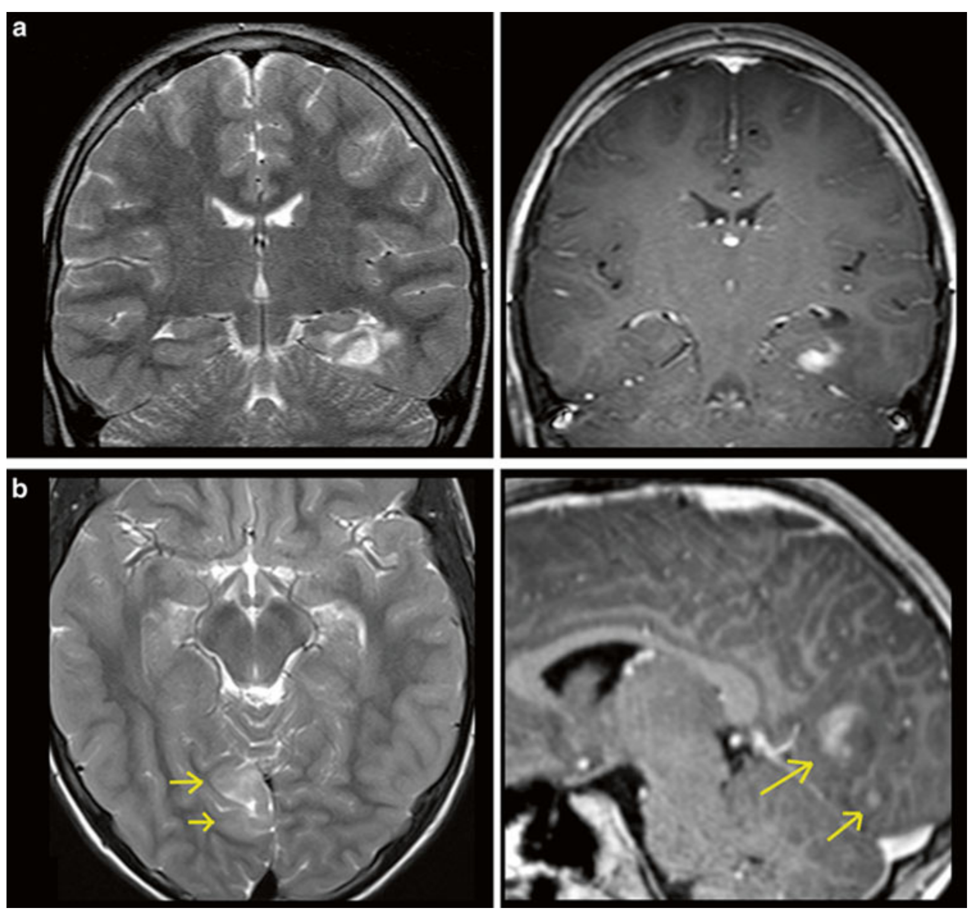

Fig. 13 Two different gangliogliomas are shown in the temporomesial lobe (**a**) as the most typical tumor site of glioneuronal tumors and in the occipital lobe (**b**). Both tumors involve the cortical ribbon and have blurred tumor margins; the occipital tumor has two areas of enhancement (*arrows*)

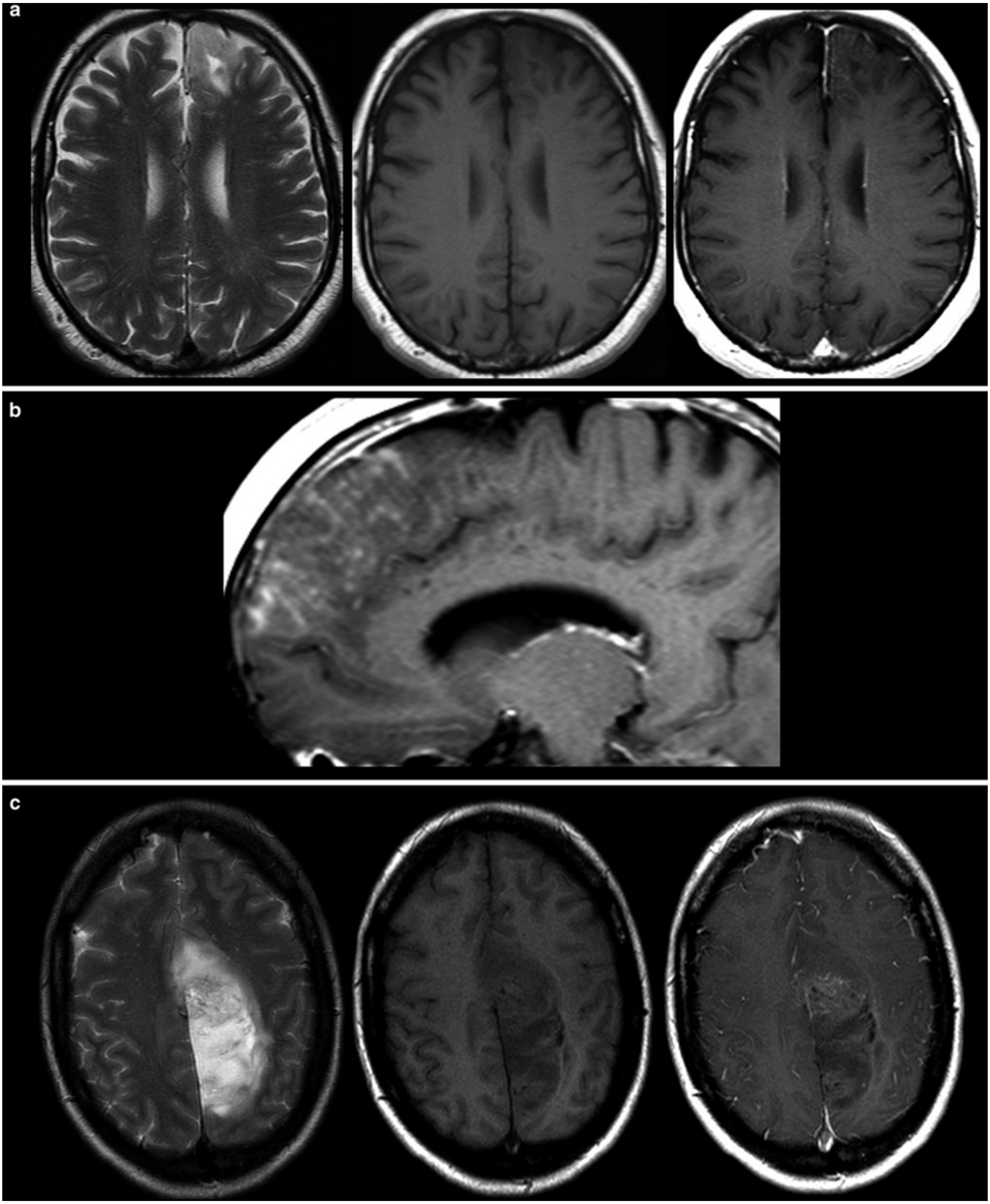

Fig. 14 Two low-grade gliomas with contrast enhancement are shown. A frontal astrocytoma WHO grade II typically infiltrating the cortical ribbon shows faint superficial enhancement (**a**), which was due to subpial infiltration of the tumor (**b**). A large parasagittal oligodendroglioma WHO grade II shows inhomogeneous enhancement in the center of the tumor. It is noteworthy that both tumors have almost no edema

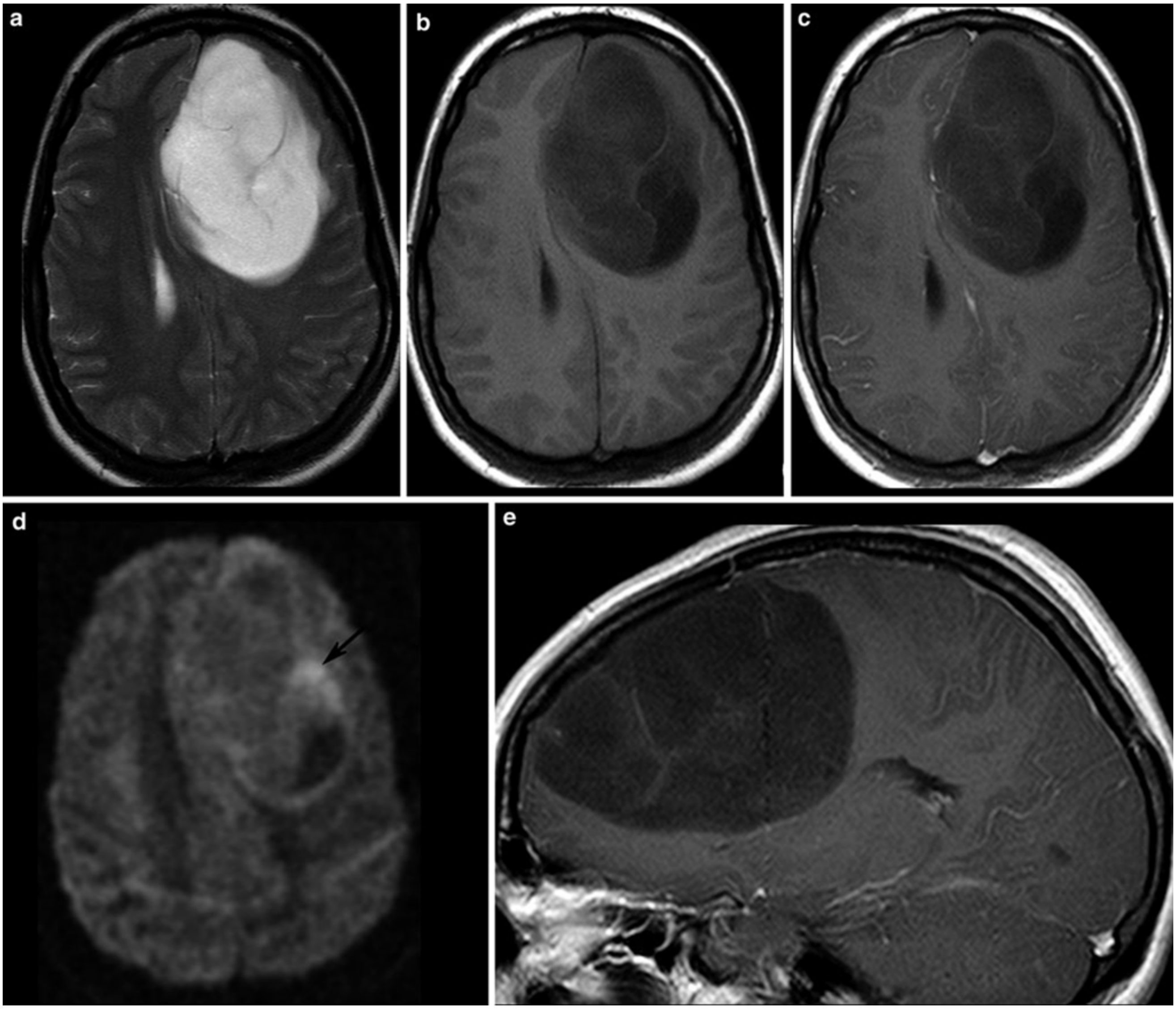

Fig. 15 A large frontal astrocytoma WHO grade III is shown with very high signal on T2WI (**a**) and low T1 signal (**b**, **c**). The DWI yields different tumor compartments with a cystic area (*low signal*), an area with presumably higher cell density (*higher signal*, *arrow*), and the huge tumor mass with intermediate signal. There is at the most faint contrast enhancement (**c**, **e**)

The measurement of contrast-enhancing lesions in irregularly shaped, necrotic, and inhomogeneous or ring-enhancing lesions is challenging and interobserver variability is high (Vos et al. 2003). The most important issue in monitoring glial tumors is to depict the tumor regardless whether or not it enhances. The imaging features of this nonenhancing tumor were more or less ignored longtime. Nonenhancing tumor, or rather brain tissue which is infiltrated by glioma cells, may look like vasogenic edema or gliosis since each of these entities increases T2 relaxation time and is thereby hyperintense on T2-weighted images. However, there are some imaging characteristics which may help to distinguish edema from brain tumor, bearing in mind that tumor cells are often found in both normal and edematous brain tissue (see also Figs. 7 and 17).

To guarantee the comparability of images, a standardized protocol should be mandatory, which has not yet been implemented. The slice thickness should not exceed 5 mm in order to minimize partial volume effects (Wen et al. 2010). Sagittal high-resolution 3D sequences might be advantageous to avoid effects from different slice angulations and partial volume effects, but they also have disadvantages considering movement artifacts and T1 contrast (see Figs. 23 and 24). Further, once there is an artifact (e.g., pulsation artifact), it might be reconstructed in three planes (MPR) simulating a real lesion

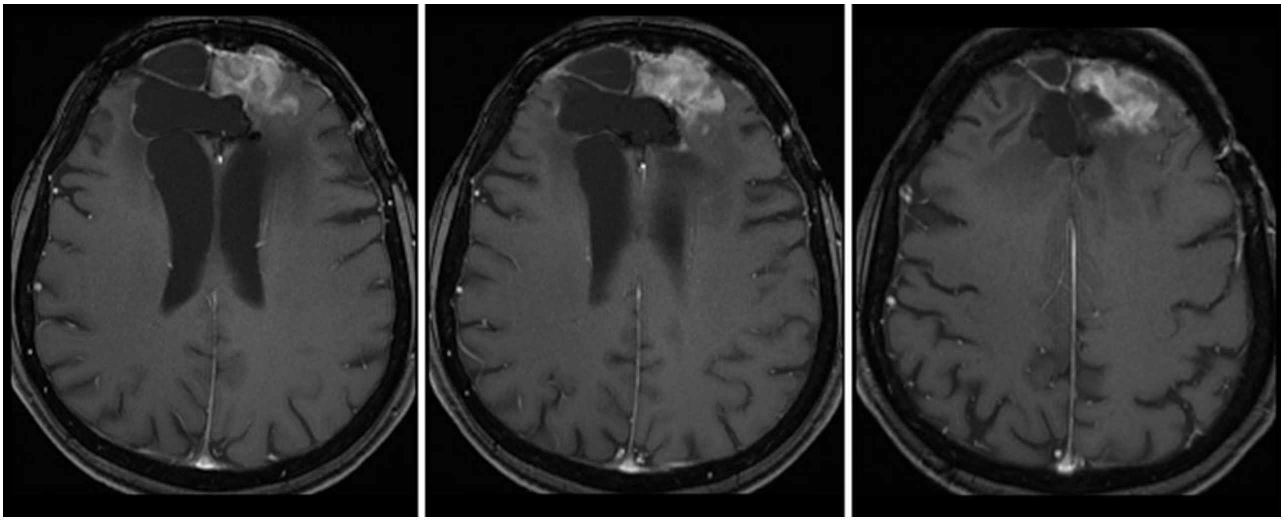

Fig. 16 Patient underwent surgical resection of a frontal glioblastoma and was treated with radiation and temozolomide. The 3 months control yielded new solid enhancement which persisted 2 months later. MR perfusion was not conclusive due to severe artifacts. Histopathological finding after resection of this contrast-enhancing area did not reveal any tumor cells

Fig. 17 Patient had a recurrent glioblastoma, showing mass effect, inhomogeneous tumor area with adjacent edema, and irregular contrast enhancement (**a**). Four weeks after starting treatment with a humanized monoclonal VEGF-antibody, contrast enhancement almost disappeared (**b**), fulfilling the criteria of partial response concerning the enhancing lesion. T2WI might give more information on treatment response (Fig. 18). Also note the hyperintense areas in precontrast T1WI under antiangiogenic treatment

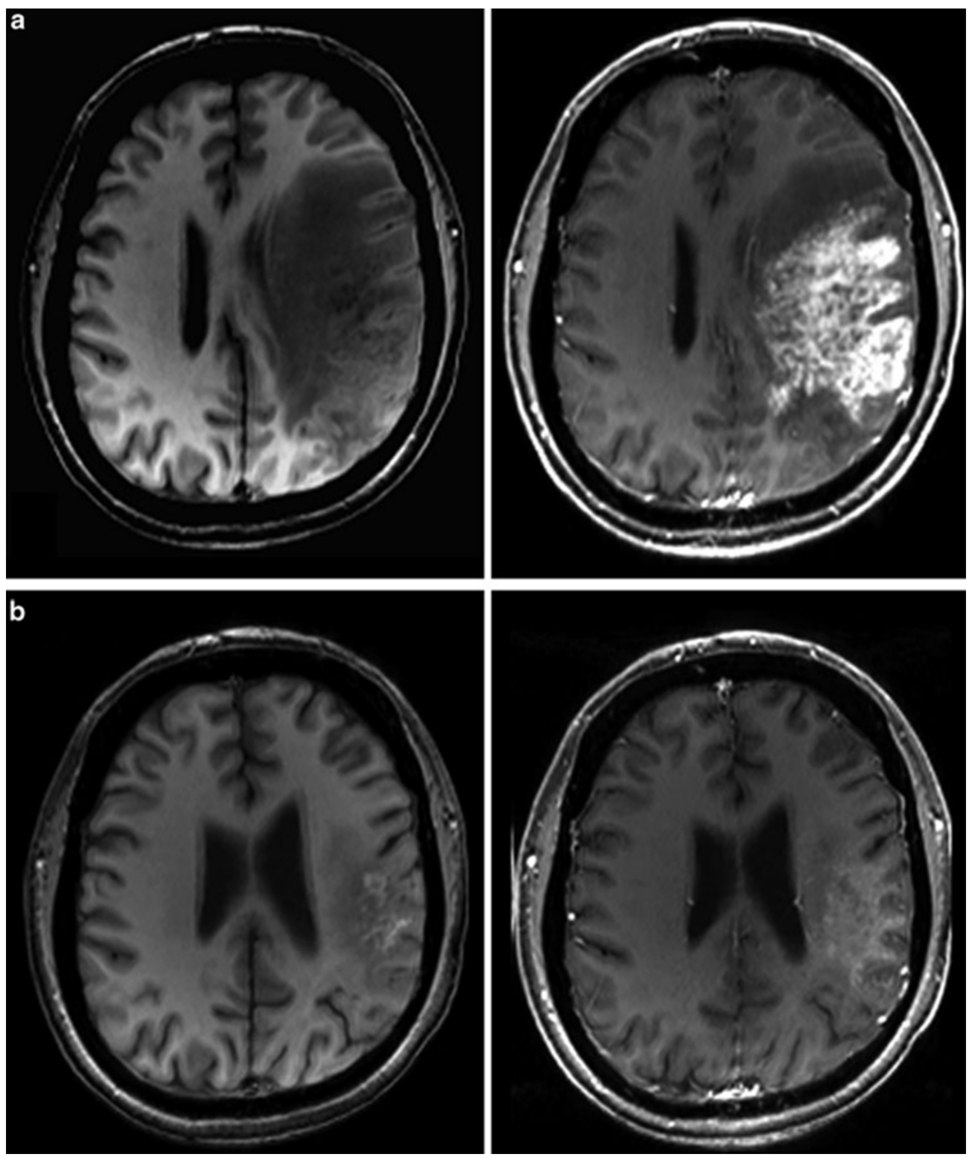

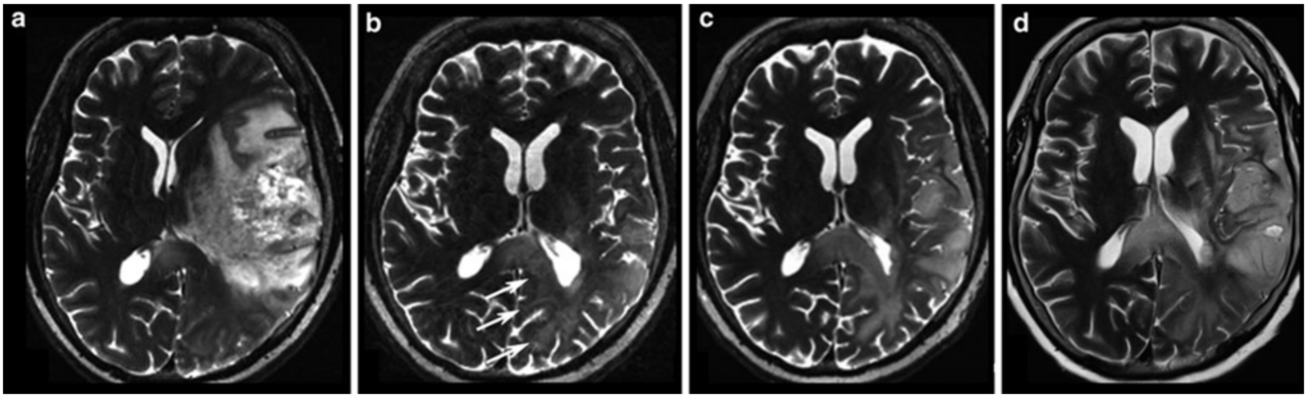

Fig. 18 Same patient as in Fig. 17: T2W slices before antiangiogenic treatment (**a**) and 8 weeks after starting therapy show impressive anti-edematous effect due to the VEGF antagonism (**b**). Mass effect and inhomogeneous tumor area also vanished under this drug, and patient's hemiparesis gradually resolved. However, some areas show new signal increase (*arrows*). In the 8-week follow-up (**c**, **d**), hyperintense areas mainly infiltrating the cortical areas continuously increase, accompanied with worsening of neurological symptoms

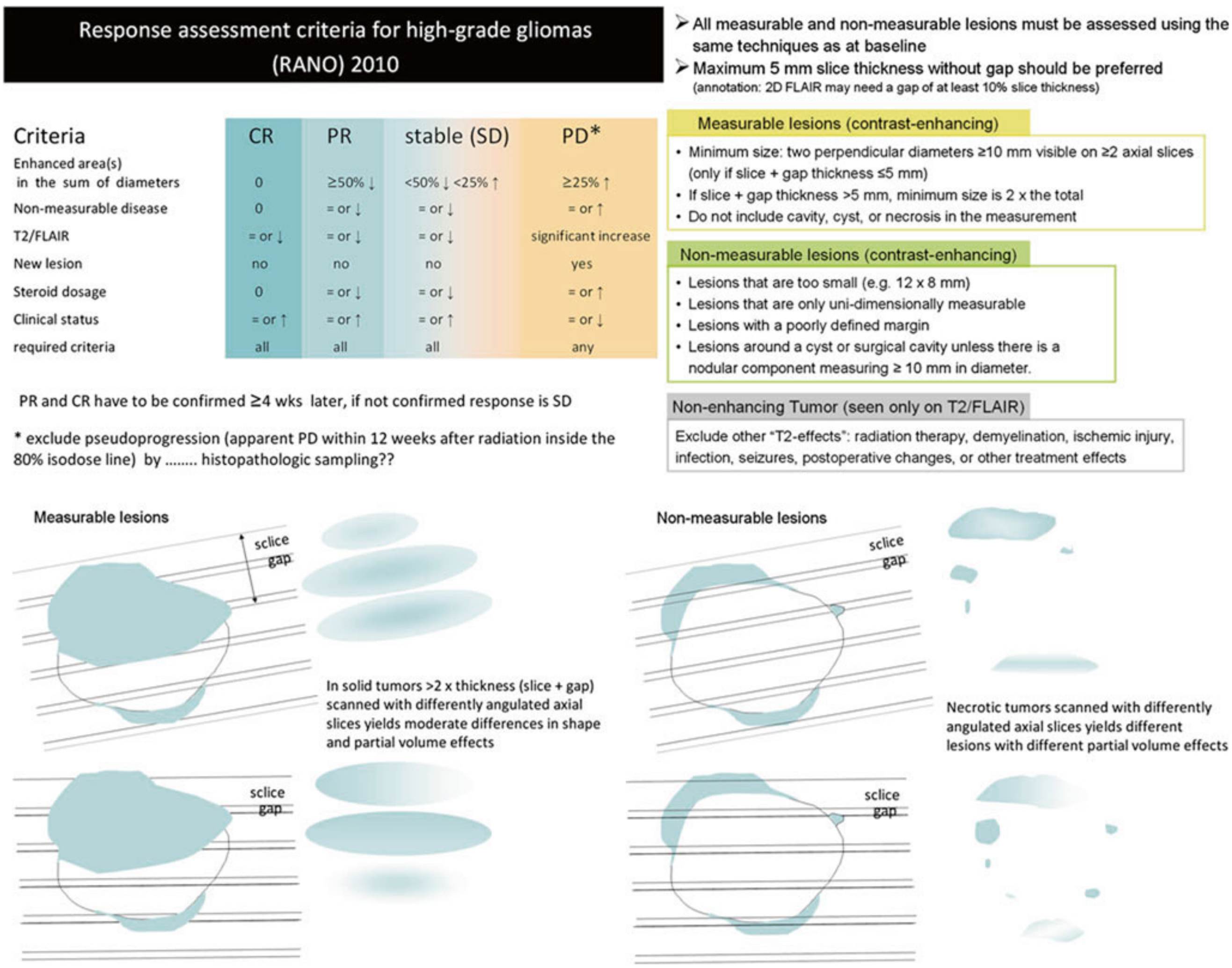

Fig. 19 Updated response assessment criteria for high-grade gliomas: response assessment in neuro-oncology working group (Wen et al. 2010). Further, the difficulties to monitor glioblastomas after surgery leaving a resection cavity are shown for axial slices

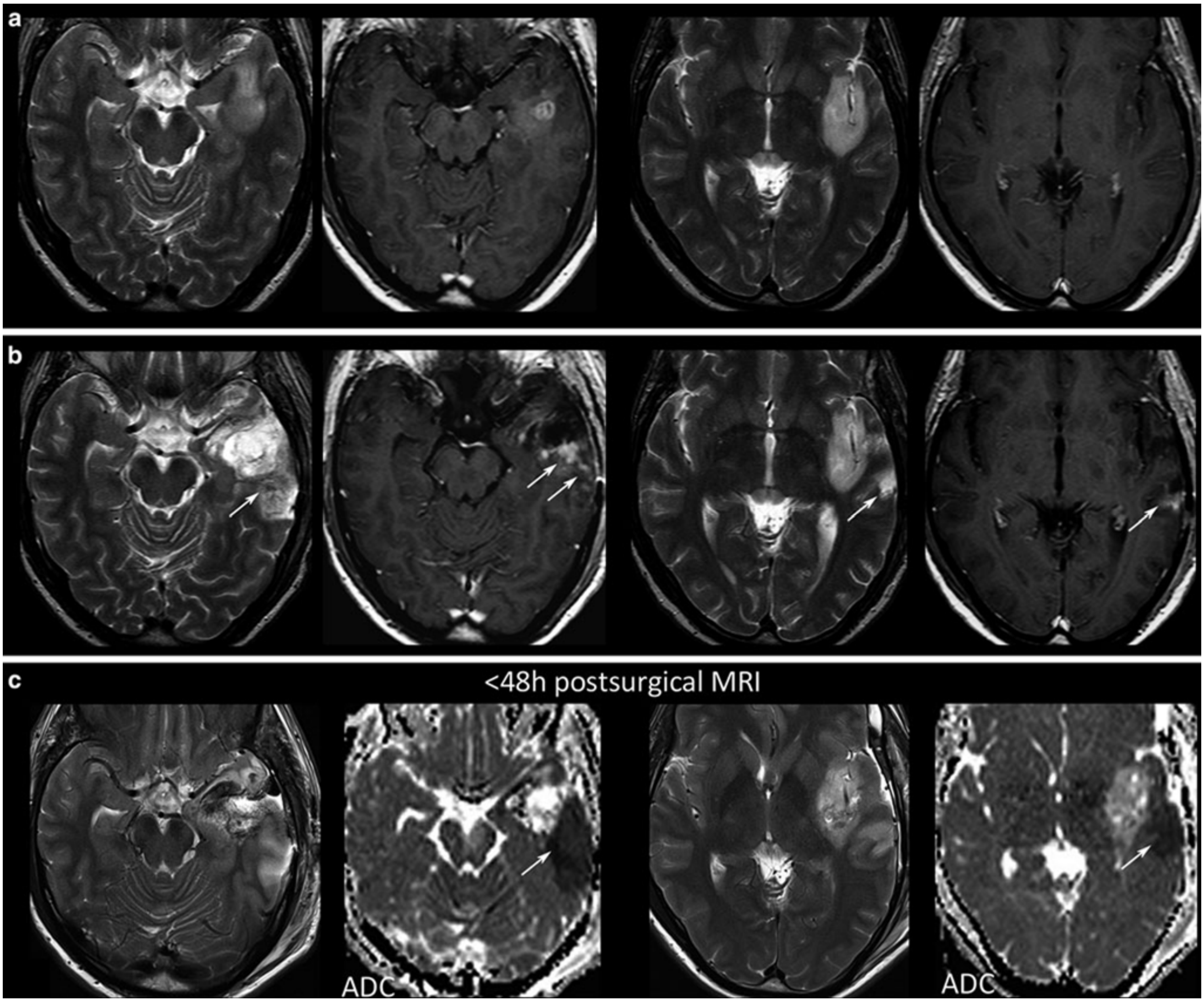

Fig. 20 Postsurgical monitoring of a patient with a high-grade glioma: The contrast-enhancing part of the tumor in the temporal white mater (**a**) was removed, while the insular part was left in place. The MRI control after 3 months showed T2-signal alterations and contrast enhancement in the dorsal margin of the tumor and also in the temporal cortex (*arrows*). These areas were suspicious for tumor recurrence. However, in retrospection to the early postsurgical MRI, (**c**) clearly reveals that these areas match with postsurgical infarction (*arrows*) and thus might not be misinterpreted as tumor progression or possible pseudoprogression

Further, each monitoring begins with an early postsurgical MRI in order to detect the residual tumor which has to be monitored thereafter. Postsurgical control should always include DWI to detect infarcts, which may show confounding enhancement in the follow-up (Fig. 20).

Tumor Monitoring

Early MRI <72 h after surgery with identical noncontrast/contrast T1WI, DWI, and T2* compared to the presurgical MRI.

2D sequences should be acquired with a slice thickness of <5 mm and max. 0.5 mm gap.

Detect enhancing and nonenhancing tumor in 2 different orientations (e.g., axial, coronal).

Perform follow-up with identical imaging protocol. Include DWI and PWI.

2.5 Imaging Protocol

The imaging protocol should (1) characterize the tumor tissue, (2) localize the tumor, (3) show the extent of the tumor, and (4) appreciate the malignancy of a brain tumor.

MRI is the method of choice to characterize soft tissue.

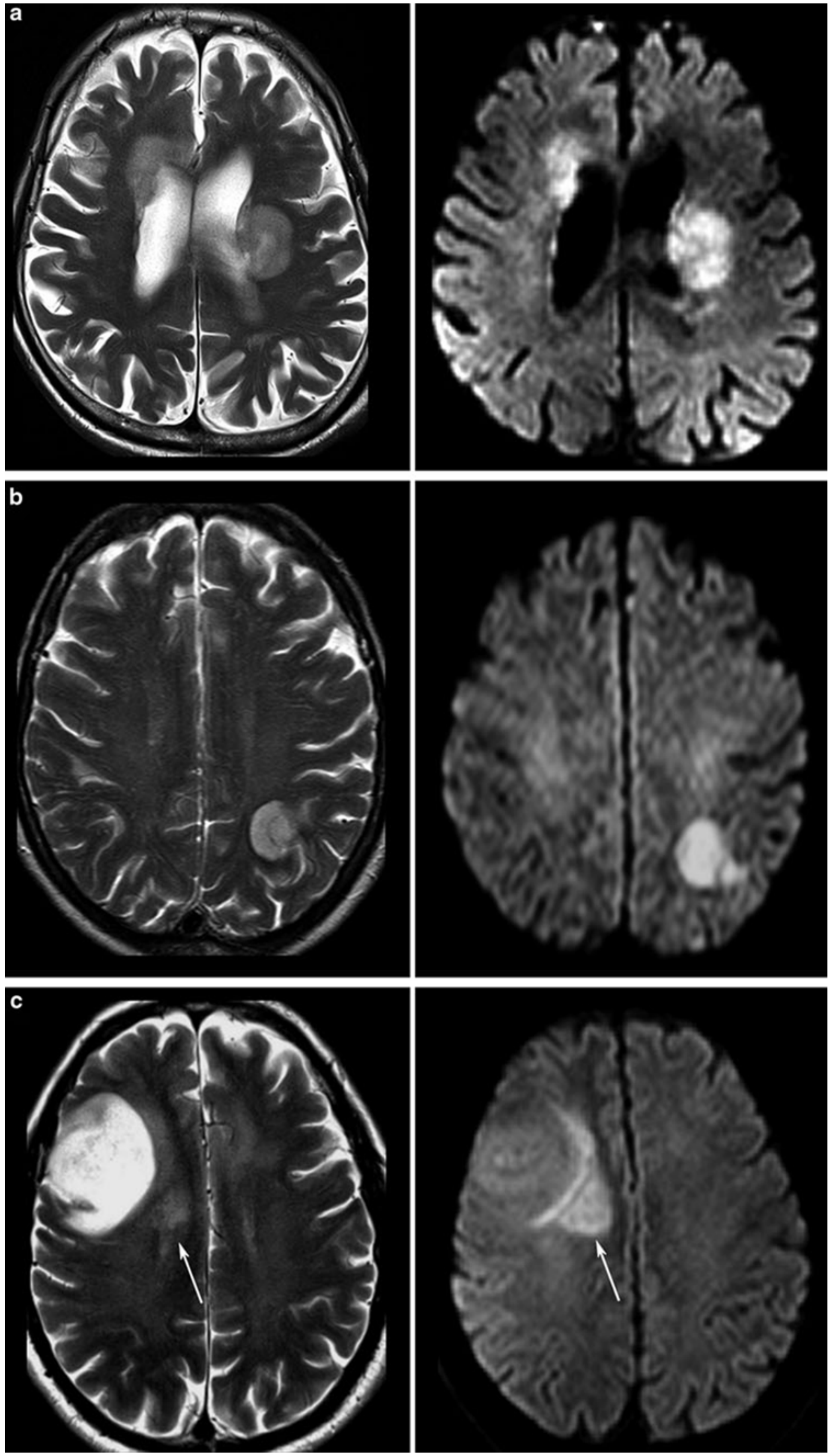

Fig. 21 Tumors with different signals on T2WI: In (**a**) the same patient with PCNSL is shown as in Fig. 6. The tumor is only slightly hyperintense to gray matter and DWI shows high signal due to the compact small cell matrix. High-grade gliomas may also show T2 and DWI signals which are similar to PCNSL if obvious necrosis is lacking (**b**). The astrocytoma WHO grade III in **c** has a large hyperintense area near the brain surface, while the adjacent brain tissue is infiltrated presumably with more densely packed tumor cells (not proven, because this area was not removed at surgery)

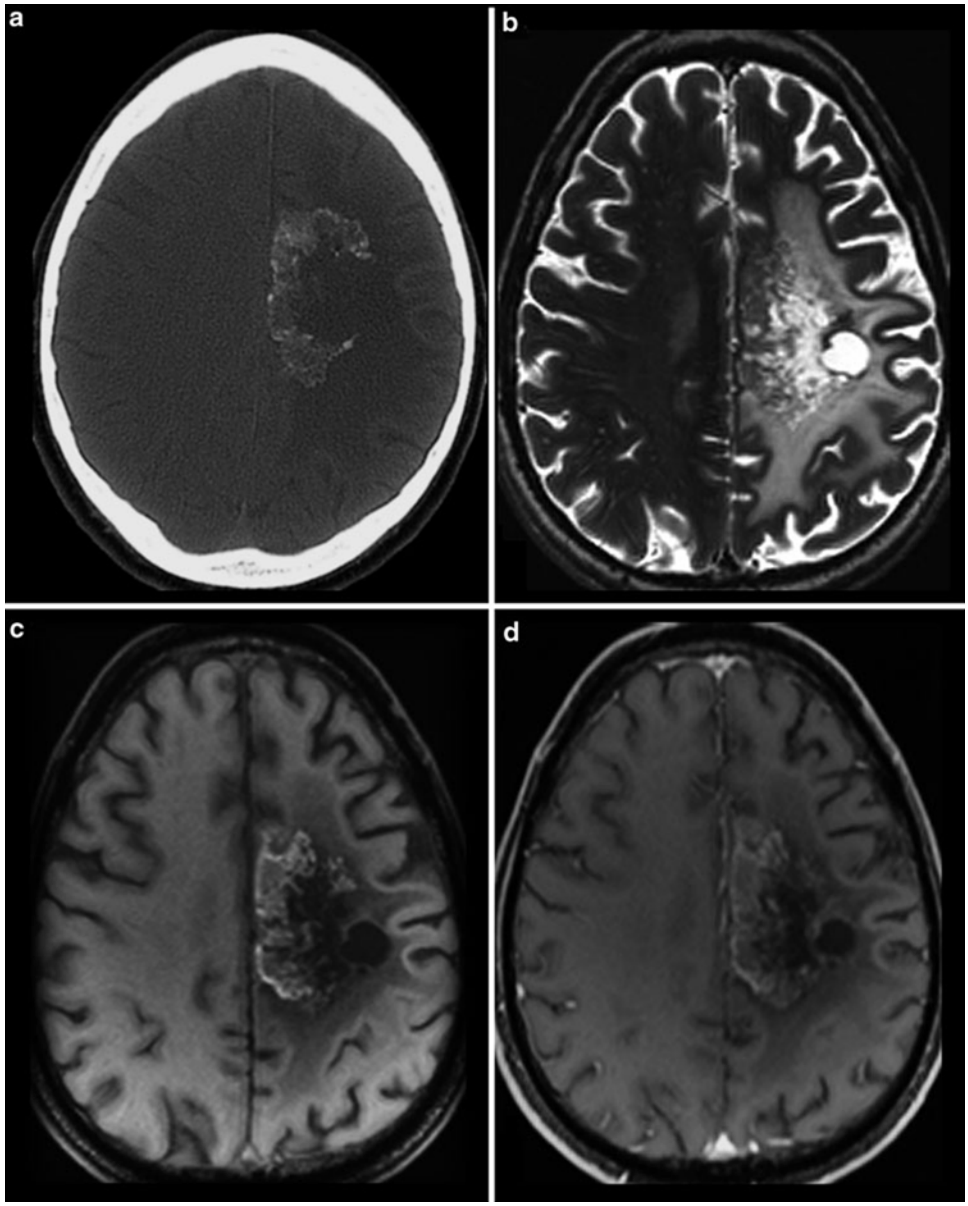

Fig. 22 CCT (**a**) and MRI (**b**–**d**) of a patient treated with antiangiogenic drug. CT yields calcifications in the tumor area which are also hyperintense in the precontrast MRI (**c**). Therefore, precontrast T1WI should be always considered because otherwise these hyperintense areas may be misinterpreted as enhancing areas (see also Fig. 17)

T2-weighted images (T2WI) reflect cell density of a tumor, because tumors with compact small cell matrix are rather isointense to gray matter. Typical tumors with dense cell structures are CNS lymphomas and the solid part of high-grade gliomas or medulloblastomas, respectively (Fig. 21). In contrast, tumors with loose cell structures are hyperintense even referred to the white matter. CSF-like signals might be necrosis, epidermoid, choroid plexus xanthogranulomas, cyst, or pus. In these cases, DWI is the method of choice to narrow differential diagnosis, showing hyperintense signals in abscesses, epidermoids, and in choroid plexus xanthogranulomas.

Tl-weighted images (T1WI) should be applied before and after application of contrast agent, actually as sequences with identical parameters. In the noncontrast T1WI images, hyperintense structures are often seen in oligodendrogliomas and in malignant brain tumors especially in those treated with bevacizumab (Fig. 22). These T1-hyperintense lesions mainly correspond to regressive calcifications (Bähr et al. 2011). Noncontrast T1WI is mandatory for the postsurgical imaging to recognize T1-hyperintense methemoglobin and effects of hemostatic material which additionally shorten T1 relaxation time (Spiller et al. 2001). T1WI might be acquired as 2D or 3D sequences, while 2D as SE or gradient echo. 2D SE sequences have several advantages over 2D or 3D GE: Tumors of the skull base and orbit as important portals of entry are best depicted in noncontrast T1SE by the loss of hyperintense fat signal. In contrast, GE sequences miss this

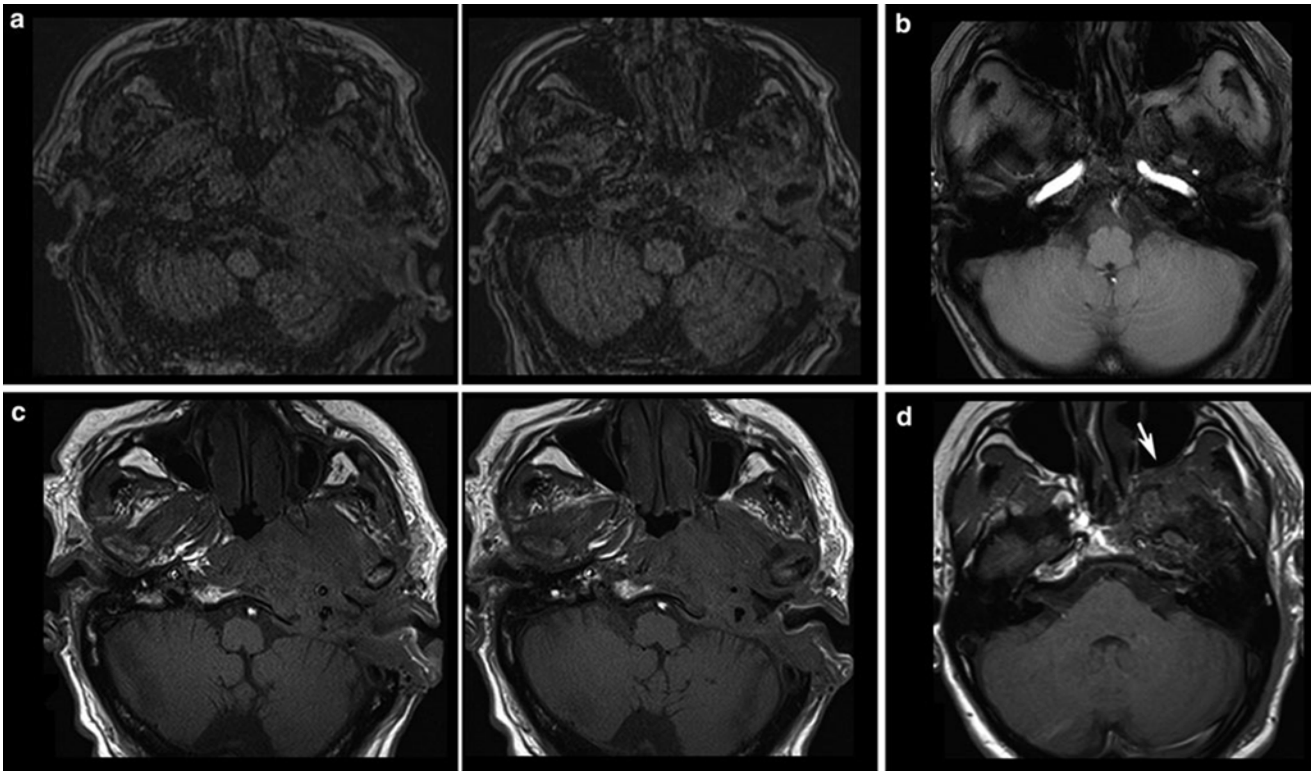

Fig. 23 Different T1-weighted sequences without contrast agent at the skull base: In (**a**) axial slices of a 3D magnetization-prepared rapid gradient echo (MPRAGE) sequence of a patient with malignant otitis externa infiltrating the skull base and in (**b**) an axial 2D FLASH sequence of a patient with a meningiomas are shown. The corresponding T1-spin echo sequences (**c**, **d**) depict much clearer the infiltration of soft tissue and bony structures by the effacement of fat signal which cannot be seen on gradient echo sequences (**a**, **b**) due to the lack of hyperintense fat signal. Also note the effaced fat signal in the pterygopalatine fossa (*arrow*)

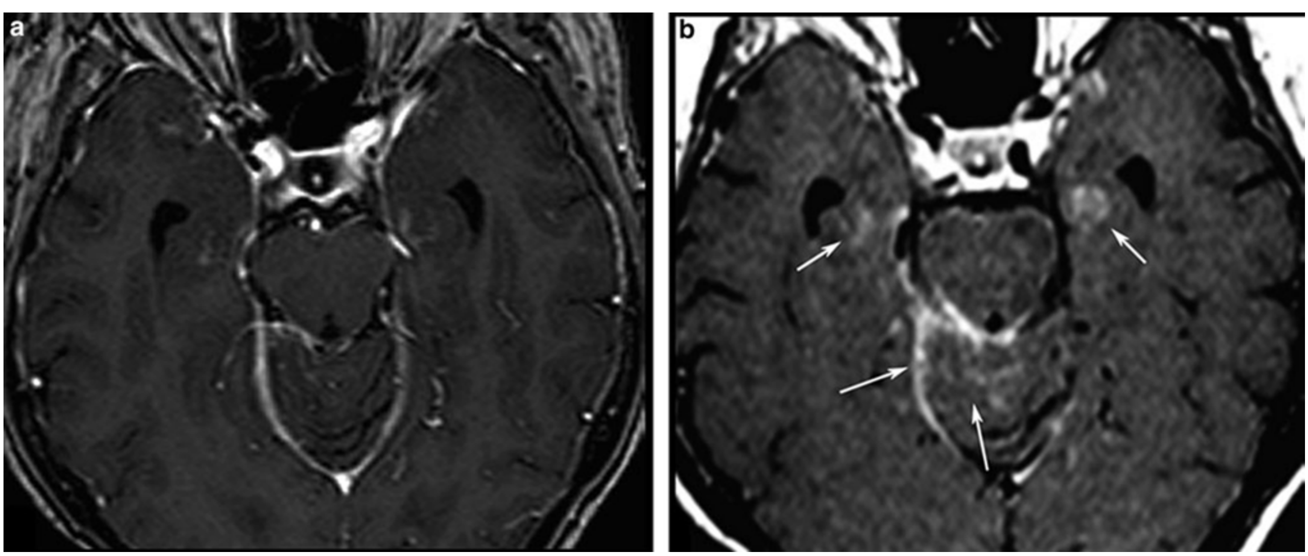

Fig. 24 3D MPRAGE or other 3D sequences incorporating an inversion pulse may be less appropriate to detect contrast enhancement. First, high signal of pial vessels and meninges may be confounding, and second, the signal of the brain tissue is not suppressed, and thus it is more difficult to appreciate the enhancing lesions (**a**). On 2D T1W spin echo sequence, (**b**) intracerebral lesions as well as leptomeningeal enhancement in the cerebellar sulci and the tentorial edge are clearly seen (*arrows*)

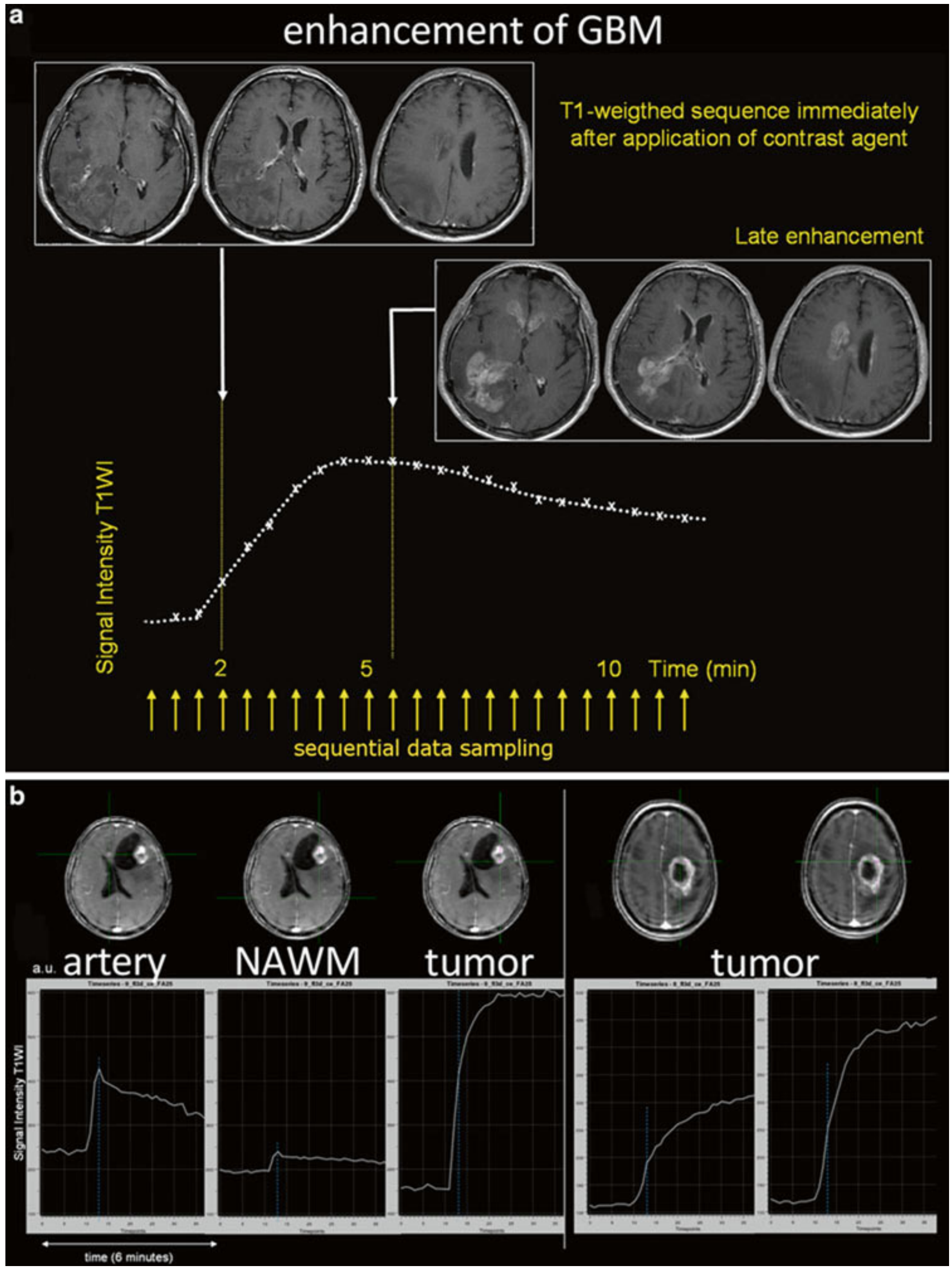

Fig. 25 The recurrent glioblastoma **a** was scanned immediately after the application of contrast agent and, 6 min later, showed impressive late enhancement of the tumor area. The signal intensity curve shows protracted enhancement of the tumor. In **b** different signal intensity curves are shown in two different GBMs depicting the rapid signal increase in the GBM on the left due to highly vascular tissue with impaired BBB, whereas in the GBM on the right had tumor areas with different enhancing dynamics

hyperintense fat signal, and air-bone-tissue interfaces cause signal losses and distortions (Fig. 23).

T1WI after intravenous application of contrast agent (CA): 3D MPRAGE may be less appropriate to detect contrast-enhancing lesions (Fig. 24), and 3D is more prone to motion artifacts compared to 2D sequences. Thus, other 3D sequences should be preferred if the contrast enhancement instead of the gray-white matter contract is of interest (Wetzel et al. 2002). Apart from the amount and pharmacokinetics of different contrast agents, contrast enhancement is a function of vessel permeability and of the delay time between application of the contrast agent and sequence acquisition (Fig. 25).

Diffusion-weighted images (DWI) depict infarction after surgery which may be misinterpreted as recurrent tumor when endothelial barrier disruption brings contrast enhancement in the follow-up (Figs. 20 and 26). The DWI signal and the corresponding apparent diffusion coefficient (ADC) also reflect the microstructure of a tumor (diffusion-weighted methods). Further, antiangiogenic therapy with bevacizumab brings new DWI pattern with stroke-like hyperintensities which are still not understood (Rieger et al. 2010) (Fig. 27).

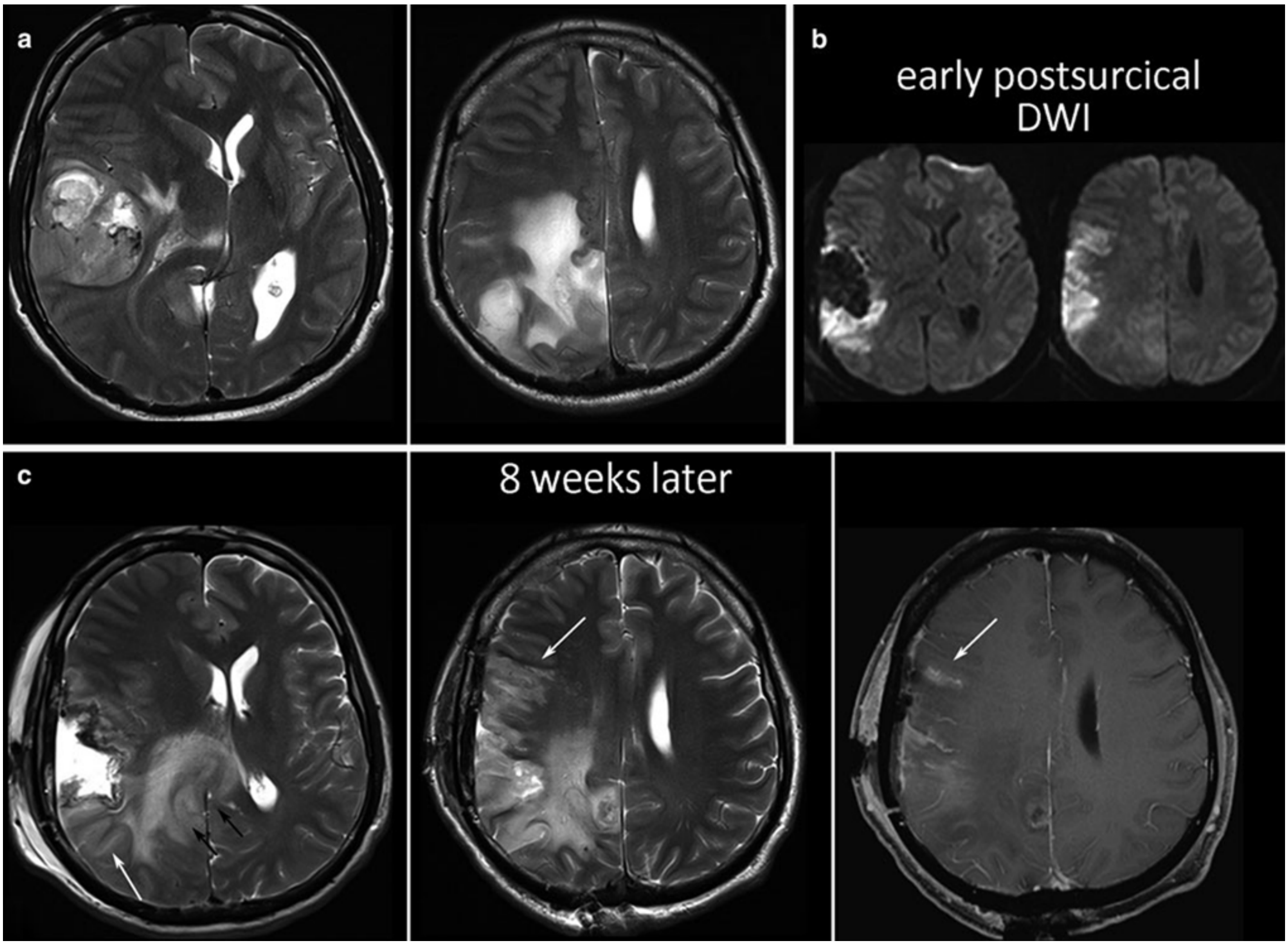

Fig. 26 Presurgical scan of a huge GBM before resection of the lateral and parietal tumor parts (**a**), postsurgical DWI (**b**), and the MRI control 2 months thereafter (**c**). There is a clear tumor progression thickening the splenium and adjacent white matter (*black arrows*), whereas the new cortical signal changes and the corresponding enhancement represent the ischemic tissue shown in (**b**)

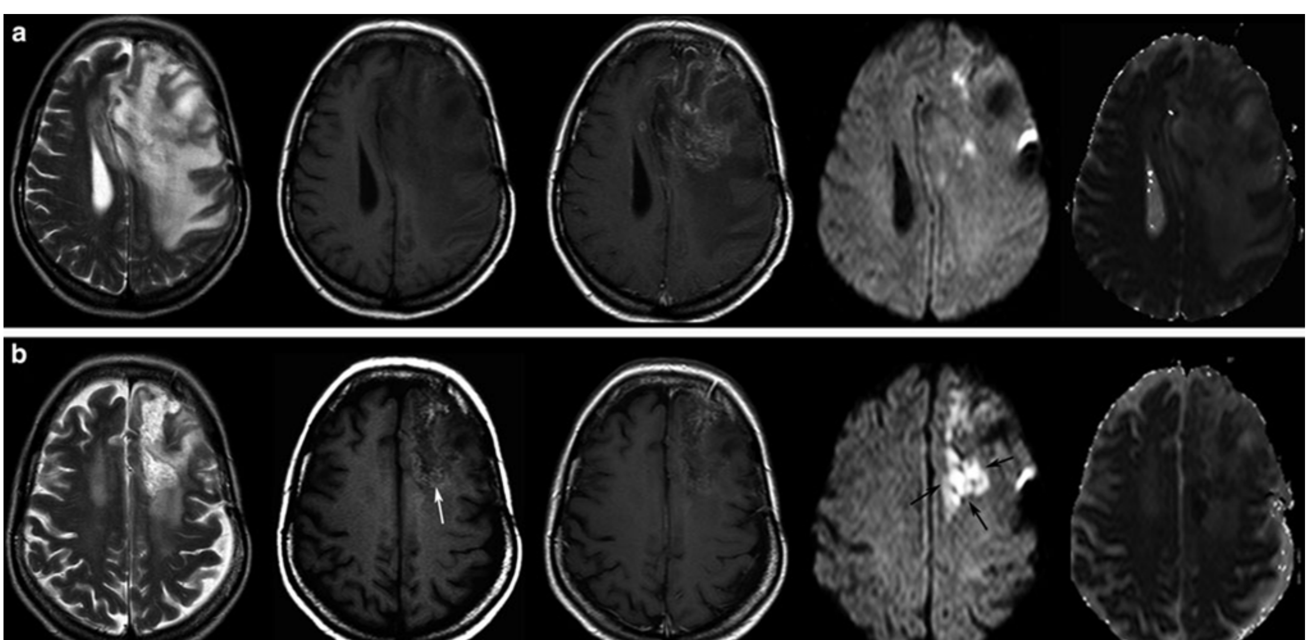

Fig. 27 A recurrent GBM before (**a**) and 8 weeks after starting antiangiogenic treatment, showing hyperintense areas on the precontrast T1WI (*white arrow*) and also bright spots on DWI with corresponding low ADC values (*black arrows*)

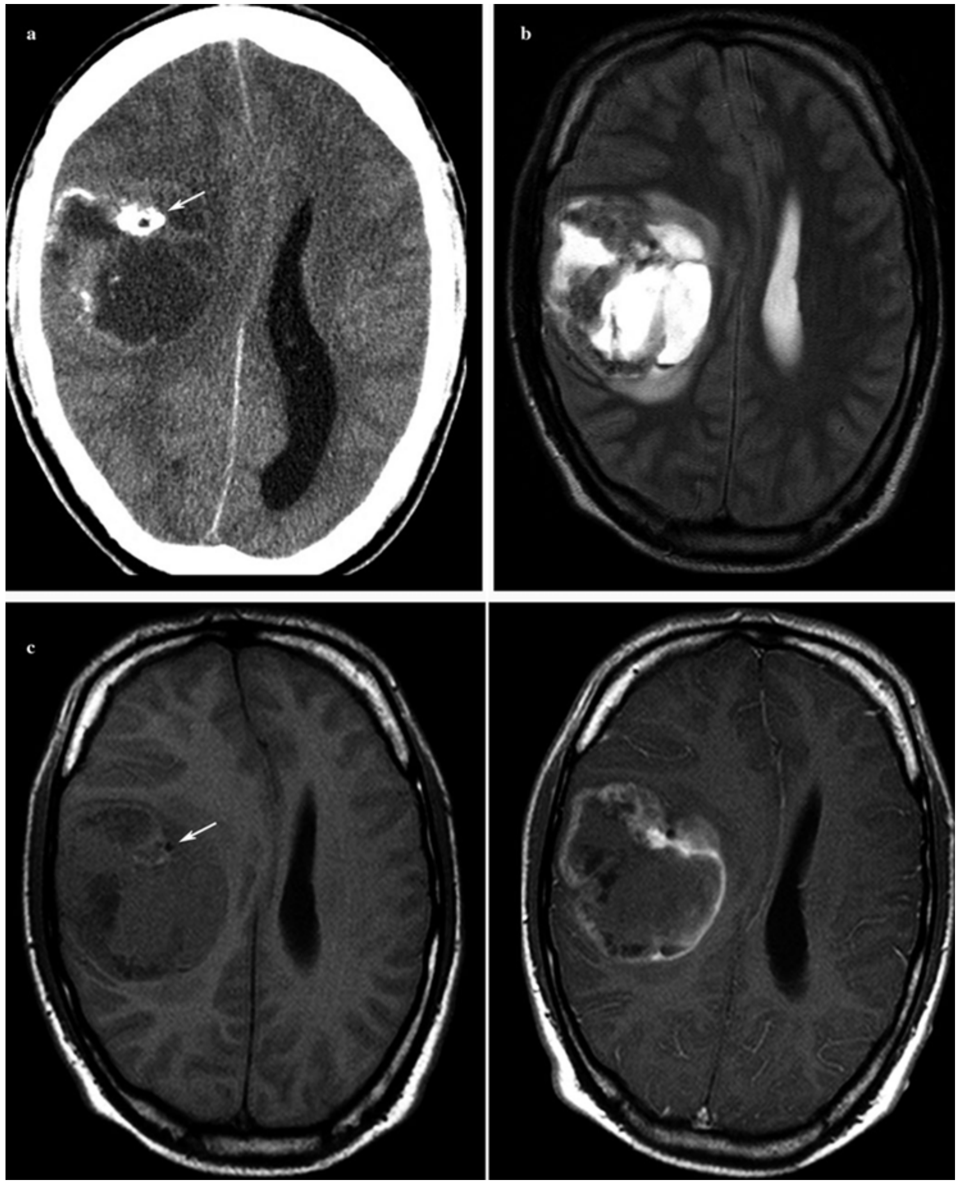

Fig. 28 The astrocytoma WHO grade II 2 years after surgery with residual peri-insular tumor on FLAIR (**a**) and T2WI (**b**): Some tumor areas (*arrows*) might be missed on FLAIR due to the T1-effect yielding intermediate signal in contrast to the hyperintense signal on T2WI

The most attention apart from contrast enhancement is given to **Fluid-attenuated inversion recovery** (FLAIR) sequences. Isovolumetric 3D FLAIR sequences allow for multiplanar reconstructions and obviate partial volume effects or artifacts of sequential 2D FLAIR. However, some basic physics of this sequence should be considered: FLAIR signal is not only influenced by the T2 relaxation time (T2-weighted) but also by the Tl relaxation time (Tl-weighted). Further, the contrast between gray and white matter and thus the delineation of anatomical structures may be inferior to T2WI. Therefore, signal changes may be more ambiguous on FLAIR than on T1WI and T2WI, and subtle infiltration of gray matter (cortical ribbon sign) may be less obvious compared to T2WI (Fig. 28), yielding differentiation between tumor and vasogenic edema more difficult. Therefore, FLAIR should not replace but supplement T2WI.

Susceptibility-weighted imaging (SWI) detects small veins and extravascular blood products including tumor-associated microhemorrhages. Recently, it has been shown that SWI after i.v. application of contrast agent visualizes architecture of tumor vessels. Increasing numbers of small vessels and intratumoral susceptibility signals seem to be hallmarks of high-grade gliomas (Pinker et al. 2007) and help to distinguish them from lymphomas.

Computer Tomography

CCT may be indicated to detect calcification which narrows the differential diagnosis. 70–90 % of oligodendrogliomas

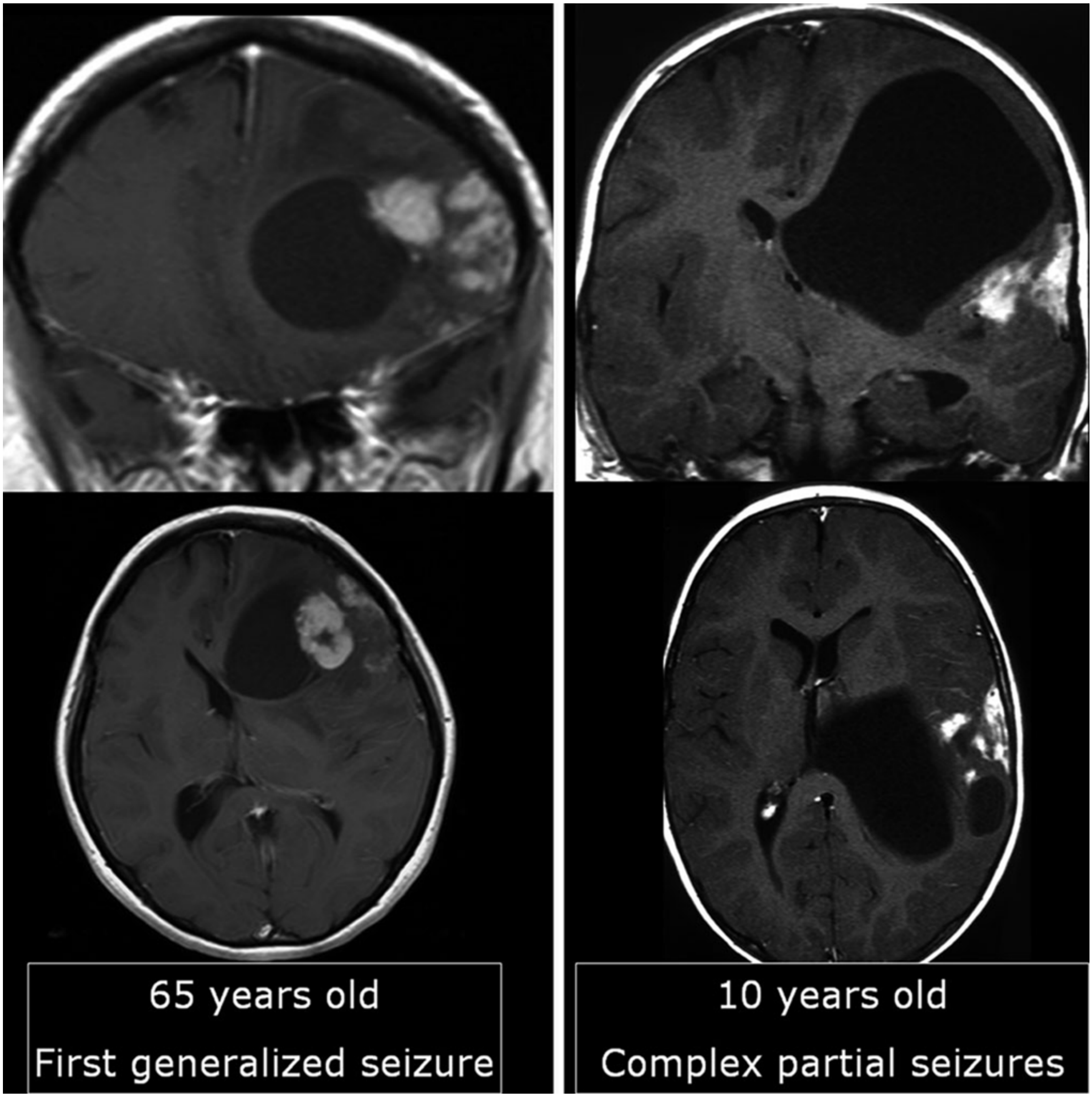

Fig. 29 Two similar tumors with enhancing nodules abutting the brain surface and large cysts: The tumor of the older patient shows some edema, whereas the tumor of the young patient lacks any edema. The older patient only had one seizure, whereas the young patient had epilepsy with complex partial seizures. The older patient had a GBM; the young patient had a pleomorphic xanthoastrocytoma

show more or less pronounced calcification on CCT. Further, it should be performed in patients with MRI contraindications. CCT may also be helpful to characterize cell density of a brain tumor in children (Sect. 3). In adults PCNSL are typical tumors with cortex-isodense appearance in contrast to most of the gliomas which are hypodense on CCT.

2.6 Case Illustrations

Although MRI has limited diagnostic accuracy, there are some clues to narrow differential diagnosis. These criteria should always include or rather begin with patient's age considering that the likelihood of malignancy in adulthood increases with age (Fig. 29).

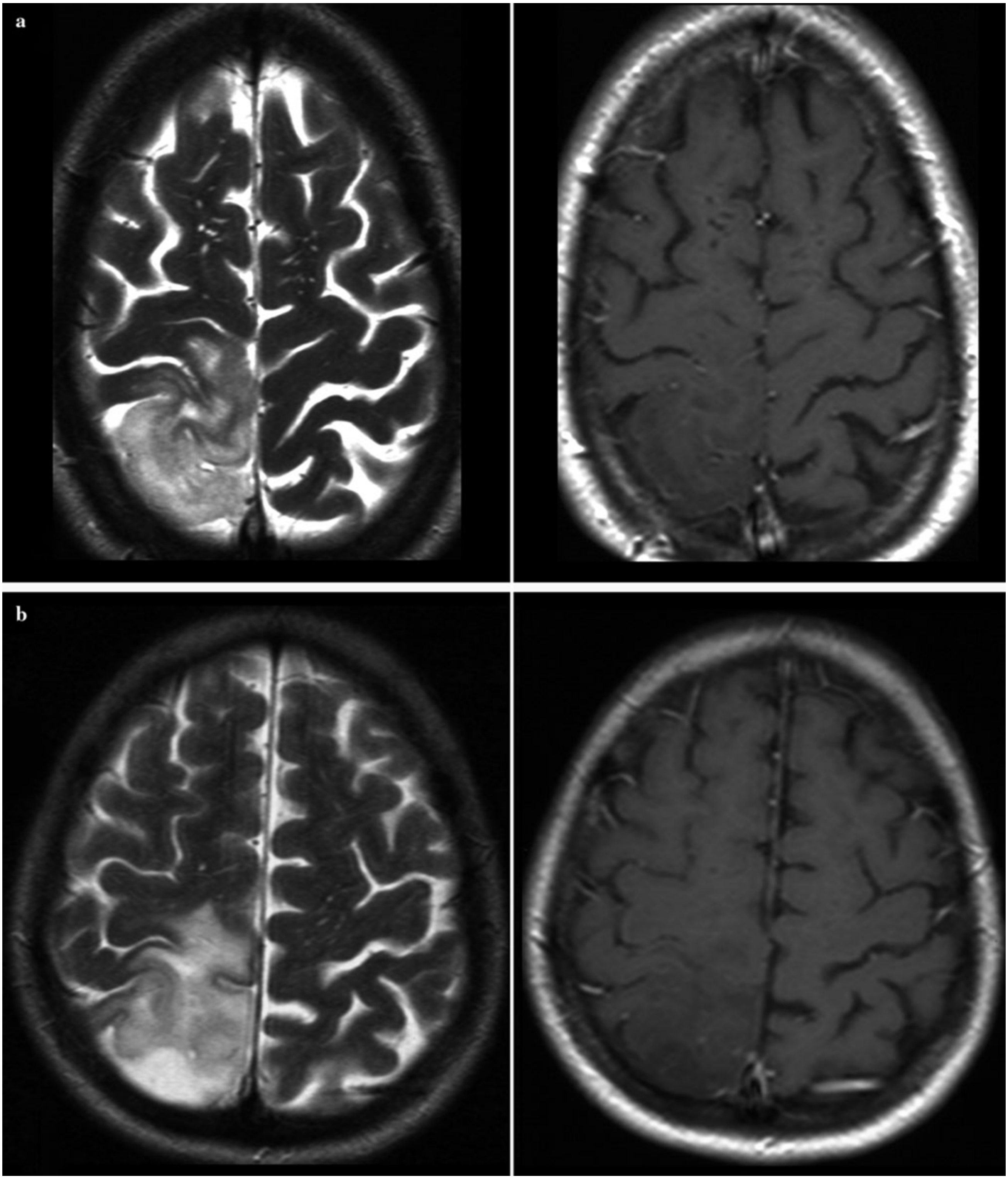

Fig. 30 Two similar histopathologically proven astrocytomas in the right parietal lobe infiltrating the cortex, both without contrast enhancement: The gyri are bloated and *gray-white* matter junction is effaced. The tumor in (**a**) **was a astrocytoma WHO grade III, whereas in** (**b**) **an astrocytoma WHO grade II was found**

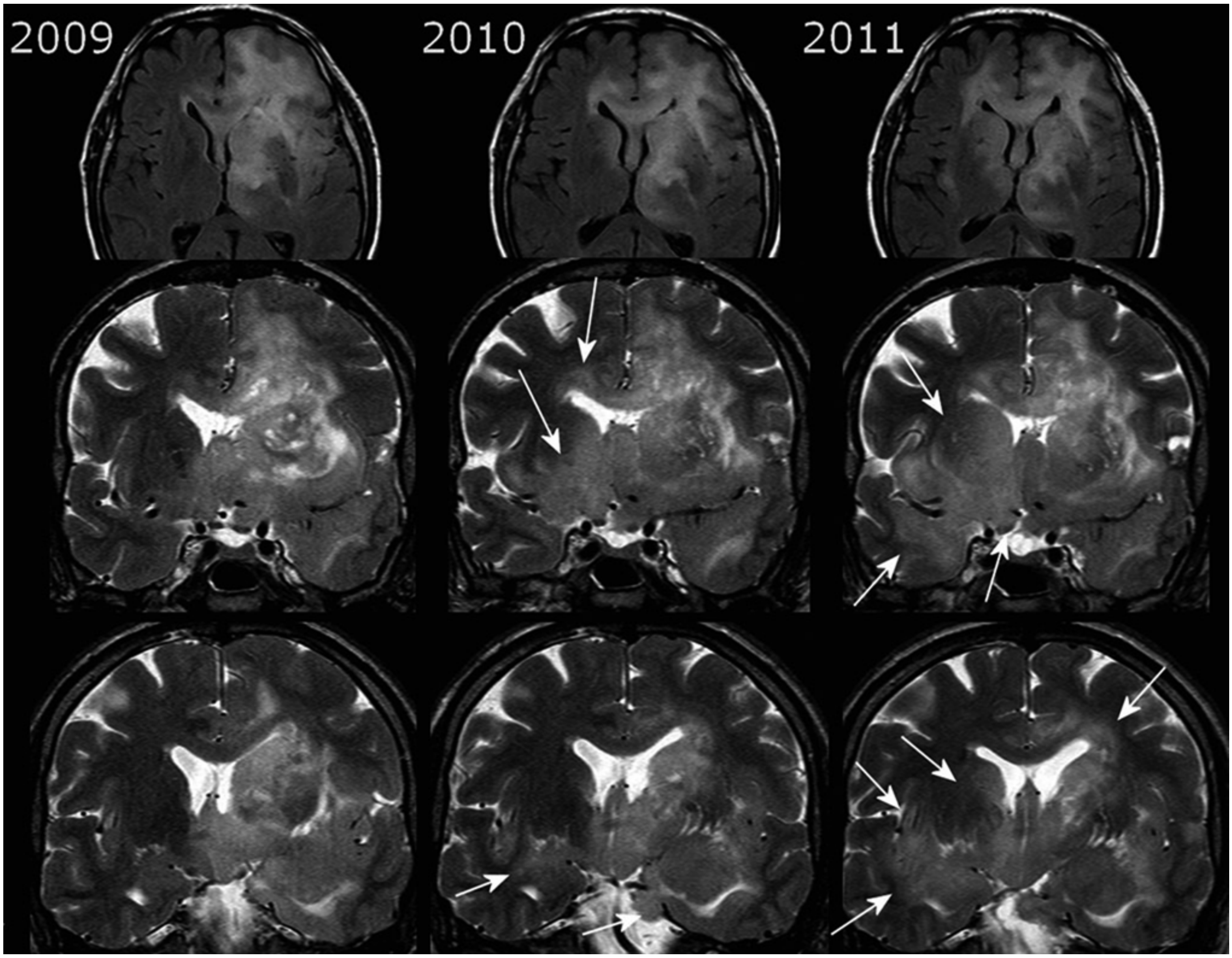

Fig. 31 The gliomatosis of the left hemisphere infiltrating the corpus callosum was treated with radiation in 2009. In 2010, the mass effect of the *left-sided* tumor declined, but tumor progressed by infiltrating the *right* temporal *white* matter, the insula, the basal ganglia, and hypothalamus bilaterally (*white arrows*). Coronal T2WI depicts the infiltration ways en face minimizing partial volume effects of axial slices, and further they visualize the blurring of gray-white matter junction due to the tumor infiltration

1. WHO grade II and III gliomas

Most low-grade gliomas or gliomas with secondary malignant transformation infiltrate cortical structures (Fig. 30). A preferential localization of low-grade astrocytoma is the frontotemporal lobe with involvement of the temporal stem, the temporomesial structures, and the insula. The infiltration way often follows white matter tracts like the anterior commissure and the corpus callosum. Coronal-oriented T2WI are very helpful in depicting the extent of low-grade tumorsand to detect tumor progression in the follow-up (Fig. 31). Due to the diffuse infiltration pattern, low-grade tumors do not expand spherically, but infiltrate the anatomical structures often without severally distorting them. Therefore, size measurement of these brain tumors is of limited value.

WHO grade III oligodendrogliomas are i.a. defined by microvascular proliferation and necrosis which give them the appearance of a highly malignant GBM (Fig. 32). WHO grade II oligodendrogliomas may already appear malignant due to their inhomogeneous tumor areas with cysts, calcifications, and hemorrhage (Fig. 33).

2. Glioneuronal tumors

The hallmarks of these tumors are the younger patient age (children and young adults) and the high association with epilepsy with complex partial seizures. Although mostly benign, one should be aware that the glial component of

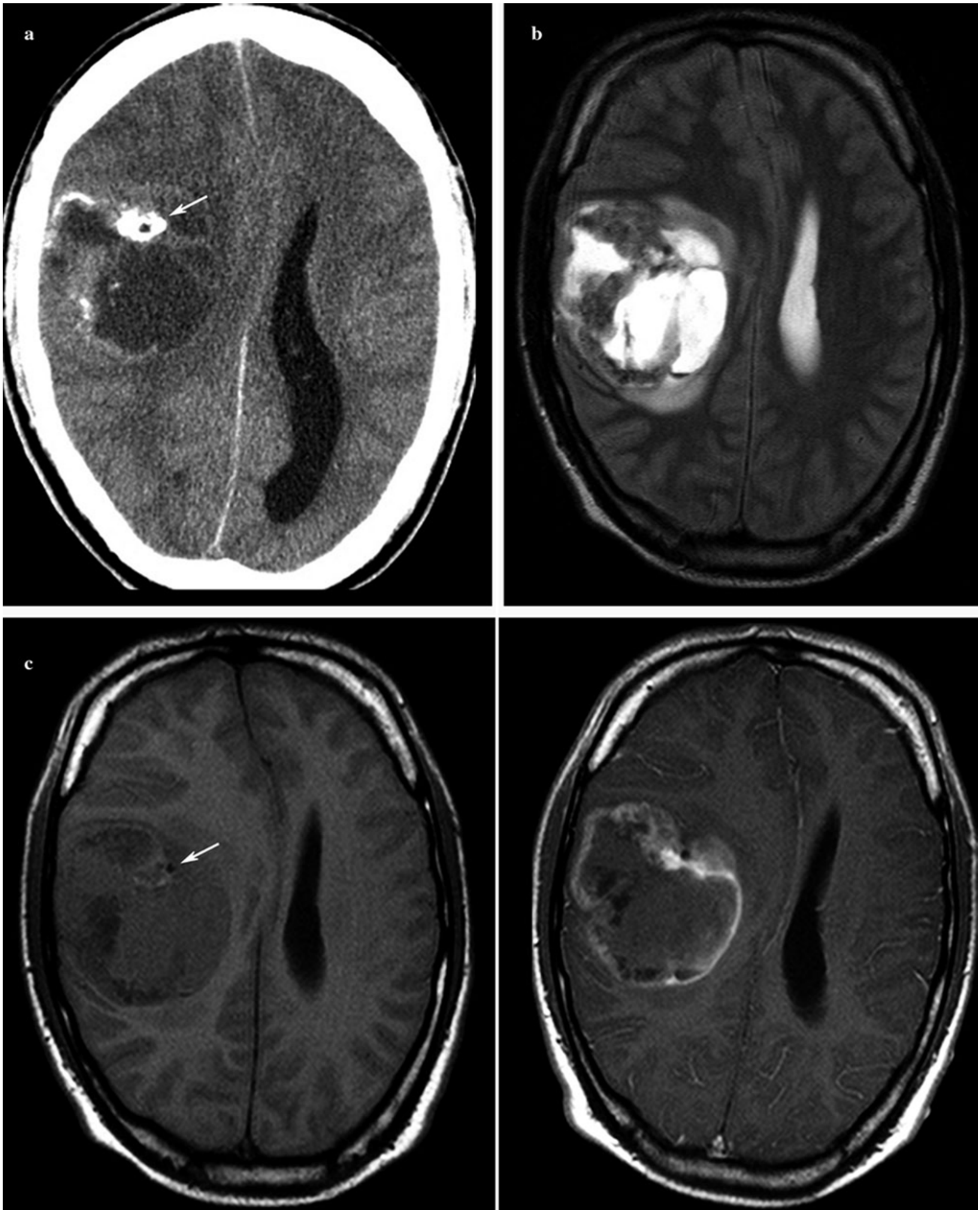

Fig. 32 Very inhomogeneous tumor with cystic areas, irregular, and patchy enhancement of the margins. It has the appearance of GBM, except for the small surrounding edema which is not typical for large necrotic GBMs (**a**, **b**). The CCT (**a**) shows calcification which yields faint hyper- and hypointense signal changes in precontrast T1WI (**c**); see also Fig. 33. Histopathology yielded an oligodendroglioma WHO grade III

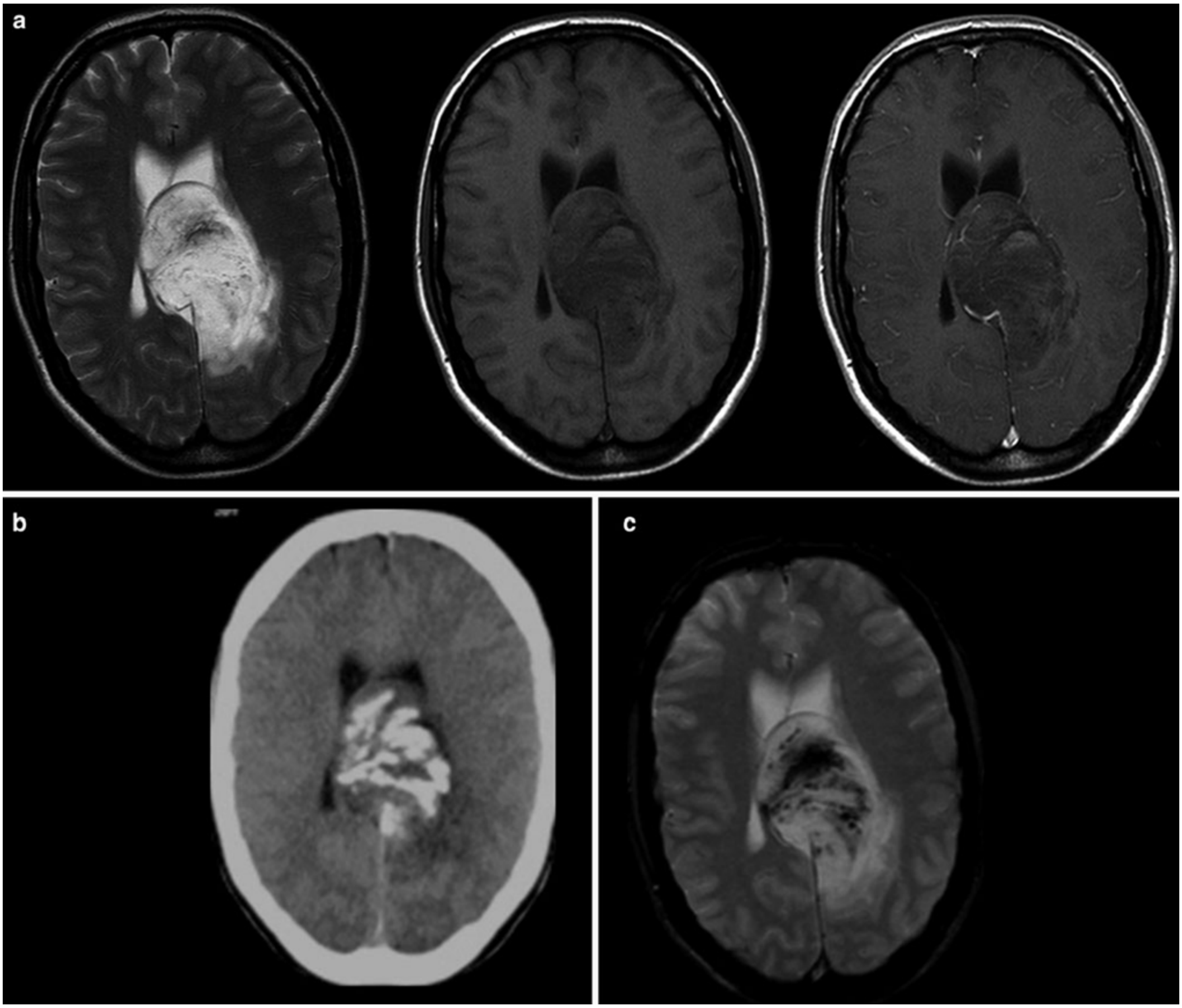

Fig. 33 The same patient as in Fig. 14c. Hypointense signals in T2WI might be due to hemorrhage, which is more often found in malignant brain tumors. The CCT yields strong calcifications which cause signal loss in T2*WI. The signal intensity of calcification may be hypointense due to its diamagnetic properties, whereas the size and configuration of calcium salt deposits as well as its interactions with other paramagnetic cations may cause T1 shortening

gangliogliomas, the most frequent glioneuronal tumor, might show malignant transformation. Glioneuronal tumors are mostly located in the temporal lobe, especially in the temporomesial region, abutting the brain surface (Figs. 13 and 34). Cystic components and partial contrast enhancement is also found. The DNET may show little cysts which might have a typical hyperintense rim on FLAIR (Fig. 35). Tumors with cystic components (which might be indistinguishable from necroses) and nodular enhancing tumor abutting the brain surface in younger adults are suspicious for glioneuronal tumors. Other differential diagnoses include very rare tumors like pleomorphic xanthoastrocytoma, originating from subpial astrocytes, and astroblastomas (Fig. 36). These tumors are large, peripheral supratentorial tumors with cystic and solid parts and a characteristic bubbly appearance (Fig. 29).

3 Pediatric Brain Tumors

3.1 Standard MRI

In children, the slice length should not exceed 4 mm. For small structures even much smaller slice lengths might be necessary. Although many surgical or radiotherapy treatment planning systems require three-dimensional sequences, these should only be additional to the core of standard imaging: It may be impossible to compare a tumor

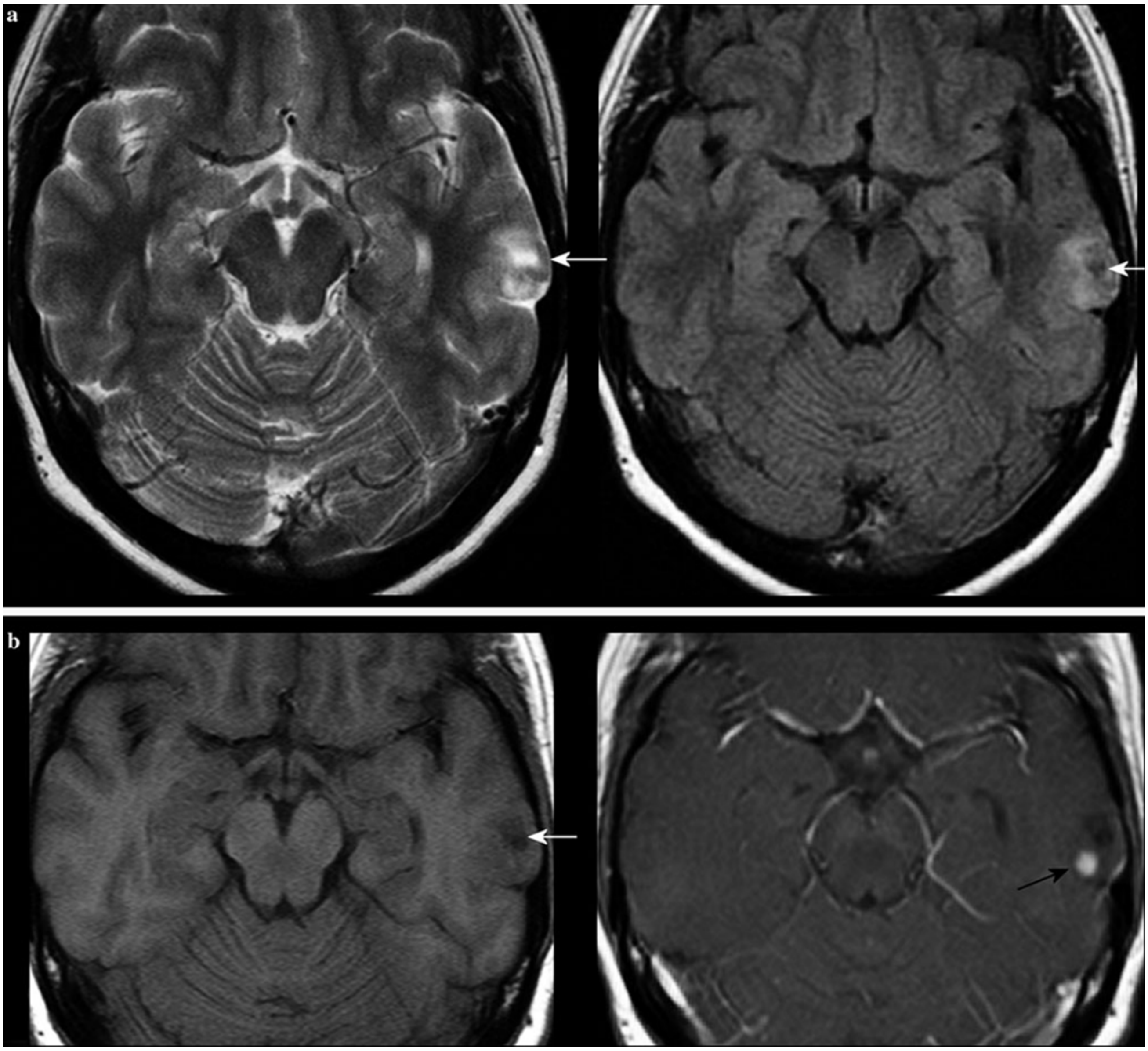

Fig. 34 Young adult with incidental finding of a small tumor in the left temporal lobe abutting the brain surface with a cystic component (*white arrows*) adjacent to an enhancing nodule (*black arrow*). Histopathology revealed a ganglioglioma

on sequential SE scans with the same tumor on 3D scans or MPR series because the contrast behavior of tumors can differ considerably on these sequences (Pinker et al. 2007). An automatized 3D volume calculation of brain tumors can only be used in single- or limited-center studies because the acquisition parameters have to be uniform.

DWI with the additional calculation of the ADC allows not only the depiction of infarcted brain but also an estimation of cellular density in the absence of hemorrhage (Kato et al. 2009). Together with the signal intensity on T2-weighted MRI, the ADC is a very useful tool for differential diagnosis (Kan et al. 2006). Susceptibility-weighted sequences are useful for the identification of calcification or blood degradation products. However, in pediatric brain tumors with the exception of craniopharyngiomas, this feature is of little importance compared to its value in the differentiation of adult high-grade gliomas (Zulfiqar et al. 2012; Tsuda et al. 1997; Pinker et al. 2007).

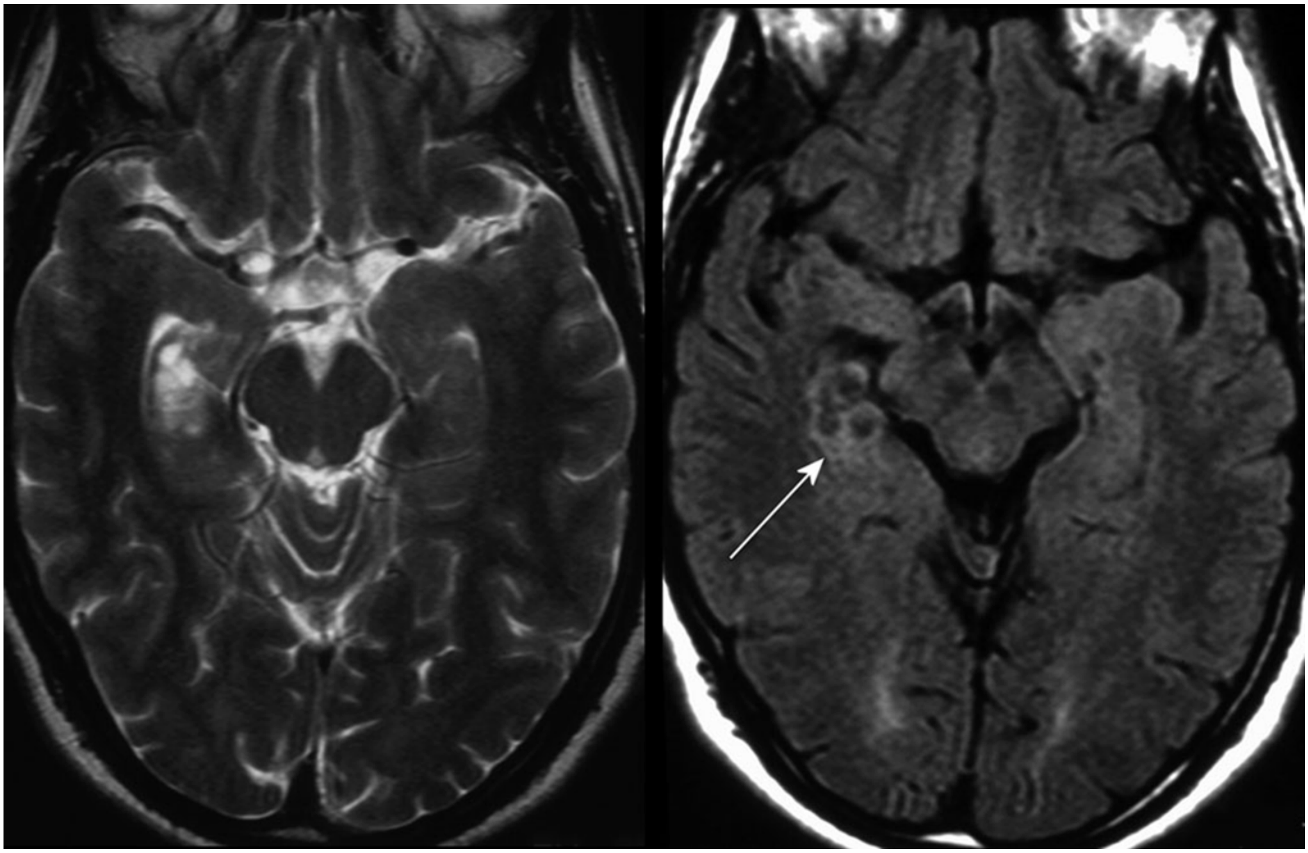

Fig. 35 The temporomesial DNET shows typical well-defined hyperintense rings on FLAIR sequence

3.2 Differential Diagnosis of Common Pediatric Brain Tumors

Pilocytic astrocytomas are the most frequent brain tumors in children in all parts of the CNS. One of the main features on histopathology also relevant for imaging features is the low cellular density. They frequently take up contrast agent and might contain cystic components, which should not be mentioned as necroses. Necrotic components are clearly features of high-grade tumors like glioblastomas or of treatment-induced necrosis. The walls of tumor cysts may enhance (Fig. 37), and enhancement allows to differentiate pilocytic astrocytomas from hemangioblastomas, also termed as Lindau tumors. This entity is most frequently localized in the cerebellum, spinal cord, and rarely—especially in adolescents and younger adults—in the supratentorial brain. It might consist of a pure nodule or a strongly enhancing nidus within a cyst. This similarity can create diagnostic problems in the discrimination from pilocytic astrocytomas (Beni-Adani et al. 2000). A hemangioblastoma can be safely excluded if cyst wall enhancement is present (Bishop et al. 2008) (Fig. 38). If cyst wall enhancement is absent, there is no way to differentiate between hemangioblastoma and pilocytic astrocytoma with standard imaging. The reduced cellular density corresponds to a high T2 signal and high ADC values (Fig. 39) facilitating the differentiation from tumors with high cell density, e.g., medulloblastomas/ependymomas (Fig. 40), or—in the suprasellar or pineal region—to germ cell tumors always showing a cell density comparable to gray matter (Fig. 41). Unenhanced CT is also very helpful to assess cell density of pediatric brain tumors (Poretti et al. 2012) (Fig. 42). Among our own unpublished studies of far more than 100 patients with medulloblastomas undergoing CT without contrast enhancement, no tumor with hypodense CT values in the solid tumor parts was found. However, in supratentorial gliomas, an accurate differentiation between low- and high-grade gliomas is not possible because the cell density of the solid components in high-grade gliomas usually remains below the cell density of PNETs or ependymomas (Fig. 43). Other ominous features like inhomogeneous texture or an increase of perifocal edema (Fig. 44) have to be taken into

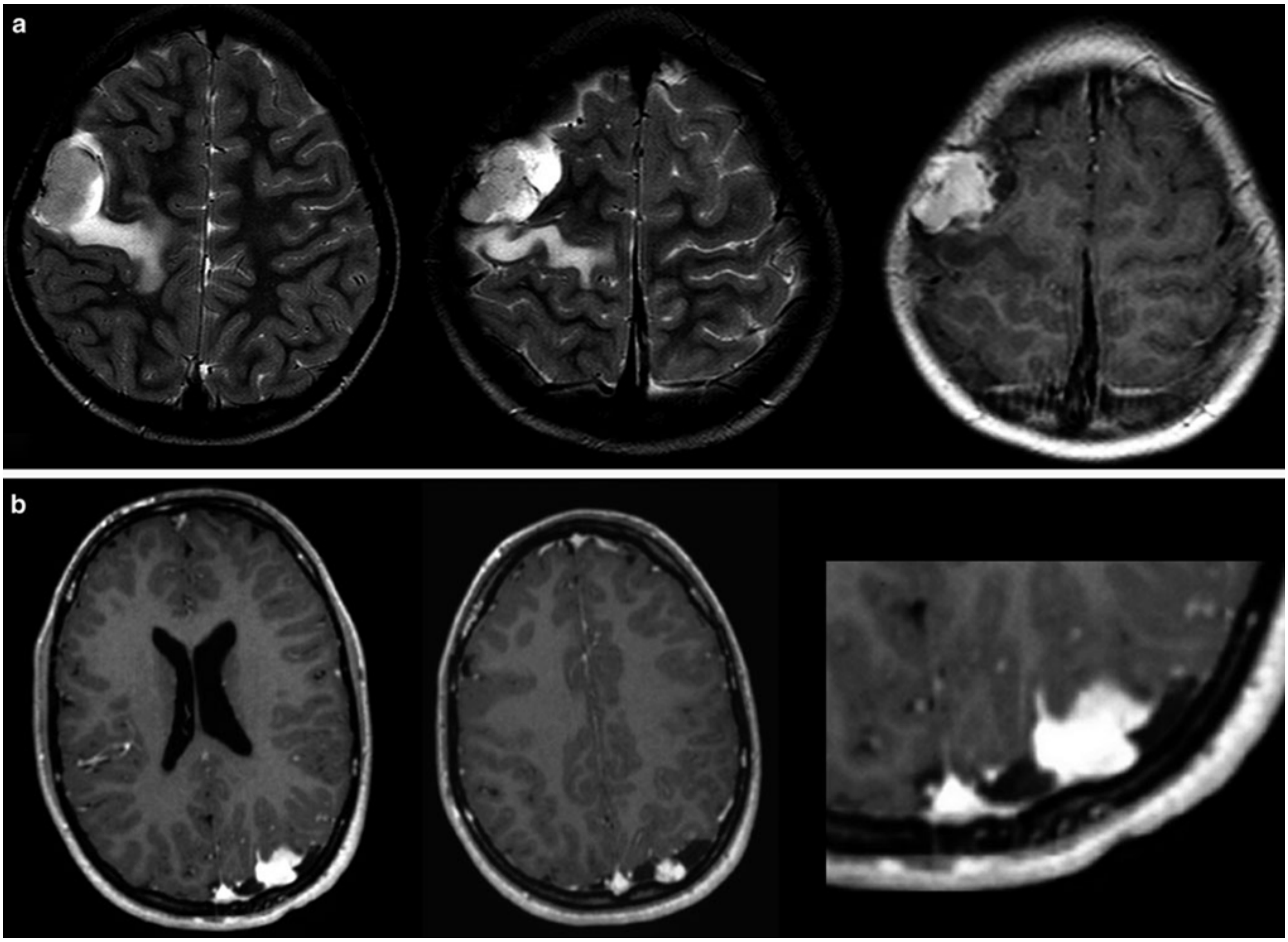

Fig. 36 Tumors abutting the brain surface in young adults, modeling the adjacent bone. Both tumors have pronounced larger enhancing tumor nodules together with small cystic areas. Histopathological diagnoses yielded an astroblastoma WHO grade II (**a**) and a xanthogranulomatous astrocytoma grade II (**b**)

account. The diagnosis of gliomatosis cerebri, which may vary on histology from WHO grade II to IV, is based on the involvement of more than two lobes of the brain (Fig. 45).

To diagnose a diffuse intrinsic pontine glioma (DIPG), typical clinical complaints in addition to typical infiltrative appearance on MRI are required (Fig. 46). Key features are an extension of more than 50 % of the pontine cross-sectional area and a clear tumor origin and center in the pons (Fischbein et al. 1996) and not other parts of the brainstem, e.g., medulla oblongata, where low-grade gliomas predominate. Contrast enhancement at the time of diagnosis might have a prognostic importance (Poussaint et al. 2011). Cysts are extremely rare and can be a sign for a low-grade histology (Fig. 47), indicating the need of a histological clarification. If biopsy does not seem to be feasible, a close follow-up is mandatory. In neurofibromatosis type 1 as well, focal and also seemingly typical DIPG can exist but usually show a much more benign clinical course (Fig. 48).

In the suprasellar compartment, the differentiation between the frequent tumors in children in this localization like craniopharyngioma, LGG, and germ cell tumor is usually possible on the basis of conventional MR/CT imaging (Table 3). Small germ cell tumors might be indistinguishable from a hypothalamo-pituitary lesion in Langerhans cell histiocytosis (Makras et al. 2006). Adamantinous craniopharyngiomas are the typical craniopharyngiomas in children and show frequently calcification and cysts. CT without contrast is the additional method of choice (Tsuda et al. 1997; Warmuth-Metz et al. 2004a, b) (Fig. 49) and can be centered on the tumor without touching the radiosensitive eye lens. Extreme dose reduction in order to protect the child should be avoided because very small calcifications might be detectable only on the soft tissue reconstruction, which needs a higher dose of radiation for adequate image quality. Varying with the individual position of the craniopharyngioma, a loss of the physiological bright posterior pituitary lobe (PPL) signal on the unenhanced T1-weighted MRI is possible and therefore sagittal thin-slice T1-weighted images are very useful (Fig. 50). A loss of the bright PPL signal indicates the disturbance of the hypothalamic-PPL axis.

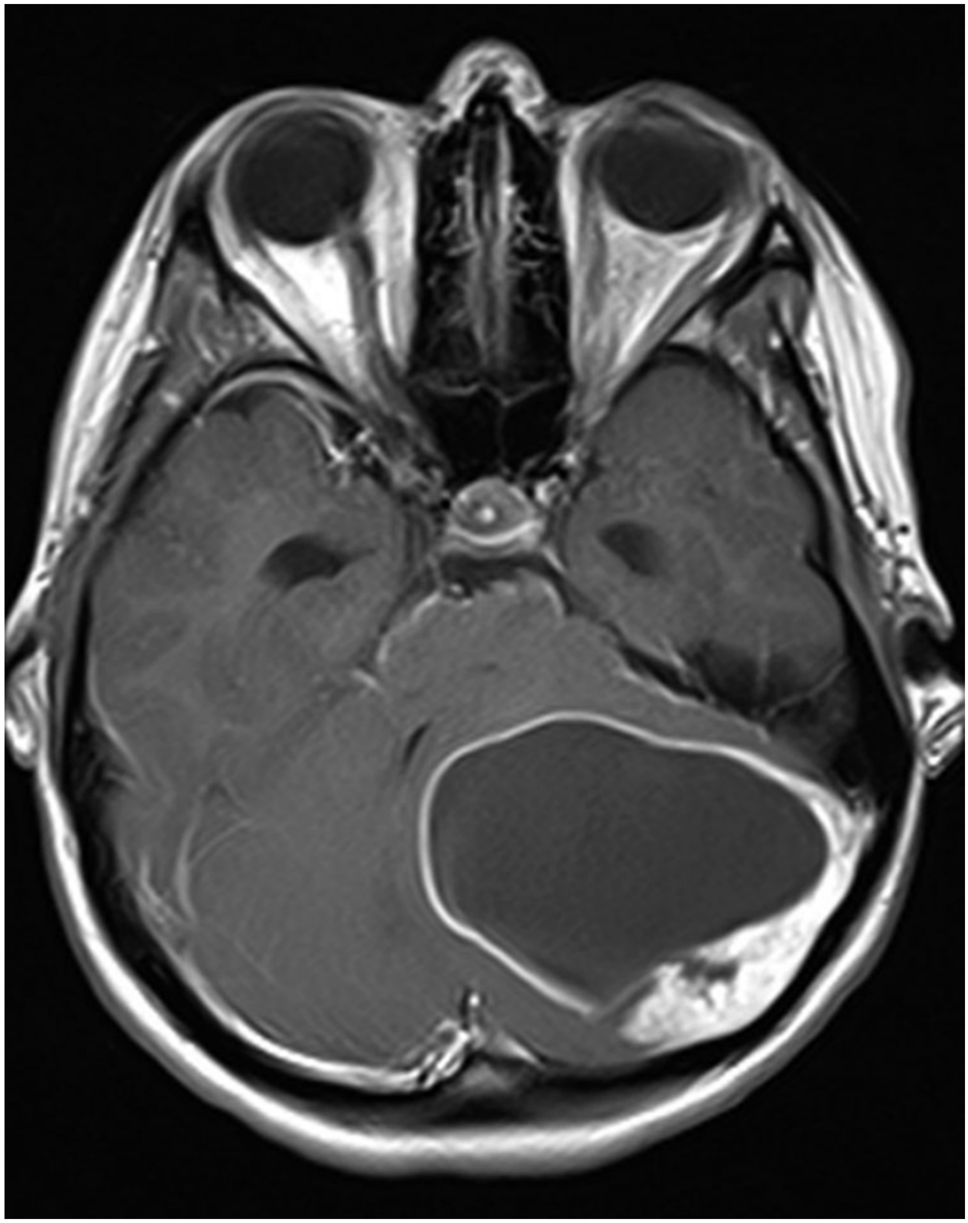

Fig. 37 Enhancement of the cyst wall as shown in this cerebellar pilocytic astrocytoma can be useful for the differential diagnosis between glioma and hemangioblastoma. Many pilocytic astrocytomas do not show cyst wall enhancement. If so, pilocytic astrocytomas should be assumed because hemangioblastomas almost always lack cyst wall enhancement

Germ cell tumors in a suprasellar position almost always have no T1-hyperintense signal in the PPL (Di Iorgi et al. 2012). Due to a high ratio between cell nuclei and cytoplasm, these tumors usually show a T2-signal comparable to gray matter, a restricted diffusion and a regular, frequently intense contrast enhancement (Liang et al. 2002; Sumida et al. 1995). The various types of germ cell tumors with the exception of the typically inhomogeneous teratomas cannot be differentiated from each other on MRI.

Pilocytic astrocytomas of the chiasm/hypothalamus are tumors with a low cellular density and therefore show a high T2 signal (Poretti et al. 2012), no restricted diffusion, and hardly ever a loss of the physiologic bright PPL signal. In very young children, tumors in this localization may be accompanied by a meningeal dissemination with an increase of protein but without tumor cell detection in the CSF (Gnekow et al. 2012).

Spinal tumors cannot be differentiated on the basis of MRI features with rare exceptions. In general, all tumors of the CNS can be localized within the spinal cord. Statistically in children, especially the younger ones, astrocytic tumors predominate (Jallo et al. 2003). Ependymomas are very vascular. Only rarely a leptomeningeal siderosis or the unusual presence of hemosiderin capping (cap sign)

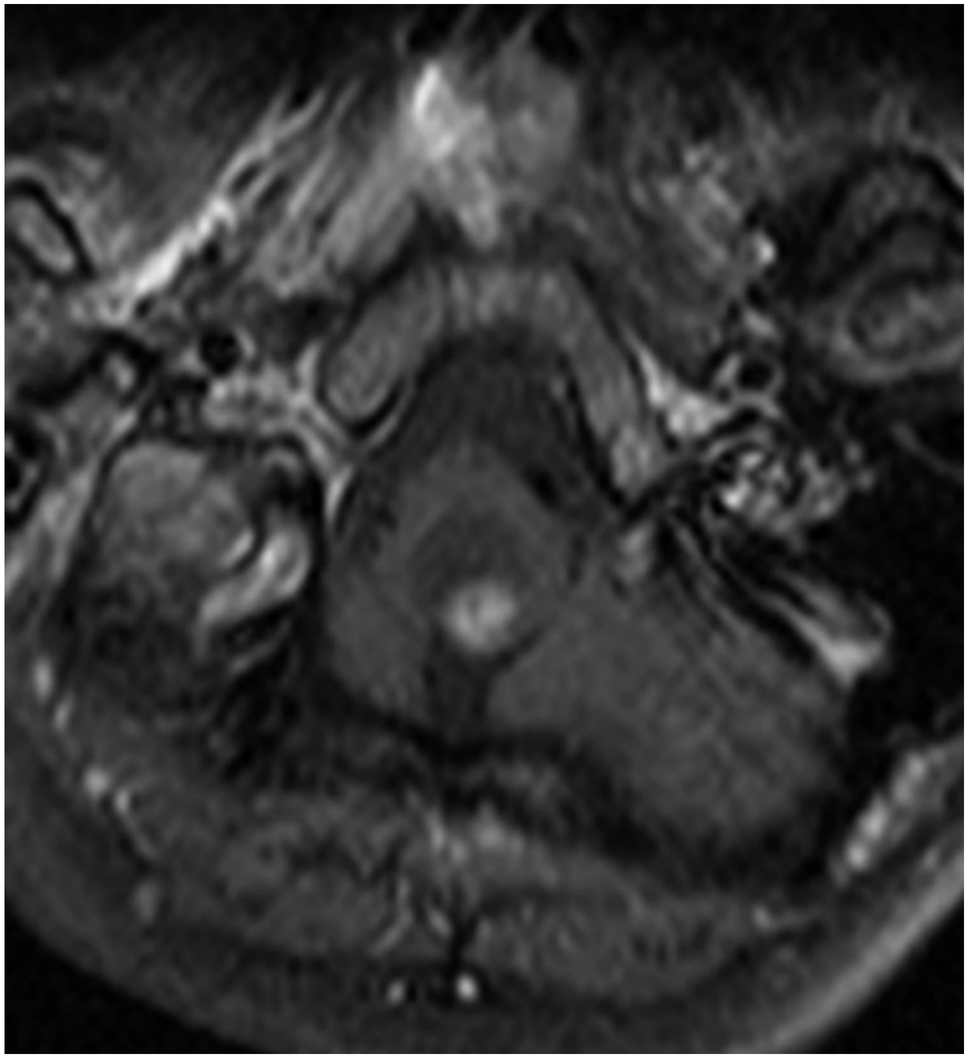

Fig. 38 Hemangioblastoma of the medulla oblongata showing the characteristic lack of cyst wall enhancement

at the borders of an ependymoma can be of diagnostic significance for this histology (Fig. 51) (Huisman 2009; Baleriaux 1999) kindly provide part label caption.

3.3 Early Postoperative Imaging

A residual tumor after resection can only be identified within the first 3 days after resection because after this time period surgical trauma may induce reactive changes of the brain which may enhance the contrast agent. These changes are virtually indistinguishable from residual tumor (Forsting et al. 1993). Unfortunately, enhancement may also occur during and very early after surgical resection—especially by using electrocoagulation—causing problems to identify possible residual tumor as well (Knauth et al. 1999). Therefore, we do not advice to perform postoperative MR scans directly from the operating theater, which seems very attractive in terms of logistics. The first and second days after surgery are ideal for the early postoperative MRI. However, if this time period is missed in a contrast-enhancing tumor, then the correct identification of a residual tumor might not be possible for a long time or even forever. Nonenhancing tumors can only be identified on the basis of their features on T2/FLAIR or PD sequences. Therefore, the comparability of MRI to the preoperative time point is of utmost importance. In addition, a change of magnetic field strength is problematic and should be avoided for the pre- and postoperative comparison and also for further follow-up.

3.4 Meningeal Dissemination

The examination of the entire dural space intracranially and in the spinal canal is necessary for a correct tumor staging. MRI is the only noninvasive method for the evaluation of a leptomeningeal dissemination of tumors or a primary medullary tumor.

Enhancement can affect the leptomeninx and the pachymeninx. Pachymeningeal enhancement is frequently a

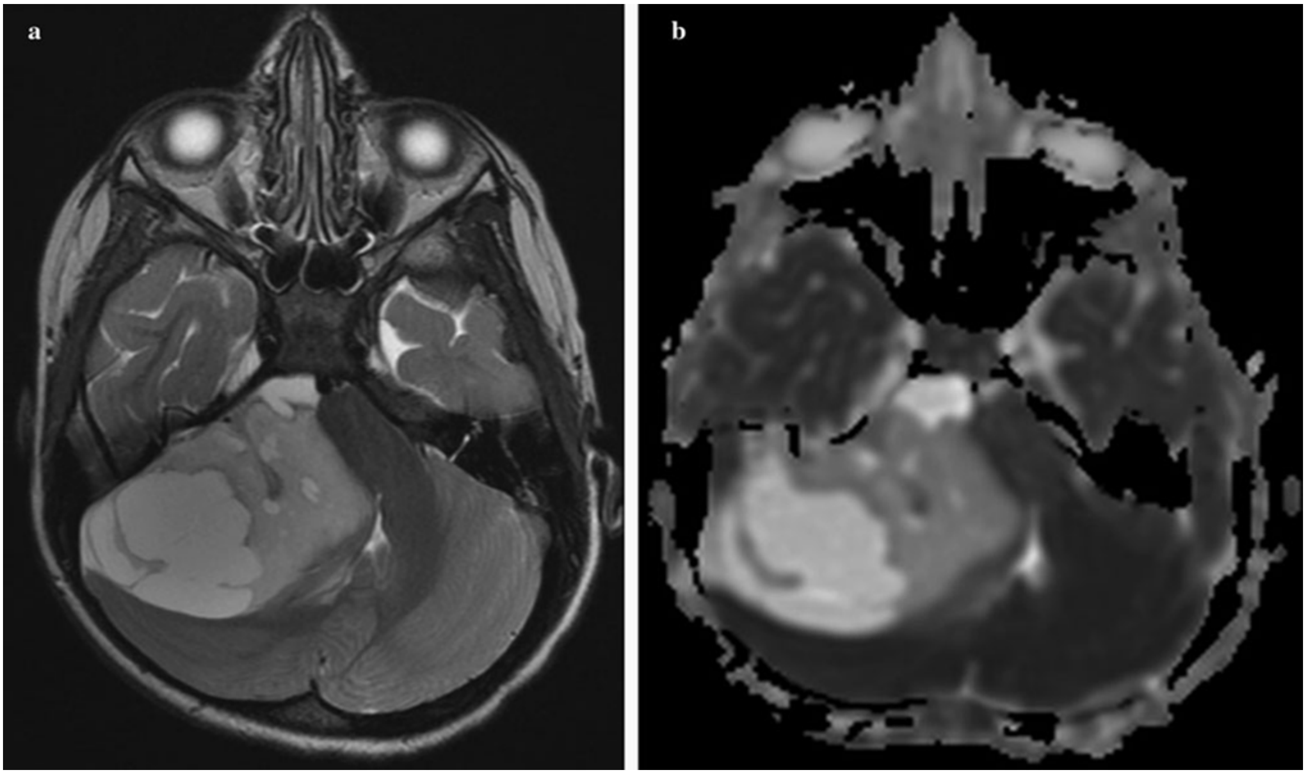

Fig. 39 Hyperintense T2 signal (**a**) in the solid parts of a pilocytic astrocytoma in the right cerebellar hemisphere representing the low cell density of these tumors. On the ADC map (**b**) the low cell density of the same pilocytic astrocytoma as shown in Fig. 3a leads to high values (seen as bright signal)

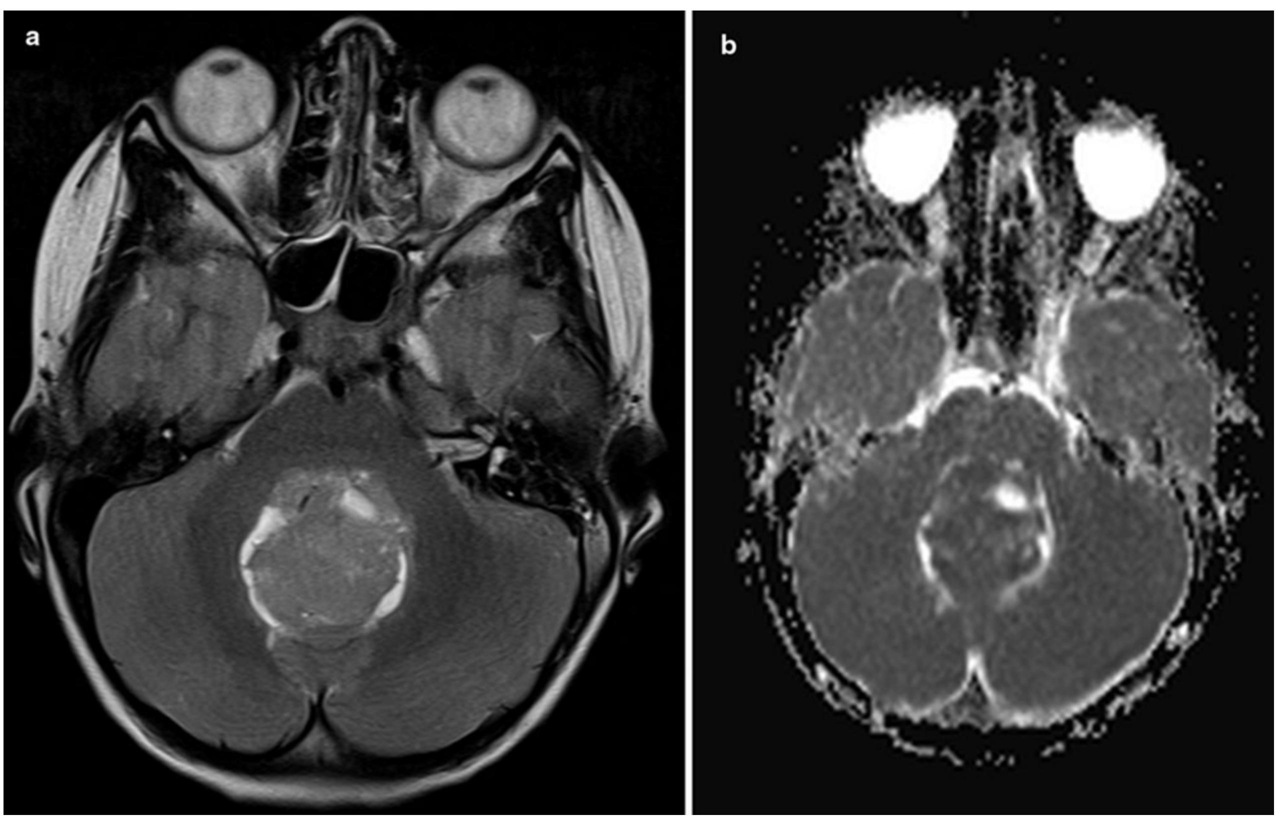

Fig. 40 Contrary to the Figs. 3a, b, the increased cellularity in case of a medulloblastoma leads to a hypointense T2 signal (**a**) and low ADC values (**b**)

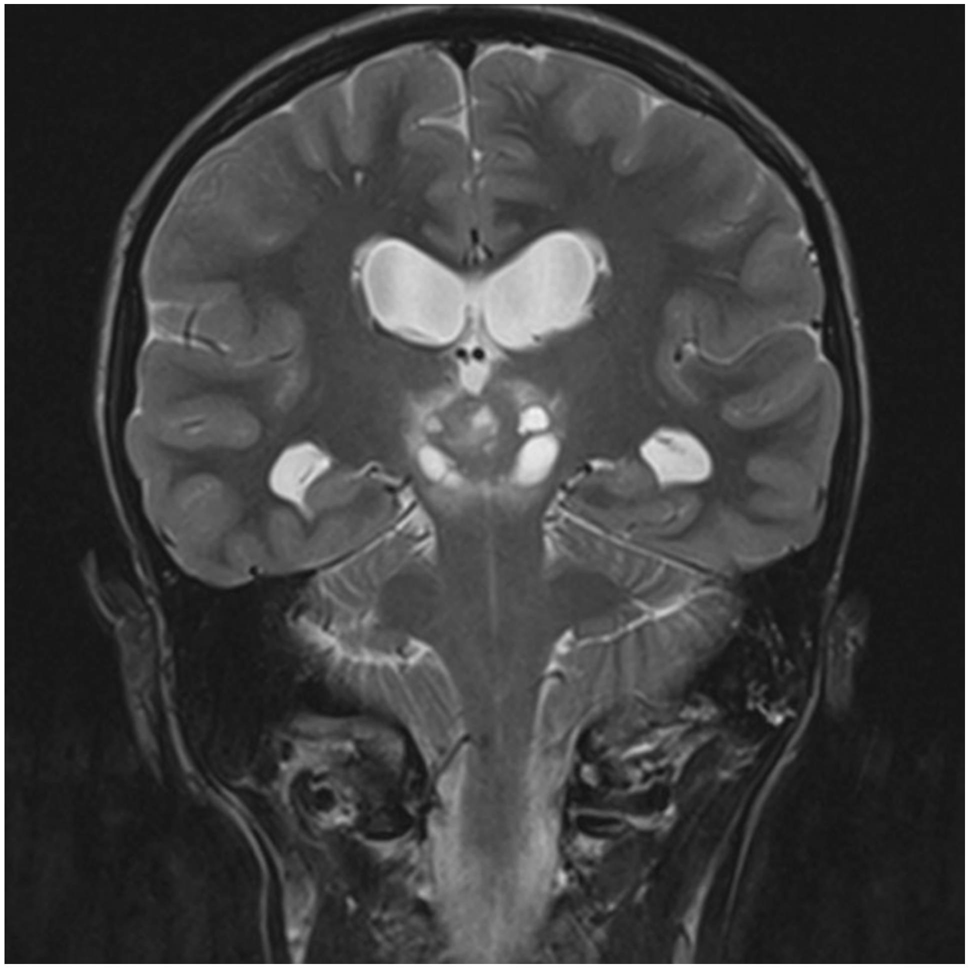

Fig. 41 In a germinoma of the pineal region, the T2 signal is hypointense as expected in a tumor with higher cell density. Small cysts are possible but large cysts are very unusual in germinomas

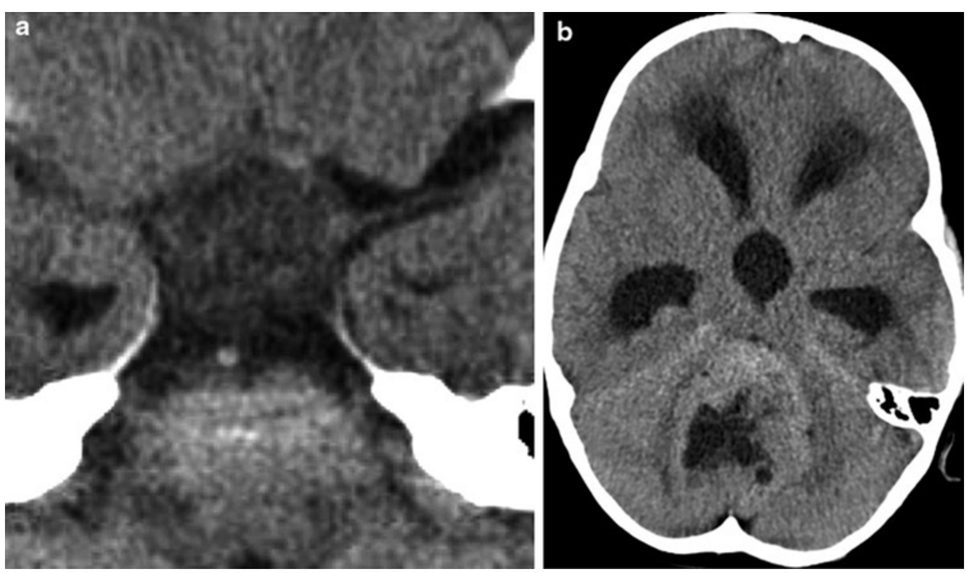

Fig. 42 On CT the cell density of tumors is reflected even more reliably than on MRI by high- or low-density values. Low density is a characteristic feature of pilocytic astrocytoma of the chiasm (**a**), and an increased density compared to gray matter is typical for a medulloblastoma (**b**). If density is equal to gray matter, both entities are possible. If calcifications exist, this discrimination might fail

Fig. 43 PNETs typically do not show a perifocal edema. More frequently enhancement is missing or only subtle (not shown)

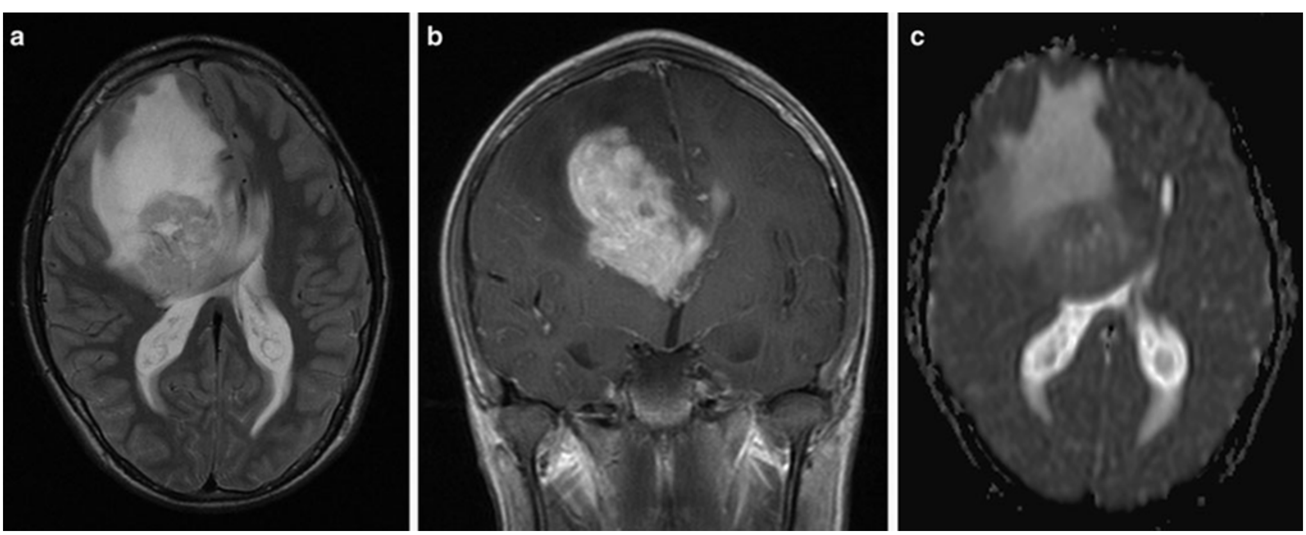

Fig. 44 In high-grade gliomas as in this anterior callosal GBM, edema is usually large and the tumor borders tend to be very indistinct (**a**: T2-weighted MRI). Enhancement (**b**) can vary but is usually more intense in GBM compared to WHO grade III gliomas. Cell density is intermediate and therefore ADC values are not strikingly lowered (**c**)

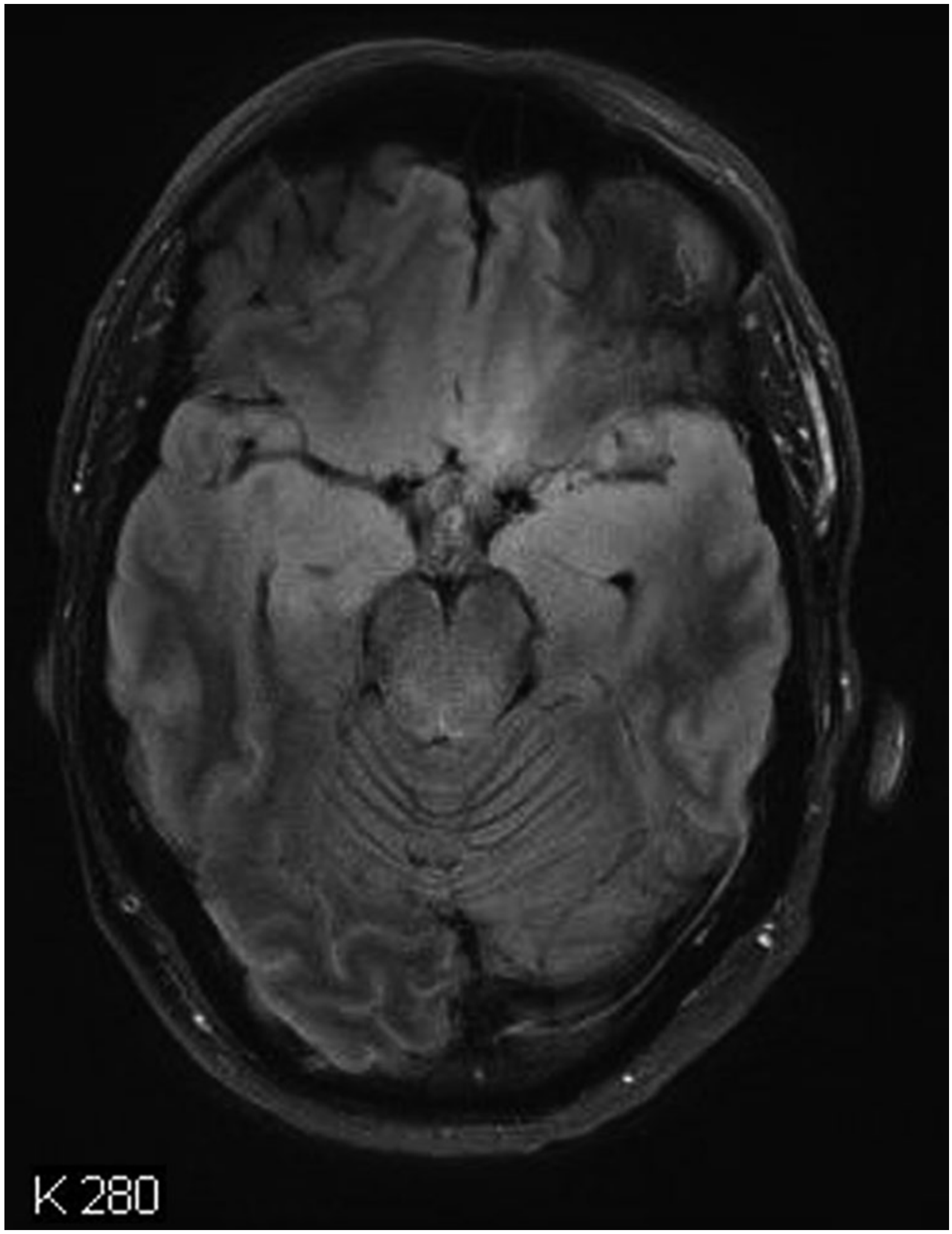

Fig. 45 Gliomatosis cerebri is defined as diffuse glioma which affects more than two lobes of the brain. The FLAIR image shows involvement of both frontal and temporal lobes and a pathology also in the cerebral peduncles bilaterally

consequence of pressure changes in the CSF space, e.g., after surgery, in case of an implanted shunting system or after lumbar punctures. In contrast, leptomeningeal enhancement either represents a neoplastic or inflammatory affection. Nodular enhancement of the leptomeninges is almost pathognomonic for nodular meningeal dissemination and is only rarely due to inflammation like sarcoidosis. In laminar enhancement, meningitis should be excluded by CSF examination.

In a considerable number of children with medulloblastomas or other tumors associated with leptomeningeal seeding, the staging examination of the spinal canal is performed after surgery. Immediately after surgery, MR scans show a physiological phenomenon, which is called nonspecific subdural spinal enhancement. This enhancement closely resembles the MR images known from idiopathic CSF hypotension syndrome (Kumar et al. 2010; Medina et al. 2010), which typically shows an affection of the pachymeninges, whereas the leptomeninges are spared. This pattern can easily be differentiated from the MRI characteristics of leptomeningeal dissemination (Fig. 52) (Medina et al. 2010; Warmuth-Metz 2004). Subdural enhancement must not be confounded with leptomeningeal disease. Patients are always without specific symptoms. In case of extensive subdural enhancement, a leptomeningeal dissemination cannot be excluded with sufficient security, and therefore the spinal MRI has to be repeated after about 1–2 weeks. Within this time period, nonspecific enhancement should be reduced or

Fig. 46 Typical diffuse intrinsic pontine glioma (DIPG) despite an obvious anterior exophytic protrusion. The definition on imaging includes a main localization within the pons, affecting more than half of the pons, and a diffuse growth in the pontine fibers. True cysts (in distinction from necroses) are very unusual

even completely resolved. From time to time, a level of spinal intradural blood after surgery can be observed and resolves spontaneously as well.

Exclusively T1-weighted images after application of contrast agent are required to visualize possible spinal leptomeningeal dissemination. Rarely T2-weighted MRI is useful for the identification of small leptomeningeal nodules. Clinical practice in the reference evaluation of children with brain tumors has shown that the T1W sequence after contrast application is usually the last of the standard spinal MR sequences. Consequently, these important postcontrast T1 images are very often deteriorated by movement artifacts in no longer compliant, awake patients or by a flattening of sedation versus the expected end of the MR examination in sedated patients. Therefore, we advice to concentrate on the T1 after the contrast enhancement only. In case of doubt, theT2-weighted MRI may be added thereafter. If a fatty filum terminale is suspected, an additional T1 with fat suppression can clarify the situation. Small deposits of leptomeningeal disease may be mistaken for physiologic vessels of the spinal cord. Vessels are easily depicted if axial slices are performed in all areas showing possible vessel enhancement on the sagittal slices.

3.5 Follow-Up Examinations

Response of tumors is traditionally evaluated by size measurement. Therefore, comparable imaging parameters have to be used to guarantee as much accuracy as possible. In tumors only measurable on T2/FLAIR images like DIPG or nonenhancing tumors, a second plane of one or both of these sequences should be provided to enable a volume calculation. In pilocytic astrocytomas, an intensification of enhancement or a new contrast enhancement must not be mistaken for a malignant degeneration and progression. In these tumors, enhancement is strongly varying and not related to prognosis with (Lesniak et al. 2003) and also without treatment (Gaudino et al. 2012).

Fig. 47 This tumor of the pons was unusual for a DIPG because of a cyst besides a long duration of clinical complaints. Histological examination revealed a pilocytic astrocytoma

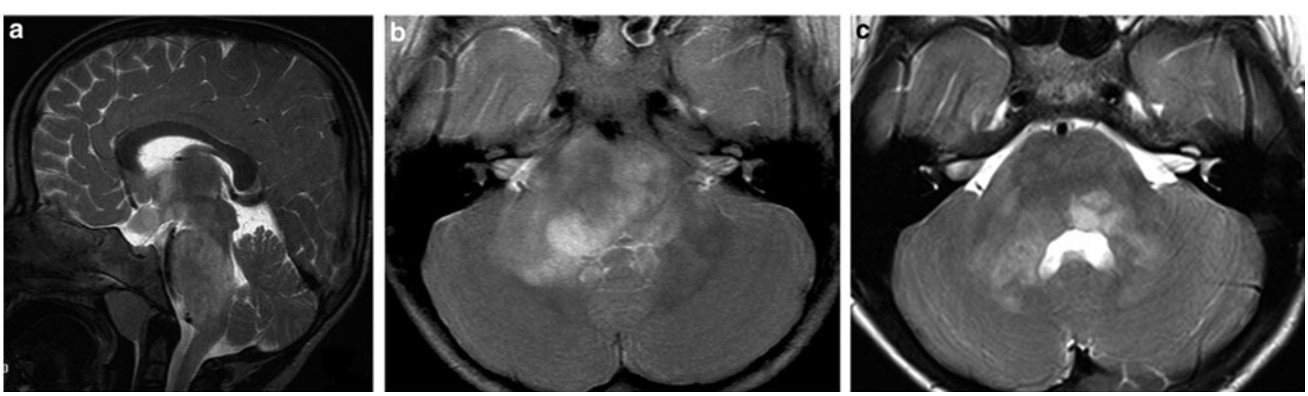

Fig. 48 Sagittal (**a**) and axial (**b**) T2-weighted images of a 4-year-old child with neurofibromatosis I and only very mild brainstem symptoms. Five years later (**c**) the swelling of the pons markedly regressed

Table 3 Typical MRI features useful for the differential diagnosis of the most frequent tumor entities of the suprasellar region in children and young adults. Sarcoidosis is not common in children and may be omitted in the differential diagnosis

Histology	LGG	GCT	Craniopharyngioma	LCH	Sarcoidosis
T2	Hyperintense	Isointense	Mixed	Hypointense	Hypointense
Enhancement	±	+	+	+	+
Internal structure	Often solid/cysts possible	Solid/small cysts possible	Predominantly cystic	Solid	Solid
HHL signal	+	–	∓	–	?

LGG low-grade glioma, *GCT* germ cell tumor, *LCH* Langerhans cell histiocytosis

Fig. 49 A circular calcification on CT (soft tissue reconstruction mode) is characteristic for an adamantinous craniopharyngioma

Fig. 50 A large partly solid craniopharyngioma of the intra- and suprasellar region has caused a loss of the physiologic bright signal of the posterior pituitary gland on unenhanced T1-weighted image. This feature is the imaging correlate of a diabetes insipidus

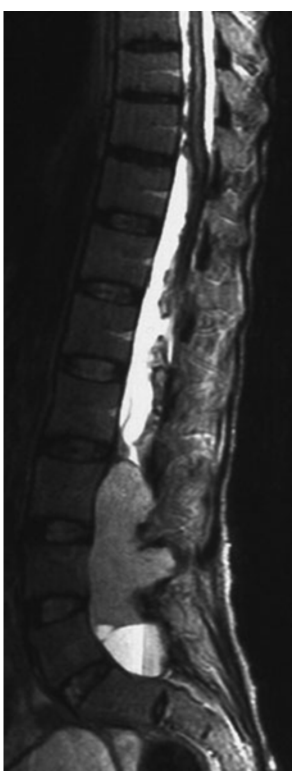

Fig. 51 Leptomeningeal siderosis with nodular and laminar areas of signal loss on a T2-weighted lumbosacral MRI in a patient with a large ependymoma of the filum terminale

Fig. 52 The spinal MRI (T1-weighted sequence after contrast) performed in the early postoperative period after resection of a medulloblastoma shows subdural enhancing structures protruding into the spinal canal from the outer dural margins. This nonspecific postoperative phenomenon precludes a reliable exclusion or diagnosis of leptomeningeal dissemination. Therefore, the staging MRI has to be repeated, and these nonspecific changes usually disappear quickly

References

Aghi M, Gaviani P, Henson JW, Batchelor TT, Louis DN, Barker FG 2nd (2005) Magnetic resonance imaging characteristics predict epidermal growth factor receptor amplification status in glioblastoma. Clin Cancer Res 11(24 Pt1):8600–8605

Bähr O, Hattingen E, Rieger J, Steinbach JP (2011) Bevacizumab induced tumor calcifications as a surrogate marker of outcome in patients with glioblastoma. Neuro Oncol 13(9):1020–1029

Baleriaux DL (1999) Spinal cord tumors. European Radiol 9(7):1252–1258

Beni-Adani L, Gomori M, Spektor S, Constantini S (2000) Cyst wall enhancement in pilocytic astrocytoma: neoplastic or reactive phenomena. Pediatr Neurosurg 32(5):234–239

Bishop FS, Liu JK, Chin SS, Fults DW (2008) Recurrent cerebellar hemangioblastoma with enhancing tumor in the cyst wall: case report. Neurosurgery 62(6):E1378–E1379

Brandsma D, Stalpers L, Taal W, Sminia P, van den Bent MJ (2008) Clinical features, mechanisms, and management of pseudoprogression in malignant gliomas. Lancet Oncol 9(5):453–461

Bühring U, Herrlinger U, Krings T, Thiex R, Weller M, Küker W (2001) MRI features of primary central nervous system lymphomas at presentation. Neurology 57(3):393–396 (Review)

Chaichana KL, McGirt MJ, Niranjan A, Olivi A, Burger PC, Quinones-Hinojosa A (2009) Prognostic significance of contrast enhancing low-grade gliomas in adults and a review of the literature. Neurol Res 31(9):931–939

Di Iorgi N, Napoli F, Allegri AE, Olivieri I, Bertelli E, Gallizia A, Rossi A, Maghnie M (2012) Diabetes insipidus–diagnosis and management. Horm Res Paediatr 77(2):69–84

Diehn M, Nardini C, Wang DS, McGovern S, Jayaraman M, Liang Y, Aldape K, Cha S, Kuo MD (2008) Identification of noninvasive imaging surrogates for brain tumor gene-expression modules. Proc Natl Acad Sci U S A 105(13):5213–5218

Eoli M, Menghi F, Bruzzone MG, De Simone T, Valletta L, Pollo B, Bissola L, Silvani A, Bianchessi D, D'Incerti L, Filippini G, Broggi G, Boiardi A, Finocchiaro G (2007) Methylation of O6-methylguanine DNA methyltransferase and loss of heterozygosity on 19q and/or 17p are overlapping features of secondary glioblastomas with prolonged survival. Clin Cancer Res 13(9):2606–2613

Fischbein NJ, Prados MD, Wara W, Russo C, Edwards MS, Barkovich AJ (1996) Radiologic classification of brain stem tumors: correlation of magnetic resonance imaging appearance with clinical outcome. Pediatr Neurosurg 24(1):9–23

Forsting M, Albert FK, Kunze S, Adams HP, Zenner D, Sartor K (1993) Extirpation of glioblastomas: MR and CT follow-up of residual tumor and regrowth patterns. AJNR Am J Neuroradiol 14(1):77–87

Gaudino S, Quaglio F, Schiarelli C, Martucci M, Tartaglione T, Gualano MR, Di Lella GM, Colosimo C (2012) Spontaneous modifications of contrast enhancement in childhood non-cerebellar pilocytic astrocytomas. Neuroradiology 54(9):989–995

Gnekow AK, Falkenstein F, von Hornstein S, Zwiener I, Berkefeld S, Bison B, Warmuth-Metz M, Driever PH, Soerensen N, Kortmann RD, Pietsch T, Faldum A (2012) Long-term follow-up of the multicenter, multidisciplinary treatment study HIT-LGG-1996 for low-grade glioma in children and adolescents of the German Speaking Society of pediatric oncology and hematology. Neuro Oncol 14(10):1265–1284

Huisman TA (2009) Pediatric tumors of the spine. Cancer Imaging 9 Spec No A:45–48

Jallo GI, Freed D, Epstein F (2003) Intramedullary spinal cord tumors in children. Child's Nervous System: ChNS: Official Journal of the International Society for Pediatric Neurosurgery 19(9):641–649

Jellison BJ, Field AS, Medow J, Lazar M, Salamat MS, Alexander AL (2004) Diffusion tensor imaging of cerebral white matter: a pictorial review of physics, fiber tract anatomy, and tumor imaging patterns. AJNR Am J Neuroradiol 25(3):356–369 (Review)

Kan P, Liu JK, Hedlund G, Brockmeyer DL, Walker ML, Kestle JR (2006) The role of diffusion-weighted magnetic resonance imaging in pediatric brain tumors. Child's Nervous System: ChNS: Official Journal of the International Society for Pediatric Neurosurgery 22(11):1435–1439

Kandt RS (2003) Tuberous sclerosis complex and neurofibromatosis type 1: the two most common neurocutaneous diseases. Neurol Clin 21(4):983–1004 (Review)

Kato Y, Higano S, Tamura H, Mugikura S, Umetsu A, Murata T, Takahashi S (2009) Usefulness of contrast-enhanced T1-weighted sampling perfection with application-optimized contrasts by using different flip angle evolutions in detection of small brain metastasis at 3T MR imaging: comparison with magnetization-prepared rapid acquisition of gradient echo imaging. AJNR Am J Neuroradiol 30(5):923–929

Kim SS, McCutcheon IE, Suki D, Weinberg JS, Sawaya R, Lang FF, Ferson D, Heimberger AB, DeMonte F, Prabhu SS (2009) Awake craniotomy for brain tumors near eloquent cortex: correlation of intraoperative cortical mapping with neurological outcomes in 309 consecutive patients. Neurosurgery 64(5):836–845

Knauth M, Aras N, Wirtz CR, Dorfler A, Engelhorn T, Sartor K (1999) Surgically induced intracranial contrast enhancement: potential source of diagnostic error in intraoperative MR imaging. AJNR Am J Neuroradiol 20(8):1547–1553

Kumar N, Miller GM, Piepgras DG, Mokri B (2010) A unifying hypothesis for a patient with superficial siderosis, low-pressure headache, intraspinal cyst, back pain, and prominent vascularity. Journal of Neurosurg 113(1):97–101

Lesniak MS, Klem JM, Weingart J, Carson BS Sr (2003) Surgical outcome following resection of contrast-enhanced pediatric brainstem gliomas. Pediatr Neurosurg 39(6):314–322

Liang L, Korogi Y, Sugahara T, Ikushima I, Shigematsu Y, Okuda T, Takahashi M, Kochi M, Ushio Y (2002) MRI of intracranial germcell tumours. Neuroradiology 44(5):382–388

Makras P, Samara C, Antoniou M, Zetos A, Papadogias D, Nikolakopoulou Z, Andreakos E, Toloumis G, Kontogeorgos G, Piaditis G, Kaltsas GA (2006) Evolving radiological features of hypothalamo-pituitary lesions in adult patients with Langerhans cell histiocytosis (LCH). Neuroradiology 48(1):37–44

Medina JH, Abrams K, Falcone S, Bhatia RG (2010) Spinal imaging findings in spontaneous intracranial hypotension. AJR Am J Radiol 195(2):459–464

Muragaki Y, Chernov M, Maruyama T, Ochiai T, Taira T, Kubo O, Nakamura R, Iseki H, Hori T, Takakura K (2008) Low-grade glioma on stereotactic biopsy: how often is the diagnosis accurate? Minim Invasive Neurosurg 51(5):275–279

Pinker K, Noebauer-Huhmann IM, Stavrou I, Hoeftberger R, Szomolanyi P, Karanikas G, Weber M, Stadlbauer A, Knosp E, Friedrich K, Trattnig S (2007) High-resolution contrast-enhanced, susceptibility-weighted MR imaging at 3T in patients with brain tumors: correlation with positron-emission tomography and histopathologic findings. AJNR Am J Neuroradiol 28(7): 1280–1286

Poretti A, Meoded A, Huisman TA (2012) Neuroimaging of pediatric posterior fossa tumors including review of the literature. J Magn Reson Imaging 35(1):32–47

Poussaint TY, Kocak M, Vajapeyam S, Packer RI, Robertson RL, Geyer R, Haas-Kogan D, Pollack IF, Vezina G, Zimmerman R, Cha S, Patay Z, Boyett JM, Kun LE (2011) MRI as a central component of clinical trials analysis in brainstem glioma: a report from the pediatric brain tumor consortium (PBTC). Neuro Oncol 13(4):417–427

Rieger J, Bähr O, Müller K, Franz K, Steinbach J, Hattingen E (2010) Bevacizumab-induced diffusion-restricted lesions in malignant glioma patients. J Neurooncol 99(1):49–56

Roux FE, Boulanouar K, Lotterie JA, Mejdoubi M, LeSage JP, Berry I (2003) Language functional magnetic resonance imaging in preoperative assessment of language areas: correlation with direct cortical stimulation. Neurosurgery 52(6):1335–1345

Ruff IM, Petrovich Brennan NM, Peck KK, Hou BL, Tabar V, Brennan CW, Holodny AI (2008) Assessment of the language laterality index in patients with brain tumor using functional MR imaging: effects of thresholding, task selection, and prior surgery. AJNR Am J Neuroradiol 29(3):528–535

Scott JN, Brasher PM, Sevick RJ (2002) How often are nonenhancing supratentorial gliomas malignant? A population study. Neurology 59:947–949

Spiller M, Tenner MS, Couldwell WT (2001) Effect of absorbable topical hemostatic agents on the relaxation time of blood: an in vitro study with implications for postoperative magnetic resonance imaging. J Neurosurg 95(4):687–693

Spreer J, Arnold S, Quiske A, Wohlfarth R, Ziyeh S, Altenmüller D, Herpers M, Kassubek J, Klisch J, Steinhoff BJ, Honegger J, Schulze-Bonhage A, Schumacher M (2002) Determination of hemisphere dominance for language: comparison of frontal and temporal fMRI activation with intracarotid amytal testing. Neuroradiology 44(6):467–474

Stephenson JA, Wiley AL Jr (1995) Current techniques in threedimensional CT simulation and radiation treatment planning. Oncology 9(11):1225–1232

Sumida M, Uozumi T, Kiya K, Mukada K, Arita K, Kurisu K, Sugiyama K, Onda J, Satoh H, Ikawa F et al (1995) MRI of intracranial germ cell tumours. Neuroradiology 37(1):32–37

Tong KA, Ashwal S, Obenaus A, Nickerson JP, Kido D, Haacke EM (2008) Susceptibility-weighted MR imaging: a review of clinical applications in children. AJNR Am J Neuroradiol 29(1):9–17

Tsuda M, Takahashi S, Higano S, Kurihara N, Ikeda H, Sakamoto K (1997) CT and MR imaging of craniopharyngioma. Eur Radiol 7(4):464–469

Vos MJ, Uitdehaag BM, Barkhof F, Heimans JJ, Baayen HC, Boogerd W, Castelijns JA, Elkhuizen PH, Postma TJ (2003) Interobserver variability in the radiological assessment of response to chemotherapy in glioma. Neurology 60(5):826–830

Warmuth-Metz M, Gnekow AK, Muller H, Solymosi L (2004a) Differential diagnosis of suprasellar tumors in children. Klin Padiatr 216(6):323–330

Warmuth-Metz M, Kuhl J, Krauss J, Solymosi L (2004b) Subdural enhancement on postoperative spinal MRI after resection of posterior cranial fossa tumours. Neuroradiology 46(3):219–223

Wen PY, Macdonald DR, Reardon DA, Cloughesy TF, Sorensen AG, Galanis E, Degroot J, Wick W, Gilbert MR, Lassman AB, Tsien C, Mikkelsen T, Wong ET, Chamberlain MC, Stupp R, Lamborn KR, Vogelbaum MA, van den Bent MJ, Chang SM (2010) Updated response assessment criteria for high-grade gliomas: response assessment in neuro-oncology working group. J Clin Oncol 28(11):1963–1972

Wetzel SG, Johnson G, Tan AG, Cha S, Knopp EA, Lee VS, Thomasson D, Rofsky NM (2002) Three-dimensional, T1-weighted gradient-echo imaging of the brain with a volumetric interpolated examination. AJNR Am J Neuroradiol 23(6):995–1002

White ML, Zhang Y, Kirby P, Ryken TC (2005) Can tumor contrast enhancement be used as a criterion for differentiating tumor grades of oligodendrogliomas? AJNR Am J Neuroradiol 26(4):784–790

Zulfiqar M, Dumrongpisutikul N, Intrapiromkul J, Yousem DM (2012) Detection of intratumoral calcification in oligodendrogliomas by susceptibility-weighted MR imaging. AJNR Am J Neuroradiol 33(5):858–864

MR Spectroscopic Imaging

Elke Hattingen and Ulrich Pilatus

Contents

E. Hattingen (✉)
Neuroradiology, Clinic of Rheinische, Friedrich-Wilhelms-University, Sigmund-Freud Straße 6, 53127 Bonn, Germany
e-mail: elke.hattingen@ukb.uni-bonn.de

U. Pilatus (✉)
Neuroradiology, Goethe University Frankfurt, Schleusenweg 2-16, 60528 Frankfurt/Main, Germany
e-mail: u.pilatus@em.uni-frankfurt.de

Abbreviations

ATRT	Atypical teratoid rhabdoid tumor
BCNU	Bis-chloroethylnitrosourea (carmustine)
GBM	Glioblastoma multiforme
HIF1α	Hypoxia-inducible factor 1-alpha
PFS	Progression-free survival
PNET	Primitive neuroectodermal tumor
PRESS	Point resolved spectroscopy
rGBM	Recurrent glioblastoma multiforme
STEAM	Stimulated echo acquisition mode
T	Tesla

MR spectroscopy (MRS) allows the noninvasive measurement of the concentrations from selected metabolites in vivo. Till now, MR spectroscopy is applied for specific purposes in brain tumor diagnostics. The metabolic profile of a brain tumor not only characterizes tumor entity, but it may also be crucial for prognosis and for therapeutic decisions. In the last decades, it has become evident that molecular genetic markers of a brain tumor may be prognostic or even predictive for a specific therapy (Weller et al. 2009; Reifenberger et al. 2012). Therefore, therapy of brain tumors is becoming increasingly complex, and histopathological features should not be the only aspect of establishing therapeutic decisions in the future. These molecular markers influence the metabolic profile and the micro milieu of the tumor. While MRI is considered as method of choice for diagnostic imaging of brain tumors, the method of MR spectroscopy, which is based on the same physical principles as MRI and can be performed with the identical setup, provides metabolic information, thereby offering a tool for studying the metabolic profile. In vitro MRS studies of tumor specimen and many in vivo studies have already shown that MR spectroscopy is able to detect these metabolic profiles or even the oncometabolites themselves (Constantin et al. 2012). Therefore, the role of MR spectroscopy may fundamentally change in the next

E. Hattingen, U. Pilatus (eds.), *Brain Tumor Imaging*,
Med Radiol Diagn Imaging (2016)
DOI 10.1007/174_2016_1031,

decades. Hitherto, MR spectroscopic studies investigated the sensitivity and diagnostic accuracy of MR spectroscopy in characterizing brain tumors and tumorlike lesions (Horská and Barker 2010). Taking into account that the accuracy is not sufficient to replace histopathological diagnosis, the value of time-consuming spectroscopic methods for differential diagnostic still remains limited. Today's primary indications of MR spectroscopy in diagnostic settings should be: (1) guiding stereotactic biopsy in heterogeneous or large non-necrotic brain tumors, (2) avoiding surgery in asymptomatic patients with small brain tumors in eloquent brain areas or young patients with chronic partial epilepsy with "benign" aspect, and (3) monitoring residual low-grade tumors after surgery. Monitoring high-grade gliomas after standard therapy (surgery, followed by radiation and chemotherapy) may be difficult or even impossible with proton MR spectroscopy. First, recurrent high-grade gliomas often occur at the margins of resection cavity and thus in areas with preexisting damaged brain tissue from radiation, peri-surgical infarction, and macro- or microbleeds. Considering that metabolites other than lipids are only present in solid and vital tumor tissue, partial volume effects from necrotic and hemorrhagic tissue may affect the metabolite concentration obtained for the targeted voxel. Second, many malignant brain tumors are located in the temporal or frontobasal lobes. In these brain areas, proton MR spectroscopy is prone to susceptibility artifacts requiring time-consuming manual shimming or even rendering the spectra useless. Some of these disadvantages do not apply to phosphorus MR spectroscopy which measures some of the most relevant compounds involved in tumor metabolism: metabolites of membrane phospholipids, the products of oxidative phosphorylation, and the intracellular pH (see Chap. Future Methods in Tumor Imaging).

This chapter focuses on the special metabolism of glial brain tumors to elucidate the role of MR spectroscopy for a more "individualized" tumor characterization.

1 Methods

1.1 Introduction to MRS

Magnetic resonance imaging (MRI) measures the signal of water protons (^{1}H nuclei) in the presence of magnetic field gradients, which, together with phase encoding, provides the localization. MRS detects water-soluble metabolites, thus presenting a method for in vivo monitoring of metabolic changes. At the magnetic field strength of a standard clinical MR scanner (1.5–3 T), the ^{1}H nuclei and to a certain extent also the ^{31}P nuclei show sufficient sensitivity to allow the in vivo detection of metabolites in small volumes (<4 ml) within reasonable acquisition time. The first in vivo ^{31}P spectrum of mouse brain was recorded in 1978 (Chance et al. 1978). Measuring ^{1}H spectra requires efficient suppression of the dominant water signal, which exceeds the metabolite signals by approximately 10^4, and is therefore technically more demanding. The first in vivo ^{1}H spectra of rat brain were recorded in 1983 using a surface coil in a vertical bore high-resolution NMR spectrometer at 8 T (Behar et al. 1983). Human brain spectra were first obtained in 1985 by Bottomley et al. (1985).

Initially, in vivo spectra were recorded with surface coils which detect signal from the entire region in the vicinity of the coil. For application to pathological lesions, it is required to obtain spectra from a targeted region of the brain (e.g., tumor tissue). This can be achieved by pulse sequences with selective excitation of three orthogonal slabs resulting into spectra from a single cuboid volume element localized at the intersection of the slabs (single voxel spectroscopy, SVS). Two methods are available, either PRESS (Bottomley et al. 1985; Ordidge et al. 1987) or STEAM (Frahm et al. 1989), each having their advantages and disadvantages as described by Moonen et al. (1989). The potential of measuring spatially resolved spectroscopic information (i.e., obtaining a matrix of spectra as demonstrated in Figs. 1 and 2) by combining spectroscopy with gradient phase encoding (spectroscopic imaging, SI or MRSI) was first demonstrated by Brown et al. (1982) for the ^{31}P nucleus, while 10 years later Fulham et al. (1992) showed first ^{1}H MR spectroscopic images of patients with brain tumors. At that time many studies on human tumors had already been performed (for review, see Negendank 1992) including several ^{31}P MR spectroscopic examinations on brain tumors applying various localization techniques. However, with the publication of the first localized water-suppressed ^{1}H spectrum of a human brain tumor by Bruhn et al. (1989), single voxel ^{1}H MRS had become the method of choice for supporting a noninvasive differential diagnosis in brain tumors. This can be attributed to the fact that the spectra show separate markers for the pathological and normal tissue: the increase in intensity of the choline signal is related to tumor cell proliferation (Herminghaus et al. 2002; Guillevin et al. 2008), while the decrease of the concentration of metabolite *N-acetyl-aspartate* marks breakdown of neuronal cells as it is shown in Fig. 1 for a patient with glioblastoma (see also Table 1).

Single voxel spectroscopy relies on the accurate definition of tumor tissue from T2-weighted or CE-enhanced MRI. But these data lack information of tumor heterogeneity and potential tumor infiltration. Further, discrimination of tumor tissue may be difficult for infiltrating gliomas. In MR spectroscopic imaging (MRSI), all spectra of a selected slice are acquired simultaneously applying encoding gradients between the excitation pulse and the acquisition period. After spatial Fourier transformation, the spectroscopic image is obtained as a matrix of the dimension $N_X \times N_Y$, where N_X and N_Y denote the number of phase encoding steps in each direction within the slice. For each matrix, a spectrum can be calculated representing the metabolic information for the voxel

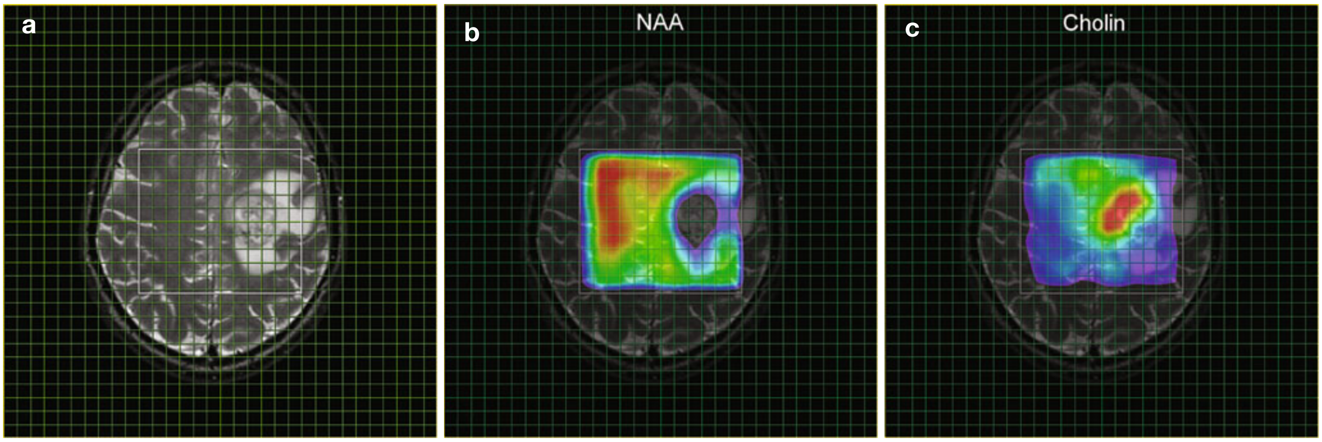

Fig. 1 MRSI parameter maps for NAA and tCho of a patient with glioblastoma. The *left panel* (**a**) shows a T2-weighted MRI with a grid overlay indicating the spatial resolution of the MRSI data. The *white frame* marks the area selected for spectroscopy using the PRESS excitation scheme. The glioblastoma is located left paracentral; the adjacent parasagittal cortex is slightly blurred on both sides with a mild increase in signal intensity. The color-coded maps show the regional distribution of the metabolites NAA (**b**, marker for intact neuronal tissue) and tCho (**c**, marker for proliferating cells). The tCho concentration increase is inhomogeneous showing tumor infiltration into the cortex of both hemispheres (Figure already published in Nervenartz 2014)

attributed to the matrix element. Signal intensities and their ratios can be visualized as a grid overlay on the anatomical image providing parameter maps for the concentrations for specific metabolites or metabolite concentrations ratios (spectroscopic image, Fig. 1). The anatomical reference image should have been recorded with identical angulation and slice offset. Such spectroscopic images provide a retrospective definition of the center and the extent of tumor tissue, while at the same time reference spectra are available from normal-appearing tissue (Fig. 2). The resolution can be as low as $0.75 \times 0.75 \times 1.00$ cm^3 at sufficient signal to noise ratio (S/N), but this requires phase encoding for the entire matrix. Consequently, acquisition of a data set with conventional MRSI techniques takes more than 15 min (see below) which might not be tolerated by many patients especially when performed in addition to the other modalities (Chaps. MR Imaging of Brain Tumors, MR Spectroscopic Imaging, MR Perfusion Imaging, and Diffusion-Weighted Methods) routinely applied in the MR examination. Modifications of the basic MRSI sequence which can reduce the data acquisition time or/and provide multi-slice data will be discussed in the next section. Details of biochemical and clinical aspects of metabolic changes will be discussed in a dedicated section.

1.2 Summary of Spectroscopic Imaging Techniques Applied in Tumor Diagnostics

For an in-plane resolution of 7.5×7.5 mm^2, the 32×32 matrix shown in Figs. 1 and 2 had to be recorded at a 240 mm^2 FOV. Acquisition of the entire k-space at a repetition time of 1.5 s would take $1{,}024 \times 1.5$ s or 26 min. Together with the preparation period (extensive shimming, adjustments for water suppression), the MRS examination may add another 30 min. to the conventional imaging examination. Reduction of measurement time and optimized automatic adjustments for the preparation period are therefore essential for a successful MRS protocol. The latter has been addressed in the modern scanners by the use of image-guided shimming procedures and implementations of routines for automatic adjustments of water suppression. These tools can reduce the preparation time to less than 1 min.

The rather extensive acquisition times required for the complete k-space can also be reduced. Without significant loss in spatial resolution, a 28×28 matrix can be recorded and extrapolated to 32×32 by adding zeroes before Fourier transformation, which will reduce the total acquisition time to 20 min. Selection of a circular (elliptical in case of rectangular FOV) k-space area centered around the origin will save another 25 % of acquisition time without seriously affecting the spatial resolution (Maudsley et al. 1994). The use of a rectangular FOV could also save up to 30 % (Golay et al. 2002) resulting in a total acquisition time between 10 and 15 min. Further reduction in acquisition time can be achieved with fast imaging techniques like echo planar spectroscopic imaging (EPSI) and parallel imaging method (Posse et al. 1995; Zierhut et al. 2009; Ozturk et al. 2006; Sabati et al. 2014) or multiple spin-echo spectroscopic imaging (MSESI) (Duyn and Moonen 1993). These techniques scan more than one phase encoding step for a single excitation pulse, providing the respective acceleration factors, and allow acquisition of 3D MRSI data with sufficient spatial resolution in reasonable scan time.

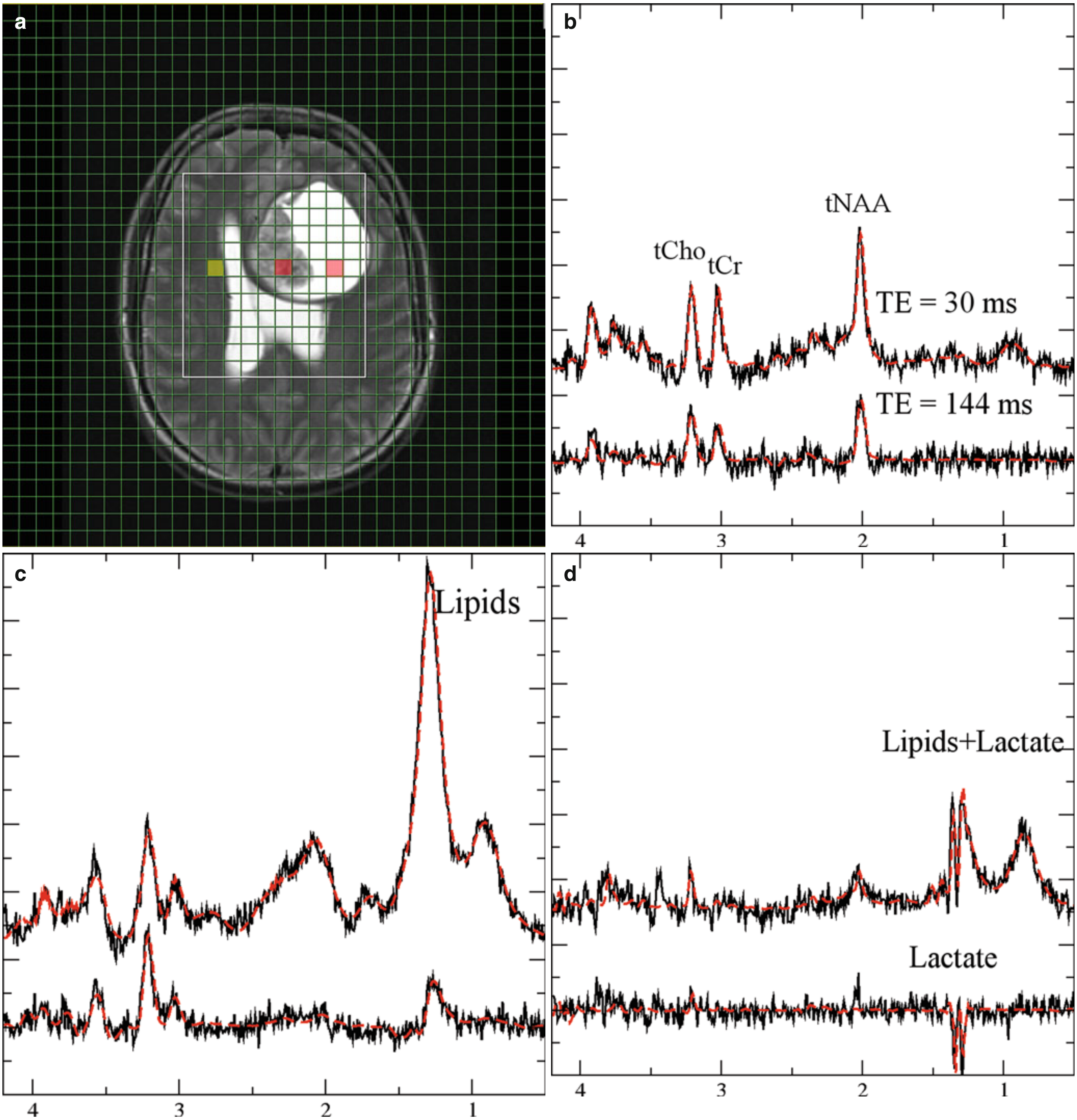

Fig. 2 Monitoring lactate. Short (30 ms, upper traces) and long (lower traces) from a patient with glioma grade IV. (**a**, T2-weighted MRI with a grid overlay indicating the spatial resolution of MRSI). The three panels with spectroscopic data show normal-appearing tissue (**b**, *yellow-marked* voxel in the MRI), necrotic tissue (**c**, *central red-marked* voxel in the MRI), and CSF (**d**, *right red-marked* voxel in the MRI). Lactate is visible as a doublet (two signals with 8 Hz distance) at 1.3 ppm. The signals are inverted at long TE. Note that the lipid signals at 1.2 ppm which are only visible at short TE are overlapping with lactate

Table 1 Important metabolites in 1H MRS and their significance in brain tumors

	Peak	Biology	Marker	Increase	Decrease
N-Acetyl-aspartate NAA	2.02 ppm	Second-most-concentrated cerebral amino acid Synthesis in neuronal mitochondria from the amino acid aspartic acid and acetyl-coenzyme A Functions still under investigation	Neuronal marker Neuronal integrity	–	Any neuronal damage (may be reversible)
Choline-containing compounds Cho	3.2 ppm	Part of the hydrophilic head of the membrane phospholipid phosphatidylcholine (lecithin)	Cell density Cell proliferation Demyelination	High-grade glioma Medulloblastoma, PNET ATRT	Cell necroses Gliosis
Total creatine (phosphocreatine + creatine) tCr (PCr + Cr)	3.03 and 3.94 ppm	PCr: storing and buffering of high phosphate-bound energy, provide quick regeneration of ATP Cr: functions still under investigations, synthesis in oligodendrocytes associated with neuronal elements Used for polyamine and methionine synthesis in tumor cells	Activation of glial cells	Gliomatosis Some solid gliomas Prognostic marker for PSF of WHO grade II and III astrocytomas	Metastases, necrosis, lymphoma, malignant glial tumors
Myo-inositol MI, m-Ins	3.56 ppm (complex signals in short TE)	Osmotic regulator within the astrocytes Precursor of phosphatidylinositol (involved in metabolic pathway activating proteolytic enzymes)	Osmolyte Not defined	Gliomatosis Low-grade astrocytomas Schwannomas Choroid plexus papilloma	Metastases High-grade gliomas
Glycine Gly	3.56 ppm	Simplest amino acid Increased synthesis in glioma cells (serine hydroxymethyltransferase) Utilized for de novo purine biosynthesis	Not defined [a]Tumor cell proliferation	High-grade gliomas Medulloblastoma	Normally not measurable, negligible
Lipids	Two large peaks at 0.8–0.9 ppm and 1.2–1.3 ppm	Mobile lipids, lipids in droplets	Cell necrosis	Necrosis of high-grade gliomas Metastases and meningioma Lymphomas Radio-necrosis	Normally not measurable, negligible (cave artifacts from skull)
Lactate	Double-peak at 1.33 ppm, in long-TE (135 ms) inverted	Product of glycolysis	Anaerobic glycolysis	Unspecific: tumor (more often in high- but also in low-grade glioma) necrosis, cysts, inflammation	Normally not measurable
Taurine	3.4 ppm (complex signals in short TE)	Abundant in developing cerebellum and isocortex; involved in cell shrinkage during apoptosis	Putative marker of apoptosis	Medulloblastoma	Low-grade pilocytic astrocytoma, choroid plexus papilloma
Alanine	Double-peak at 1.5 ppm in long-TE (135 ms) inverted	Amino acid		Meningioma, abscess	Normally not measurable

[a]Jain et al. (2012)

1.3 Partial Volume Effects Due to Low Resolution

Metabolite concentrations from lesions smaller than the grid resolution will be affected by the concentration in the surrounding tissue and changes may be masked, i.e., choline concentrations will be underestimated while NAA concentrations will be overestimated. Also, special care should be taken when nominal matrix size (i.e., the number of phase encoding steps in each direction before extrapolation by adding zeroes) is rather small ($<16 \times 16$), since this causes significant blurring due to the poor point spread function leading to "bleeding" of signal intensity between adjacent voxels. Signal bleeding also becomes significant when the grid resolution (resolution after adding zeroes) exceeds the nominal resolution significantly; thus, digital resolution enhancement by more than a factor of 2 should be avoided. Partial volume effects should definitely be taken into account when the absolute quantification of spectroscopic data is considered.

1.4 Evaluation of Metabolite Concentrations

Spectroscopic data reflect the concentration of a subset of brain metabolites. The accuracy of the related information depends crucially on the approach used for data quantification. Generally, the spectrum is evaluated by measuring the area under the metabolite signals. This can be done either by numerical integration of metabolite peaks in phased (real) or magnitude (modulus) spectra or by using more sophisticated tools which basically perform a nonlinear fit of the entire spectrum. Depending on the tool, the fit is performed in the time domain using constraints (jMRUI (Naressi et al. 2001; Vanhamme et al. 1997), an offline tool which requires export of the data to an external workstation) or frequency domain (most processing tools which are provided by the vendor and operate on the scanner console; LCModel (Provencher 1993), offline data evaluation). All methods report signal intensities which are proportional to the respective metabolite concentration in the volume of interest (VOI). Conversion of the hardware-specific units to absolute concentrations (i.e., mMol/l) requires a set of correction factors which depend on the used pulse sequence, hardware parameters like signal amplification and coil loading, relaxation times (T1, T2) of the metabolites, as well as fractions of GM, WM, and CSF in the VOI (partial volume effects). Hardware parameters can be corrected for by using either the so-called phantom replacement method (Michaelis et al. 1993) or scaling relative to the water signal (Barker et al. 1993). The water must be recorded in a separate measurement, either as a separate MRSI data set which has to be corrected for T1 and T2 relaxations or by an imaging sequence with proton density contrast. Relaxation terms for metabolite signals from regular (healthy) tissue are available in several publications, but they may be changed in tumor tissue (Träber et al. 2004; Hattingen et al. 2007; Isobe et al. 2002). Further, the presence of contrast agents can lead to a decrease of signal intensity between 10 and 15 % (Smith et al. 2000; Sijens et al. 1997; Murphy et al. 2002). Correction for partial volume effects requires at least one more additional imaging sequence and further calculations. A rather quick method which only takes into account the CSF fraction was described by Horská et al. (2002), while analysis of GM, WM, and CSF fraction requires tissue segmentation which can be very time consuming. Therefore, a thorough data evaluation in terms of absolute concentrations should be reserved for research studies aimed at metabolic differences between different groups of patients (e.g., different tumor entities) and longitudinal studies, while for diagnostic purposes a semiquantitative approach just comparing metabolite intensities from tumor tissue and normal-appearing tissue from the contralateral side may be sufficient. Immediate information of the extent of change of metabolite concentrations or their ratios can be visualized in the MRSI metabolite map (Figs. 1 and 3). However, one should be aware of artifacts (see below).

1.5 Artifacts in Metabolite Maps

Spectroscopic imaging data are frequently visualized as metabolite maps, i.e., for each metabolite the concentration is displayed either as a grayscale image or as a color-coded overlay on an anatomical image. While this provides the most intuitive picture of the results, special care should be taken when interpreting these maps. Local field inhomogeneities due to calcification or deposits of paramagnetic hemosiderin which occur in the vicinity of areas with former bleeding can shift and distort signals, spoiling the data analysis algorithm applied to obtain the signal intensities for the specific metabolites. Especially for voxels crucial for diagnostic decision (e.g., with highest choline), the choline hot spots or Cho/NAA signal intensities require an inspection of the entire spectrum to exclude excessive line broadening and baseline distortions which usually prohibit a reasonable signal analysis by integration or fitting routines, leading to false values for metabolite concentrations or their ratios. Intense lipid signals originating from necrotic areas as well as from fat deposits in the skull base, soft tissue, and orbit can also distort the baseline. These lipid signals can even appear in the spectra and should not be misinterpreted as tumor necrosis (Fig. 4a). An excellent description how to judge the quality of the spectra is given by Kreis (2004). Rapidly growing tumor cells typically have marked increase of glycolytic rates even if oxygen is abundant (Warburg effect (Warburg 1956), see below), and lactate is considered as a marker for increased glycolysis. Lactate in tumor tissue coincides with the lipid signal but can be easily distinguished from lipid (Kuesel et al. 1996), since only lactate shows a doublet signal (i.e., two peaks of identical intensity separated by 7.4 Hz) which will be inverted at an echo time of 135 ms (Fig. 2). At B0 field strength of 3 T, the doublet structure of lactate may be less visible due to increased line broadening at higher field strengths but signal inversion can still be exploited for discrimination of lactate from lipid.

2 Tumor Metabolism

A major characteristic of brain tumors is the altered metabolism. In recent years it has become clear that biological modifications in tumor tissue are evident through metabolic alterations which may be of great importance in therapy resistance (Tennant et al. 2010). This chapter describes changes in metabolic pathways which are typical for tumor tissue and can

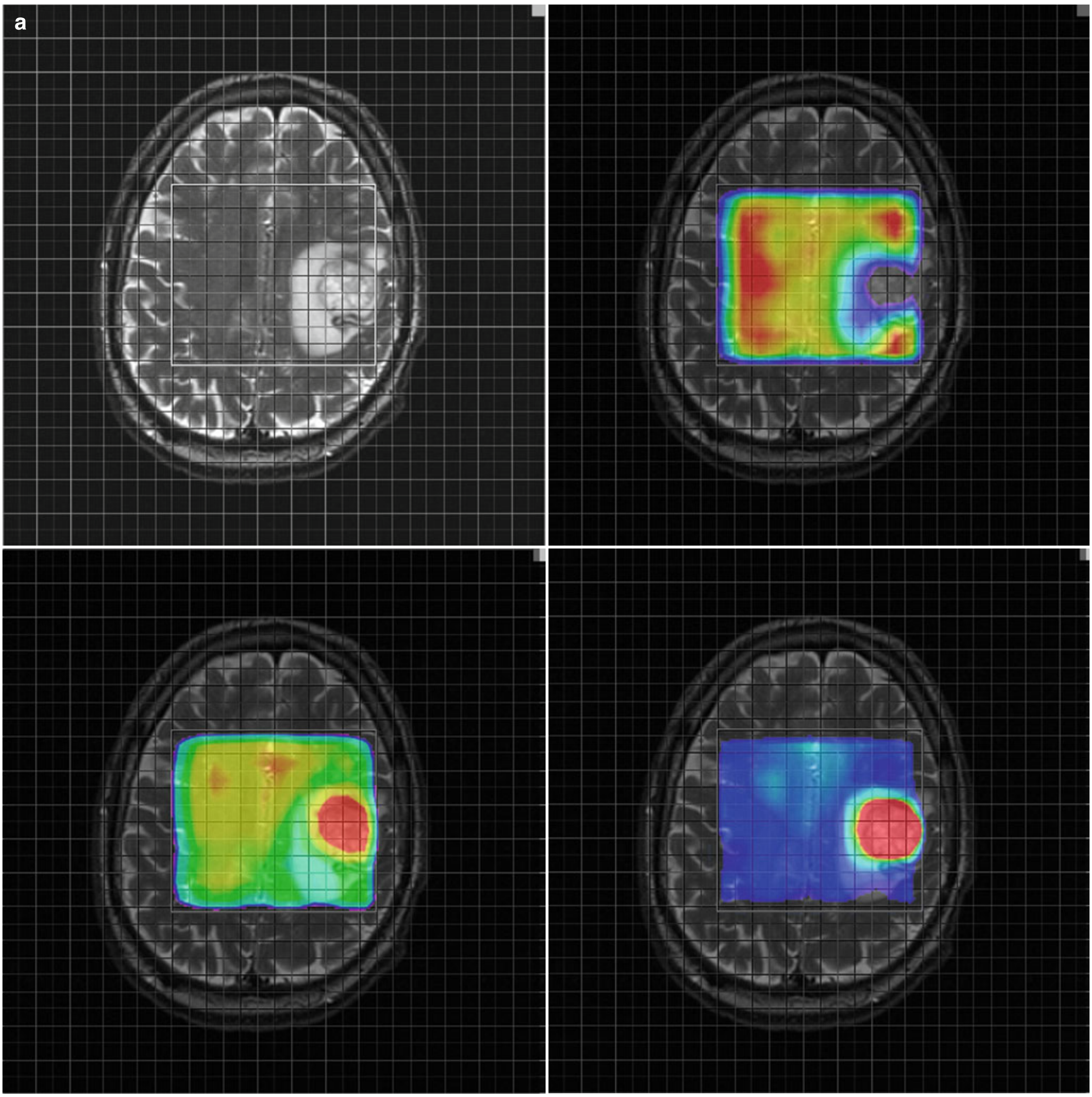

Fig. 3 Parameter maps for NAA (*upper right*) Cho (*lower left*) and the ratio Cho/NAA (*lower right*) from a glioblastoma (**a**) and a metastasis (**b**). Note the higher relative ratio Cho/NAA compared to the normal tissue in the glioblastoma (**a**) compared to the metastasis (**b**) due to a marked increase of choline signal intensity in the glioblastoma (**a**). The Cho/NAA ratios of the glioblastoma (**a**) are moderately increased outside the tumor mass, indicating tumor cell infiltration. In contrast, the Cho/NAA map of the metastasis shows clearer margins of the tumor (**b**)

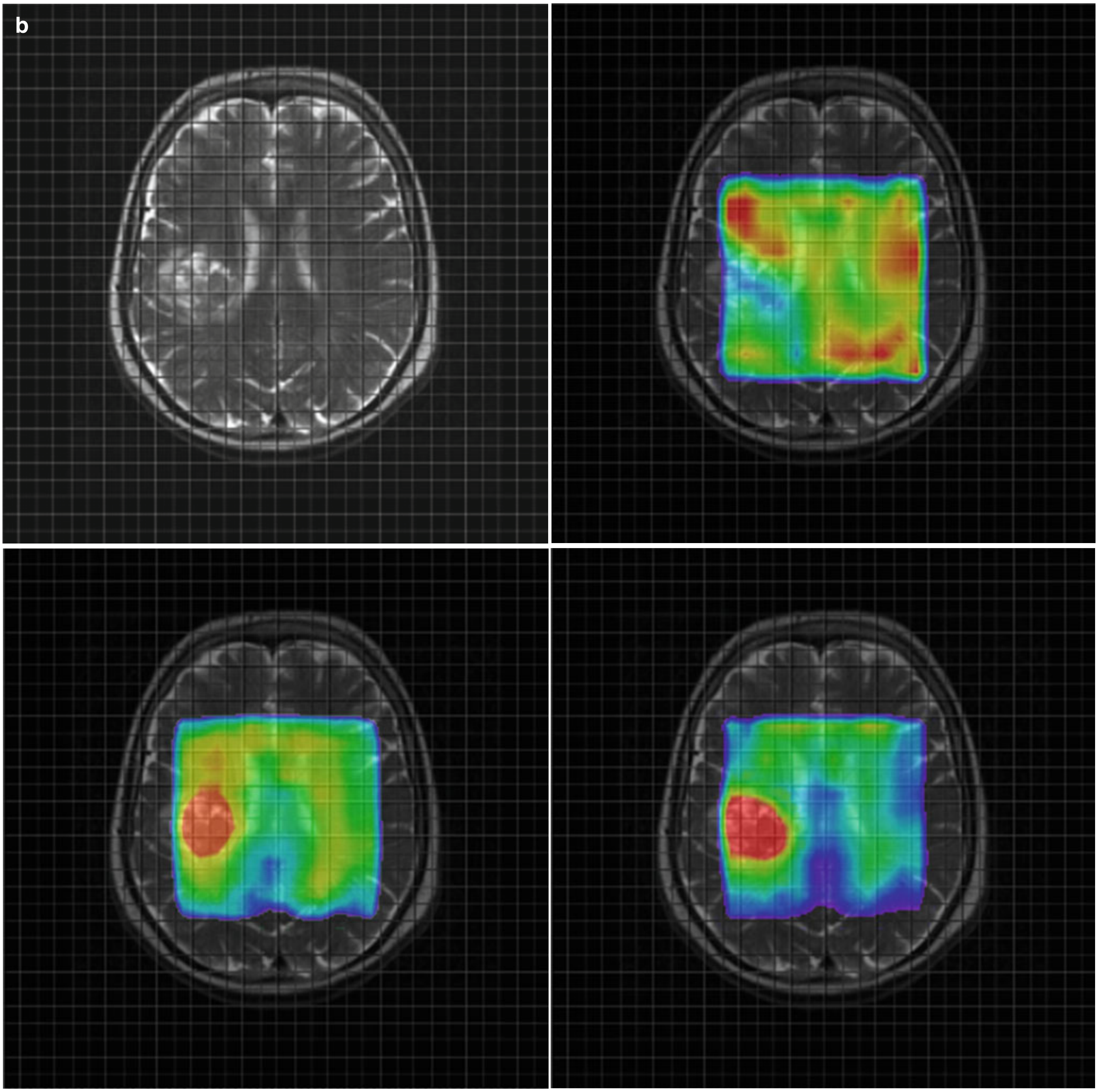

Fig. 3 (continued)

be measured by MR spectroscopy. Identifying those features may be useful for the diagnosis or treatment of brain tumors.

Tables 1 and 2 show an overview of the most important ^{1}H and ^{31}P metabolites for brain tumors. Representative ^{1}H and ^{31}P spectra from gliomas with different tumor grades are shown in Figs. 4 and 5.

A basic metabolic alteration in malignant cells is the phenotype which performs aerobic glycolysis even in the presence of oxygen whereas oxidative phosphorylation is suppressed (Warburg 1956). Enhanced lactic acid production through glycolysis causes extracellular acidosis. To counteract the intracellular proton accumulation, the activity of H^+ extruding and buffering pathways like the Na^+/H^+ exchanger or the transmembrane carbonic anhydrases is upregulated (Chiche et al. 2009; McLean et al. 2000). Thus, the extracellular environment gets more acidic while the intracellular pH increases. The maintenance of an alkaline intracellular pH in tumor cells supports cellular proliferation, whereas extracellular acidosis promotes angiogenesis. Phosphorus spectroscopy is the only noninvasive method measuring both intracellular pH and the high-energy phosphate compounds ATP and PCr (Negendank 1992; Hattingen et al. 2011).

Suppressed oxidative energy metabolism as a result of tumor hypoxia and repressed mitochondrial function may induce a decrease in high-energy phosphates like ATP and phosphocreatine (Papandreou et al. 2006).

Further, energy consumption is increased in neoplastic transformations to provide protein and nucleotide synthesis (Susa et al. 1989). The glycolytic pathway is linked with amino acid production. Serine as intermediate from 3-phosphoglycerate seems to be increased in proliferating cells (Snell 1984). Serine hydroxymethyltransferase, catalyzing the reversible reaction of serine to glycine, is highly activated in cultures of rat glioma cells (Kohl et al. 1980). Glycine, one product of this reaction, is measurable by proton spectroscopy. It has been shown that glycine is increased

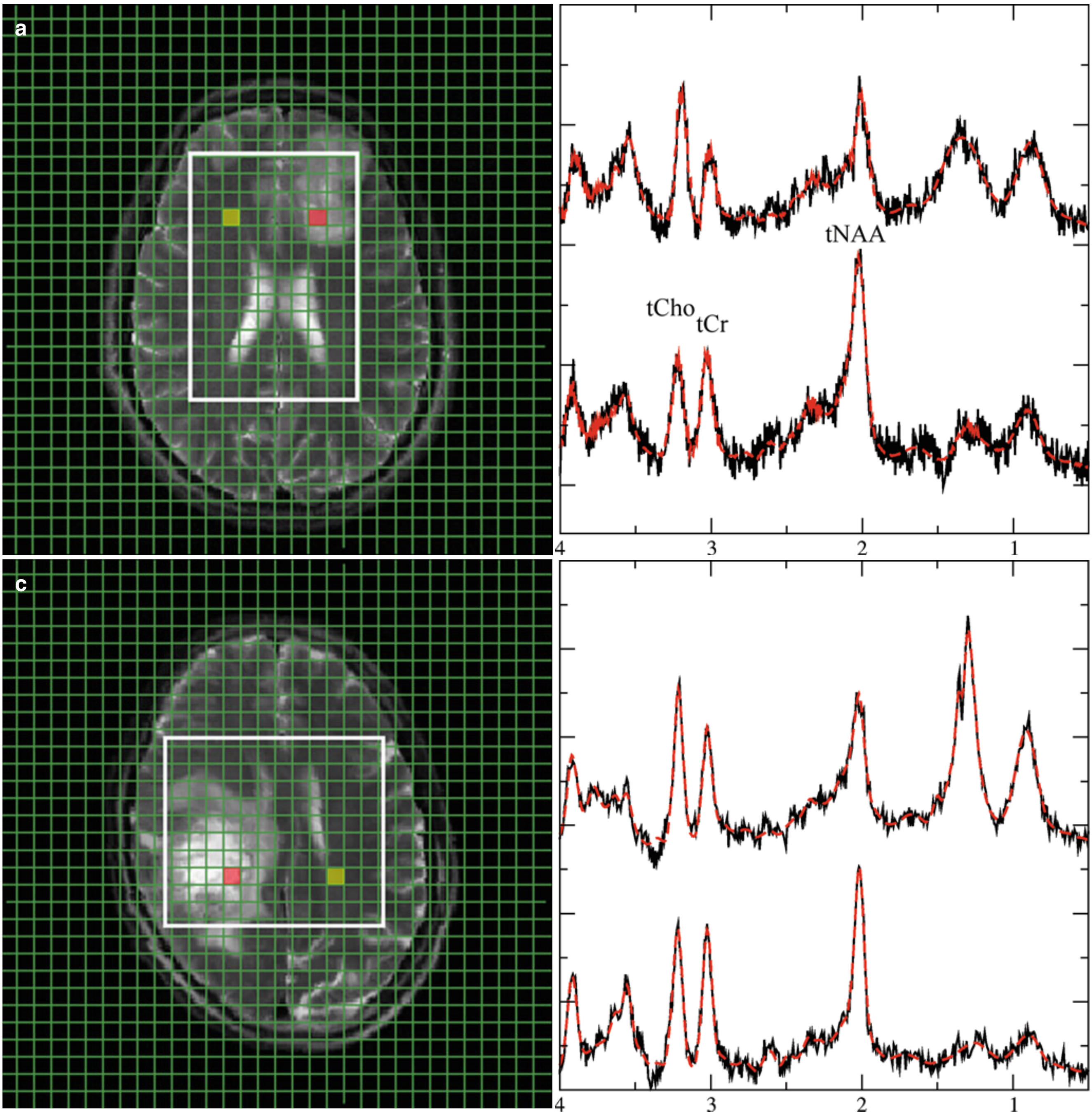

Fig. 4 Representative [1]H spectra in gliomas of different WHO grades. Short TE (30 ms) from brain tumors depicting a low-grade (**a**), a grade III (**b**), and a heterogeneous grade IV tumor (**c**). Each panel with spectroscopic data shows spectra from the voxels marked in the respective MRI on the left with the upper trace referring to the tumor voxel (*red*) and the lower trace referring to the contralateral, normal appearing tissue voxel (*yellow*). Due to its more frontal position, spectra from the low-grade tumor are broadened and therefore plotted with an extended y-scale. Note: The grade III tumor shows the most enhanced tCho signal

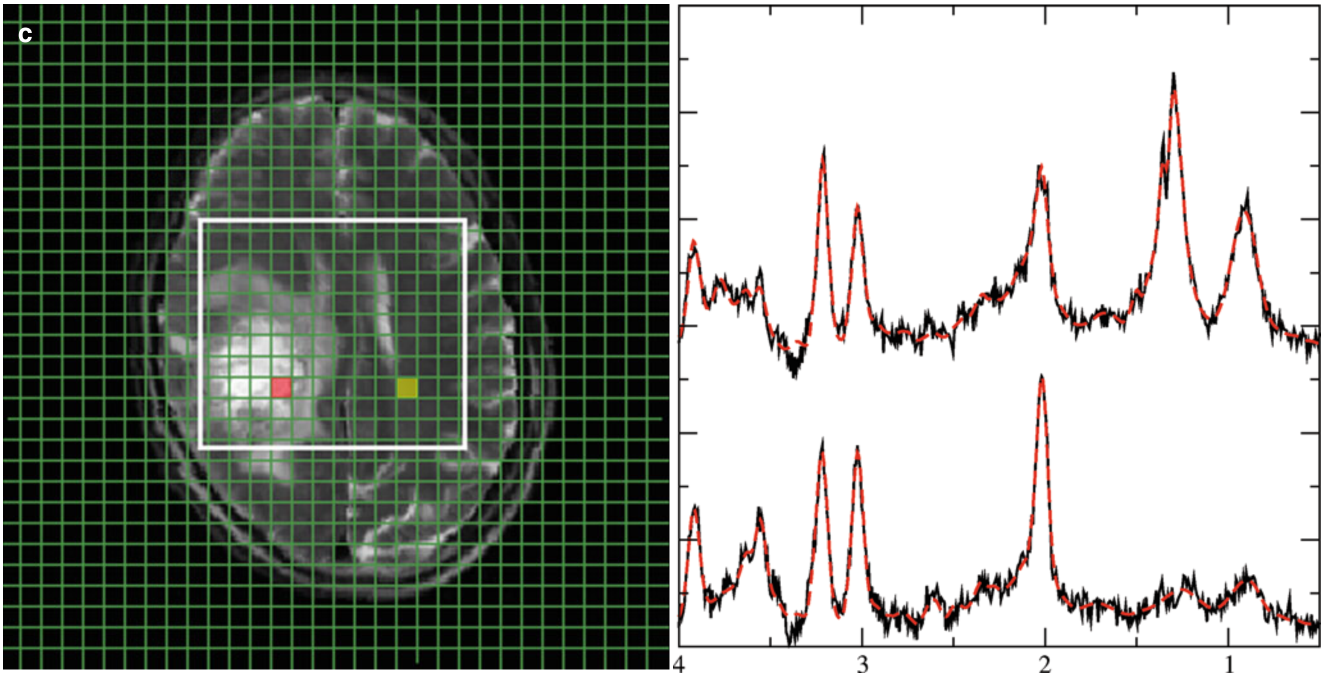

Fig. 4 (continued)

in malignant gliomas (Jain et al. 2012; Lehnhardt et al. 2005; Hattingen et al. 2009; Kinoshita et al. 1994; Maudsley et al. 2014). The other product, 5,10-methylene-tetrahydroxyfolate, is utilized for purine and nucleotide synthesis. Therefore, glycine might be considered as a surrogate marker of enhanced glycolysis and nucleotide synthesis.

However, the glycine signal is overlapping with the signal from myoinositol (MI) at 3.56 ppm, requiring special measures for discriminating MI from glycine as described in Chap. Future Methods in Tumor Imaging). Increased MI concentrations or ratios of MI to creatine were detected in tumors, but also in multiple sclerosis, Alzheimer's disease, and in other metabolic and inflammatory white matter diseases as well as in tuberous sclerosis. Common to all of these pathologies is augmented astrocytic proliferation and demyelinization. Therefore, the role of this metabolite in maintaining cell volume in reactive astrocytes is discussed (detailed discussion and references in Hattingen et al. 2008).

An increased choline signal intensity is frequently observed in ^{1}H MRS data from tumor tissue (Figs. 3a, 4b, and 6) and has been attributed to rapidly proliferating cells (Herminghaus et al. 2002; Guillevin et al. 2008). In conjunction with the decrease of the NAA (*N*-acetyl-aspartate and *N*-acetyl-aspartylglutamate) signal intensity due to neuronal loss, the tCho/NAA ratio is considered as the most prominent marker for tumor tissue in MRS (Figs. 1, 3a, 4b, and 6). Modulations of phospholipid turnover, which is in part described by the Kennedy pathway (Kennedy 1957), play a pivotal role in the tumor metabolism (Podo 1999). In brief, this pathway describes synthesis of phosphatidylcholine via choline and phosphocholine (PCho) and its breakdown via glycerophosphocholine (GPC). However, ^{1}H MR spectroscopy detects only total choline (tCho) as the sum of free choline, PCho, and GPC. Consequently, ^{1}H MRS cannot differentiate between PCho and GPC changes, whereas ^{31}P spectroscopy can (Fig. 5). There is increasing evidence that the metabolites PCho and GPC play an important role in tumorigenesis with high PCho/GPC ratios indicating malignant phenotype of a brain tumor (Hattingen et al. 2013).

In vitro studies showed that PCho is the dominant membrane lipid metabolite in proliferating tumor cells and tumor tissues (Gillies et al. 1994). PCho is formed by phosphorylation of choline by the cholinkinase α which is over-expressed in many malignant tumors including glioma cell lines (Glunde and Bhujwalla 2007). Several oncogenes increase choline kinase activity and hypoxia-inducible factor 1 alpha signaling upregulates choline kinase expression (Glunde et al. 2008). Apart from its role as a phospholipid membrane precursor, PCho may also act as a second messenger in cell growth signaling (Gillies et al. 1994; Cuadrado et al. 1993; Aiken and Gillies 1996). Aiken and Gillie 1996 found increased PCho content of rat glioma cells, which decreased during the conversion from the exponential growth to stationary growth phase. Ex vivo MR spectroscopic

Table 2 Metabolites measurable with in vivo ^{31}P MR phosphorus spectroscopy in brain tumor

Metabolite	Peak	Biology	Marker	Increase	Decrease
Phosphocholine PCho, PC	6.2 ppm	Precursor of the membrane phospholipid phosphatidylcholine (lecithine) Cho phosphorylation is catalyzed by choline kinase (CK) High levels of expression and activity of CK promotes tumor cell growth	Tumor cell proliferation	Proliferating high-grade glioma cells (animal model) Elevated PCho/GPC implies transformation of grade II to grade IV glioma (Elkhaled et al. 2014)[a] and GBM progression	Putative decrease under HIF1α inhibitor treatment (Venkatesh et al. 2012)[a]
Glyceropho-sphocholine GPC	2.9 ppm	Metabolite of the degradation pathway of phosphatidyl-choline by phospholipases		Low-grade glioma (relative increase to tCho) (Righi et al. 2009)	High-grade glioma (Elkhaled et al. 2014; Righi et al. 2009; Venkatesh et al. 2012) rGBM (Hattingen et al. 2013)
Phospho-ethanolamine PEth, PE	6.8 ppm	Precursor of the membrane phospholipid phosphatidylethanolamine (cephaline)	Tumor cell metabolism	In vivo tumors (Mintz et al. 2008) Elevated PEth/GPE in rGBM (Hattingen et al. 2013) Lymphoma (ex vivo liquid chromatography) (Kinoshita et al. 1994)	
Glycerophospho-ethanolamine GPE	3.5 ppm	Metabolite of the degradation pathway of phosphatidyl-ethanolamine by phospholipases	Putative marker of GBM	Tumor cell apoptosis (rat glioma) (Valonen et al. 2005)[a]	Recurrent GBM (Hattingen et al. 2013)
Phosphocreatine PCr	0.0 ppm	Reserve of high-energy phosphates Donator of the phosphate group to ADP to form ATP catalyzed by phosphokinase	High-energy storage	ATP/Pi increase under BCNU (animals)	Brain tumors (rat glioma) (Ross et al. 1988), rGBM (Hattingen et al. 2013)
Adeosine triphosphate ATP	−2.5 ppm (doublet) −7.6 ppm (doublet) −16.1 ppm (triplet)	High-energy source for many cellular processes such as cell division and biosynthetic reaction ATP is replenished from ADP an Pi mainly by energy from cellular respiration	High-energy metabolism	Not clear (most studies used ratios), ATP/Pi increase under BCNU (animals)	(Pre)treated brain tumors (animal tumors, rGBM) (Naruse et al. 1985; Hattingen et al. 2013)
Inorganic phosphate Pi	4.7–5.4 ppm (position changes with pH)	Low-energy state of phosphate	Part of phosphokinase reaction	(Pre)treated brain tumors (animal tumors, rGBM) (Naruse et al. 1985; Hattingen et al. 2013)	
Intracellular pH	Chemical shift difference between PCr and Pi	Upregulation of H^+ extruding and buffering pathways (Na^+/H^+ exchanger, transmembrane carbonic anhydrases) More acidic extracellular environment enhances the tumor invasiveness and angiogenesis	Intracellular H^+ production (through glycolysis)	Intracellular alkalosis in high-grade gliomas (Oberhaensli et al. 1986)	

Chemical shift values are referenced to PCr, which was set to 0 ppm

[a]Observations are results from *ex vivo* proton high-resolution magic angle spinning spectroscopy

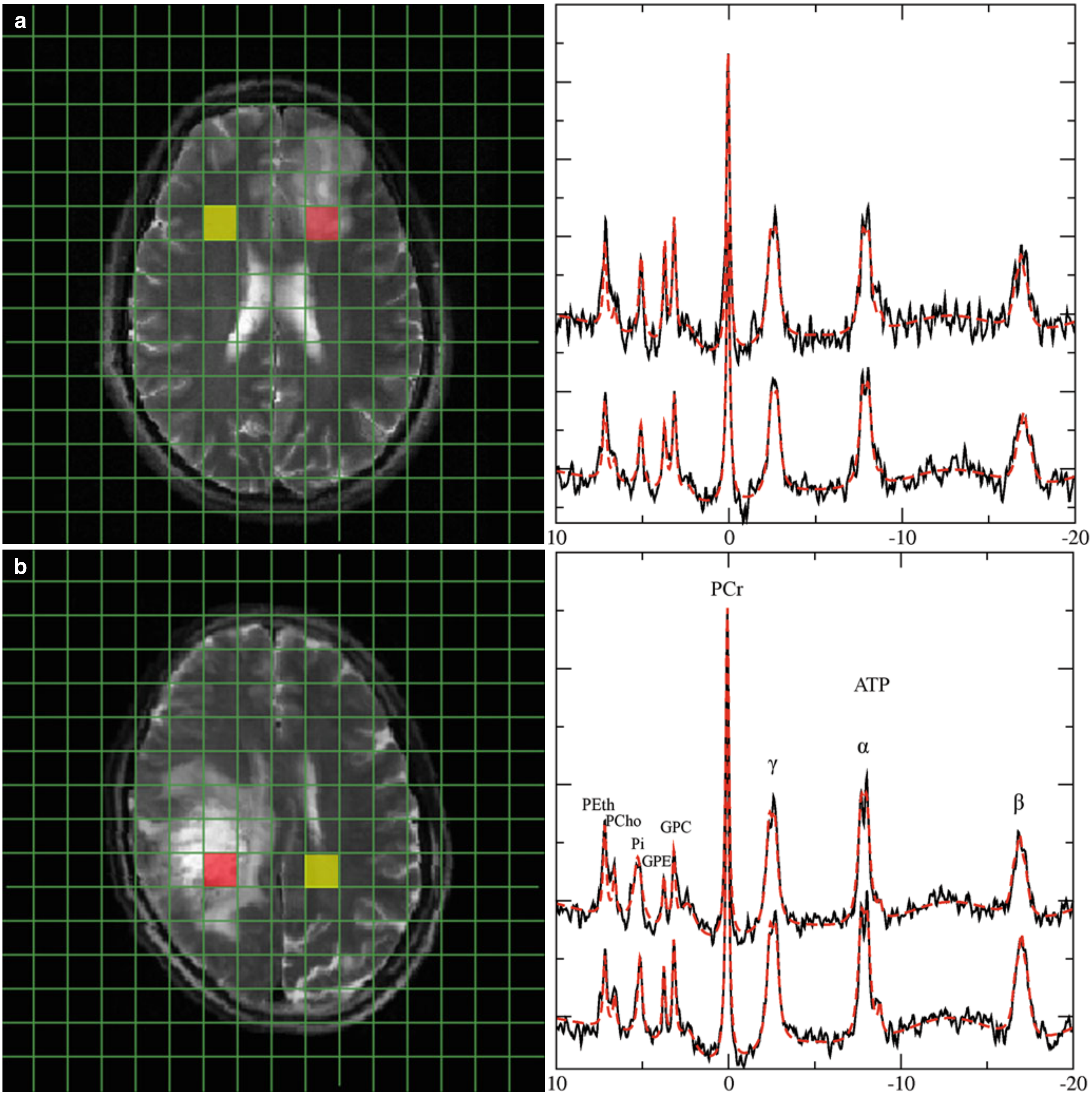

Fig. 5 Representative ^{31}P spectra in gliomas of different WHO grades. ^{31}P spectra from a low-grade glioma (**a**) and a heterogeneous glioma grade IV (**b**). Upper traces represent data of tumor tissue from the *red-marked* voxel in the MRI, while lower traces refer to the contralateral normal-appearing tissue from the *yellow* voxel in the MRI. Note: Increased GPE and PE signals in the low-grade tumor, while GPE is decreased in the glioma grade IV. Broadening of the inorganic phosphate signal in the glioma grade IV indicates increased intracellular pH in the tumor tissue

studies of human brain tumors could further show that the PCho concentration is increased in high-grade gliomas compared to low-grade tumors (McKnight et al. 2011; Vettukattil et al. 2013), but the same studies yielded inconclusive results regarding the GPC concentrations in these glioma specimens. It remains unclear whether low-grade gliomas have higher GPC concentrations compared to high-grade tumors. The amount of GPC might be predominantly influenced by molecular genetic markers and not by the tumor grade. It has been shown that glioma tissue specimens with oncogenic

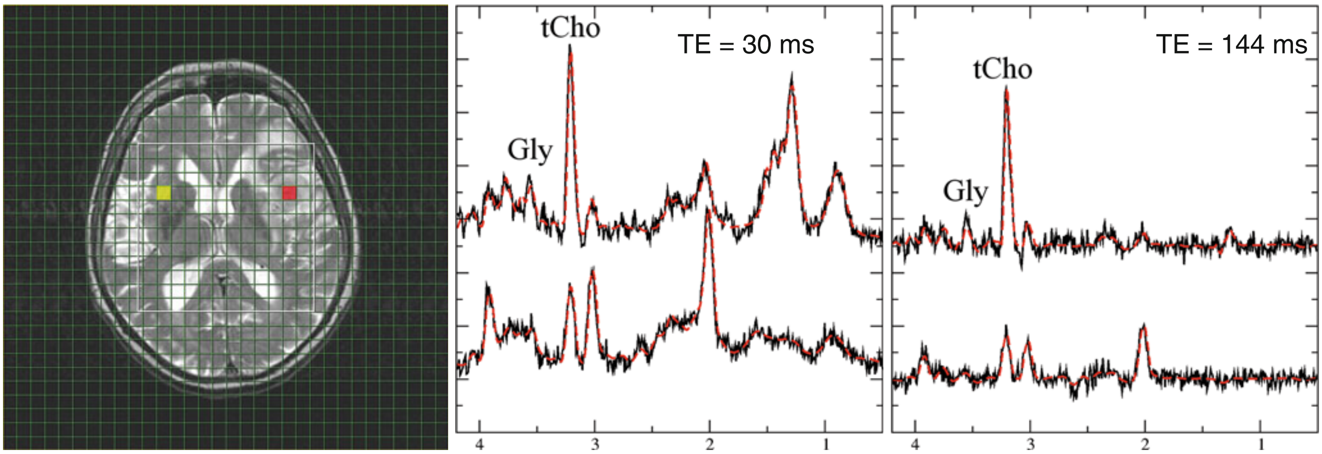

Fig. 6 Diagnostic information from combined long and short TE spectra in high-grade gliomas. Short (30 ms, middle panel and long (144 ms, *right panel*) TE spectra from glioma grade IV. The upper traces represent tumor tissue from the *red-marked* voxel in the MRI, while lower traces show contralateral normal-appearing tissue (*yellow-marked* voxel in the MRI). Note that only the short TE spectrum of the tumor shows a prominent lipid signal at 1.3 ppm. The signal at 3.6 ppm in normal-appearing tissue almost disappears at the long TE, while this signal is clearly visible in tumor tissue for both TE. This indicates that the signal in tumor rather originates from glycine than from myoinositol

IDH1 mutations have significant higher GPC concentration levels compared to tumors without this mutation (Constantin et al. 2012). Studies in endometrial and ovarian cancers showed that higher activity of the GPC-cleaving enzyme glycerophosphodiesterase increases migration capacity of tumor cells (Papanagiotou et al. 2007). High activity of this enzyme lowers the GPC concentration releasing free choline which can be converted into PCho.

Most of the in vitro results were obtained from tumor cell cultures or tumor xenografts in animal models, representing cells growing as focal mass similar to the majority of body tumors. In contrast, diffuse human gliomas frequently infiltrate large areas of normal brain tissue without significant functional and structural impairment of the host tissue until tumor necrosis and angioneogenesis occur. The prototype of this growth pattern is the gliomatosis cerebri which largely infiltrates different lobes of the brain by sparsely distributed glioma cells in mostly oligo-symptomatic patients. Further, the mitotic rate of human gliomas is quite low compared to most experimental tumor models. Thus, concentrations of metabolites indicating growing tumor cells might be below the detectable limit due to large contributions from regular brain tissue. However, cells from infiltrated normal brain tissue may react to the presence of tumor cells by changing their metabolism too. Some metabolites detected in gliomas by proton spectroscopy may represent this activated non-neoplastic brain tissue. Especially myoinositol and creatine, which are increased in gliomatosis cerebri and some low-grade tumors, seem to be rather markers of reactive gliosis than indicators of typical tumor metabolism (Hattingen et al. 2008).

3 Tumor Grading and Heterogeneity

MR spectroscopy is only one part in the diagnostic work-up of a space-occupying lesion. There is neither a specific tumor metabolite nor a specific spectroscopic pattern which allows unambiguous diagnosis of a glioma. Further, larger glial tumors are commonly heterogeneous with regard to their malignancy and invasiveness, yielding regional-dependent spectral pattern which can be determined with MRSI. Consequently, this is the method of choice to depict tumor heterogeneity which is manifested in heterogeneous distribution of metabolite concentrations (Fig. 1). Further, the location of the MRSI slice can be adjusted to sample the contralateral side providing individual reference metabolite concentrations from normal-appearing brain tissue in the same measurement. In tumors with vast necrotic areas, a vital debris dilutes all metabolites and sometimes only gives rise to large lipid signals which may even spoil the spectral quality (Fig. 2c).

Fortunately, there is a spectroscopic pattern which is very characteristic for gliomas. As already mentioned, gliomas have high tCho signals reflecting higher membrane turnover and cellular density, whereas NAA as marker of viable neuronal tissue is considerably lowered. Thus, drawing a line connecting the tCho peak with the NAA peak normally yields a positive slope, while for non-necrotic high-grade gliomas, the slope is negative (Fig. 4b). Diagnosis of a cerebral tumor is unlikely if the NAA concentration is normal and partial volume effects are excluded (Papanagiotou et al. 2007; Hattingen et al. 2010). Although regular NAA concentrations rule out tumor diagnosis, a decreased NAA signal is not specific for a tumor: NAA is synthesized in neuronal mitochondria and any brain disease severely affecting neuronal tissue can decrease NAA concentration levels. This is especially true for encephalitis or cerebritis, tumefactive demyelinating lesions, and infarction. Similarly, regular tCho signal intensity in all voxels of a non-necrotic space-occupying lesion will exclude high-grade gliomas with high accuracy. But a normal tCho does not exclude any glioma, since glioneuronal tumors, WHO grade II astrocytomas, and gliomatoses often show normal or only slightly increased choline concentrations (Fig. 4a). On the other hand, high tCho signals may be found in pilocytic astrocytomas (Porto et al. 2010), acute brain diseases with high cell membrane turnover like encephalitis, acute demyelinating diseases (Blasel et al. 2011a), active dysmyelination, tuberculosis, and acute radiation injury. Further, lipid signals and lactate are frequently described as tumor metabolites. Lipid signals may occur in tumors without obvious necrosis on conventional MRI, indicating microscopic or even intracellular lipids in high-grade gliomas. However, each of the above mentioned aggressive brain diseases may also yield lipid and lactate signals from necroses and hypoxia. High concentrations of myoinositol and creatine are reported in gliomatosis cerebri and lower-grade astrocytomas, but also in other brain diseases with augmented astrocytic proliferation and demyelinization (detailed discussion and references in Hattingen et al. 2008).

Several studies investigated the accuracy of proton spectroscopy to differentiate between tumors and non-neoplastic lesions and to differentiate low-grade from high-grade gliomas. The differentiation between high-grade and low-grade tumors and differentiation between astrocytoma and oligodendroglial tumors are both decisive for therapeutic decisions. High-grade brain tumors are usually treated more aggressively than low-grade tumors, and higher-grade oligodendroglial tumors are more sensitive to chemotherapy than other tumor entities. A detailed overview and description of these studies is provided by Horská and Barker (2010). The main drawback of the presented studies is the limited comparability due to the differing methodological approaches: SVS versus MRSI, different echo times, different post processing, and various metabolite ratios. Using ratios between different metabolites has the advantage of higher sensitivity if it is obvious that both metabolite concentrations change in the opposite direction. This is the case for the Cho/NAA resp NAA/Cho ratio in neoplastic lesions (Fig. 3a) (Stadlbauer et al. 2007; Vuori et al. 2004; Nelson 2001). However, for some metabolites like creatine and myoinositol, increase and decrease in concentrations were observed. The evaluation of creatine and myoinositol in brain tumors has important diagnostic and also prognostic value. Normally, both metabolite concentrations are decreased in brain tumors. However, elevated creatine and myoinositol levels have been found especially in low-grade gliomas. Higher creatine concentrations compared to normal brain tissue were correlated with shorter progression-free survival (Hattingen et al. 2010). Higher myoinositol levels in brain tumors may support the diagnosis of a low-grade astrocytoma (Castillo et al. 2000), whereas higher glycine concentrations were found in high-grade gliomas as demonstrated in Fig. 6 (Hattingen et al. 2009; Davies et al. 2010).

Alternatively, heterogeneity of a tumor can be evaluated with MRSI analyzing a maximum metabolite level of the tumor related to the same metabolite from the contralateral healthy tissue (Di Costanzo et al. 2008). This approach yields a normalized value which takes interindividual and regional metabolite variations into account. The maximum normalized tCho (hot spot) is also a qualified value for grading non-necrotic gliomas, and the respective voxel might be the target of stereotactic biopsy (Hermann et al. 2008; Senft et al. 2009). The selection of voxel with potentially most malignant tumor tissue is important for tumors in eloquent brain regions which have to be left partially in place.

The peri-enhancing tumor regions should also be sampled and analyzed with MRSI. In contrast to metastases, gliomas infiltrate brain areas beyond the enhancing area, showing elevated tCho concentrations (Fig. 1) and increased Cho/NAA ratios (Fig. 3a) in surrounding tissue (Stadlbauer et al. 2007; Di Costanzo et al. 2008). An investigation of the peri-enhancing border zone has also therapeutic relevance. Considering that all areas of viable tumor have to be targeted with high radiation dose, the "invisible" marginal zone might be undertreated. Recurrent tumors mostly occur in these marginal zones (Blasel et al. 2011b). Thus, integration of MRSI and/or MR perfusion in the treatment planning of high-grade gliomas would target more tumor tissue and might prolong progression-free survival of the patients. This has already been shown for Gamma Knife surgery (Chan et al. 2004).

Although phosphorus spectroscopy seems to be closer to the tumor biology, investigation of tumor heterogeneity or peri-enhancing tumor area is not possible due to its limited spatial resolution. An impression of the rather coarse grid size for ^{31}P MRS can be obtained by comparing the grids in Figs. 4 and 5.

3.1 Some Aspects of Differential Diagnosis

Bearing in mind the above described limitations, MR spectroscopy should only be used in conjunction with MR imaging and age and clinical symptoms of the patient to avoid misdiagnosis. The best diagnostic accuracy can be achieved by combining advanced imaging techniques (Tzika et al. 2003; Chang et al. 2009). Diffusion-weighted imaging is the best method to diagnose an abscess; MR perfusion of the tumor and the peri-enhancing region is highly accurate in grading gliomas and in differentiating infiltrated from focal, non-infiltrating brain tumors (Di Costanzo et al. 2008). Hereby, it is worth to mention that primary CNS lymphomas

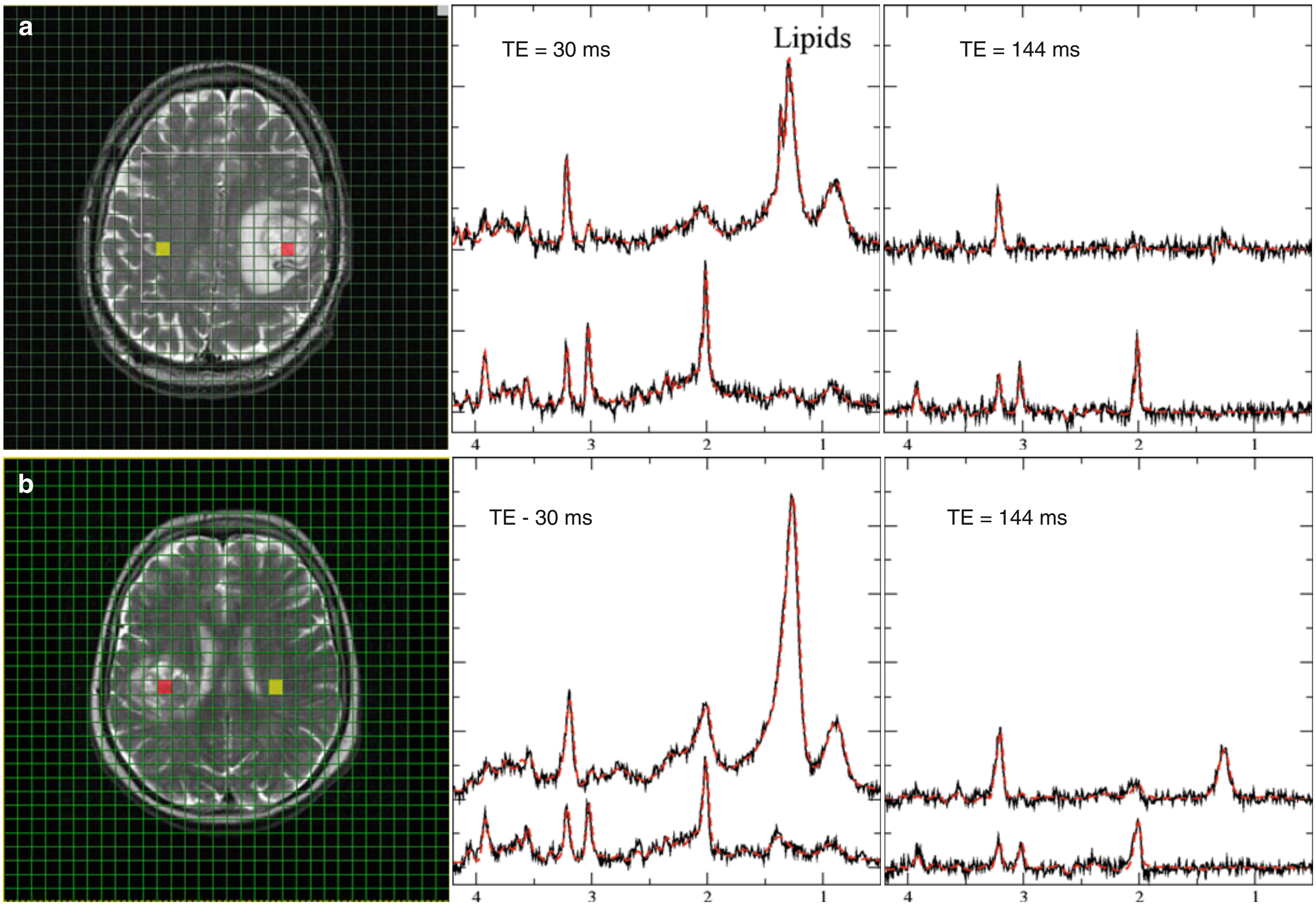

Fig. 7 Monitoring lipids. Typical spectra from the two cases shown as parameter maps in Fig. 3. Lower traces show the normal-appearing tissue (*yellow mark* in the MRI at *left panel*) while upper traces show tumor tissue (*red mark* in the MRI). Note that lipid signals visible at short TE (spectra in *middle panel*, upper trace) for the glioblastoma (**a**) are not visible in the long TE spectra (*right panel*), while for the metastasis (**b**) spectra for both TE show lipids

are also infiltrating brain tumors showing increased blood volume outside the enhancing area (Blasel et al. 2013). Inside the enhancing area of CNS lymphoma, the spectroscopic pattern is "an intermediate" between high-grade gliomas and metastases, showing intermediate tCho increase and prominent lipid peaks at short TE (Harting et al. 2003). The lipid increase might be invisible in long TE MR spectra.

Metastases from different primary tumors show diverse spectroscopic pattern according to their biological heterogeneity. The Cho signal intensity is elevated in solid and proliferating metastases, but most metastases show only moderate Cho increase (Fig. 4b). Huge lipid signals are found in necrotic glioblastomas, but lipids are also the dominant peaks in most of the metastases (Fig. 7) (Poptani et al. 1995). Further, the Cho/NAA ratios of metastases from peritumoral areas differ from the ratios in infiltrating gliomas, indicating the lack of tumor infiltration in the former (Server et al. 2010).

There are some metabolites which are indicative, but not absolutely specific for special tumor entities (Table 1). Taurine is an organic acid with many fundamental biological roles such as osmoregulation, antioxidation, membrane stabilization, and modulation of calcium signaling. High taurine signal intensities have been found in primitive neuroectodermal tumors (PNET) including medulloblastomas (Panigrahy et al. 2006; Kovanlikaya et al. 2005). Alanine, an amino acid, is found in meningiomas (Poptani et al. 1995; Kugel et al. 1992), but also in abscesses. The spectra of the later typically also show an increase of other amino acids. Multiplets of amino acids (0.9 ppm), lactate (at 1.3 ppm), and alanine (at 1.5 ppm) can be differentiated from lipids by their inversion with a long TE (135–144 ms) (see also Fig. 2 for detection of lactate). Amino acid increase in bacterial abscesses results from enhanced glycolysis yielding high levels of pyruvate, which is the substrate for the amino acid synthesis of alanine and others.

3.1.1 Using Sophisticated Analysis Schemes and/or Pattern Recognition Techniques

Apart from the above-described method of parameterizing MRS data in terms of metabolite concentrations, a different attempt has been made in using pattern recognition techniques for the entire spectrum, determining spectral profiles for each tumor type (Opstad et al. 2007; Tate et al. 1998, 2006).

4 Prognostic Markers

Prognostic markers are applicable to tumors without treatment, whereas in treated tumors only the predictive value of a metabolite can be evaluated. Only few studies with limited patient numbers investigated predictive or prognostic value of tumor metabolites. Multimodal approaches combining different values from various methods may lack of practicality and comparability between institutions. The impact of most spectroscopic studies in this area is limited by partial or even total lack of histopathological confirmation. Histopathologically proven studies showed that monitoring a tumor with MR spectroscopy may increase sensitivity and specificity to detect tumor progress or malignant transformation (Rock et al. 2002). Tedeschi et al. reported a continuous increase in the tCho signal to the time point of malignant transformation in low-grade tumors (Tedeschi et al. 1997), and Graves at al. found a tCho increase in recurrent malignant gliomas after Gamma Knife radiosurgery (Graves et al. 2001). But one should keep in mind that transient tCho increase might also occur in the radiated brain tissue.

As already mentioned, high normalized creatine concentrations in untreated WHO grade II and III gliomas are correlated with shorter progression-free survival. The role of creatine in glial tumors is unknown. Most spectroscopic studies used metabolite ratios related to creatine, which lacks information on the real creatine concentrations. No creatine increase was found in glioma cells ex vivo, suggesting that the increase rather originates from (reactive) glial cells of the infiltrated brain. Further, as the creatine signal in ^{1}H spectra represents the sum from unphosphorylated and phosphorylated creatine, the information on tumor energy metabolism obtained from intensity changes of this signal is limited and relies on additional assumptions regarding its composition and compartmentalization (Hattingen et al. 2010).

5 Treatment Monitoring

The main drawback of proton spectroscopy in treated high-grade gliomas is the small fraction of viable and solid tumor tissue in a brain area with sufficient field homogeneity to provide artifact-free spectra. Almost all patients are treated with radiation, and most patients receive at least one chemotherapeutic regime. Therefore, most lesions are heterogeneous consisting of both progressive tumor and a considerable amount of pre-injured tissue (Rock et al. 2002). In our experience, a large amount of spectroscopic data do not match the criteria for spectral quality (Kreis 2004) to allow a reliable analysis of the metabolite concentrations. The same seems true for distinguishing pseudoprogression and true tumor progression. The so-called pseudoprogression is regarded as intense reaction to combined radiochemotherapy, which decreases without additional treatments thereafter. Until now, MR spectroscopy was not very successful in differentiating pseudoprogression from real progression (Hygino da Cruz et al. 2011).

Therapy-induced brain injuries occur in about 20–30 % of patients treated with temozolomide radiochemotherapy. These lesions enhance early after radiation which may imitate tumor progression (Brandes et al. 2008). For adequate therapy decisions, additional methods are required to differentiate these reactions from real tumor growth.

Phosphorus spectroscopy might be the more appropriate method for treatment monitoring, since it is less prone to artifacts and, although of inferior spatial resolution, could be more specific by differentiating between the phosphomonoesters and phosphodiesters. First data on a cohort of patients with recurrent glioblastomas, all treated with bevacizumab in the second line, yielded that PCho/GPC seems to be appropriate to predict survival time and also to detect tumor progress (Hattingen et al. 2013).

References

Aiken NR, Gillies RJ (1996) Phosphomonoester metabolism as a function of cell proliferative status, exogenous precursors. Anticancer Res 16:1393–1397

Barker PB, Soher B, Blackb SJ, Chatham JC, Mathews VP, Bryan RN (1993) Quantitation of proton NMR spectra of the human brain using tissue water as an internal concentration reference. NMR Biomed 6:89–94

Behar KL, den Hollander JA, Stromski ME, Ogino T, Shulman RG, Petroff OA, Prichard JW (1983) High-resolution 1H nuclear magnetic resonance study of cerebral hypoxia in vivo. Proc Natl Acad Sci U S A 80:4945–4948

Blasel S, Pfeilschifter W, Jansen V, Mueller K, Zanella F, Hattingen E (2011a) Metabolism and regional cerebral blood volume in autoimmune inflammatory demyelinating lesions mimicking malignant gliomas. J Neurol 258:113–122

Blasel S, Franz K, Ackermann H, Weidauer S, Zanella F, Hattingen E (2011b) Stripe-like increase of rCBV beyond the visible border of glioblastomas: site of tumor infiltration growing after neurosurgery. J Neurooncol 103:575–584

Blasel S, Jurcoane A, Bähr O, Weise L, Harter PN, Hattingen E (2013) MR perfusion in and around the contrast-enhancement of primary CNS lymphomas. J Neurooncol 114:127–134

Bottomley PA, Edelstein WA, Foster TH, Adams WA (1985) In vivo solvent-suppressed localized hydrogen nuclear magnetic resonance spectroscopy: a window to metabolism? Proc Natl Acad Sci U S A 82:2148–2152

Brandes AA, Tosoni A, Spagnolli F, Frezza G, Leonardi M, Calbucci F, Franceschi E (2008) Disease progression or pseudoprogression after concomitant radiochemotherapy treatment: pitfalls in neurooncology. Neuro Oncol 10:361–367

Brown TR, Kincaid BM, Ugurbil K (1982) NMR chemical shift imaging in three dimensions. Proc Natl Acad Sci U S A 79: 3523–3526

Bruhn H, Frahm J, Gyngell ML, Merboldt KD, Hänicke W, Sauter R, Hamburger C (1989) Noninvasive differentiation of tumors with use of localized H-1 MR spectroscopy in vivo: initial experience in patients with cerebral tumors. Radiology 172:541–548

Castillo M, Smith JK, Kwock L (2000) Correlation of myo-inositol levels and grading of cerebral astrocytomas. AJNR Am J Neuroradiol 21:1645–1649

Chan AA, Lau A, Pirzkall A, Chang SM, Verhey LJ, Larson D, McDermott MW, Dillon WP, Nelson SJ (2004) Proton magnetic resonance spectroscopy imaging in the evaluation of patients undergoing gamma knife surgery for Grade IV glioma. J Neurosurg 101:467–475

Chance B, Nakase Y, Bond M, Leigh J Jr, McDonald G (1978) Detection of 31P nuclear magnetic resonance signals in brain by in vivo and freeze-trapped assays. Proc Natl Acad Sci U S A 75:4925–4929

Chang SM, Nelson S, Vandenberg S, Cha S, Prados M, Butowski N, McDermott M, Parsa AT, Aghi M, Clarke J, Berger M (2009) Integration of preoperative anatomic, metabolic physiologic imaging of newly diagnosed glioma. J Neurooncol 92:401–415

Chiche J, Ilc K, Laferrière J, Trottier E, Dayan F, Mazure NM, Brahimi-Horn MC, Pouysségur J (2009) Hypoxia-inducible carbonic anhydrase IX and XII promote tumor cell growth by counteracting acidosis through the regulation of the intracellular pH. Cancer Res 69:358–368

Constantin A, Elkhaled A, Jalbert L, Srinivasan R, Cha S, Chang SM, Bajcsy R, Nelson SJ (2012) Identifying malignant transformations in recurrent low grade gliomas using high resolution magic angle spinning spectroscopy. Artif Intell Med 55:61–70

Cuadrado A, Carnero A, Dolfi F, Jiménez B, Lacal JC (1993) Phosphorylcholine: a novel second messenger essential for mitogenic activity of growth factors. Oncogene 8:2959–2968

Davies NP, Wilson M, Natarajan K, Sun Y, MacPherson L, Brundler M-A, Arvanitis TN, Grundy RG, Peet AC (2010) Non-invasive detection of glycine as a biomarker of malignancy in childhood brain tumours using in-vivo 1H MRS at 15 tesla confirmed by ex-vivo high-resolution magic-angle spinning NMR. NMR Biomed 23:80–87

Di Costanzo A, Scarabino T, Trojsi F, Popolizio T, Catapano D, Giannatempo GM, Bonavita S, Portaluri M, Tosetti M, d'Angelo VA, Salvolini U, Tedeschi G (2008) Proton MR spectroscopy of cerebral gliomas at 3 T: spatial heterogeneity, tumour grade and extent. Eur Radiol 18:1727–1735

Duyn JH, Moonen CT (1993) Fast proton spectroscopic imaging of human brain using multiple spin-echoes. Magn Reson Med 30:409–414

Elkhaled A, Jalbert L, Constantin A, Yoshihara HA, Phillips JJ, Molinaro AM, Chang SM, Nelson SJ (2014) Characterization of metabolites in infiltrating gliomas using ex vivo ^{1}H high-resolution magic angle spinning spectroscopy. NMR Biomed 27:578–593

Frahm J, Bruhn H, Gyngell ML, Merboldt K, Hänicke W, Sauter R (1989) Localized high-resolution proton NMR spectroscopy using stimulated echoes: initial applications to human brain in vivo. Magn Reson Med 9:79–93

Fulham M, Bizzi A, Dietz MJ, Shih HH, Raman R, Sobering GS, Frank JA, Dwyer AJ, Alger JR, Di Chiro G (1992) Mapping of brain tumor metabolites with proton MR spectroscopic imaging: clinical relevance. Radiology 185:675–686

Gillies RJ, Barry JA, Ross BD (1994) In vitro, in vivo 13C and 31P NMR analyses of phosphocholine metabolism in rat glioma cells. Magn Reson Med 32:310–318

Glunde K, Bhujwalla ZM (2007) Choline kinase alpha in cancer prognosis and treatment. Lancet Oncol 8:855–857

Glunde K, Shah T, Winnard PT Jr, Raman V, Takagi T, Vesuna F, Artemov D, Bhujwalla ZM (2008) Hypoxia regulates choline kinase expression through hypoxia-inducible factor-1 alpha signaling in a human prostate cancer model. Cancer Res 68:172–180

Golay X, Gillen J, van Zijl PCM, Barker PB (2002) Scan time reduction in proton magnetic resonance spectroscopic imaging of the human brain. Magn Reson Med 47:384–387

Graves EE, Nelson SJ, Vigneron DB, Verhey L, McDermott M, Larson D, Chang S, Prados MD, Dillon WP (2001) Serial proton MR spectroscopic imaging of recurrent malignant gliomas after gamma knife radiosurgery. AJNR Am J Neuroradiol 22:613–624

Guillevin R, Menuel C, Duffau H, Kujas M, Capelle L, Aubert A, Taillibert S, Idbaih A, Pallud J, Demarco G, Costalat R, Hoang-Xuan K, Chiras J, Vallée J-N (2008) Proton magnetic resonance spectroscopy predicts proliferative activity in diffuse low-grade gliomas. J Neurooncol 87:181–187

Harting I, Hartmann M, Jost G, Sommer C, Ahmadi R, Heiland S, Sartor K (2003) Differentiating primary central nervous system lymphoma from glioma in humans using localised proton magnetic resonance spectroscopy. Neurosci Lett 342:163–166

Hattingen E, Pilatus U, Franz K, Zanella FE, Lanfermann H (2007) Evaluation of optimal echo time for 1H-spectroscopic imaging of brain tumors at 3 Tesla. J Magn Reson Imaging 26:427–431

Hattingen E, Raab P, Franz K, Zanella FE, Lanfermann H, Pilatus U (2008) Myo-inositol: a marker of reactive astrogliosis in glial tumors? NMR Biomed 21:233–241

Hattingen E, Lanfermann H, Quick J, Franz K, Zanella FE, Pilatus U (2009) (1)H MR spectroscopic imaging with short and long echo time to discriminate glycine in glial tumours. MAGMA 22: 33–41

Hattingen E, Delic O, Franz K, Pilatus U, Raab P, Lanfermann H, Gerlach R (2010) (1)H MRSI and progression-free survival in patients with WHO grades II and III gliomas. Neurol Res 32:593–602

Hattingen E, Jurcoane A, Bähr O, Rieger J, Magerkurth J, Anti S, Steinbach JP, Pilatus U (2011) Bevacizumab impairs oxidative energy metabolism and shows antitumoral effects in recurrent glioblastomas: a 31P/1H MRSI and quantitative magnetic resonance imaging study. Neuro Oncol 13(12):1349–1363

Hattingen E, Bähr O, Rieger J, Blasel S, Steinbach J, Pilatus U (2013) Phospholipid metabolites in recurrent glioblastoma: in vivo markers detect different tumor phenotypes before and under antiangiogenic therapy. PLoS One 8:e56439

Hermann EJ, Hattingen E, Krauss JK, Marquardt G, Pilatus U, Franz K, Setzer M, Gasser T, Tews DS, Zanella FE, Seifert V, Lanfermann H (2008) Stereotactic biopsy in gliomas guided by 3-tesla 1H-chemical-shift imaging of choline. Stereotact Funct Neurosurg 86:300–307

Herminghaus S, Pilatus U, Möller-Hartmann W, Raab P, Lanfermann H, Schlote W, Zanella FE (2002) Increased choline levels coincide with enhanced proliferative activity of human neuroepithelial brain tumors. NMR Biomed 15:385–392

Horská A, Barker PB (2010) Imaging of brain tumors: MR spectroscopy and metabolic imaging. Neuroimaging Clin N Am 20:293–310

Horská A, Calhoun VD, Bradshaw DH, Barker PB (2002) Rapid method for correction of CSF partial volume in quantitative proton MR spectroscopic imaging. Magn Reson Med 48:555–558

Hygino da Cruz L Jr, Rodriguez I, Domingues RC, Gasparetto EL, Sorensen AG (2011) Pseudoprogression, pseudoresponse: imaging challenges in the assessment of posttreatment glioma. AJNR Am J Neuroradiol 32:1978–1985

Isobe T, Matsumura A, Anno I, Yoshizawa T, Nagatomo Y, Itai Y, Nose T (2002) Quantification of cerebral metabolites in glioma patients with proton MR spectroscopy using T2 relaxation time correction. Magn Reson Imaging 20:343–349

Jain M, Nilsson R, Sharma S, Madhusudhan N, Kitami T, Souza AL, Kafri R, Kirschner MW, Clish CB, Mootha VK (2012) Metabolite profiling identifies a key role for glycine in rapid cancer cell proliferation. Science 336:1040–1044

Kennedy EP (1957) Metabolism of lipides. Annu Rev Biochem 26:119–148

Kinoshita Y, Kajiwara H, Yokota A, Koga Y (1994) Proton magnetic resonance spectroscopy of brain tumors: an in vitro study. Neurosurgery 35:606–613; discussion 613–614

Kinoshita Y, Yokota A, Koga Y (1994) Phosphorylethanolamine content of human brain tumors. Neurol Med Chir (Tokyo) 34:803–806

Kohl RL, Perez-Polo JR, Quay WB (1980) Effect of methionine glycine and serine on serine hydroxymethyltransferase activity in rat glioma and human neuroblastoma cells. J Neurosci Res 5:271–280

Kovanlikaya A, Panigrahy A, Krieger MD, Gonzalez-Gomez I, Ghugre N, McComb JG, Gilles FH, Nelson MD, Blüml S (2005) Untreated pediatric primitive neuroectodermal tumor in vivo: quantitation of taurine with MR spectroscopy. Radiology 236:1020–1025

Kreis R (2004) Issues of spectral quality in clinical 1H-magnetic resonance spectroscopy and a gallery of artifacts. NMR Biomed 17:361–381

Kuesel AC, Briere KM, Halliday WC, Sutherland GR, Donnelly SM, Smith IC (1996) Mobile lipid accumulation in necrotic tissue of high grade astrocytomas. Anticancer Res 16:1485–1489

Kugel H, Heindel W, Ernestus RI, Bunke J, du Mesnil R, Friedmann G (1992) Human brain tumors: spectral patterns detected with localized H-1 MR spectroscopy. Radiology 183:701–709

Lehnhardt F-G, Bock C, Röhn G, Ernestus R-I, Hoehn M (2005) Metabolic differences between primary and recurrent human brain tumors: a 1H NMR spectroscopic investigation. NMR Biomed 18:371–382

Maudsley AA, Matson GB, Hugg JW, Weiner MW (1994) Reduced phase encoding in spectroscopic imaging. Magn Reson Med 31:645–651

Maudsley AA, Gupta RK, Stoyanova R, Parra NA, Roy B, Sheriff S, Hussain N, Behari S (2014) Mapping of glycine distributions in gliomas. AJNR Am J Neuroradiol 35:S31–S36

McKnight TR, Smith KJ, Chu PW, Chiu KS, Cloyd CP, Chang SM, Phillips J, Berger MS (2011) Choline metabolism proliferation and angiogenesis in nonenhancing grades 2 and 3 astrocytoma. J Magn Reson Imaging 33:808–816

McLean LA, Roscoe J, Jorgensen NK, Gorin FA, Cala PM (2000) Malignant gliomas display altered pH regulation by NHE1 compared with nontransformed astrocytes. Am J Physiol Cell Physiol 278:C676–C688

Michaelis T, Merboldt KD, Bruhn H, Hänicke W, Frahm J (1993) Absolute concentrations of metabolites in the adult human brain in vivo: quantification of localized proton MR spectra. Radiology 187:219–227

Mintz A, Wang L, Ponde DE (2008) Comparison of radiolabeled choline and ethanolamine as probe for cancer detection. Cancer Biol Ther 7:742–747

Moonen CT, von Kienlin M, van Zijl PC, Cohen J, Gillen J, Daly P, Wolf G (1989) Comparison of single-shot localization methods (STEAM and PRESS) for in vivo proton NMR spectroscopy. NMR Biomed 2:201–208

Murphy PS, Dzik-Jurasz ASK, Leach MO, Rowl IJ (2002) The effect of Gd-DTPA on T(1)-weighted choline signal in human brain tumours. Magn Reson Imaging 20:127–130

Naressi A, Couturier C, Devos JM, Janssen M, Mangeat C, de Beer R, Graveron-Demilly D (2001) Java-based graphical user interface for the MRUI quantitation package. MAGMA 12:141–152

Negendank W (1992) Studies of human tumors by MRS: a review. NMR Biomed 5:303–324

Naruse S, Hirakawa K, Horikawa Y, Tanaka C, Higuchi T, Ueda S, Nishikawa H, Watari H (1985) Measurements of in vivo 31P nuclear magnetic resonance spectra in neuroectodermal tumors for the evaluation of the effects of chemotherapy. Cancer Res 45:2429–2433

Nelson SJ (2001) Analysis of volume MRI and MR spectroscopic imaging data for the evaluation of patients with brain tumors. Magn Reson Med 46:228–239

Oberhaensli RD, Hilton-Jones D, Bore PJ, Hands LJ, Rampling RP, Radda GK (1986) Biochemical investigation of human tumours in vivo with phosphorus-31 magnetic resonance spectroscopy. Lancet 2(8497):8–11

Opstad KS, Ladroue C, Bell BA, Griffiths JR, Howe FA (2007) Linear discriminant analysis of brain tumour (1)H MR spectra: a comparison of classification using whole spectra versus metabolite quantification. NMR Biomed 20:763–770

Ordidge RJ, Mansfield P, Lohman JA, Prime SB (1987) Volume selection using gradients and selective pulses. Ann N Y Acad Sci 508:376–385

Ozturk E, Banerjee S, Majumdar S, Nelson SJ (2006) Partially parallel MR spectroscopic imaging of gliomas at 3T. Conf Proc IEEE Eng Med Biol Soc 1:493–496

Panigrahy A, Krieger MD, Gonzalez-Gomez I, Liu X, McComb JG, Finlay JL, Nelson MD, Gilles FH Jr, Blüml S (2006) Quantitative short echo time 1H-MR spectroscopy of untreated pediatric brain tumors: preoperative diagnosis and characterization. AJNR Am J Neuroradiol 27:560–672

Papanagiotou P, Backens M, Grunwald IQ, Farmakis G, Politi M, Roth C, Reith W (2007) MR spectroscopy in brain tumors. Radiologe 47:520–529

Papandreou I, Cairns RA, Fontana L, Lim AL, Denko NC (2006) HIF-1 mediates adaptation to hypoxia by actively downregulating mitochondrial oxygen consumption. Cell Metab 3:187–197

Podo F (1999) Tumour phospholipid metabolism. NMR Biomed 12:413–439

Poptani H, Gupta RK, Roy R, Pandey R, Jain VK, Chhabra DK (1995) Characterization of intracranial mass lesions with in vivo proton MR spectroscopy. AJNR Am J Neuroradiol 16:1593–1603

Porto L, Kieslich M, Franz K, Lehrbecher T, Pilatus U, Hattingen E (2010) Proton magnetic resonance spectroscopic imaging in pediatric low-grade gliomas. Brain Tumor Pathol 27:65–70

Posse S, Tedeschi G, Risinger R, Ogg R, Le Bihan D (1995) High speed 1H spectroscopic imaging in human brain by echo planar spatial-spectral encoding. Magn Reson Med 33:34–40

Provencher SW (1993) Estimation of metabolite concentrations from localized in vivo proton NMR spectra. Magn Reson Med 30:672–679

Reifenberger G, Hentschel B, Felsberg J, Schackert G, Simon M, Schnell O, Westphal M, Wick W, Pietsch T, Loeffler M, Weller M, German Glioma Network (2012) Predictive impact of MGMT promoter methylation in glioblastoma of the elderly. Int J Cancer 131:1342–1350

Righi V, Roda JM, Paz J, Mucci A, Tugnoli V, Rodriguez-Tarduchy G, Barrios L, Schenetti L, Cerdán S, García-Martín ML (2009) 1H HR-MAS and genomic analysis of human tumor biopsies discriminate between high and low grade astrocytomas. NMR Biomed 22:629–637

Rock JP, Hearshen D, Scarpace L, Croteau D, Gutierrez J, Fisher JL, Rosenblum ML, Mikkelsen T (2002) Correlations between magnetic resonance spectroscopy and image-guided histopathology with special attention to radiation necrosis. Neurosurgery 51:912–919; discussion 919–920

Ross BD, Higgins RJ, Boggan JE, Knittel B, Garwood M (1988) 31P NMR spectroscopy of the in vivo metabolism of an intracerebral glioma in the rat. Magn Reson Med 6:403–417

Sabati M, Zhan J, Govind V, Arheart KL, Maudsley AA (2014) Impact of reduced k-space acquisition on pathologic detectability for volumetric MR spectroscopic imaging. J Magn Reson Imaging 39:224–234

Senft C, Hattingen E, Pilatus U, Franz K, Schänzer A, Lanfermann H, Seifert V, Gasser T (2009) Diagnostic value of proton magnetic resonance spectroscopy in the noninvasive grading of solid gliomas:

comparison of maximum and mean choline values. Neurosurgery 65:908–913; discussion 913

Server A, Josefsen R, Kulle B, Maehlen J, Schellhorn T, Gadmar Ø, Kumar T, Haakonsen M, Langberg CW, Nakstad PH (2010) Proton magnetic resonance spectroscopy in the distinction of high-grade cerebral gliomas from single metastatic brain tumors. Acta Radiol 51:316–325

Sijens PE, van den Bent MJ, Nowak PJ, van Dijk P, Oudkerk M (1997) 1H chemical shift imaging reveals loss of brain tumor choline signal after administration of Gd-contrast. Magn Reson Med 37: 222–225

Smith JK, Kwock L, Castillo M (2000) Effects of contrast material on single-volume proton MR spectroscopy. AJNR Am J Neuroradiol 21:1084–1089

Snell K (1984) Enzymes of serine metabolism in normal developing and neoplastic rat tissues. Adv Enzyme Regul 22:325–400

Stadlbauer A, Nimsky C, Buslei R, Pinker K, Gruber S, Hammen T, Buchfelder M, Ganslandt O (2007) Proton magnetic resonance spectroscopic imaging in the border zone of gliomas: correlation of metabolic and histological changes at low tumor infiltration–initial results. Invest Radiol 42:218–223

Susa M, Olivier AR, Fabbro D, Thomas G (1989) EGF induces biphasic S6 kinase activation: late phase is protein kinase C-dependent, contributes to mitogenicity. Cell 57:817–824

Tate AR, Griffiths JR, Martínez-Pérez I, Moreno A, Barba I, Cabañas ME, Watson D, Alonso J, Bartumeus F, Isamat F, Ferrer I, Vila F, Ferrer E, Capdevila A, Arús C (1998) Towards a method for automated classification of 1H MRS spectra from brain tumours. NMR Biomed 11:177–191

Tate AR, Underwood J, Acosta M, Julià-Sapé M, Majós C, Moreno-Torres A, Howe FA, van der Graaf M, Lefournier V, Murphy MM, Loosemore A, Ladroue C, Wesseling P, Bosson JL, Cabañas ME, Simonetti AW, Gajewicz W, Calvar J, Capdevila A, Wilkins PR, Bell BA, Rémy C, Heerschap A, Watson D, Griffiths JR, Arús C (2006) Development of a decision support system for diagnosis, grading of brain tumours using in vivo magnetic resonance single voxel spectra. NMR Biomed 19:411–434

Tedeschi G, Lundbom N, Raman R, Bonavita S, Duyn JH, Alger JR, Di Chiro G (1997) Increased choline signal coinciding with malignant degeneration of cerebral gliomas: a serial proton magnetic resonance spectroscopy imaging study. J Neurosurg 87:516–524

Tennant DA, Durán RV, Gottlieb E (2010) Targeting metabolic transformation for cancer therapy. Nat Rev Cancer 10:267–277

Träber F, Block W, Lamerichs R, Gieseke J, Schild HH (2004) 1H metabolite relaxation times at 3.0 tesla: measurements of T1, T2 values in normal brain and determination of regional differences in transverse relaxation. J Magn Reson Imaging 19:537–545

Tzika AA, Astrakas LG, Zarifi MK, Petridou N, Young-Poussaint T, Goumnerova L, Zurakowski D, Anthony DC, Black PM (2003) Multiparametric MR assessment of pediatric brain tumors. Neuroradiology 45:1–10

Valonen PK, Griffin JL, Lehtimäki KK, Liimatainen T, Nicholson JK, Gröhn OH, Kauppinen RA (2005) High-resolution magic-angle-spinning 1H NMR spectroscopy reveals different responses in choline-containing metabolites upon gene therapy-induced programmed cell death in rat brain glioma. NMR Biomed 18:252–259

Vanhamme L, van den Boogaart A, Van Huffel S (1997) Improved method for accurate, efficient quantification of MRS data with use of prior knowledge. J Magn Reson 129:35–43

Venkatesh HS, Chaumeil MM, Ward CS, Haas-Kogan DA, James CD, Ronen SM (2012) Reduced phosphocholine and hyperpolarized lactate provide magnetic resonance biomarkers of PI3K/Akt/mTOR inhibition in glioblastoma. Neuro Oncol 14:315–325

Vettukattil R, Gulati M, Sjøbakk TE, Jakola AS, Kvernmo NAM, Torp SH, Bathen TF, Gulati S, Gribbestad IS (2013) Differentiating diffuse World Health Organization grade II and IV astrocytomas with ex vivo magnetic resonance spectroscopy. Neurosurgery 72:186–195; discussion 195

Vuori K, Kankaanranta L, Häkkinen A-M, Gaily E, Valanne L, Granström M-L, Joensuu H, Blomstedt G, Paetau A, Lundbom N (2004) Low-grade gliomas and focal cortical developmental malformations: differentiation with proton MR spectroscopy. Radiology 230:703–708

Warburg O (1956) On the origin of cancer cells. Science 123: 309–314

Weller M, Felsberg J, Hartmann C, Berger H, Steinbach JP, Schramm J, Westphal M, Schackert G, Simon M, Tonn JC, Heese O, Krex D, Nikkhah G, Pietsch T, Wiestler O, Reifenberger G, von Deimling A, Loeffler M (2009) Molecular predictors of progression-free and overall survival in patients with newly diagnosed glioblastoma: a prospective translational study of the German Glioma Network. J Clin Oncol 27:5743–5750

Zierhut ML, Ozturk-Isik E, Chen AP, Park I, Vigneron D, Nelson SJ (2009) (1)H spectroscopic imaging of human brain at 3 Tesla: comparison of fast three-dimensional magnetic resonance spectroscopic imaging techniques. J Magn Reson Imaging 30:473–480

MR Perfusion Imaging

Christine Preibisch, Vivien Tóth, and Claus Zimmer

Contents

Abstract

Perfusion imaging is a powerful tool in the imaging of brain tumors, improving differential diagnostics, tumor grading, and the planning and monitoring of different therapy modalities. Several technical approaches are available to characterize tumor perfusion; these methods are widely available, easy to apply, and the results provide essential additional information on brain tumor pathophysiology. This chapter provides a review of different perfusion measurement techniques with exogenous or endogenous tracers. The clinical application of perfusion measurements in neuro-oncological imaging is discussed in view of the pathophysiological background. The practical use of perfusion imaging in differential diagnosis and tumor grading is presented with regard to the prognostic value of the method. Applications in biopsy targeting and therapy planning are also discussed. In the last section of this chapter, advantages and limitations of perfusion imaging in the follow-up of brain tumors are summarized.

Abbreviations

DSC	Dynamic susceptibility contrast
DCE	Dynamic contrast enhanced
CBF	Cerebral blood flow [mL/100 mL/min]
CBV	Cerebral blood volume [mL/100 mL]
MTT	Mean transit time
TTP	Time to peak
AIF	Arterial input function
K^{trans}	Transfer coefficient

1 Key Points

- Tumor vessels are tortuous, wide, highly dense, and permeable—resulting in perfusion anomalies.

C. Preibisch • V. Tóth • C. Zimmer (✉)
Department of Neuroradiology, Klinikum Rechts der Isar, TU Munich, Munich, Germany
e-mail: claus.zimmer@tum.de

E. Hattingen, U. Pilatus (eds.), *Brain Tumor Imaging*,
Medical Radiology. Diagnostic Imaging,
DOI: 10.1007/174_2016_954,

- Perfusion parameters rCBV, CBF, and K^{trans}—and their combinations—are good predictors of tumor grade (especially low-grade vs. high-grade) and outcome.
- Diagnostic accuracy is essentially augmented by perfusion data.
- Perfusion data combined with other metabolic imaging modalities helps in detection of pseudoprogression and pseudoresponse of gliomas.

2 Methods

The delivery of oxygen and nutrients to cells via arterial blood through capillaries in biological tissue is referred to as perfusion. Blood flow—commonly used as a synonym of perfusion—denotes the rate of delivery of arterial blood to the capillary bed.

In a neuroradiological context, several surrogate markers have been derived to characterize tissue perfusion. The basic principle behind the measurement of perfusion-related parameters is the application of a tracer to the bloodstream, the distribution of which is then observed in the tissue. Since Stewart's pioneering experiments, dating 1894 (Stewart 1894), a variety of approaches have been developed. Appropriately sized microspheres being trapped in tissue have for a long time been considered to be the gold standard in perfusion imaging, at least in animal studies (Bassingthwaighte et al. 1990; Heymann et al. 1977). More recently, freely diffusible tracers and positron emission tomography (PET) made perfusion measurement sufficiently noninvasive to allow an application in patients (Ter-Pogossian and Herscovitch 1985; Raichle et al. 1983; Frackowiak et al. 1980).

The first magnetic resonance imaging (MRI)-based concepts of perfusion imaging emerged more than 20 years ago (Le Bihan 1992; Rosen et al. 1990; Villringer et al. 1988; Tofts and Kermode 1991) and have ever since been the subject of intense basic and clinical research. Because it yields valuable insights into tumor physiology and is widely available, MR perfusion imaging plays an important role in tumor differential diagnosis and grading as well as in therapy monitoring and follow-up (Faehndrich et al. 2011; Fatterpekar et al. 2012; Hattingen et al. 2008; Larsen et al. 2013; Mills et al. 2012; Wagner et al. 2011; Blasel et al. 2010).

In this section, we outline the principles of MR-based perfusion imaging with respect to different contrast mechanisms based on the manipulation of the longitudinal (T1) and transverse relaxation times (T2, T2*) as well as the implications of exogenous and endogenous contrast agent. Based on theoretical models that link MRI parameters with physiology, several surrogate markers of tissue perfusion can be deducted. In the first line, these are the cerebral blood flow (CBF) denoting the rate of delivery of arterial blood to the tissue (commonly measured in [mL/100 mL/min]), the cerebral blood volume (CBV), i.e., the volume fraction of tissue occupied by blood vessels (commonly measured in [mL/100 mL] or [%]) and the mean transit time (MTT = CBV/CBF). Useful phenomenological parameters are the bolus arrival time (BAT), time to peak (TTP), and relative MTT (rMTT, i.e., the full width at half maximum of the tissue concentration time curve). Furthermore, it is possible to determine a number of other markers characterizing vascular permeability and morphology like the volume transfer coefficient K^{trans} and the vessel size index (VSI).

2.1 Exogenous Tracer Methods

The most widespread methods for MR perfusion imaging rely on exogenous tracers, and the most common, clinically used contrast agents are chelates of paramagnetic gadolinium (Caravan et al. 1999), e.g., Gadolinium diethylene-triamine-pentacetate (Gd-DTPA). These extracellular fluid agents are considered as intravascular agents within the brain—as long as the blood–brain barrier is intact.

MRI contrast agents generally induce a shortening of MR relaxation times (i.e., an increase in corresponding relaxation rates). For longitudinal T1 relaxation, this is induced by a dipolar interaction between nuclear proton spins and unpaired electrons of the paramagnetic contrast agent (Caravan et al. 1999; Hendrick and Haacke 1993) which produces a signal increase in T1 weighted images. In areas with a disrupted blood–brain barrier, T1-based methods also allow estimation of vascular permeability (Tofts and Kermode 1991). On the other hand, the compartmentalization of a high magnetic susceptibility contrast agent within blood vessels produces long-range microscopic susceptibility gradients around the vessels, which accelerate transverse relaxation and thus effect a signal decrease in T2 or T2* weighted images (Villringer et al. 1988). The respective signal changes are measured via different imaging approaches, and perfusion-related parameters are deducted via appropriate physiological models. In principle, it is possible to measure CBV by obtaining measurements in the steady state before and after the application of an intravascular contrast agent with either T2* (Varallyay et al. 2013) or T1 weighted images (Lu et al. 2005; Wirestam et al. 2007). However, the most common methods applied in modern brain tumor perfusion imaging rely on dynamic imaging, which are described in the following sections.

2.1.1 Dynamic Susceptibility Contrast MRI

In this most commonly applied method for perfusion imaging, the passage of a bolus of contrast agent is observed via T2* weighted imaging, and perfusion parameters are

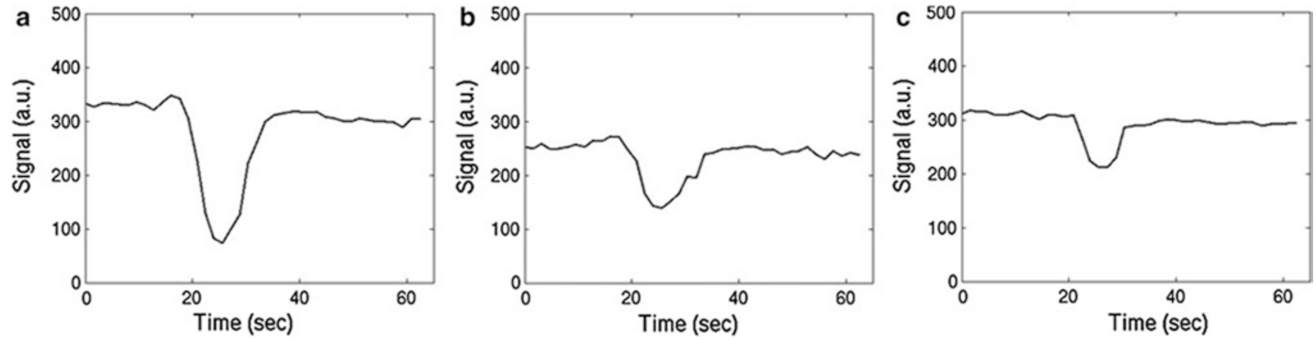

Fig. 1 Exemplary DSC signal–time curves obtained in arterial vessels (**a**), gray matter (**b**), and white matter (**c**)

derived by means of tracer dilution theories. First experiments were presented by Villringer et al. (1988). An introduction to the basic principles of tracer kinetic models as well as their application to bolus tracking MRI is given by Buxton (2009a), and a number of reviews cover all possible aspects of dynamic susceptibility contrast perfusion imaging (Le Bihan 1992; Calamante et al. 2002; Ostergaard 2004, 2005; McGehee et al. 2012).

In practice, a short bolus of contrast agent is injected into a peripheral vein and the subsequent signal changes occurring in the brain are monitored via T2* weighted imaging. Since the transit time of an intravascular agent is rather short (i.e., a few seconds), fast imaging methods are necessary to obtain a sufficient temporal resolution. Hence, echo planar imaging (EPI) (Turner et al. 1991), often in combination with parallel imaging (Deshmane et al. 2012), is commonly used as it allows to cover large portions of the brain with a reasonable temporal resolution of about 1 s. While T2* weighted gradient echo EPI is the most common method, T2 weighted spin echo EPI can also be used (Speck et al. 2000). Figure 1 shows characteristic signal–time curves obtained with T2* weighted dynamic susceptibility contrast (DSC) imaging.

The challenge is now to transform the measured signal changes into valid measures of perfusion. Kinetic models relate the tracer concentrations in arterial blood $C_a(t)$ and tissue $C_t(t)$ to CBF, CBV, and MTT (Buxton 2009a). For an arbitrary arterial concentration–time course $C_a(t)$ (arterial input function, AIF), the tissue concentration–time course $C_t(t)$ (output function) depends on the local cerebral blood flow (CBF) as follows:

$$C_t(t) = C_a(t) \otimes \left[CBF \cdot r(t) \right] \tag{1}$$

where $r(t)$ is the local residue function and $\otimes$ indicates convolution. The $r(t)$ can be considered as the fraction of contrast agent molecules entering the tissue at time $t=0$ and still being present at a time $t>0$. Thus, the residue function is a monotonically decreasing function with $r(t=0)=1$; it contains the complexities concerning details of contrast agent distribution and kinetics. For a single well-mixed compartment, $r(t)$ is usually assumed to decay exponentially. The product $CBF \cdot r(t)$ is also denoted as impulse response. Figure 2 illustrates the result of the convolution of idealized representations of an arterial concentration–time curve and an impulse response to yield an idealized tissue concentration–time curve.

Based on Eq. (1) it can be shown that the peak of the impulse response is determined by CBF, while the area under the impulse response corresponds to the partition coefficient λ, which for common MR contrast agents can be considered as the distribution volume of the tracer, corresponding to CBV for intravascular agents (Buxton 2009a). According to the central volume theorem, the mean transit time MTT is given by CBV/CBF (Meier and Zierler 1954).

Using dynamic susceptibility contrast, it is relatively straightforward to calculate a relative CBV (rCBV) from the area under the measured signal–time curve. Because it is quite insensitive to the actual shape of the AIF, this quantity is considered to be a quite robust measure of rCBV as long as the relation between tissue concentration and signal intensity is the same throughout the brain (Buxton 2009a; Calamante et al. 2000). rCBV values are frequently normalized to healthy-appearing white matter to facilitate comparison between patients. Cerebral blood flow is much more difficult to obtain since for intravascular tracers the transit time is very short and thus the influence of CBF on the tissue concentration–time curve is rather subtle. Therefore, the bolus arrival time (BAT), the time to peak (TTP), and the relative mean transit time (rMTT), i.e., the full width at half maximum of the signal–time curve, are frequently used as surrogate markers of perfusion (Ostergaard 2004).

In order to obtain quantitative perfusion parameters from bolus tracking data, a deconvolution of the tissue concentration–time curve $C_t(t)$ with the arterial concentration–time curve $C_a(t)$ (arterial input function, AIF) needs to be performed. However, unlike PET—where tracer concentrations are measurable quantities—the MR signal is only indirectly related to the contrast agent concentration. Usually, it is

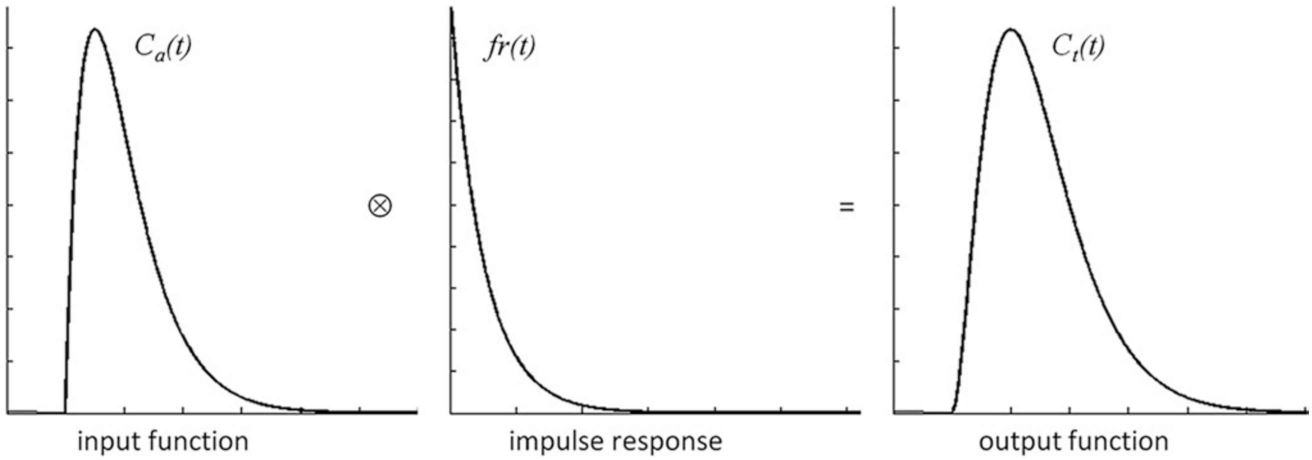

Fig. 2 Relation of idealized concentration–time curves and impulse response according to Eq. (1)

assumed that the change in the transverse relaxation rate ΔR_2^* is linearly related to the tissue concentration of contrast agent (Rosen et al. 1990; Hendrick and Haacke 1993):

$$\Delta R_2^* = k \,.\, C(t) \tag{2}$$

with a proportionality constant k. There are strong indications that this assumption of a linear relationship between the transverse relaxation rate and the concentration of the contrast agent is too simple (Blockley et al. 2008), because the mechanisms of signal loss in magnetically inhomogeneous media are highly complex (Blockley et al. 2008; Kjolby et al. 2006) and also depend on the vascular architecture (Johnson et al. 2000). Differential T2 and T2* relaxation behavior even allows to derive information on vessel diameter, size, and density (Kiselev 2005; Kiselev et al. 2005; Lemasson et al. 2013; Boxerman et al. 1995). Moreover, the contrast mechanisms within blood vessels and tissue are different (Kiselev 2001), and water exchange between tissue compartments actually needs to be taken into account (Landis et al. 2000; Li et al. 2010; Yankeelov et al. 2003). Nevertheless, Eq. (2) is usually employed to calculate tissue and arterial concentration–time curves from the measured MR signal with the echo time TE:

$$S(t) = S_0 \mathrm{e}^{-\mathrm{TE}\cdot\Delta R_2^*(t)} \tag{3}$$

For an absolute quantification of CBV, CBF, and MTT, the arterial input function, i.e., the arterial concentration–time curve $C_a(t)$, needs to be measured with high accuracy, and in this respect, several additional difficulties occur. Usually, the AIF is measured in large arterial vessels crossing the imaging plane. However, because of the need for a high imaging speed, the spatial resolution is usually not sufficient to obtain pure blood voxels. This implies that partial volume effects most likely confound arterial signal intensity. At high arterial contrast concentrations, a complete signal loss may occur inside large arterial vessels especially if EPI with long TE is used for data acquisition, which additionally distorts the AIF. While the AIF merely serves as a global scaling factor for CBV quantification, estimates of the local AIF would actually be required for valid measurement of CBF. This is related to the observation that any broadening and delay in the arterial input confounds the measured CBF (Calamante 2005; Calamante et al. 2004; Duhamel et al. 2006; Ko et al. 2007). Even with an appropriate AIF, valid CBF measurement with DSC remains a challenge. Given the fact that the influence of CBF on the measured tissue concentration–time curve is rather weak, the deconvolution process is very delicate and sensitive to noise (Ostergaard 2004, 2005; Ostergaard et al. 1996a, b). Hence, absolute quantification of perfusion parameters is rarely performed in clinical practice; instead, relative perfusion measures are normalized to healthy appearing WM or contralateral tissue. Therefore, valid comparisons for multicenter or longitudinal studies are hardly possible.

Additional difficulties arise from recirculation and extravasation of contrast agent to the tissue. While recirculation may cause a second broader and smaller peak about 30–60 s after the first pass of the bolus, extravasation prevents the signal from returning to baseline values. Therefore, a gamma-variate function is frequently fitted to the initial part of the signal–time curve (Belliveau et al. 1991; Boxerman et al. 1997) to remove the influence of recirculation and increase the reliability of CBV measurement. However, contrast agent extravasation, as in tumor areas with disrupted blood–brain barrier, causes more severe problems. Gd-DTPA outside the vasculature enhances T1 relaxation of tissue water, counteracting the susceptibility-induced signal loss in T2* weighted images, which may lead to an underestimation of CBV (Rosen et al. 1990; Knopp et al. 1999; Quarles et al. 2009; Uematsu and Maeda

2006; Essig et al. 2002). However, if the contrast agent outside the vasculature causes significant susceptibility gradients, an overestimation of CBV is likewise possible (Bjornerud et al. 2011). There are several methods to account for contrast agent leakage in DSC-based CBV measurement. One practical possibility to reduce the influence of T1 relaxation is the administration of a pre-bolus of contrast agent in order to saturate the tissue in the leakage area (Paulson and Schmainda 2008; Boxerman et al. 2012). More elaborate approaches comprise double echo acquisitions (Uematsu and Maeda 2006; Paulson and Schmainda 2008; Miyati et al. 1997; Heiland et al. 1999; Vonken et al. 2000) or sophisticated data analysis (Rosen et al. 1990; Quarles et al. 2005, 2009; Bjornerud et al. 2011; Uematsu et al. 2000; Johnson et al. 2004), which also provides information on vessel permeability and seems to reveal a benefit when compared to the application of a pre-bolus alone (Boxerman et al. 2012). Valid quantification of perfusion using DSC, especially in areas with contrast agent leakage, is a matter of intense research. Since the blood–brain barrier in tumors is frequently disrupted, new developments would be highly relevant.

In spite of these issues, DSC-MRI is by far the most frequently used perfusion imaging method, as it is easy to perform and yields robust information on tissue perfusion, i.e., rCBV.

2.1.2 Dynamic Contrast-Enhanced MRI

A qualitatively similar approach to perfusion imaging relies on the acquisition of a time series of T1 weighted images during bolus application (Fig. 3). This method is termed dynamic contrast-enhanced (DCE) imaging and allows quantification of vessel permeability, which is merely a confounding factor in DSC-based perfusion imaging. Generally, DCE-MRI requires the acquisition of a time series of T1 weighted images over several minutes to observe the wash-in and washout of contrast agent in extravascular extracellular space. Qualitative or semi-quantitative measurements of leakage-related parameters are relatively easy to perform. The slope of the wash-in and washout portions of the time course can be evaluated within the regions of interest, allowing the distinction of tumor (fast rise) and radiation necrosis (slow rise) (McGehee et al. 2012). Also, semiquantitative parametric maps of the wash-in and washout slopes, maximal enhancement, and arrival time can easily be created. Integration of the initial area under the DCE tissue concentration curve (initial AUC) yields a more quantitative parameter (Li et al. 2012; Sourbron et al. 2009; Sourbron 2010) without the need for a sophisticated model. However, the influence of underlying physiologic processes like vessel permeability, extravascular extracellular volume, and blood flow is rather unclear (Donahue et al. 1996).

Similar to the DSC method, quantitative DCE-based perfusion measurements are quite elaborate (Yankeelov and Gore 2009; Sourbron and Buckley 2012, 2013). Quantitative approaches require complex pharmacokinetic models, a quantitative relation between MR signal and contrast agent concentration, as well as an appropriate AIF. Pharmacokinetic models describe the distribution and elimination of contrast agents within and from the tissue with respect to the underlying physiology. Most frequently, a two-compartment model is used based on the pioneering work of Kety (1951). This model describes the tissue as consisting of an intravascular space (plasma volume v_p) and an extravascular extracellular space (EES, volume v_e) (Fig. 4). The distribution of the contrast agent is characterized by arterial delivery and venous elimination rates k_a and k_e as well as distribution and redistribution rate constants k_{12} and k_{21}, which describe the diffusion into EES. Commonly measured parameters are the volume transfer constant K^{trans} between blood plasma and EES

$$K^{\text{trans}} = E \cdot \text{CBF} \cdot (1 - \text{Hct}) \tag{4}$$

(with extraction fraction E and hematocrit Hct), the EES volume fraction v_e, and the rate constant between EES and blood plasma $k_{ep} = K^{trans}/v_e$. However, the interpretation of K^{trans} depends on the physiological conditions: when the vessel permeability is much higher than blood flow (flow-limited condition), K^{trans} corresponds to the blood plasma flow per unit volume of tissue; when blood flow is much higher than vessel permeability (permeability-limited condition), K^{trans} corresponds to the permeability surface area product per unit volume of tissue (Sourbron and Buckley 2011).

First quantitative approaches were hampered by a rather low temporal resolution of T1 weighted imaging data and therefore only allowed to obtain K^{trans} and v_e as primary parameters for tissue characterization (Tofts and Kermode 1991; Tofts 1997; Tofts et al. 1999; Larsson et al. 1990; Brix et al. 1991). As technical progress permitted T1 weighted imaging with sufficiently high temporal resolution, advanced models have been developed which additionally allow measurement of CBV and CBF (Sourbron and Buckley 2012; Henderson et al. 2000; Pradel et al. 2003; Brix et al. 2004; Larsson et al. 2009; Li et al. 2012; Sourbron et al. 2009). Comprehensive reviews on these methods are given by Yankeelov and Gore (2009) as well as Sourbron and Buckley (2012, 2013), Sourbron (2010).

The majority of DCE-based MRI experiments are based on a model originally developed by Tofts (Tofts and Kermode 1991). According to that, the intravascular signal contribution is neglected and the relation between the contrast agent concentrations in tissue $C_t(t)$ and blood

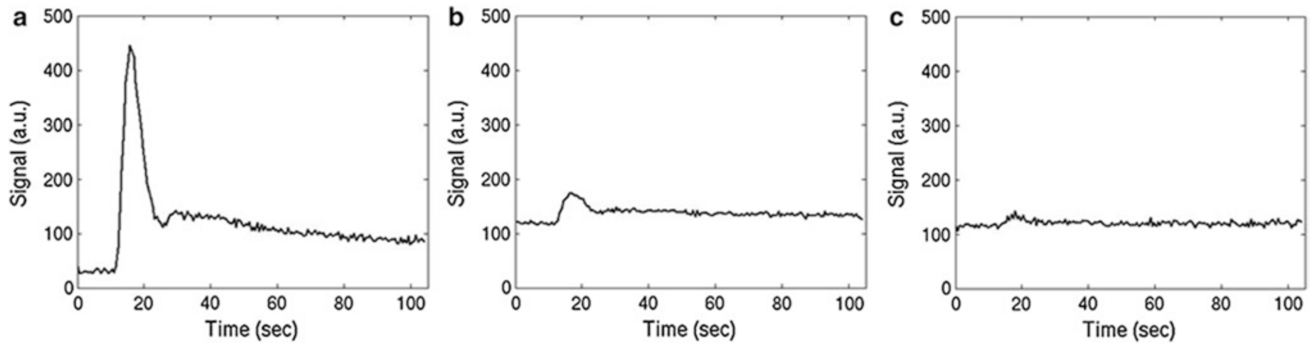

Fig. 3 Typical DCE signal–time curves obtained in arterial vessels (**a**), gray matter (**b**), and white matter (**c**)

plasma $C_P(t)$ is described by (Yankeelov and Gore 2009; Tofts et al. 1999)

$$C_t(t) = K^{trans} \cdot \int C_P(t) \cdot \exp\left(\frac{K^{trans}(t-t')}{v_e}\right) dt'. \tag{5}$$

Inclusion of a plasma compartment with a volume v_p yields the extended Tofts model (Sourbron and Buckley 2012; Brix et al. 2004):

$$C_t(t) = v_P \cdot C_P(t) + K^{trans} \cdot \int C_P(t) \cdot \exp\left(\frac{K^{trans}(t-t')}{v_e}\right) dt'. \tag{6}$$

Estimates of perfusion parameters are usually obtained by multiparametric nonlinear fitting of these equations to measured concentration–time curves. Besides that, a large number of different approaches have been developed. A recent comprehensive review of a variety of currently existing models for DCE-based perfusion measurement is given in Sourbron and Buckley (2013).

Similar to the DSC method, the measured T1 weighted MRI signal needs to be converted to contrast agent concentration before quantitative evaluations can be performed. Usually, a linear relation between the change in the longitudinal relaxation rate R_1 (= 1/T1) and contrast agent concentration is assumed (Landis et al. 2000; Yankeelov and Gore 2009):

$$R_1(t) = r_1 \cdot C(t) + R_{10} \tag{7}$$

with the contrast agent relaxivity r_1 and the precontrast relaxation rate R_{10}. This assumption regards biological tissue as a single well-mixed compartment or at least requires a fast exchange of water between all tissue compartments. However, there are indications that water exchange is not fast enough in the presence of contrast agent (Donahue et al. 1996; Parkes and Tofts 2002; Schwarzbauer et al. 1997). Accounting for the water exchange rates between different tissue compartments even allows determination of intravascular or extravascular intracellular lifetimes of water molecules (Yankeelov and Gore 2009). Since a high temporal resolution is needed, $R_1(t)$ cannot be measured directly. Instead, $R_1(t)$ is determined from the T1 weighted signal–time curve s(t) and a precontrast measurement of tissue R_{10} where the exact formula depends on the imaging sequence. For a saturation recovery sequence with time delay TD, the tissue concentration curve is calculated according to

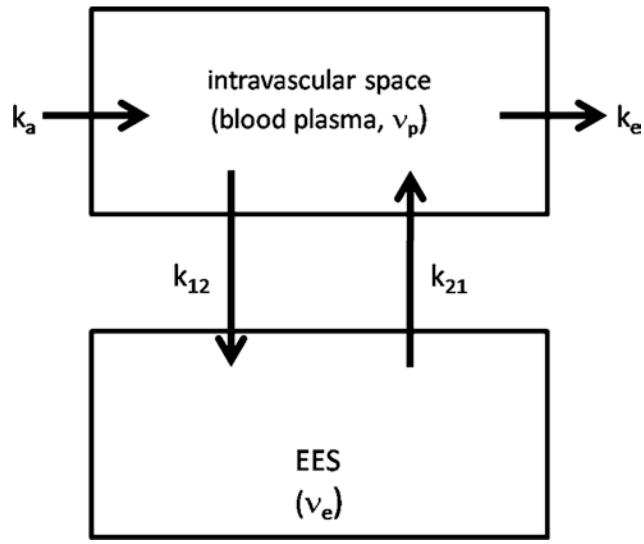

Fig. 4 Two-compartment model: Contrast agent is delivered to the intravascular space with a rate constant k_a and is eliminated with a rate constant k_e. The CA diffuses into and outside of the extravascular extracellular (EES) space with a distribution rate constant k_{12} and a redistribution rate constant k_{21}

$$C(t) = -\frac{1}{r_1 \cdot TD} \ln\left(1 - \frac{s(t)}{s_0}\right) - \frac{R_{10}}{r_1} \tag{8}$$

Precontrast T1 mapping is frequently performed using the variable flip angle approach because it allows fast imaging with whole brain coverage (Yankeelov and Gore 2009; Li et al. 2012; Roberts et al. 2006; Harrer et al. 2004).

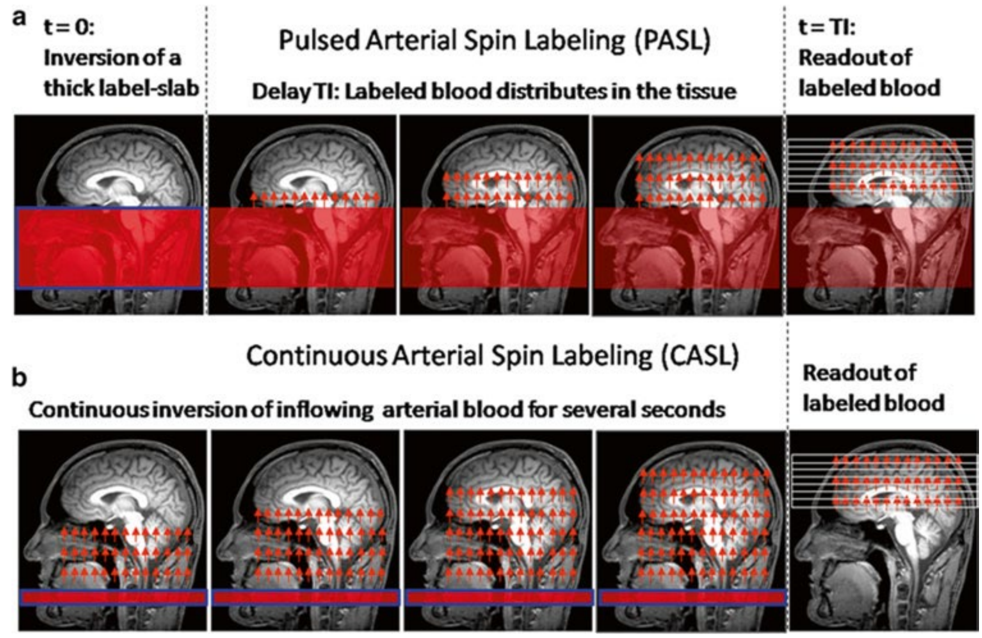

Fig. 5 Schematic order of events for pulsed (**a**) and continuous (**b**) arterial spin labeling (*ASL*)

However, this method needs careful spoiling or correction for the influence of residual magnetization to be accurate. At field strengths of 3 T and above, additional mapping of the local flip angle is required (Preibisch and Deichmann 2009). Therefore, saturation or inversion recovery methods are also frequently used (Larsson et al. 2008; Deichmann 2005; Henderson et al. 1999; Zhu and Penn 2005).

Also, a valid AIF, i.e., the plasma concentration of contrast agent $C_P(t)$, needs to be determined for quantitative perfusion measurements. In this respect, similar limitations as in DSC imaging apply, e.g., with respect to partial volume effects, broadening, and delays (Yankeelov and Gore 2009). However, unlike in DSC imaging, the linearity of signal change inside vessels is of less concern since there is no complication due to complete signal loss at high contrast agent concentrations.

The major drawback of DCE-MRI in comparison to DSC-based perfusion imaging is the significantly reduced signal change, which results in rather low SNR in the calculated parameter maps. In practice, it is also much more demanding to achieve a reasonable spatial coverage and temporal resolution with T1 weighted imaging methods, and it is more difficult to choose an appropriate method from the large variety of different approaches (see Sourbron and Buckley 2013 for a recent review).

2.2 Endogenous Tracer Methods: Arterial Spin Labeling

Arterial spin labeling is an alternative agglomeration of methods for measurement of cerebral blood flow which uses magnetically labeled water in blood vessels as endogenous diffusible tracer. The basic idea is to acquire two data sets, one with labeling of inflowing blood and one without. The difference signal is proportional to the delivered magnetization and hence to blood flow. Because labeled water acts as a freely diffusible tracer with accordingly prolonged tissue transit times, CBF derived from arterial spin labeling (ASL) is principally more robust than CBF derived from bolus tracking based on intravascular tracers (Buxton 2009b). Figure 5 depicts the basic order of events for the two fundamental types of pulsed (PASL) and continuous arterial spin labeling (CASL).

In the PASL labeling condition, a thick slab proximal to the imaging volume of interest (blue framed slab in (a)) is usually inverted at time $t = 0$ by a short RF pulse. After a delay time (inversion time, T1, typically ≈1.5 s), which allows labeled blood to distribute within the imaging volume, labeled images are acquired. CASL approaches use extended labeling periods where inflowing blood is inverted continuously by long RF pulses (several seconds) in a thin slice in the neck area. Labeled images are acquired after termination of the labeling pulse. A recent development is the pseudocontinuous ASL (pCASL) approach, where series of short RF and gradient pulses achieve more efficient labeling (compared to PASL) and reduced specific absorption rate (SAR) and magnetization transfer effects (compared to CASL) (Silva and Kim 1999; Wu et al. 2007; Helle et al. 2012). Remarkably, it is also possible to selectively label individual arterial vessels, which enables imaging of vascular territories (Helle et al. 2012; Golay et al. 2005; Paiva et al. 2007; van Laar et al. 2008).

Qualitative perfusion images can easily be derived because the difference between labeled and unlabeled images is proportional to CBF, but absolute quantification is again quite difficult. A good introduction to ASL is given by Buxton (2009b) and a number of recent reviews cover all possible methodological issues (Wu et al. 2010; Deibler et al. 2008; Golay and Petersen 2006; Golay et al. 2004; Williams 2006; Parkes 2005; Petersen et al. 2006a, b) with regard to ASL-based CBF quantification.

Generally, care needs to be taken with regard to the control experiments because the labeling pulse, though applied off resonance, may nevertheless affect the magnetization within the imaging volume mainly via magnetization transfer effects (McLaughlin et al. 1997; Pekar et al. 1996; Zhang et al. 1992). Since the signal change inferred by blood flow only is on the order of about 1 %, even small effects may introduce large errors. To control for magnetization transfer effects, an equivalent off-resonant RF pulse needs to be applied during the control condition without labeling the inflowing spins. A number of techniques have been developed for all types of ASL methods, even though the effect is much more severe in CASL due to the long duration of its labeling pulse (Buxton 2009b). PASL approaches mainly vary by different placement of the control RF pulse (Edelman et al. 1994; Kwong et al. 1995; Wong et al. 1997; Kim 1995), while some CASL techniques even use separate labeling coils in the neck (Shen and Duong 2011; Paiva et al. 2008; Talagala et al. 2004). In PASL, slice profile effects due to the close proximity of the labeling slab and the imaging slice are also a problem and are usually diminished by a gap between labeling and imaging slice. Because the ASL difference signal change is so small, suppression of the static tissue signal (background suppression) in the imaging slices was found to be beneficial (Garcia et al. 2005; Mani et al. 1997; Ye et al. 2000).

Major confounding factors are transit delays Δt between the labeling plane and the imaging slice (Zhang et al. 1992; Wong et al. 1997; Alsop and Detre 1996; Buxton et al. 1998), the bolus duration T (Buxton 2009b; Wong et al. 1998; Luh et al. 1999), and relaxation effects (Buxton 2009b). The transit delay Δt may vary across the brain by several tenth of milliseconds (Wong et al. 1997) causing systematic errors even in qualitative CBF maps. An effective means to reduce the influence of transit delays in CASL is to insert a delay after the end of the labeling pulse (Alsop and Detre 1996); for PASL, the inversion time needs to be longer than the longest Δt. In CASL, the duration of the arterial bolus is well defined by the duration of the labeling RF pulse. In PASL, however, the thickness of the labeling slab determines the amount of labeled blood, and the bolus duration thus depends on global flow (Buxton 2009b). In order to create a bolus with a well-defined duration, saturation pulses can be applied to the labeling slab after an inversion time TI_1 (Wong et al. 1998; Luh et al. 1999). The most complex effect is caused by water exchange between vessels and tissue. Initially, when labeled water is delivered to the tissue, relaxation of water spins occurs within the vessels with the arterial longitudinal relaxation time T_{1A}, while after exchange—within the brain parenchyma—the tissue relaxation time T_{1t} applies. This is difficult to model, especially since the exchange time T_{ex} (on the order of a few tenth of seconds) is not well known (Buxton 2009b).

Quantitative evaluations need to account for these effects. Early approaches used a modified Bloch equation to account for the influence of CBF on the difference signal (Kwong et al. 1992, 1995; Kim 1995; Detre et al. 1992). More recently, tracer kinetic modeling has also been used to derive CBF from ASL data (Buxton et al. 1998). In this approach, the amount of magnetization delivered to the imaging voxel by arterial blood $\Delta M(t)$ (i.e., the magnetization difference between control and label condition) is regarded to correspond to the tracer concentration. Based on this presumption, tracer kinetic principles can be applied to describe the influence of physiological processes on $\Delta M(t)$ by means of a delivery function $c(t)$, a residue function $r(t)$, and a magnetization relaxation function $m(t)$ (Buxton 2009b; Buxton et al. 1998):

$$\Delta M(t) = 2M_{0A} \cdot CBF \cdot c(t) \otimes \left[r(t) m(t) \right] \tag{9}$$

where $\otimes$ denotes convolution. The equilibrium magnetization of arterial blood M_{0A} is difficult to measure, but a useful approximation can be obtained from the CSF signal (Chalela et al. 2000). Appropriate definitions of the functions $c(t)$, $r(t)$, and $m(t)$ allow to include the effects of transit delays Δt and delayed water exchange T_{ex} (Buxton 2009b):

$$\begin{aligned}
c(t) &= \begin{cases} 0 & 0 < t < \Delta t \\ \alpha e^{-t/T_{1A}} \ \text{(PASL)} & \Delta t < t < \Delta t + T \\ \alpha e^{-t/T_{1A}} \ \text{(CASL)} & \Delta t < t < \Delta t + T \\ 0 & \Delta t < T < t \end{cases} \\
r(t) &= e^{-CBF \cdot t/\lambda} \\
m(t) &= \begin{cases} e^{-t/T_{1A}} & t > T_{ex} \\ e^{-T_{ex}/T_{1A}} e^{-(t-t_{ex})/T_{1t}} & t > T_{ex} \end{cases}
\end{aligned} \tag{10}$$

with bolus length T, inversion efficiency α (Alsop and Detre 1996; Zhang et al. 1993), and the longitudinal relaxation times of water in arterial blood and tissue T_{1A} and T_{1t}. Generally, absolute CBF quantification is quite laborious because several time points need to be acquired after the end of the labeling pulses for proper modeling in CASL as well as PASL (Petersen et al. 2006a, b, 2010). This is aggravated by the fact that the SNR of a single difference image is quite low meaning that several (≈50) averages need to be acquired. T_{1A} of arterial blood is usually assumed from the literature, but mapping of local tissue T_1 is considered to be necessary, especially with CASL because the longer labeling duration allows more time for exchange (Buxton 2009b; Parkes 2005). Reduced inversion efficiency is rather a problem in CASL (Alsop and Detre 1996; Zhang et al. 1993), while proper definition of bolus duration is a bigger issue in PASL (Wong et al. 1998; Luh et al. 1999). There are a number of

Table 1 Overview of MR perfusion imaging methods

Method	Indicators	Imaging	Advantages	Disadvantages
DSC	(r)CBV (r)CBF (r)MTT AT TTP	Time series of T2*w images (usually EPI) during CA bolus application Acquisition time ≈1–2 min	Implemented on commercial MR systems Relatively easy to perform Robust estimates of relative CBV	Compromised by contrast agent leakage Not easily quantifiable
DCE	K^{trans} CBV CBF	Time series of T1w images during CA bolus application Acquisition time: several min	Straightforward characterization of vessel permeability	No established standard method Not widely implemented on commercial MR systems Low SNR
ASL	CBF	Pairs of label/control images (usually EPI) Acquisition time: several min	No contrast application necessary Robust estimate of relative CBF	Low SNR

other difficulties which complicate absolute quantification of CBF via ASL like inhomogeneities of the receiver coil (Wang et al. 2005), T2* relaxation (St Lawrence and Wang 2005), and labeled water within arteries (Petersen et al. 2006a, b). CBF quantification using ASL is an area of active research steadily yielding innovations, e.g., a time efficient strategy for sampling at multiple TI using the Look–Locker approach was proposed by Gunther et al. (2001). However, many refinements with regard to accuracy go along with decreased SNR and reduced stability. Thus, in clinical practice, where measurement time is heavily restricted, qualitative ASL or PASL methods aiming at CBF quantification with a single inversion (Wong et al. 1998; Luh et al. 1999) are most frequently applied.

The Perfusion Study Group of the International Society for Magnetic Resonance in Medicine (ISMRM) (Perfusion Study Group ISMRM 2013) is currently compiling a consensus paper on MR perfusion imaging, which is supposed to contain recommendations for scan protocols as well as evaluation procedures for a number of applications. This consensus paper is expected to be a huge step toward more standardized MR perfusion imaging methods (Table 1).

3 Clinical Application

3.1 General Aspects

Perfusion imaging in brain tumors is—as of today—not yet part of the imaging modalities included in the response assessment in neuro-oncology (RANO) criteria, where response to treatment in patients with malignant gliomas is determined by post-therapeutic changes in conventional T2 and contrast-enhanced T1 imaging along with clinical parameters (Wen et al. 2010). The omission of the novel functional MRI methods is explained by a lack of standardization and thus impaired comparability of multicenter data; however, further application for individual patient evaluation is strongly recommended, since perfusion imaging is accepted as a standard tool of neuro-oncological diagnostics today.

The technical aspects of perfusion imaging are discussed in detail in the first section of this chapter. In everyday clinical practice, the DSC method is most commonly available, providing perfusion data in under a minute's measurement time. ASL and DCE methods are less widespread due to technical limitations. A combination of the methods, if available, may provide additional information. However, the patient's well-being must always be put first: long examinations may be less tolerated by critically ill patients—and motion artifacts due to unease impair data independent of the perfusion imaging method used. A special advantage of ASL methods is the lack of external contrast agent; therefore, they can be applied in patients with contraindications to contrast agent administration, i.e., impaired renal function or severe gadolinium allergy.

Most MRI systems provide an online calculation of DSC-based perfusion maps, with manual masking, smoothing, AIF definition, and ROI placement. While these maps can quickly be inspected and readily transmitted into local PACS systems, they have the drawbacks of being operator dependent and not quantitative. Several approaches for quantitative assessment, e.g., histogram and kurtosis analysis, are available and widely used for scientific evaluation; however, these are mostly in-house developments and only allow offline evaluations.

Perfusion characteristics of brain tumors are most frequently compared with those of normal appearing brain tissue in the same patient, relying on a relative value, e.g., rCBV. A high rate of perfusion is typically defined as higher than normal appearing gray matter. Perfusion heterogeneity is a common feature in brain tumors and the localization of "hot spots," i.e., focally highest values, is of special interest. While (semi)quantification is feasible, the definition of a threshold value valid across patients is nearly impossible, also due to diverging physiological parameters such as heart rate. Special attention must be paid to "artificially" high perfusion values in vascular structures. A correlation with conventional imaging—where vessels appear as flow voids and tubular enhancements—is therefore indispensable.

A controversial topic in perfusion MRI of brain tumors is the correction for contrast agent leakage in the presence of a disrupted blood–brain barrier (BBB). The development of a leaky BBB is an important step in the malignant transformation of a tumor and BBB changes may also be a relevant effect of tumor therapy. Therefore, the effect of a disrupted BBB and consequent contrast agent leakage on perfusion data must be accounted for when attempting tumor grading or assessing therapy response. In order to achieve comparability of perfusion measurements at different clinical sites, the measurements and post-processing steps must be standardized. While simple techniques to minimize leakage effects, e.g., the preinjection of contrast agent to "saturate" the extracellular space, are easy to perform (for further description of such techniques, see Methods), the standardization of more sophisticated postprocessing algorithms might be favorable (Boxerman et al. 2012; Heiland et al. 2010). Separate information on cerebrovascular parameters (CBV, CBF) and on BBB permeability may be acquired; several possibilities for this are discussed in the "Methods" section of this chapter.

The vast majority of clinical studies have investigated the parameter rCBV—measured by the most robust DSC method—in correlation with other descriptive tumor characteristics and with outcome. Other perfusion parameters like rCBF and permeability have also been introduced to clinical practice with the use of ASL and DCE (Warmuth et al. 2003). First clinical studies using these parameters have largely reproduced previous (rCBV) results in most clinical questions.

Perfusion imaging, when performed and interpreted with care, can play a significant role in major clinical decisions regarding diagnosis, therapy, and follow-up.

3.2 Pathophysiological Background: Neovascularization in Brain Tumors

Neovascularization, i.e., the development of new vessels, is a vital process in the embryonic differentiation processes as well as in later stages of life where wound repair and inflammation, etc. require additional vascular supply. A marking step in the research of tumor pathophysiology was the detection of neovascularization of tumors as part of their malignant transformation (Brem 1976). Once the angiogenic phenotype is switched on in a tumor, its malignancy is definite and its growth exponential. The development of tumor vessels is especially intriguing in brain tumors, as they represent a direct correlate of tumor grade, are largely responsible for symptomatic tumor edema and bleeding, and represent an obstacle to drug delivery. While low-grade tumors grow along preexisting vessels (vascular co-option), higher-grade tumors start to generate own tumor vessels in the process of growing, which are different from normal vessels in appearance and structure. Glioblastoma vessels mainly originate from local endothelial cells (angiogenesis)—after destruction of preexisting vessels—or sometimes from bone marrow-derived endothelial precursor cells (vasculogenesis); further mechanisms include vascular mimicry and the transdifferentiation of GBM cells into endothelial cells (Hardee and Zagzag 2012). Genetic and epigenetic factors include an alteration of oncogenes with upregulation of hypoxia-inducible factor HIF-1α and members of the family of vascular endothelial growth factor (VEGFs); these factors promote the destruction of pericytes and of the extracellular matrix with matrix metalloproteinases; they recruit endothelial cells and promote vascular remodeling and sprouting. The resulting tumor vessels are tortuous, wide, and dense, while their borders are blurred due to incomplete endothelial and pericyte coverage resulting in a breakdown of the blood–brain barrier and increased permeability (Soda et al. 2013).

In neuropathology, description of tumor vascularity is an important criterion for tumor grading with higher vascularity representing a higher grade of malignancy. WHO °II tumors mainly incorporate preexisting vessels, while high-grade gliomas develop new, heterogeneous, and tortuous vessels with higher density (Fig. 6). Higher microvascular density is a prognostic factor for shorter postoperative survival in astroglial brain tumors (Leon et al. 1996; Folkerth 2004).

In histopathological studies combined with previous MR perfusion imaging, tumor regions with high rCBV were found to correlate with a high microvascular density in mouse models as well as in human brain tumor specimens (Cha et al. 2003). Contrast enhancement and permeability measures in MRI reliably characterized the blood–brain barrier and its permeability as seen in histopathology. These findings confirm the theoretical assumption that perfusion imaging represents the variations and changes in tumor microvasculature (Cha 2004).

3.3 Differential Diagnosis of Tumors

The differential diagnosis of the three major groups of malignant intracranial intra-axial tumors—glioma, lymphoma, and metastases—is often difficult in conventional (T2w, T1w) MR imaging. Their features in conventional imaging—typical localization, the presence or absence of hemorrhage, necrosis, and T2 signal intensities—may help differential diagnosis but are not always conclusive. While

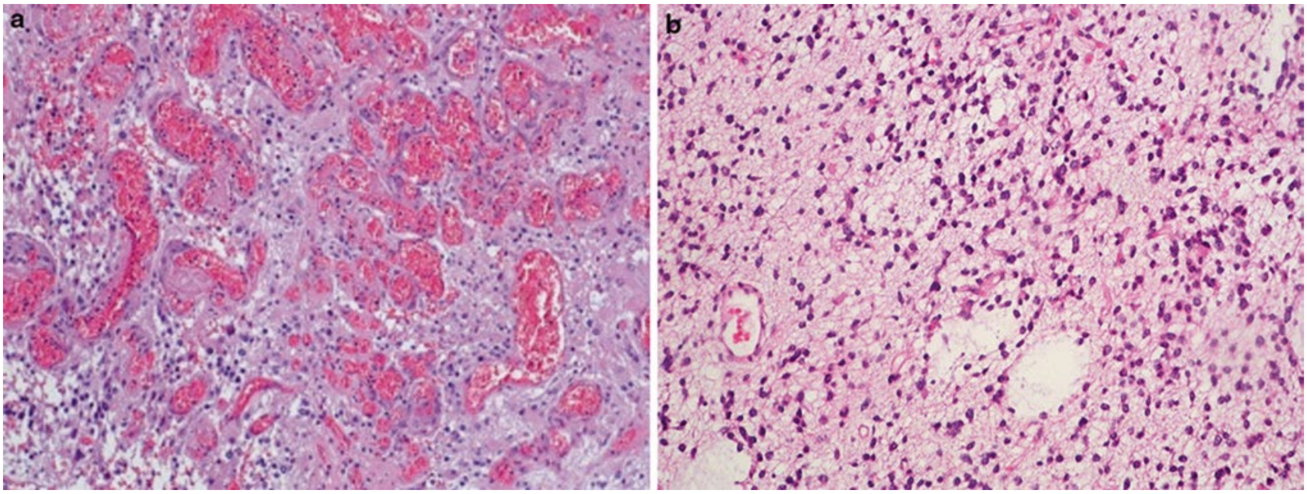

Fig. 6 (**a**) Histopathological view of pathological tumor vessels in a WHO °II glioma exhibits no pathological tumor vessels (Image glio-blastoma specimen. Note the densely packed tortuous vessels with courtesy of Claire Delbridge MD, Department of Neuropathology, incomplete endothelial coating. (**b**) In contrast, the biopsy specimen of a Klinikum Rechts der Isar, TU Munich)

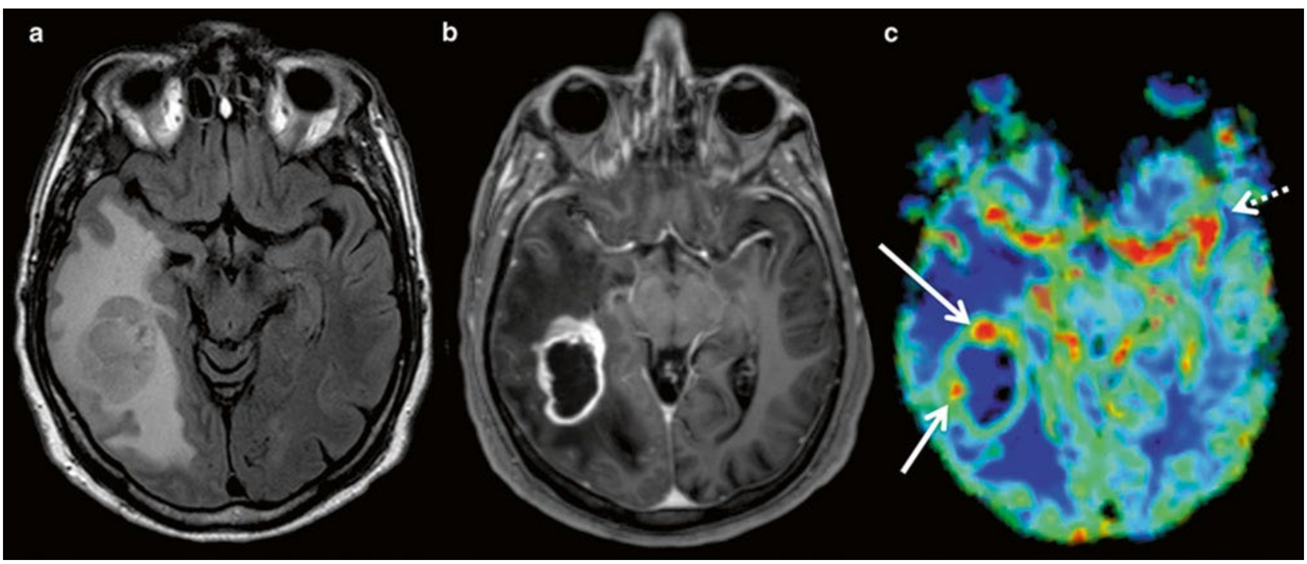

Fig. 7 Imaging of a glioblastoma: (**a**) axial FLAIR, (**b**) post-Gd T1w, and (**c**) DSC rCBV map of a selected slice. The contrast-enhancing lesion shows high rCBV values as compared to WM, with focal peaks in the rostral and lateral parts of the tumor (*red dots* marked with *arrows*) corresponding to tumor hot spots. High rCBV values are also seen lateral to the contrast-enhancing lesion, corresponding to the tumor infiltration zone (*lower arrow*). Note the high signal corresponding to the carotid and middle cerebral arteries (*dotted arrow*)

periventricular localization is typical for lymphomas and metastases are more often cortex associated, each of these entities may appear in another localization—therefore, periventricular or cortical localization is not a distinctive feature. Contrast enhancement and focal necrosis are common in all high-grade brain tumors irrespective of their origin. Therefore, in most cases, conventional imaging does not allow a definite diagnostic statement. However, the intrinsically different histology and vascularization pattern of these entities makes perfusion imaging a useful tool in their differentiation.

High-grade gliomas are characterized by high cellular density and pleomorphism, mitoses, palisading necrosis, and vascularization. The latter results in very high tumor perfusion, i.e., high rCBV values throughout the tumor (as compared with healthy contralateral tissue), with focal peaks probably representing the most malign tumor foci, the so-called tumor hot spots (Fig. 7). Glial tumors show an extremely infiltrative growth pattern beyond the contrast-enhancing lesion into the peritumoral edema. Consequently, rCBV values are typically elevated beyond the contrast-enhancing lesion in peritumoral regions as well.

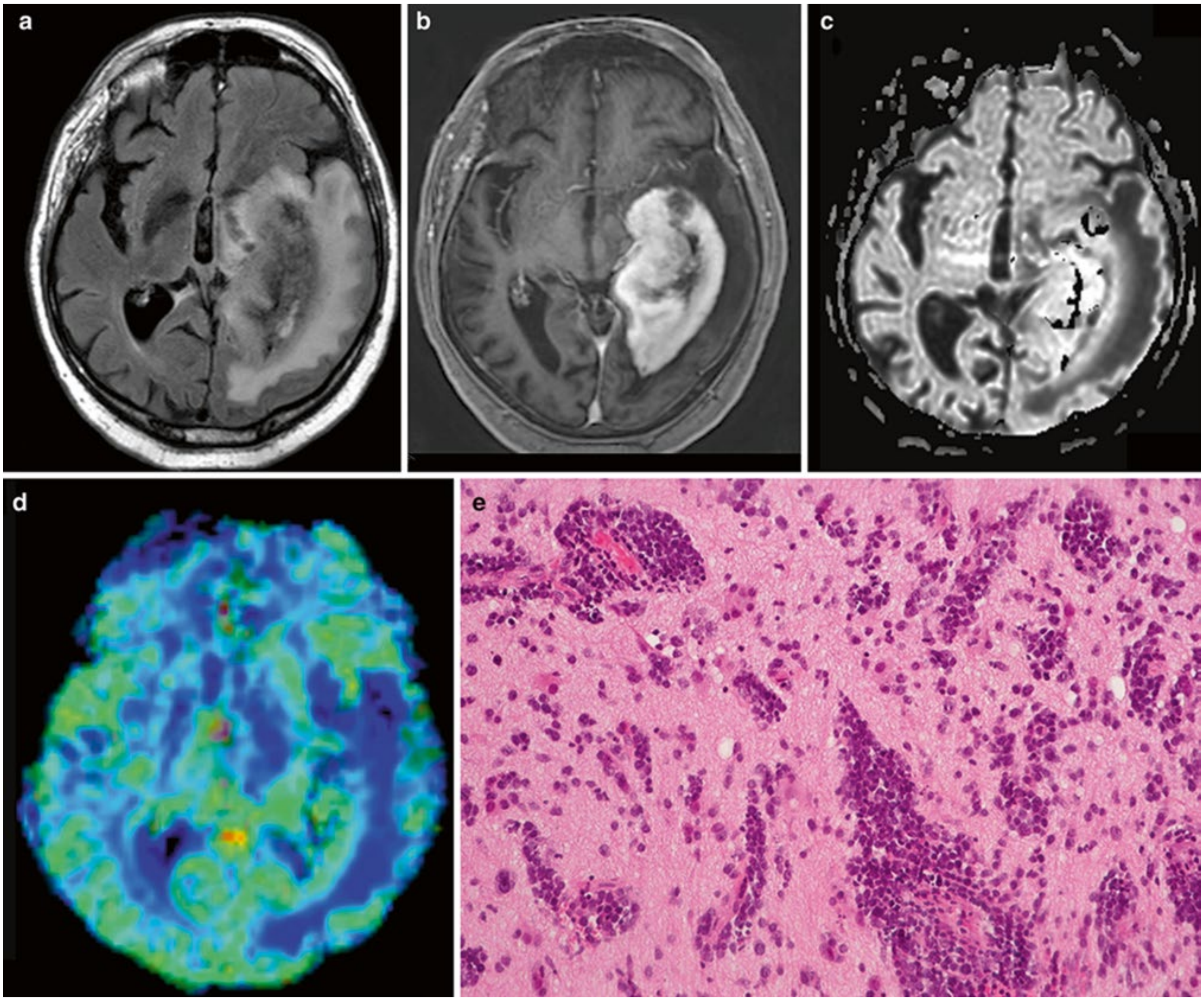

Fig. 8 Primary CNS lymphoma: (**a**) axial FLAIR, (**b**) post-Gd T1w; (**c**) DWI, and (**d**) DSC rCBV map of a selected slice. Despite strong diffuse contrast enhancement, only moderate local rCBV elevation is seen. Diffusion restriction pleads for a tumor with high cellular density. In the histopathological view (**e**: Image courtesy of Claire Delbridge, MD, Department of Neuropathology, Klinikum Rechts der Isar, TU Munich), note the high cell density and the growth pattern around preexisting vessels

Primary CNS lymphoma also shows high cellular density and diffuse infiltration; however, they typically exhibit an angiocentric growth pattern around preexisting vessels. Therefore, this entity generally has lower rCBV than glioblastoma, yet somewhat higher values than healthy brain tissue, mainly due to a limited but existing neoangiogenesis (Fig. 8). In single cases, it can still be very difficult to differentiate between lymphoma and glioblastoma even with perfusion imaging. A specific characteristic of lymphoma perfusion may be the signal change in the time–intensity curve from the DSC perfusion: lymphomas, unlike glioblastomas, may show a characteristic pattern, where the signal recovery exceeds the baseline level after the first pass, which was described in Blasel et al. (2013) and Liao et al. (2009).

Cerebral metastases spread via hematogenous routes and can therefore be well vascularized, depending on the origin of the tumor. However, metastases are well delineated, without a diffuse infiltration zone but a typically large peritumoral edema. While rCBV in the enhancing tumor regions in metastases is just as high as in glioblastomas, the peritumoral region shows significantly lower perfusion in metastases (Law et al. 2002) (Fig. 9).

3.4 Tumor Grading and Prognosis

Perfusion imaging—as an indirect measure of tumor vascularization—was shown to correlate with the histological grade of gliomas in several studies and with different

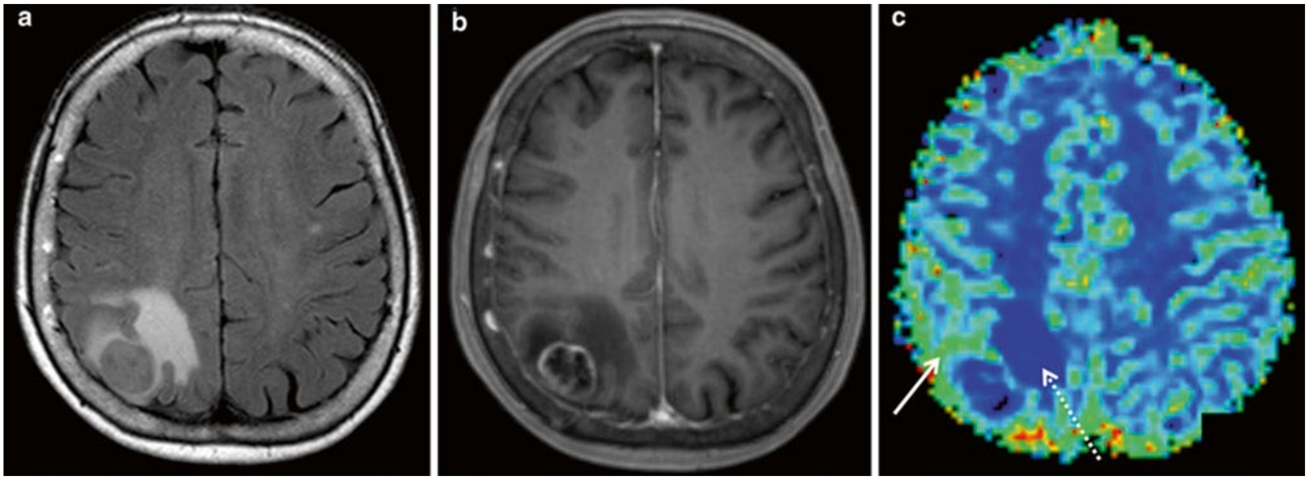

Fig. 9 Metastasis of a bronchial carcinoma (NSCLC): (**a**) axial FLAIR, (**b**) post-Gd T1w, and (**c**) DSC rCBV map of a selected slice. Elevated rCBV values are seen in the rostral part of the contrast-enhancing lesion (*arrow*) but not in the perifocal edema (*dotted arrow*)

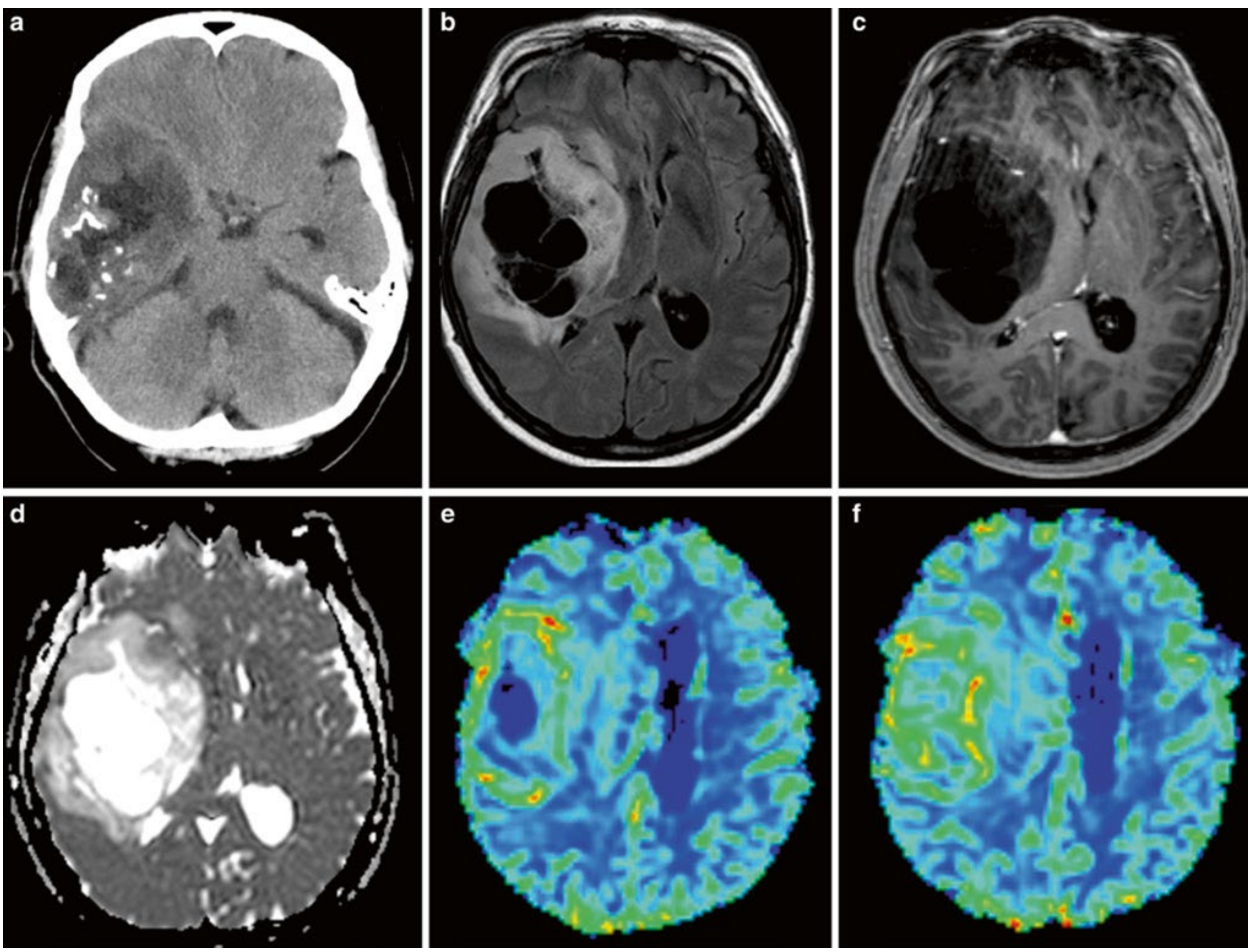

Fig. 10 Oligodendroglioma, an example for an atypical low-grade glioma: *upper row* (**a**) axial nonenhanced CT, (**b**) FLAIR, and (**c**) post-Gd T1w image; *lower row* (**d**) ADC map, (**e**, **f**) DSC rCBV map in a right temporofrontal space-occupying lesion. Calcifications, multiple cysts, and a cortical localization are characteristic features. Despite the lack of contrast enhancement, high rCBV values are seen throughout the solid tumor

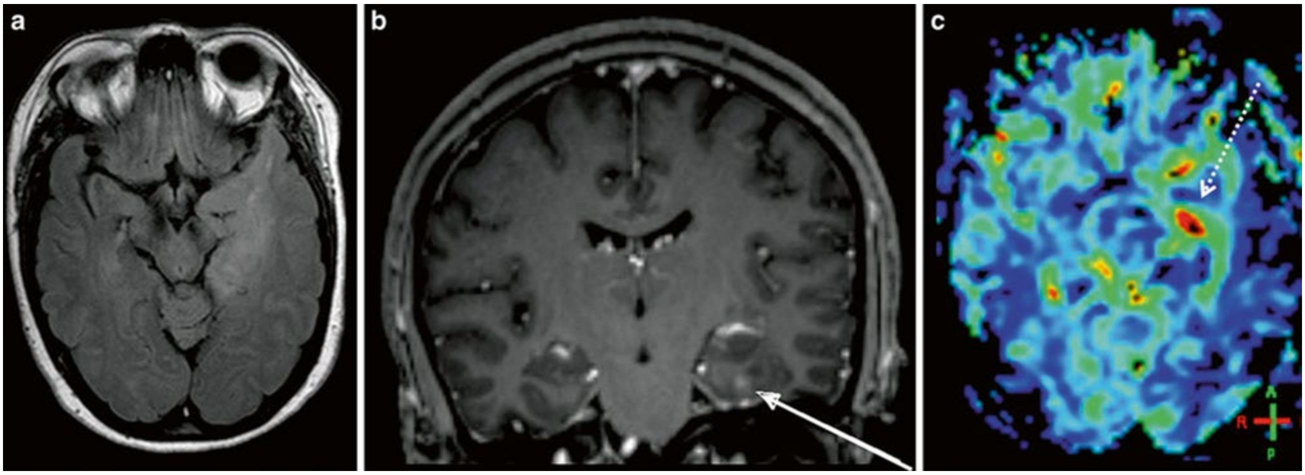

Fig. 11 Imaging of a diffusely infiltrating, moderately space-occupying lesion in the left temporal lobe with only a punctual contrast enhancement (*arrow*): (**a**) axial FLAIR, (**b**) coronal post-Gd T1w image, and (**c**) DSC rCBV map of a selected slice. The lesion is diffusely hyperperfused with elevated rCBV values throughout the tumor and focal hot spots (*dotted arrow*) indicating malignity. Histological diagnosis: anaplastic oligoastrocytoma WHO °III

imaging methods (Aronen et al. 1994; Donahue et al. 2000; Hakyemez et al. 2005; Schmainda et al. 2004; Jarnum et al. 2010). The underlying pathophysiology could also be proven histopathologically: The WHO grade of gliomas partly depends on vascularity, and a higher microvascular density was found in tumor specimens with higher rCBV (Cha et al. 2003). rCBV was identified as a particularly important imaging parameter among 161 different tumor characteristics in a pattern classification study (Zacharaki et al. 2009). The correlation of rCBV and glioma grade is independent of the evaluation method: operator-independent histogram analysis (where a big ROI is drawn around the whole tumor) was just as effective as operator-dependent $rCBV_{max}$-ROI analysis (Law et al. 2007).

Among the different perfusion parameters, rCBV correlates best with glioma grade whereas permeability showed a somewhat weaker correlation (Law et al. 2004). However, the two parameters demonstrate different tumor characteristics—and with respect to drug delivery, permeability imaging gains more and more importance (Levy 2005). Recently, a combined approach—rCBV together with CBF and K^{trans}—was proven to be a better predictor of glioma grade (Law et al. 2004, 2006; Shin et al. 2002; Roy et al. 2013; Zhang et al. 2012).

Contrast agent leakage is a particularly important factor in perfusion imaging of brain tumors. This also applies to tumor grade prediction. The most widely applied DSC method may underestimate rCBV in the presence of contrast leakage, which might result in an undergrading of a lesion. Therefore, leakage correction—at least a pre-bolus or preferably a postprocessing leakage correction algorithm—is essential in neuro-oncological studies (Boxerman et al. 2006).

Low-grade brain tumors—like astrocytomas (WHO II) and oligodendrogliomas—are not necrotic and their enhancement pattern is variable. While typical nonenhancing tumor regions usually show normal rCBV values (in the range of healthy tissue), there is an exception to the rule: low-grade oligodendrogliomas (Cha et al. 2005)—with or without contrast enhancement—may show higher rCBV due to an increased vessel density even without further hints of malignization (Cha et al. 2005; Lev et al. 2004) (Fig. 10).

Increased perfusion is seen in the enhancing tumor areas in WHO °III gliomas (Figs. 11 and 12) and even more so in glioblastomas; even the nonenhancing tumor infiltration region is hyperperfused in these tumors (Lupo et al. 2005).

Functional imaging including perfusion data may provide additional information about tumor vitality beyond the characteristics used for histopathological grading. The density of tumor vasculature correlates with overall survival in astrocytic tumors: high vascularity was linked to shorter time to progression and with reduced overall survival (Law et al. 2008; Sanz-Requena et al. 2013). Correspondingly, rCBV was shown to be equally or more important for prognosis and overall survival than histological grade, even in low-grade gliomas (Majchrzak et al. 2012). DSC perfusion imaging can be used to predict median time to progression in patients with gliomas, independent of pathological findings: baseline rCBV values above a threshold—either in high-grade or in low-grade gliomas—detect progressive disease and predict tumor recurrence and time to progression (Law et al. 2008; Caseiras et al. 2010; Bisdas et al. 2009). It is important to note that these findings could not be reproduced for tumors with oligodendroglial components where dense vascularization occurs in

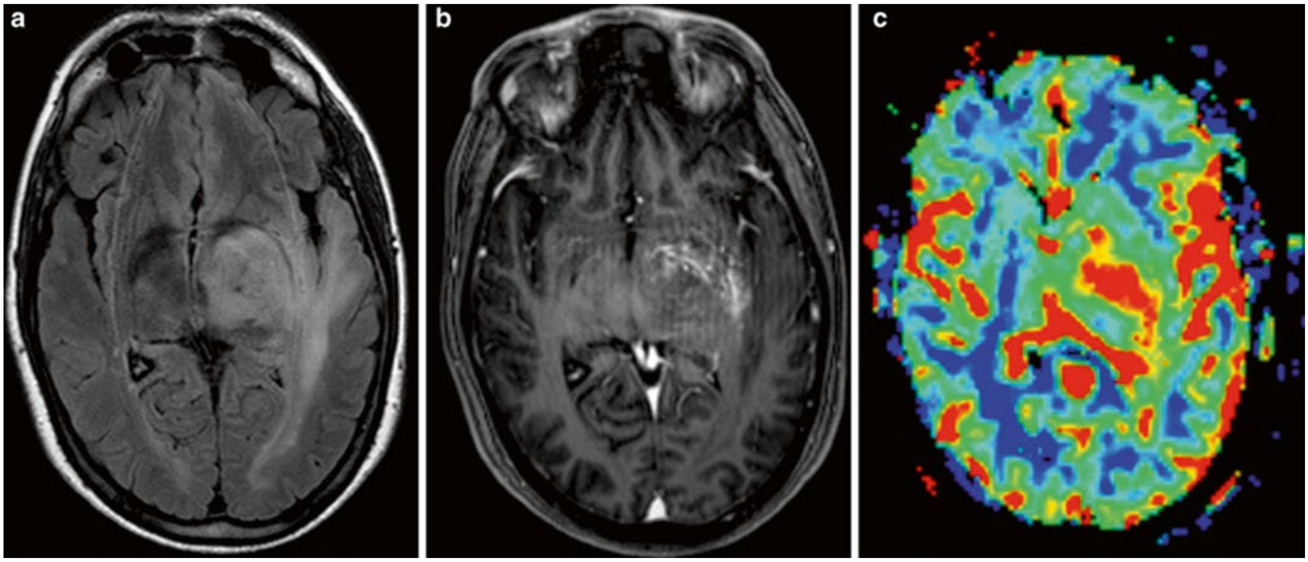

Fig. 12 Imaging of a diffusely infiltrating lesion in the left thalamus: (**a**) axial FLAIR, (**b**) axial post-Gd T1w MPRAGE, (**c**) DSC rCBV map of a selected slice. There is little space-occupying effect and moderate, diffuse enhancement without necrosis. rCBV values, however, are elevated throughout the lesion and in its surroundings. Histological diagnosis stated an anaplastic astrocytoma WHO °III

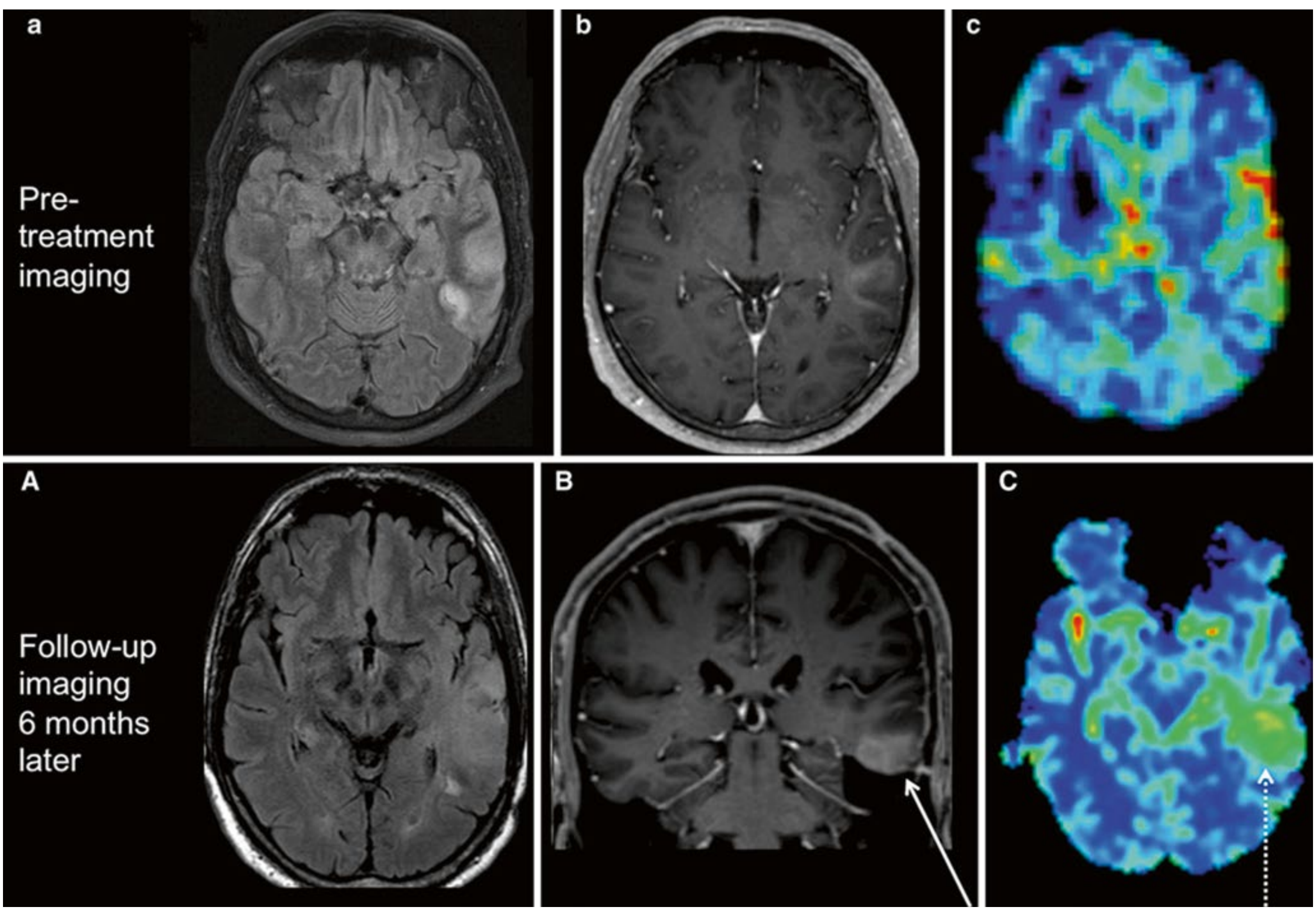

Fig. 13 Astrocytoma progression. (*Upper row*) First imaging of a patient with an epileptic seizure; (**a**) axial FLAIR, (**b**) axial T1w post-Gd, and (**c**) DSC rCBV map of a selected slice. Peripheral diffuse T2 lesion of the temporal lobe with slight enhancement and minimally elevated rCBV values. Note the linear *red* signal cortical, corresponding to a large cortical vein in the T1w post-Gd. Histological report stated an astrocytoma WHO °II. (*Lower row*) Follow-up of the same patient 6 months later; (**A**) axial FLAIR, (**B**) coronal T1w post-Gd, and (**C**) DSC rCBV map. Progression of the T2 lesion, now rather space occupying, and of the contrast enhancement (*arrow*). rCBV values are highly elevated throughout the lesion (*dotted arrow*). Histology revealed malignization to an astrocytoma WHO °III

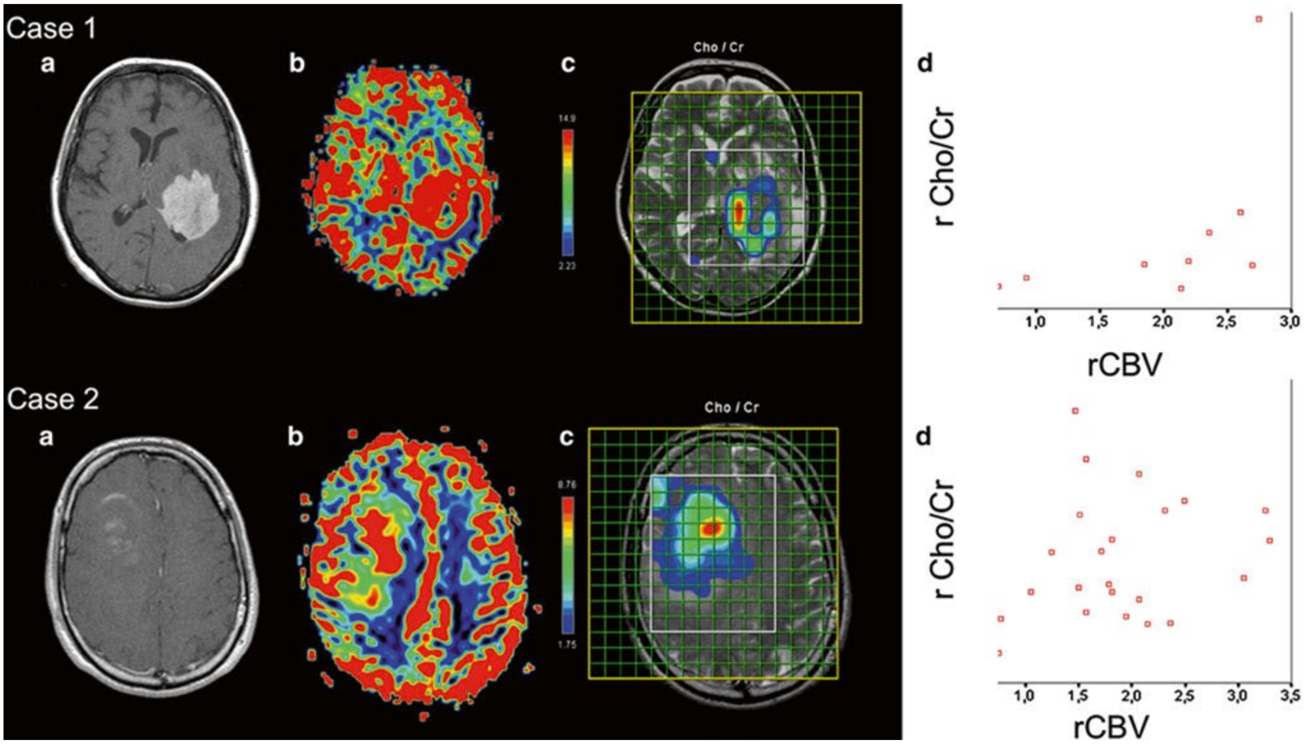

Fig. 14 Illustration of the tumor heterogeneity with an example of two GBM (WHO °IV) cases. In *Case 1*, the diffusely contrast-enhancing tumor (**a**) shows a large hyperperfused portion (DSC rCBV map in **b**) and spectroscopic choline peaks in the mesial and dorsal part (**c**); the voxelwise comparison of the perfusion and the spectroscopic hot spots in (**d**) shows a reasonable correlation. In *Case 2*, the tumor enhances only in small parts (**a**); the mesial and dorsal parts are hyperperfused (**b**); the spectroscopic peak is in the central part of the tumor (**c**); and there is little correlation between the two methods (**d**), indicating tumor heterogeneity

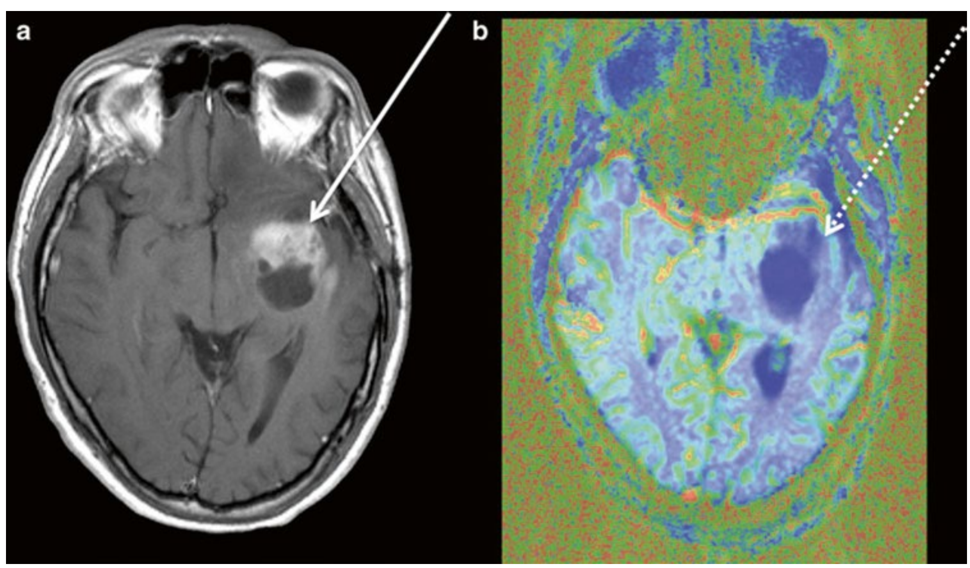

Fig. 15 Follow-up imaging of a patient with a glioblastoma (3 months postsurgery). There is a new contrast-enhancing lesion in the post-contrast T1w image (**a**) rostral from the resected lesion in the left temporal lobe (*arrow*). Perfusion imaging with ASL (**b**) shows decreased rCBF (*dotted arrow*), suggesting radiation necrosis, which was confirmed by histology

low-grade tumors as well (Bisdas et al. 2009). In the follow-up of low-grade astrocytic tumors, however, elevated perfusion may be the first sign of a malign transformation (Fig. 13). Therefore, use of perfusion data in combination with histological information is essential in predicting prognosis in glioma patients.

3.5 Guidance for Biopsy and Radiation Therapy Planning

An important clinical topic where perfusion imaging can play a relevant part is in the definition of “tumor hot spots,” i.e., most malignant (or highest grade) niches of heterogeneous

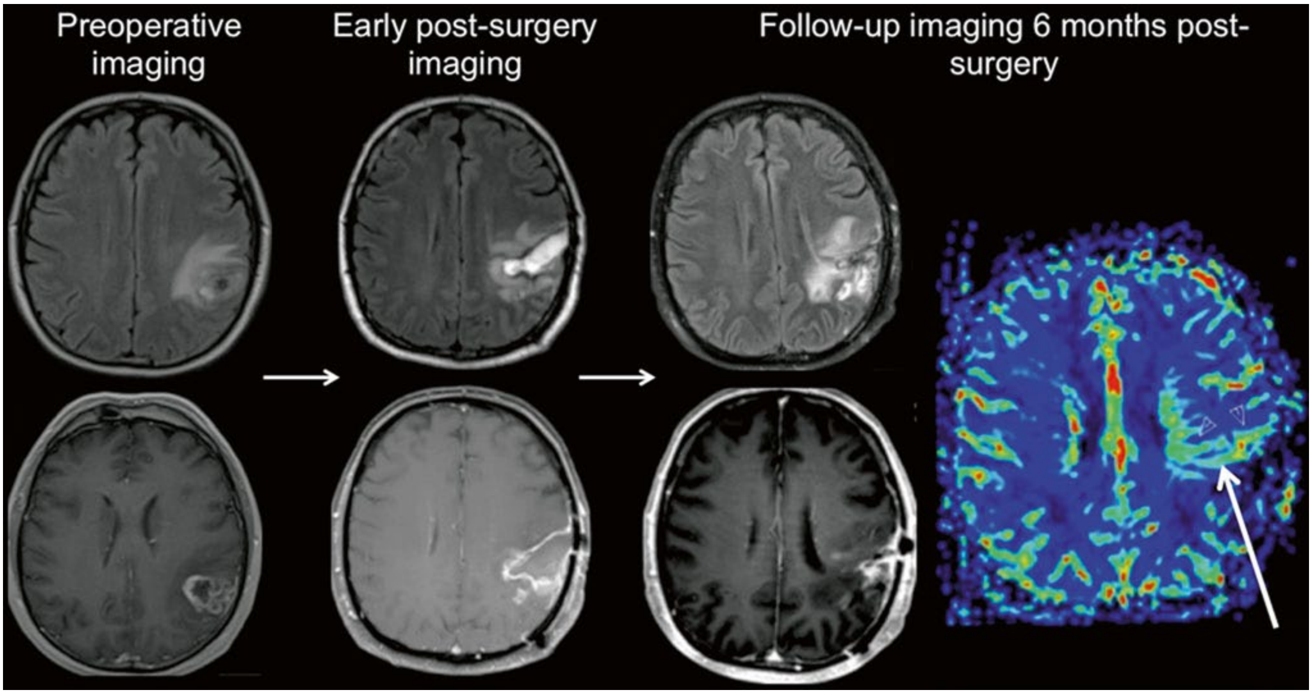

Fig. 16 Imaging follow-up of a glioblastoma patient. Preoperative imaging (axial FLAIR and post-Gd T1w) shows a partially necrotic tumor with infiltrating borders and contrast enhancement. Early post-surgery imaging (axial FLAIR and post-Gd T1w) shows persisting T2 lesion and no enhancement (T1w hyperintensities correspond to blood products). Follow-up at 6 months after radiochemotherapy (axial FLAIR, post-Gd T1w, and DSC rCBV perfusion map): T2 lesion is progredient; rCBV elevation in a contrast-enhancing lesion suggests tumor recurrence, verified by histology

tumor tissue. Their definition is important for the guidance of biopsy procedures, to prevent the undergrading of a tumor and to focus surgical efforts. Perfusion imaging was shown to identify tissue biopsy specimens with higher tumor proliferation, necrosis, and vascular hyperplasia (Barajas et al. 2012). In the same study, diffusion weighted imaging identified regions of tumor infiltration. Other studies found that perfusion hot spots did not coincide with spectroscopic tumor hot spots, indicating a spatial divergence of neovascularization and tumor cell proliferation (Wagner et al. 2011). These data demonstrate that the use of multimodal imaging identifies tumor parts with different histological characteristics (Fig. 14). A multimodal approach remains, therefore, essential in biopsy planning.

Recently, multimodal imaging has also been introduced to the planning of radiotherapy, allowing the delivery of focused higher doses (dose-painting or intensity-modulated radiotherapy) to new target volumes characterized by functional data (e.g., perfusion or spectroscopy) (Ken et al. 2013; Grosu et al. 2007).

3.6 Treatment Monitoring

Therapeutic interventions—resection, radiation, and chemotherapy—affect tumor vascularization in a way that is difficult to keep track of with conventional imaging. Perfusion imaging could be an especially valuable aid in post-therapeutic tumor imaging.

The first medication given to a patient with the diagnosis of a brain tumor is often a steroid like dexamethasone; therefore, it is important to be aware of its potential impact on imaging results. Steroid treatment has a great effect on tumor perfusion: even shortly after administration, the volume of enhancing tumor, rCBV, and permeability decreases drastically (Ostergaard et al. 1999; Armitage et al. 2007), which is due to a transient decrease in total vessel volume (Darpolor et al. 2011).

The primary focus of surgical resection is the contrast-enhancing tumor mass with disrupted blood–brain barrier. Postsurgery imaging must exclude the presence of postsurgical infarcts with the help of diffusion weighted imaging (Smith et al. 2005; Gempt et al. 2013a, b). In early postsurgery imaging (<24–48 h after resection), contrast enhancement most probably represents residual tumor, while postsurgical infarcts and reactive gliosis start to enhance somewhat later. The amount of nonenhancing tumor residual is often overestimated in these scans, which can be related to edema and postsurgical infarcts (Belhawi et al. 2011). Perfusion imaging in addition to DWI can help in the differentiation of these lesions.

Current standard adjuvant therapy of glioblastoma includes radiotherapy and concomitant chemotherapy. The

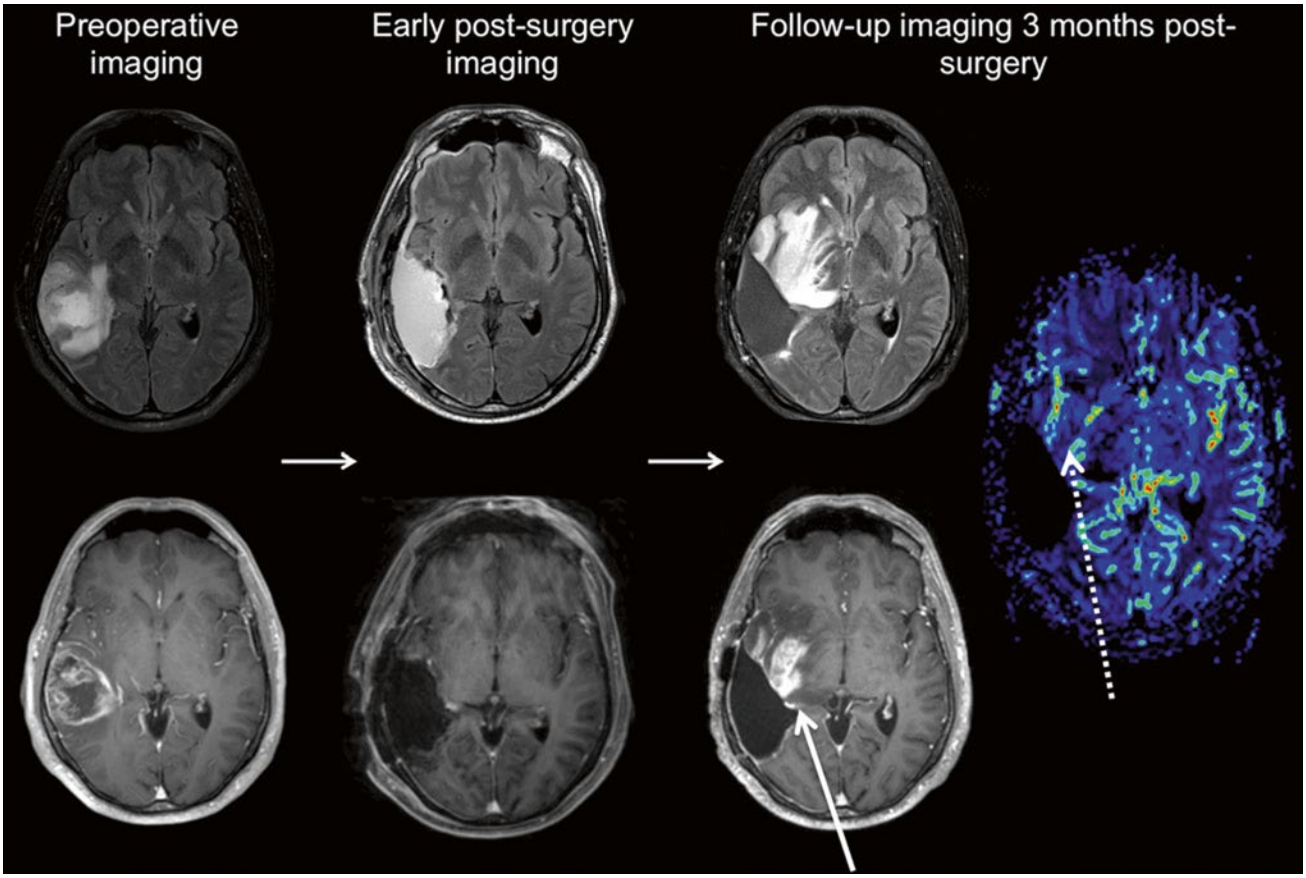

Fig. 17 Imaging follow-up of another glioblastoma patient. Preoperative imaging (axial FLAIR and post-Gd T1w) shows—just like in Fig. 15—a partially necrotic tumor with infiltrating borders and contrast enhancement. Early postsurgery imaging (axial FLAIR and post-Gd T1w) shows no residual tumor. Follow-up at 3 months after chemotherapy (axial FLAIR, post-Gd T1w, and DSC rCBV perfusion map): extensive new T2 lesion and contrast enhancement; rCBV, however, is only partly and moderately elevated, suggesting pseudoprogression

imaging follow-up of these patients may reveal early imaging changes such as a progressive T2 lesion, contrast enhancement, and necroses even in patients who are doing well and in later follow-up these lesions regress. This phenomenon is called pseudoprogression because the conventional imaging changes are indistinguishable from tumor. Pseudoprogression may be caused by chemotherapy—mainly due to a breakdown of the blood–brain barrier and cytotoxic effects—or by radiation effects. Radiation necrosis may also result in delayed changes, months later (Sundgren and Cao 2009), by reducing overall tissue perfusion and increases permeability in both tumorous and healthy tissue, due to a decline in vessel density and an increase in vessel tortuosity (Lee et al. 2005; Fuss et al. 2000). The injured tissue is characterized by tissue edema and contrast enhancement in conventional MRI, but perfusion weighted imaging may provide more insight into tissue pathology underlying these changes (Fig. 15).

Lesions in pseudoprogression and postoperative scars show significantly lower perfusion than early tumor progression (Choi et al. 2013). High rCBV strongly suggests tumor recurrence (see Fig. 15), while normal rCBV speaks for treatment-related changes (Sugahara et al. 2000; Hu et al. 2009) (Fig. 16).

Pseudoresponse, on the other hand, is a term related to the use of anti-angiogenic therapies. These agents—antagonists of the previously mentioned angiogenic factors like VEGF—act by inhibiting the development of new tumor vessels and "normalizing" the existing ones (O'Connor et al. 2007). In perfusion imaging, there is a drastic rCBV decrease even after administration of a single dose of such drugs; overall permeability is also decreased, resulting in disappearing contrast enhancement (Vidiri et al. 2012) and reduced vasogenic edema. These changes in tumor vascularization may have controversial effects on tumor biology, and up to now, perfusion characteristics of glioblastoma under anti-angiogenic treatment cannot predict patient outcome (Figs. 17 and 18).

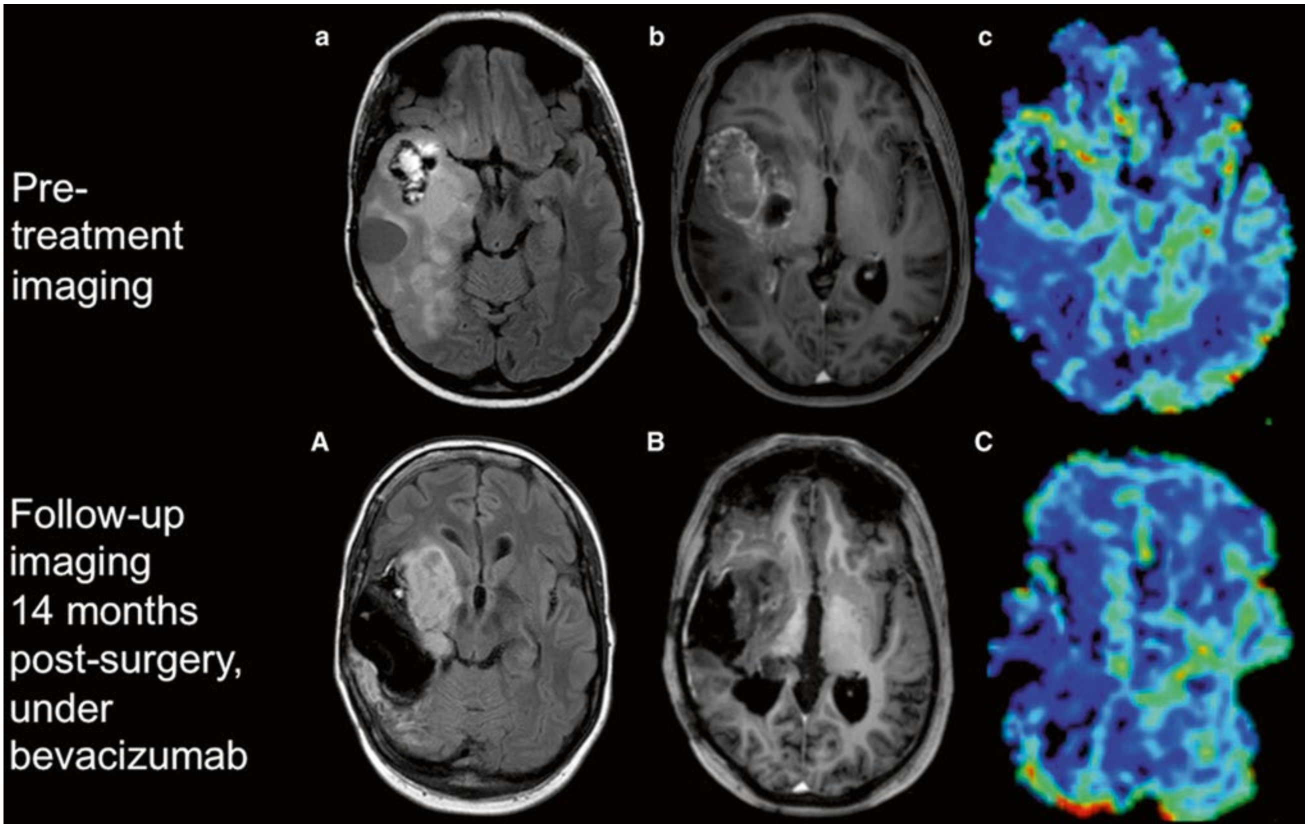

Fig. 18 Glioblastoma with anti-angiogenic treatment. (*Upper row*) Pretherapeutic imaging (axial FLAIR, T1w post-Gd, DSC rCBV map). The large, enhancing, partly cystic tumor of the right temporal lobe shows high rCBV values in the solid tumor regions as well as in the infiltration zone (not shown). (*Lower row*) Follow-up of the same patient 14 months later (at this time point receiving bevacizumab treatment). While there is a space-occupying FLAIR lesion on the medial rostral resection rim, no enhancement is seen and rCBV values are rather low. Biopsy revealed tumor recurrence

References

Alsop DC, Detre JA (1996) Reduced transit-time sensitivity in noninvasive magnetic resonance imaging of human cerebral blood flow. J Cereb Blood Flow Metab 16:1236–1249

Armitage PA, Schwindack C, Bastin ME et al (2007) Quantitative assessment of intracranial tumor response to dexamethasone using diffusion, perfusion and permeability magnetic resonance imaging. Magn Reson Imaging 25:303–310

Aronen HJ, Gazit IE, Louis DN et al (1994) Cerebral blood volume maps of gliomas: comparison with tumor grade and histologic findings. Radiology 191:41–51

Barajas RF, Phillips JJ, Parvataneni R et al (2012) Regional variation in histopathologic features of tumor specimens from treatment-naive glioblastoma correlates with anatomic and physiologic MR Imaging. Neuro Oncol 14:942–954

Bassingthwaighte JB, Malone MA, Moffett TC et al (1990) Molecular and particulate depositions for regional myocardial flows in sheep. Circ Res 66:1328–1344

Belhawi SM, Hoefnagels FW, Baaijen JC et al (2011) Early postoperative MRI overestimates residual tumour after resection of gliomas with no or minimal enhancement. Eur Radiol 21:1526–1534

Belliveau JW, Kennedy DN Jr, McKinstry RC et al (1991) Functional mapping of the human visual cortex by magnetic resonance imaging. Science 254:716–719

Bisdas S, Kirkpatrick M, Giglio P et al (2009) Cerebral blood volume measurements by perfusion-weighted MR imaging in gliomas: ready for prime time in predicting short-term outcome and recurrent disease? Am J Neuroradiol 30:681–688

Bjornerud A, Sorensen AG, Mouridsen K et al (2011) T1- and T2*-dominant extravasation correction in DSC-MRI: part I—theoretical considerations and implications for assessment of tumor hemodynamic properties. J Cereb Blood Flow Metab 31:2041–2053

Blasel S, Franz K, Mittelbronn M et al (2010) The striate sign: peritumoural perfusion pattern of infiltrative primary and recurrent gliomas. Neurosurg Rev 33:193–203 (discussion 194–203)

Blasel S, Jurcoane A, Bähr O et al (2013) MR perfusion in and around the contrast-enhancement of primary CNS lymphomas. J Neurooncol 114:127–134

Blockley NP, Jiang L, Gardener AG et al (2008) Field strength dependence of R1 and R2* relaxivities of human whole blood to ProHance, Vasovist, and deoxyhemoglobin. Magn Reson Med 60:1313–1320

Boxerman JL, Hamberg LM, Rosen BR et al (1995) MR contrast due to intravascular magnetic susceptibility perturbations. Magn Reson Med 34:555–566

Boxerman JL, Rosen BR, Weisskoff RM (1997) Signal-to-noise analysis of cerebral blood volume maps from dynamic NMR imaging studies. J Magn Reson Imaging 7:528–537

Boxerman JL, Schmainda KM, Weisskoff RM (2006) Relative cerebral blood volume maps corrected for contrast agent

extravasation significantly correlate with glioma tumor grade, whereas uncorrected maps do not. Am J Neuroradiol 27:859–867
Boxerman JL, Prah DE, Paulson ES et al (2012) The Role of preload and leakage correction in gadolinium-based cerebral blood volume estimation determined by comparison with MION as a criterion standard. Am J Neuroradiol 33:1081–1087
Brem S (1976) The role of vascular proliferation in the growth of brain tumors. Clin Neurosurg 23:440–453
Brix G, Semmler W, Port R et al (1991) Pharmacokinetic parameters in CNS Gd-DTPA enhanced MR imaging. J Comput Assist Tomogr 15:621–628
Brix G, Kiessling F, Lucht R et al (2004) Microcirculation and microvasculature in breast tumors: pharmacokinetic analysis of dynamic MR image series. Magn Reson Med 52:420–429
Buxton RB (2009a) Contrast agent techniques. Introduction to functional magnetic resonance imaging, 2nd edn. Cambridge University press, Cambridge
Buxton RB (2009b) Arterial spin labeling techniques. Introduction to functional magnetic resonance imaging, 2nd edn. Cambridge University press, Cambridge
Buxton RB, Frank LR, Wong EC et al (1998) A general kinetic model for quantitative perfusion imaging with arterial spin labeling. Magn Reson Med 40:383–396
Calamante F (2005) Bolus dispersion issues related to the quantification of perfusion MRI data. J Magn Reson Imaging 22:718–722
Calamante F, Gadian DG, Connelly A (2000) Delay and dispersion effects in dynamic susceptibility contrast MRI: simulations using singular value decomposition. Magn Reson Med 44:466–473
Calamante F, Gadian DG, Connelly A (2002) Quantification of perfusion using bolus tracking magnetic resonance imaging in stroke: assumptions, limitations, and potential implications for clinical use. Stroke 33:1146–1151
Calamante F, Morup M, Hansen LK (2004) Defining a local arterial input function for perfusion MRI using independent component analysis. Magn Reson Med 52:789–797
Caravan P, Ellison JJ, McMurry TJ et al (1999) Gadolinium(III) chelates as MRI contrast agents: structure, dynamics, and applications. Chem Rev 99:2293–2352
Caseiras GB, Chheang S, Babb J et al (2010) Relative cerebral blood volume measurements of low-grade gliomas predict patient outcome in a multi-institution setting. Eur J Radiol 73:215–220
Cha S (2004) Perfusion MR imaging of brain tumors. Top Magn Reson Imaging 15:279–289
Cha S, Johnson G, Wadghiri YZ et al (2003) Dynamic, contrast-enhanced perfusion MRI in mouse gliomas: correlation with histopathology. Magn Reson Med 49:848–855
Cha S, Tihan T, Crawford F et al (2005) Differentiation of low-grade oligodendrogliomas from low-grade astrocytomas by using quantitative blood-volume measurements derived from dynamic susceptibility contrast-enhanced MR imaging. Am J Neuroradiol 26:266–273
Chalela JA, Alsop DC, Gonzalez-Atavales JB et al (2000) Magnetic resonance perfusion imaging in acute ischemic stroke using continuous arterial spin labeling. Stroke 31:680–687
Choi YJ, Kim HS, Jahng GH et al (2013) Pseudoprogression in patients with glioblastoma: added value of arterial spin labeling to dynamic susceptibility contrast perfusion MR imaging. Acta Radiol 55(3):361–369
Darpolor MM, Molthen RC, Schmainda KM (2011) Multimodality imaging of abnormal vascular perfusion and morphology in preclinical 9L gliosarcoma model. PLoS One 6:e16621
Deibler AR, Pollock JM, Kraft RA et al (2008) Arterial spin-labeling in routine clinical practice, part 1: technique and artifacts. Am J Neuroradiol 29:1228–1234
Deichmann R (2005) Fast high-resolution T1 mapping of the human brain. Magn Reson Med 54:20–27
Deshmane A, Gulani V, Griswold MA et al (2012) Parallel MR imaging. J Magn Reson Imaging 36:55–72
Detre JA, Leigh JS, Williams DS et al (1992) Perfusion imaging. Magn Reson Med 23:37–45
Donahue KM, Weisskoff RM, Chesler DA et al (1996) Improving MR quantification of regional blood volume with intravascular T1 contrast agents: accuracy, precision, and water exchange. Magn Reson Med 36:858–867
Donahue KM, Krouwer HG, Rand SD et al (2000) Utility of simultaneously acquired gradient-echo and spin-echo cerebral blood volume and morphology maps in brain tumor patients. Magn Reson Med 43:845–853
Duhamel G, Schlaug G, Alsop DC (2006) Measurement of arterial input functions for dynamic susceptibility contrast magnetic resonance imaging using echoplanar images: comparison of physical simulations with in vivo results. Magn Reson Med 55:514–523
Edelman RR, Siewert B, Adamis M et al (1994) Signal targeting with alternating radiofrequency (STAR) sequences: application to MR angiography. Magn Reson Med 31:233–238
Essig M, Wenz F, Scholdei R et al (2002) Dynamic susceptibility contrast-enhanced echo-planar imaging of cerebral gliomas. Effect of contrast medium extravasation. Acta Radiol 43:354–359
Faehndrich J, Weidauer S, Pilatus U et al (2011) Neuroradiological viewpoint on the diagnostics of space-occupying brain lesions. Clin Neuroradiol 21:123–139
Fatterpekar GM, Galheigo D, Narayana A et al (2012) Treatment-related change versus tumor recurrence in high-grade gliomas: a diagnostic conundrum–use of dynamic susceptibility contrast-enhanced (DSC) perfusion MRI. Am J Roentgenol 198:19–26
Folkerth RD (2004) Histologic measures of angiogenesis in human primary brain tumors. Cancer Treat Res 117:79–95
Frackowiak RS, Lenzi GL, Jones T et al (1980) Quantitative measurement of regional cerebral blood flow and oxygen metabolism in man using 15O and positron emission tomography: theory, procedure, and normal values. J Comput Assist Tomogr 4:727–736
Fuss M, Wenz F, Scholdei R et al (2000) Radiation-induced regional cerebral blood volume (rCBV) changes in normal brain and low-grade astrocytomas: quantification and time and dose-dependent occurrence. Int J Radiat Oncol Biol Phys 48:53–58
Garcia DM, Duhamel G, Alsop DC (2005) Efficiency of inversion pulses for background suppressed arterial spin labeling. Magn Reson Med 54:366–372
Gempt J, Förschler A, Buchmann N et al (2013a) Postoperative ischemic changes following resection of newly diagnosed and recurrent gliomas and their clinical relevance. J Neurosurg 118:801–808
Gempt J, Gerhardt J, Toth V et al (2013b) Postoperative ischemic changes following brain metastasis resection as measured by diffusion-weighted magnetic resonance imaging. J Neurosurg 3(5):437–445
Golay X, Petersen ET (2006) Arterial spin labeling: benefits and pitfalls of high magnetic field. Neuroimaging Clin N Am 16:259–268, x
Golay X, Hendrikse J, Lim TC (2004) Perfusion imaging using arterial spin labeling. Top Magn Reson Imaging 15:10–27
Golay X, Petersen ET, Hui F (2005) Pulsed star labeling of arterial regions (PULSAR): a robust regional perfusion technique for high field imaging. Magn Reson Med 53:15–21
Grosu AL, Souvatzoglou M, Röper B et al (2007) Hypoxia imaging with FAZA-PET and theoretical considerations with regard to dose painting for individualization of radiotherapy in patients with head and neck cancer. Int J Radiat Oncol Biol Phys 69:541–551

Gunther M, Bock M, Schad LR (2001) Arterial spin labeling in combination with a look-locker sampling strategy: inflow turbo-sampling EPI-FAIR (ITS-FAIR). Magn Reson Med 46:974–984

Hakyemez B, Erdogan C, Ercan I et al (2005) High-grade and low-grade gliomas: differentiation by using perfusion MR imaging. Clin Radiol 60:493–502

Hardee ME, Zagzag D (2012) Mechanisms of glioma-associated neovascularization. Am J Pathol 181:1126–1141

Harrer JU, Parker GJ, Haroon HA et al (2004) Comparative study of methods for determining vascular permeability and blood volume in human gliomas. J Magn Reson Imaging 20:748–757

Hattingen E, Blasel S, Dettmann E et al (2008) Perfusion-weighted MRI to evaluate cerebral autoregulation in aneurysmal subarach-noid haemorrhage. Neuroradiology 50:929–938

Heiland S, Benner T, Debus J et al (1999) Simultaneous assessment of cerebral hemodynamics and contrast agent uptake in lesions with disrupted blood–brain-barrier. Magn Reson Imaging 17:21–27

Heiland S, Wick W, Bendszus M (2010) Perfusion magnetic resonance imaging for parametric response maps in tumors: is it really that easy? J Clin Oncol 28:e591 (author reply e592)

Helle M, Rufer S, van Osch MJ et al (2012) Selective multivessel labeling approach for perfusion territory imaging in pseudo-continuous arterial spin labeling. Magn Reson Med 68:214–219

Henderson E, McKinnon G, Lee TY et al (1999) A fast 3D look-locker method for volumetric T1 mapping. Magn Reson Imaging 17:1163–1171

Henderson E, Sykes J, Drost D et al (2000) Simultaneous MRI measurement of blood flow, blood volume, and capillary permeability in mammary tumors using two different contrast agents. J Magn Reson Imaging 12:991–1003

Hendrick RE, Haacke EM (1993) Basic physics of MR contrast agents and maximization of image contrast. J Magn Reson Imaging 3:137–148

Heymann MA, Payne BD, Hoffman JI et al (1977) Blood flow measurements with radionuclide-labeled particles. Prog Cardiovasc Dis 20:55–79

Hu LS, Baxter LC, Smith KA et al (2009) Relative cerebral blood volume values to differentiate high-grade glioma recurrence from posttreatment radiation effect: direct correlation between image-guided tissue histopathology and localized dynamic susceptibility-weighted contrast-enhanced perfusion MR imaging measurements. Am J Neuroradiol 30:552–558

Jarnum H, Steffensen EG, Knutsson L et al (2010) Perfusion MRI of brain tumours: a comparative study of pseudo-continuous arterial spin labelling and dynamic susceptibility contrast imaging. Neuroradiology 52:307–317

Johnson KM, Tao JZ, Kennan RP et al (2000) Intravascular susceptibility agent effects on tissue transverse relaxation rates in vivo. Magn Reson Med 44:909–914

Johnson G, Wetzel SG, Cha S et al (2004) Measuring blood volume and vascular transfer constant from dynamic, T(2)*-weighted contrast-enhanced MRI. Magn Reson Med 51:961–968

Ken S, Vieillevigne L, Franceries X et al (2013) Integration method of 3D MR spectroscopy into treatment planning system for glioblastoma IMRT dose painting with integrated simultaneous boost. Radiat Oncol 8:1

Kety SS (1951) The theory and applications of the exchange of inert gas at the lungs and tissues. Pharmacol Rev 3:1–41

Kim SG (1995) Quantification of relative cerebral blood flow change by flow-sensitive alternating inversion recovery (FAIR) technique: application to functional mapping. Magn Reson Med 34:293–301

Kiselev VG (2001) On the theoretical basis of perfusion measurements by dynamic susceptibility contrast MRI. Magn Reson Med 46:1113–1122

Kiselev VG (2005) Transverse relaxation effect of MRI contrast agents: a crucial issue for quantitative measurements of cerebral perfusion. J Magn Reson Imaging 22:693–696

Kiselev VG, Strecker R, Ziyeh S et al (2005) Vessel size imaging in humans. Magn Reson Med 53:553–563

Kjolby BF, Ostergaard L, Kiselev VG (2006) Theoretical model of intravascular paramagnetic tracers effect on tissue relaxation. Magn Reson Med 56:187–197

Knopp EA, Cha S, Johnson G et al (1999) Glial neoplasms: dynamic contrast-enhanced T2*-weighted MR imaging. Radiology 211:791–798

Ko L, Salluzzi M, Frayne R et al (2007) Reexamining the quantification of perfusion MRI data in the presence of bolus dispersion. J Magn Reson Imaging 25:639–643

Kwong KK, Belliveau JW, Chesler DA et al (1992) Dynamic magnetic resonance imaging of human brain activity during primary sensory stimulation. Proc Natl Acad Sci U S A 89:5675–5679

Kwong KK, Chesler DA, Weisskoff RM et al (1995) MR perfusion studies with T1-weighted echo planar imaging. Magn Reson Med 34:878–887

Landis CS, Li X, Telang FW et al (2000) Determination of the MRI contrast agent concentration time course in vivo following bolus injection: effect of equilibrium transcytolemmal water exchange. Magn Reson Med 44:563–574

Larsen VA, Simonsen HJ, Law I et al (2013) Evaluation of dynamic contrast-enhanced T1-weighted perfusion MRI in the differentiation of tumor recurrence from radiation necrosis. Neuroradiology (Epub ahead of print) 55(3):361–369

Larsson HB, Stubgaard M, Frederiksen JL et al (1990) Quantitation of blood-brain barrier defect by magnetic resonance imaging and gadolinium-DTPA in patients with multiple sclerosis and brain tumors. Magn Reson Med 16:117–131

Larsson HB, Hansen AE, Berg HK et al (2008) Dynamic contrastenhanced quantitative perfusion measurement of the brain using T1-weighted MRI at 3 T. J Magn Reson Imaging 27:754–762

Larsson HB, Courivaud F, Rostrup E et al (2009) Measurement of brain perfusion, blood volume, and blood-brain barrier permeability, using dynamic contrast-enhanced T(1)-weighted MRI at 3 tesla. Magn Reson Med 62:1270–1281

Law M, Cha S, Knopp EA et al (2002) High-grade gliomas and solitary metastases: differentiation by using perfusion and proton spectroscopic MR imaging. Radiology 222:715–721

Law M, Yang S, Babb JS et al (2004) Comparison of cerebral blood volume and vascular permeability from dynamic susceptibility contrast-enhanced perfusion MR imaging with glioma grade. Am J Neuroradiol 25:746–755

Law M, Young R, Babb J et al (2006) Comparing perfusion metrics obtained from a single compartment versus pharmacokinetic modeling methods using dynamic susceptibility contrast-enhanced perfusion MR imaging with glioma grade. Am J Neuroradiol 27:1975–1982

Law M, Young R, Babb J et al (2007) Histogram analysis versus region of interest analysis of dynamic susceptibility contrast perfusion MR imaging data in the grading of cerebral gliomas. Am J Neuroradiol 28:761–766

Law M, Young RJ, Babb JS et al (2008) Gliomas: predicting time to progression or survival with cerebral blood volume measurements at dynamic susceptibility-weighted contrast-enhanced perfusion MR imaging. Radiology 247:490–498

Le Bihan D (1992) Theoretical principles of perfusion imaging. Application to magnetic resonance imaging. Invest Radiol 27(Suppl 2):S6–11

Lee MC, Cha S, Chang SM et al (2005) Dynamic susceptibility contrast perfusion imaging of radiation effects in normal-appearing

MR Perfusion Imaging brain tissue: changes in the first-pass and recirculation phases. J Magn Reson Imaging 21:683–693
Lemasson B, Valable S, Farion R et al (2013) In vivo imaging of vessel diameter, size, and density: a comparative study between MRI and histology. Magn Reson Med 69:18–26
Leon SP, Folkerth RD, Black PM (1996) Microvessel density is a prognostic indicator for patients with astroglial brain tumors. Cancer 77:362–372
Lev MH, Ozsunar Y, Henson JW et al (2004) Glial tumor grading and outcome prediction using dynamic spin-echo MR susceptibility mapping compared with conventional contrast-enhanced MR: confounding effect of elevated rCBV of oligodendrogliomas (corrected). Am J Neuroradiol 25:214–221
Levy LM (2005) What is right about MRI permeability studies. Am J Neuroradiol 26:3–4
Li X, Rooney WD, Varallyay CG et al (2010) Dynamic-contrast-enhanced-MRI with extravasating contrast reagent: rat cerebral glioma blood volume determination. J Magn Reson 206:190–199
Li KL, Buonaccorsi G, Thompson G et al (2012) An improved coverage and spatial resolution—using dual injection dynamic contrast-enhanced (ICE-DICE) MRI: a novel dynamic contrast-enhanced technique for cerebral tumors. Magn Reson Med 68:452–462
Liao W, Liu Y, Wang X et al (2009) Differentiation of primary central nervous system lymphoma and high-grade glioma with dynamic susceptibility contrast—enhanced perfusion magnetic resonance imaging. Acta Radiol 50:217–225
Lu H, Law M, Johnson G et al (2005) Novel approach to the measurement of absolute cerebral blood volume using vascularspace-occupancy magnetic resonance imaging. Magn Reson Med 54:1403–1411
Luh WM, Wong EC, Bandettini PA et al (1999) QUIPSS II with thinslice TI1 periodic saturation: a method for improving accuracy of quantitative perfusion imaging using pulsed arterial spin labeling. Magn Reson Med 41:1246–1254
Lupo JM, Cha S, Chang SM et al (2005) Dynamic susceptibility-weighted perfusion imaging of high-grade gliomas: characterization of spatial heterogeneity. Am J Neuroradiol 26:1446–1454
Majchrzak K, Kaspera W, Bobek-Billewicz B et al (2012) The assessment of prognostic factors in surgical treatment of low-grade gliomas: a prospective study. Clin Neurol Neurosurg 114:1135–1144
Mani S, Pauly J, Conolly S et al (1997) Background suppression with multiple inversion recovery nulling: applications to projective angiography. Magn Reson Med 37:898–905
McGehee BE, Pollock JM, Maldjian JA (2012) Brain perfusion imaging: how does it work and what should I use? J Magn Reson Imaging 36:1257
McLaughlin AC, Ye FQ, Pekar JJ et al (1997) Effect of magnetization transfer on the measurement of cerebral blood flow using steady-state arterial spin tagging approaches: a theoretical investigation. Magn Reson Med 37:501–510
Meier P, Zierler KL (1954) On the theory of the indicator-dilution method for measurement of blood flow and volume. J Appl Physiol 6:731–744
Mills SJ, Thompson G, Jackson A (2012) Advanced magnetic resonance imaging biomarkers of cerebral metastases. Cancer Imaging 12:245–252
Miyati T, Banno T, Mase M et al (1997) Dual dynamic contrast-enhanced MR imaging. J Magn Reson Imaging 7:230–235
O'Connor JP, Jackson A, Parker GJ et al (2007) DCE-MRI biomarkers in the clinical evaluation of antiangiogenic and vascular disrupting agents. Br J Cancer 96:189–195
Ostergaard L (2004) Cerebral perfusion imaging by bolus tracking. Top Magn Reson Imaging 15:3–9
Ostergaard L (2005) Principles of cerebral perfusion imaging by bolus tracking. J Magn Reson Imaging 22:710–717
Ostergaard L, Sorensen AG, Kwong KK et al (1996a) High resolution measurement of cerebral blood flow using intravascular tracer bolus passages. Part II: experimental comparison and preliminary results. Magn Reson Med 36:726–736
Ostergaard L, Weisskoff RM, Chesler DA et al (1996b) High resolution measurement of cerebral blood flow using intravascular tracer bolus passages. Part I: mathematical approach and statistical analysis. Magn Reson Med 36:715–725
Ostergaard L, Hochberg FH, Rabinov JD et al (1999) Early changes measured by magnetic resonance imaging in cerebral blood flow, blood volume, and blood-brain barrier permeability following dexamethasone treatment in patients with brain tumors. J Neurosurg 90:300–305
Paiva FF, Tannus A, Silva AC (2007) Measurement of cerebral perfusion territories using arterial spin labelling. NMR Biomed 20:633–642
Paiva FF, Tannus A, Talagala SL et al (2008) Arterial spin labeling of cerebral perfusion territories using a separate labeling coil. J Magn Reson Imaging 27:970–977
Parkes LM (2005) Quantification of cerebral perfusion using arterial spin labeling: two-compartment models. J Magn Reson Imaging 22:732–736
Parkes LM, Tofts PS (2002) Improved accuracy of human cerebral blood perfusion measurements using arterial spin labeling: accounting for capillary water permeability. Magn Reson Med 48:27–41
Paulson ES, Schmainda KM (2008) Comparison of dynamic susceptibility-weighted contrast-enhanced MR methods: recommendations for measuring relative cerebral blood volume in brain tumors. Radiology 249:601–613
Pekar J, Jezzard P, Roberts DA et al (1996) Perfusion imaging with compensation for asymmetric magnetization transfer effects. Magn Reson Med 35:70–79
Perfusion Study Group ISMRM (2013) http://www.ismrm.org/12/SG/Perfusion_Motion.htm
Petersen ET, Zimine I, Ho YC et al (2006a) Non-invasive measurement of perfusion: a critical review of arterial spin labelling techniques. Br J Radiol 79:688–701
Petersen ET, Lim T, Golay X (2006b) Model-free arterial spin labeling quantification approach for perfusion MRI. Magn Reson Med 55:219–232
Petersen ET, Mouridsen K, Golay X (2010) The QUASAR reproducibility study, Part II: results from a multi-center arterial spin labeling test-retest study. Neuroimage 49:104–113
Pradel C, Siauve N, Bruneteau G et al (2003) Reduced capillary perfusion and permeability in human tumour xenografts treated with the VEGF signalling inhibitor ZD4190: an in vivo assessment using dynamic MR imaging and macromolecular contrast media. Magn Reson Imaging 21:845–851
Preibisch C, Deichmann R (2009) Influence of RF spoiling on the stability and accuracy of T1 mapping based on spoiled FLASH with varying flip angles. Magn Reson Med 61:125–135
Quarles CC, Ward BD, Schmainda KM (2005) Improving the reliability of obtaining tumor hemodynamic parameters in the presence of contrast agent extravasation. Magn Reson Med 53:1307–1316
Quarles CC, Gochberg DF, Gore JC et al (2009) A theoretical framework to model DSC-MRI data acquired in the presence of contrast agent extravasation. Phys Med Biol 54:5749–5766
Raichle ME, Martin WR, Herscovitch P et al (1983) Brain blood flow measured with intravenous H2(15)O. II. Implementation and validation. J Nucl Med 24:790–798
Roberts C, Issa B, Stone A et al (2006) Comparative study into the robustness of compartmental modeling and model-free analysis in DCE-MRI studies. J Magn Reson Imaging 23:554–563
Rosen BR, Belliveau JW, Vevea JM et al (1990) Perfusion imaging with NMR contrast agents. Magn Reson Med 14:249–265

Roy B, Gupta RK, Maudsley AA et al (2013) Utility of multiparametric 3-T MRI for glioma characterization. Neuroradiology 55:603–613
Sanz-Requena R, Revert-Ventura A, Martí-Bonmatí L et al (2013) Quantitative MR perfusion parameters related to survival time in high-grade gliomas. Eur Radiol 23(12):3456–3465
Schmainda KM, Rand SD, Joseph AM et al (2004) Characterization of a first-pass gradient-echo spin-echo method to predict brain tumor grade and angiogenesis. Am J Neuroradiol 25:1524–1532
Schwarzbauer C, Morrissey SP, Deichmann R et al (1997) Quantitative magnetic resonance imaging of capillary water permeability and regional blood volume with an intravascular MR contrast agent. Magn Reson Med 37:769–777
Shen Q, Duong TQ (2011) Background suppression in arterial spin labeling MRI with a separate neck labeling coil. NMR Biomed 24:1111–1118
Shin JH, Lee HK, Kwun BD et al (2002) Using relative cerebral blood flow and volume to evaluate the histopathologic grade of cerebral gliomas: preliminary results. Am J Roentgenol 179:783–789
Silva AC, Kim SG (1999) Pseudo-continuous arterial spin labeling technique for measuring CBF dynamics with high temporal resolution. Magn Reson Med 42:425–429
Smith JS, Cha S, Mayo MC et al (2005) Serial diffusion-weighted magnetic resonance imaging in cases of glioma: distinguishing tumor recurrence from postresection injury. J Neurosurg 103:428–438
Soda Y, Myskiw C, Rommel A et al (2013) Mechanisms of neovascularization and resistance to anti-angiogenic therapies in glioblastoma multiforme. J Mol Med (Berl) 91:439–448
Sourbron S (2010) Technical aspects of MR perfusion. Eur J Radiol 76:304–313
Sourbron SP, Buckley DL (2011) On the scope and interpretation of the Tofts models for DCE-MRI. Magn Reson Med 66:735–745
Sourbron SP, Buckley DL (2012) Tracer kinetic modelling in MRI: estimating perfusion and capillary permeability. Phys Med Biol 57:R1–R33
Sourbron SP, Buckley DL (2013) Classic models for dynamic contrast-enhanced MRI. NMR Biomed 26:1004–1027
Sourbron S, Ingrisch M, Siefert A et al (2009) Quantification of cerebral blood flow, cerebral blood volume, and blood–brain-barrier leakage with DCE-MRI. Magn Reson Med 62:205–217
Speck O, Chang L, DeSilva NM et al (2000) Perfusion MRI of the human brain with dynamic susceptibility contrast: gradient-echo versus spin-echo techniques. J Magn Reson Imaging 12:381–387
St Lawrence KS, Wang J (2005) Effects of the apparent transverse relaxation time on cerebral blood flow measurements obtained by arterial spin labeling. Magn Reson Med 53:425–433
Stewart GN (1894) Researches on the circulation time in organs and on the influences which affect it. Parts I–III. J Physiol 15:1–89
Sugahara T, Korogi Y, Tomiguchi S et al (2000) Posttherapeutic intraaxial brain tumor: the value of perfusion-sensitive contrast-enhanced MR imaging for differentiating tumor recurrence from nonneoplastic contrast-enhancing tissue. Am J Neuroradiol 21:901–909
Sundgren PC, Cao Y (2009) Brain irradiation: effects on normal brain parenchyma and radiation injury. Neuroimaging Clin N Am 19:657–668
Talagala SL, Ye FQ, Ledden PJ et al (2004) Whole-brain 3D perfusion MRI at 3.0 T using CASL with a separate labeling coil. Magn Reson Med 52:131–140
Ter-Pogossian MM, Herscovitch P (1985) Radioactive oxygen-15 in the study of cerebral blood flow, blood volume, and oxygen metabolism. Semin Nucl Med 15:377–394
Tofts PS (1997) Modeling tracer kinetics in dynamic Gd-DTPA MR imaging. J Magn Reson Imaging 7:91–101
Tofts PS, Kermode AG (1991) Measurement of the blood-brain barrier permeability and leakage space using dynamic MR imaging. 1. Fundamental concepts. Magn Reson Med 17:357–367
Tofts PS, Brix G, Buckley DL et al (1999) Estimating kinetic parameters from dynamic contrast-enhanced T(1)-weighted MRI of a diffusable tracer: standardized quantities and symbols. J Magn Reson Imaging 10:223–232
Turner R, Le Bihan D, Chesnick AS (1991) Echo-planar imaging of diffusion and perfusion. Magn Reson Med 19:247–253
Uematsu H, Maeda M (2006) Double-echo perfusion-weighted MR imaging: basic concepts and application in brain tumors for the assessment of tumor blood volume and vascular permeability. Eur Radiol 16:180–186
Uematsu H, Maeda M, Sadato N et al (2000) Vascular permeability: quantitative measurement with double-echo dynamic MR imagingtheory and clinical application. Radiology 214: 912–917
van Laar PJ, van der Grond J, Hendrikse J (2008) Brain perfusion territory imaging: methods and clinical applications of selective arterial spin-labeling MR imaging. Radiology 246:354–364
Varallyay CG, Nesbit E, Fu R et al (2013) High-resolution steady-state cerebral blood volume maps in patients with central nervous system neoplasms using ferumoxytol, a superparamagnetic iron oxide nanoparticle. J Cereb Blood Flow Metab 33:780–786
Vidiri A, Pace A, Fabi A et al (2012) Early perfusion changes in patients with recurrent high-grade brain tumor treated with Bevacizumab: preliminary results by a quantitative evaluation. J Exp Clin Cancer Res 31:33
Villringer A, Rosen BR, Belliveau JW et al (1988) Dynamic imaging with lanthanide chelates in normal brain: contrast due to magnetic susceptibility effects. Magn Reson Med 6:164–174
Vonken EP, van Osch MJ, Bakker CJ et al (2000) Simultaneous quantitative cerebral perfusion and Gd-DTPA extravasation measurement with dual-echo dynamic susceptibility contrast MRI. Magn Reson Med 43:820–827
Wagner M, Nafe R, Jurcoane A et al (2011) Heterogeneity in malignant gliomas: a magnetic resonance analysis of spatial distribution of metabolite changes and regional blood volume. J Neurooncol 103:663–672
Wang J, Qiu M, Constable RT (2005) In vivo method for correcting transmit/receive nonuniformities with phased array coils. Magn Reson Med 53:666–674
Warmuth C, Gunther M, Zimmer C (2003) Quantification of blood flow in brain tumors: comparison of arterial spin labeling and dynamic susceptibility-weighted contrast-enhanced MR imaging. Radiology 228:523–532
Wen PY, Macdonald DR, Reardon DA et al (2010) Updated response assessment criteria for high-grade gliomas: response assessment in neuro-oncology working group. J Clin Oncol 28:1963–1972
Williams DS (2006) Quantitative perfusion imaging using arterial spin labeling. Methods Mol Med 124:151–173
Wirestam R, Knutsson L, Risberg J et al (2007) Attempts to improve absolute quantification of cerebral blood flow in dynamic susceptibility contrast magnetic resonance imaging: a simplified T1-weighted steady-state cerebral blood volume approach. Acta Radiol 48:550–556
Wong EC, Buxton RB, Frank LR (1997) Implementation of quantitative perfusion imaging techniques for functional brain mapping using pulsed arterial spin labeling. NMR Biomed 10:237–249
Wong EC, Buxton RB, Frank LR (1998) Quantitative imaging of perfusion using a single subtraction (QUIPSS and QUIPSS II). Magn Reson Med 39:702–708

Wu WC, Fernandez-Seara M, Detre JA et al (2007) A theoretical and experimental investigation of the tagging efficiency of pseudocontinuous arterial spin labeling. Magn Reson Med 58:1020–1027

Wu WC, St Lawrence KS, Licht DJ et al (2010) Quantification issues in arterial spin labeling perfusion magnetic resonance imaging. Top Magn Reson Imaging 21:65–73

Yankeelov TE, Gore JC (2009) Dynamic contrast enhanced magnetic resonance imaging in oncology: theory, data acquisition, analysis, and examples. Curr Med Imaging Rev 3:91–107

Yankeelov TE, Rooney WD, Li X et al (2003) Variation of the relaxographic "shutter-speed" for transcytolemmal water exchange affects the CR bolus-tracking curve shape. Magn Reson Med 50:1151–1169

Ye FQ, Frank JA, Weinberger DR et al (2000) Noise reduction in 3D perfusion imaging by attenuating the static signal in arterial spin tagging (ASSIST). Magn Reson Med 44:92–100

Zacharaki EI, Wang S, Chawla S et al (2009) Classification of brain tumor type and grade using MRI texture and shape in a machine learning scheme. Magn Reson Med 62:1609–1618

Zhang W, Williams DS, Detre JA et al (1992) Measurement of brain perfusion by volume-localized NMR spectroscopy using inversion of arterial water spins: accounting for transit time and cross-relaxation. Magn Reson Med 25:362–371

Zhang W, Williams DS, Koretsky AP (1993) Measurement of rat brain perfusion by NMR using spin labeling of arterial water: in vivo determination of the degree of spin labeling. Magn Reson Med 29:416–421

Zhang N, Zhang L, Qiu B et al (2012) Correlation of volume transfer coefficient K trans with histopathologic grades of gliomas. J Magn Reson Imaging 36:355–363

Zhu DC, Penn RD (2005) Full-brain T1 mapping through inversion recovery fast spin echo imaging with time-efficient slice ordering. Magn Reson Med 54:725–731

Diffusion-Weighted Methods

Peter Raab and Heinrich Lanfermann

Contents

P. Raab, MD (✉) • H. Lanfermann, MD, PhD
Institute of Diagnostic and Interventional Neuroradiology, Hannover Medical School, Carl-Neuberg-Str. 1, Hannover 30625, Germany
e-mail: raab.peter@mh-hannover.de; Lanfermann.Heinrich@MH-Hannover.de

Abstract

During the last two decades the technical advancements of Diffusion Weighted Imaging have enabled the precise and repeatable characterization of brain tumor microstructure non-invasively, mainly by the use of the apparent diffusion coefficient (ADC) as a biomarker. This has led to many applications aiding in tumor grading, prognosis assessment and treatment monitoring.

Diffusion-weighted imaging (DWI) has been widely investigated for tumor imaging to localize a tumor, to estimate its borders, and to discriminate nonneoplastic masses from proliferating tumors or tumor types and grades. Further DWI was used for the separation of tumor infiltration from reversible edematous tissue changes, the detection of white matter tracts for surgical planning and postsurgical controls, the monitoring of radiation or drug therapy response of tumors, and the separation of recurrent tumor from radiation necrosis (Field and Alexander 2004). Diffusion-weighted imaging contributes pathophysiological as well as microstructural information and is therefore another piece in the puzzle of the whole picture of a brain tumor.

1 Methods

Diffusion is a natural molecular transport mechanism caused by thermal energy, leading to perpetual random mixing of molecules. In biological systems this thermal motion, which is described by Brown's law (Brown 1828), is dominating over diffusion caused by concentration differences being described by Fick's first law (Fick 1855). In water, as an example of a free medium, this random mixing of molecules leads to a three-dimensional Gaussian displacement distribution of the molecules (Le Bihan 1995; Basser and Özarslan 2009; Le Bihan and Johansen-Berg 2012). During a given amount of

E. Hattingen, U. Pilatus (eds.), *Brain Tumor Imaging*,
Med Radiol Diagn Imaging (2016)
DOI: 10.1007/174_2016_1052, © Springer Berlin Heidelberg

time, the molecules can randomly travel a certain distance, which is best described by the diffusion coefficient "D":

$$\langle X^2 \rangle = 2DT_d$$

X^2 – average mean-squared diffusion distance along one direction
D – diffusion coefficient
T_d – diffusion time (adopted from Le Bihan and Johansen-Berg 2012)

The diffusion coefficient is dependent on the medium and its viscosity, the size of the diffusing molecule, and the temperature. In biological systems, the microstructural features of the environment also influence the diffusion coefficient, leading to a non-Gaussian displacement distribution. Compared to free water, the diffusion coefficient is reduced in biological tissues due to the interaction of the molecules with cells, cell membranes, fibers, or macromolecules (Le Bihan and Johansen-Berg 2012). During a short diffusion time, the diffusion coefficient is mainly influenced by the viscosity of the medium, and at longer diffusion times the effect of the microstructure becomes more important. This is the main effect for MR diffusion imaging given the typical MR diffusion sequences and their parameters. Although the typical MR image resolution is in the mm scale, the underlying diffusion characteristics caused by the interaction of macromolecules with tissue microstructure are in the μm scale. Therefore, diffusion-weighted imaging provides clues about microstructure and geometric organization of healthy as well as pathologically altered tissues.

The basics for nowadays DWI methods were laid down by Purcell and Carr (Purcell et al. 1946; Carr and Purcell 1954), Hahn (1950) as well as Stejskal and Tanner (1965). One of the first diffusion-weighted human brain images was published in 1986 by LeBihan et al. (1986). The sequences used today still rely mainly on the pulsed field gradient (PFG) method. This method uses gradients for labeling space along a certain direction and time and sensitizes the MR signal to molecule/proton displacement. Molecule displacement leads to signal attenuation, A, which is linked to the diffusion coefficient, D, by

$$A = \exp(-bD)$$

b represents the so-called b-factor, which is a function of timing, amplitude, and length of the diffusion gradients (Le Bihan and Johansen-Berg 2012; Le Bihan et al. 1986). The degree of diffusion weighting can be set by the value of b, and higher b-values lead to increased diffusion weighting. A b-value of zero leads to an image without diffusion encoding. In order to get quantitative diffusion images, one has to acquire images without and with diffusion encoding (b_0 and b) and calculate D based on the equation mentioned before. A typical b-value for the brain is 1,000 s/mm^2. It is advisable as well to acquire diffusion-weighted images with at least three different direction encodings in order to get so-called combined "trace" DW images and an *apparent diffusion coefficient* (ADC) being independent of the head orientation in the scanner. The trace is the sum of the three orthogonal diffusion coefficients; the orientationally averaged *mean diffusivity* (MD) can be thought of trace/3 (Jones 2009). LeBihan introduced the global statistical parameter of apparent diffusion coefficient in 1986 since the MR imaging scale is much bigger than the microscopic diffusion scale and since the estimation of the real diffusion coefficient D and diffusion process is challenging and the diffusion coefficient in biological tissues appears to be smaller than in free water (Le Bihan et al. 1986).

The preferred sequence type for DWI is single-shot echo planar imaging, which is robust in spite of artificial head motion and allows for rapid acquisition. On the downside this sequence type is susceptible to magnetic field distortions leading to geometric warping, eddy currents, and ghosting artifacts leading to geometric warping as well (Jones and Cercignani 2010; Pipe 2009) and intravoxel dephasing effects on image resolution, which have to be accounted for in data analysis. The distortions and artifacts are most pronounced at the skull base and close to tissue calcifications and hemorrhages. Recent developments of DW sequences led to reduced distortions and better image quality (e.g., Maier et al. 1998; Bammer 2003).

A more detailed characterization of the diffusion process can be realized with at least six different diffusion direction encodings allowing for the calculation of the diffusion *fractional anisotropy* (FA) and eigenvalues (Basser 1995; Basser and Pierpaoli 1996; Chenevert et al. 1990, 2006). The diffusion tensor means a mathematical 3D model of the diffusion in space, being represented by an ellipsoid whose dimensions are given by the eigenvalues and estimate the diffusivity in the respective direction. Diffusion anisotropy is a unit-less number and represents the amount of diffusion directionality within one voxel; its value ranges between zero and one (see Fig. 1). Anisotropy in the brain is mainly dependent on the organization of white matter in bundles of differently myelinated axon fibers with parallel orientation, and the diffusion speed along the fiber axis is faster compared to a perpendicular direction by a factor of 3–6x for myelinated fibers (Le Bihan and Johansen-Berg 2012). Information about diffusion anisotropy and eigenvalues is part of *diffusion tensor imaging* (DTI) and can be transferred into tractography (Basser et al. 1994; Le Bihan and van Zijl 2002), which allows for the reconstruction of primary diffusion directions representing white matter fiber tracts (Lazar 2010). Basis for this tensor calculation is a mathematical model, which assumes a 3D Gaussian diffusion in a voxel and a monoexponential signal decay during the diffusion

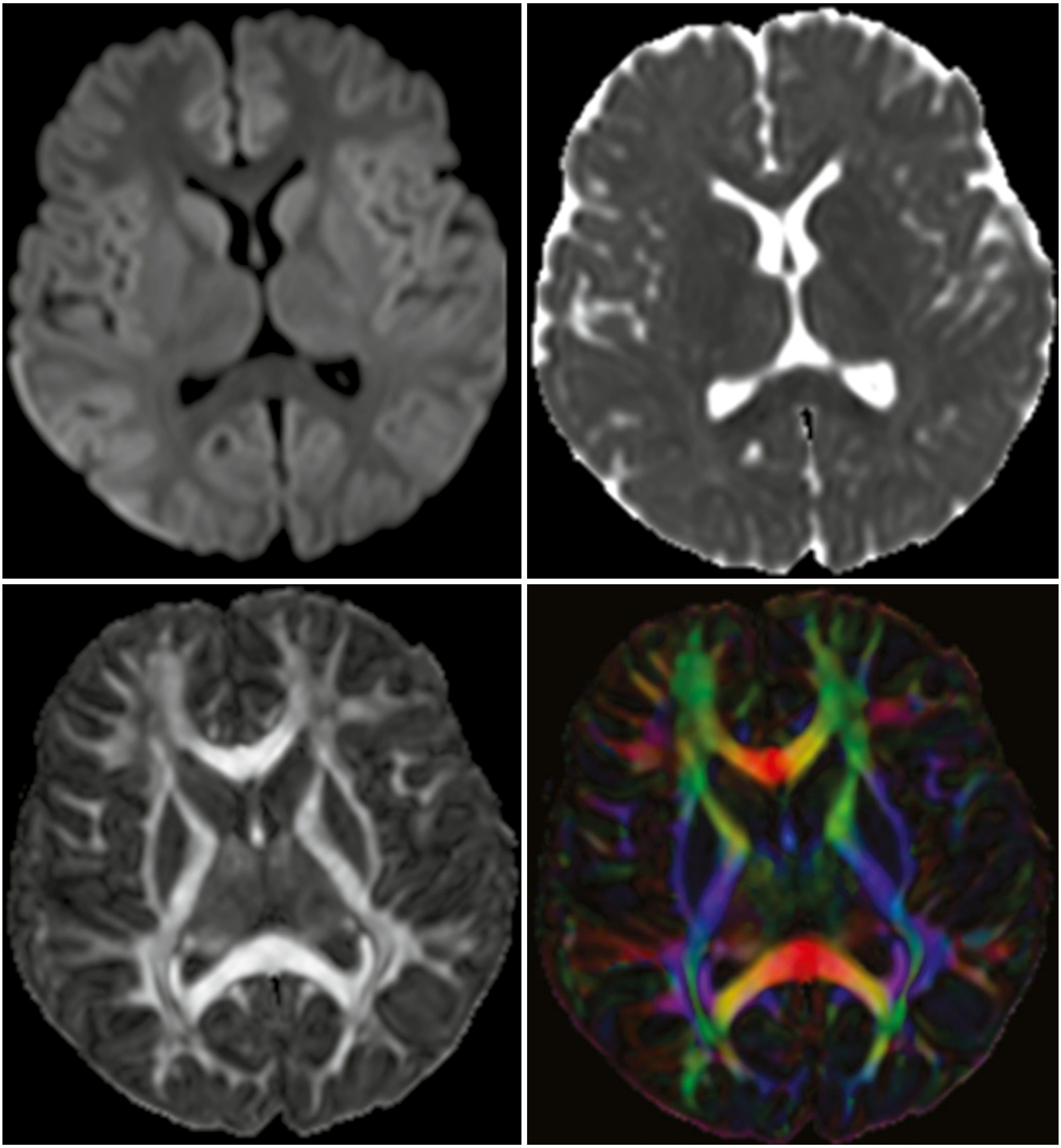

Fig. 1 Normal diffusion-weighted image ($b = 1{,}000$ s/mm^2) of a 6-year-old child (*top left*). Typical ADC images (*top right*). Parameter map of fractional anisotropy (FA) as intensity map (*bottom left*); high intensity indicates high anisotropy like in the corpus callosum. Color-coded FA parameter map; the colors indicate the main diffusion direction within the voxel (*red* right to left, *green* anterior to posterior, *blue* cranial to caudal). Color mixtures are possible depending on the diffusion direction

experiment, both of which are not always true in biological tissues. Nonetheless, DTI and tractography are widely used, and they have proved to be helpful in understanding normal brain structure as well as in detecting changes caused by various diseases.

Recent developments introduced a new diffusion metric called *diffusion kurtosis imaging* (DKI), which can be calculated from data with at least 15 direction encodings and 2 non-zero *b*-values (Jensen et al. 2005; Lu et al. 2006; Tabesh et al. 2010). DKI describes the non-Gaussian water movement in biological tissues and can be interpreted as quantitative characterization of microstructural tissue complexity. It is a model-free approach to diffusion characterization.

By the use of an extended *b*-factor range of up to 5,000 s/mm^2 without calculation of the kurtosis, one can also analyze the non-monoexponential diffusion-related signal decay (Maier et al. 2010; Mulkern et al. 2009). This approach is also not yet part of routine imaging due to increased scanning times, a rather difficult mathematical fitting of the data and debatable models and assumptions; so is the mathematical basis only valid for a single diffusion-encoding direction. This approach assumes that there are slow and fast diffusing water pools within the tissue with slow and fast diffusion coefficients, respectively. This method cannot be used widely in anisotropic tissues, but usually the anisotropy in the core of brain neoplasms is rather low (Maier et al. 2010). Following this idea one can try to explain differences of ADC values between different tumors, for instance, by different slow or fast diffusing water pool sizes, thereby supposing that slow diffusing water molecules are closely located to proteins or cellular membranes inside of the cells.

Diffusion-weighted imaging can also be used for an estimation of tissue perfusion. Already early during the development of diffusion-weighted imaging, LeBihan and colleagues described an influence of the microcirculation on the diffusion-weighted signal attenuation (Le Bihan et al. 1986). *Intravoxel incoherent motion* (IVIM) caused by blood flow within capillary vessels leads to a distribution of phases during the influence of magnetic field gradients; this phase distribution then leads to signal attenuation of the voxel. The IVIM effect can be observed at *b*-values below 300 s/mm^2 and is still under investigation (Le Bihan 2012; Federau and O'Brien 2015).

In 2009 a consensus report summarized the recommendations for using diffusion-weighted imaging as a *cancer biomarker* (Padhani et al. 2009).

Therefore, DWI sequences should be part of standard MR examination in patients with cerebral masses and in patients under treatment of a brain tumor.

2 Microstructural Changes

Two distinct compartments are in the brain based on their main diffusion characteristics, which influence quantitative comparisons. The anisotropic compartment and its microstructure is mainly accounted for by the white matter contents, which are densely packed axons with their myelin sheets, the macroglia consisting of oligodendrocytes and astrocytes, and the microglia. Intracellular neurofilaments and microtubules with their associated axonal transport mechanisms might also contribute to diffusion characteristics (Beaulieu 2009), although in vitro experiments question this (Beaulieu and Allen 1994a, b; Takahashi et al. 2002). In gray matter as the more isotropic compartment, the neurons and their directionally varying connections, tangles of dendrites, axon endings, and glial cell processes are the basic determining components for the microstructure. Mean diffusivity is very similar in white and gray matter, although the anisotropy is varying greatly among these tissue types. Even within the normal white matter, FA values as the measure of anisotropy vary depending on the tissue composition, being influenced by the number of axons, axon density and size, packing, myelin thickness, and amount of crossing fibers (Pierpaoli et al. 1996). Typical *ADC values* for normal white matter are about 0.7 μm/ms^2 (Maier et al. 1998) and for deep gray matter about 0.75 μm/ms^2 (Helenius et al. 2002), and these values are valid for a *b*-value of 1,000 s^2/mm. Besides this also MR acquisition parameters (e.g., *b*-value, diffusion time, SNR, matrix) influence the calculated diffusion parameters.

Based on this it is not possible to compare one tract in the brain with another and to infer the myelin thickness or number of axons from diffusion values, for instance (Beaulieu 2009). However, if one compares diffusional characteristics longitudinally or specific tracts and brain structures between patients and controls, interpretations can become possible.

Tumors can have several effects on the surrounding tissues leading to microstructural changes. They can cause (1) dislocation of normal structures, (2) infiltration of adjacent tissue, (3) destruction of neighboring structures like white matter tracts, or (4) edema formation (Maier et al. 2010); in reality one can find a mixed pattern with no clear differentiation between these effects. Tumors itself differ from each other with respect to cellularity, microstructural complexity, amount of necrosis, and vascularity.

ADC values of brain tumors span a broad range from about $0.6*10^{-3}$ mm^2/s in case of medulloblastomas to about $2.5*10^{-3}$ mm^2/s in case of dysembryoplastic neuroectodermal tumors (Yamasaki et al. 2005). In most tumors, the ADC values are reported to be higher than ADC values of normal brain tissue, indicating microstructural differences between the two. Due to peritumoral edema with ADC values of about 1.3 mm^2/s, it can be difficult to determine the tumor border by ADC values alone. The *tumor-infiltrated edema* surrounding gliomas has been the focus of several investigators, trying to find differences from pure vasogenic edema surrounding meningiomas or metastases (Kono et al. 2001; Provenzale et al. 2004; Pavlisa et al. 2009; Lee et al. 2011). Kono et al. (2001) as well as Provenzale et al. (2004) found no significant ADC differences in the peritumoral edema of glioblastomas and meningiomas, whereas Lee et al. (2011) found a higher minimum ADC around glioblastomas compared to metastases. When using FA as the diffusion marker, the results were differing. Provenzale found lower *peritumoral FA* values in gliomas compared to meningiomas, while no difference was found in studies comparing FA values around gliomas and metastases (Lu et al. (2003, 2004) and Tsuchiya et al. (2005)). In 2004 the group of Lu et al. (2004) introduced a "tumor infiltration index," which they found to be helpful in differentiating edema around metastases, meningiomas, and gliomas. Based on the varying results, the detection of infiltrated edema based on ADC and FA values remains a challenge. Price et al. used diffusion tensor imaging for their approach to delineate glioma margins (Price et al. 2006). They employed an analysis method that separates the diffusion tensor into the isotropic and anisotropic components, and they reported the successful identification of the infiltrating glioma margins with high sensitivity and specificity (98 and 81 %, respectively).

3 Tumor Grading, Typing, and Heterogeneity

The gold standard of tumor grading nowadays is still the histopathological evaluation under the microscope of tissue characteristics like cell density, tissue architecture with cell arrangement, cellular atypia in size and shape and changes of the nucleus, as well as occurrence of microvessel proliferations and necrosis. Recently, genetic molecular profiling of brain tumors gained more interest, because important genetic alterations might be without histomorphological counterparts.

Diffusion-weighted imaging has the advantage of a more complete sampling of information of the whole tumor by probing the water diffusion over distances corresponding to cell sizes. In many studies an inverse relationship between ADC values and tumor grading has been described (Alvarez-Linera et al. 2008; Arvinda et al. 2009; Bai et al. 2011; Bulakbasi et al. 2004; Poretti et al. 2013), thereby also indicating an inverse relationship between ADC values and tumor cellularity – tumors with low grade tend to show higher ADC values, and higher-grade tumors tend to have lower ADC values in their solid parts. Such a relation was also shown for cerebral lymphomas and high-grade gliomas (Guo et al. 2002); in this ROI-based study, lower mean ADC values were found in lymphomas compared to high-grade gliomas. An explanation for this inverse relationship could be that the amount of membranes, which are obstacles to free diffusion, is increased with increasing cellularity. Maier et al. (2010) pointed out that within a certain tumor type also intracellular membranes like the endoplasmic reticulum can have an effect on the diffusion coefficient, and schwannomas with their high cellularity but surprisingly high average ADC values were used by him as a counterexample. Low ADC values of highly cellular tumors could be caused by an increased fraction of slowly diffusing water pools within the tumor according to the fast and slow pool theory. Low-grade tumors might have a higher water content inside or between cells, so one has to consider other mechanisms like protein/water interactions as well besides cellular membranes being obstacles to diffusion. Alvarez-Linera et al. found increased DWI signals on high *b*-value images ($b = 3{,}000$ s/mm^2) in high-grade gliomas, while the majority of the low-grade gliomas in their study group showed no areas of increased signal intensity (Alvarez-Linera et al. 2008). Increasing the *b*-value reduces the amount of the T2 shine-through leading to a higher conspicuity of tissues with restricted diffusion.

Using the recent development method of diffusion kurtosis imaging (Jensen et al. 2005; Jensen and Helpern 2003, 2010), we could show that kurtosis metrics were superior to diffusivity values in separating glioma grades, especially also WHO grades II and III (Raab et al. 2010). Van Cauter et al. confirmed our findings (Van Cauter et al. 2012).

It is well known that brain tumors can be very inhomogeneous, making a decision, for instance, on the site of biopsy difficult. DWI can quickly cover the whole tumor and is able to show inhomogeneous tissue areas (see Fig. 2).

Apart from grading of gliomas, the characterization of different brain tumors and their subtypes has also been investigated with diffusion-weighted imaging. The discrimination between metastases and glioblastomas and especially the differential diagnosis of a single rim enhancing and centrally necrotic tumors can be difficult on standard MR imaging, since a cerebral abscess and hemorrhage can mimic these two tumor types based on standard imaging.

Early work already could demonstrate a clear benefit from diffusion-weighted imaging for the identification of an abscess by showing restricted diffusion within the cyst-like cavity of the tumor representing the purulent fluid collection (Desprechins et al. 1999; Ebisu et al. 1996; Toh et al. 2011). One has to keep in mind that acute and subacute hemorrhages can present with reduced ADC values (Atlas et al. 2000; Busch et al. 1998; Ebisu et al. 1997) possibly mimicking a brain abscess in the situation of a hemorrhagic tumor.

For the separation of metastasis from glioblastomas, several studies have shown that lower ADC values in solid tumor parts tend to indicate metastasis (Byrnes et al. 2011), whereas higher peritumoral FA values indicate a glioblastoma (Tsuchiya et al. 2005). Certain tumor types can even be recognized almost only by diffusion-weighted imaging in combination with the tumor location. *Central neurocytomas*

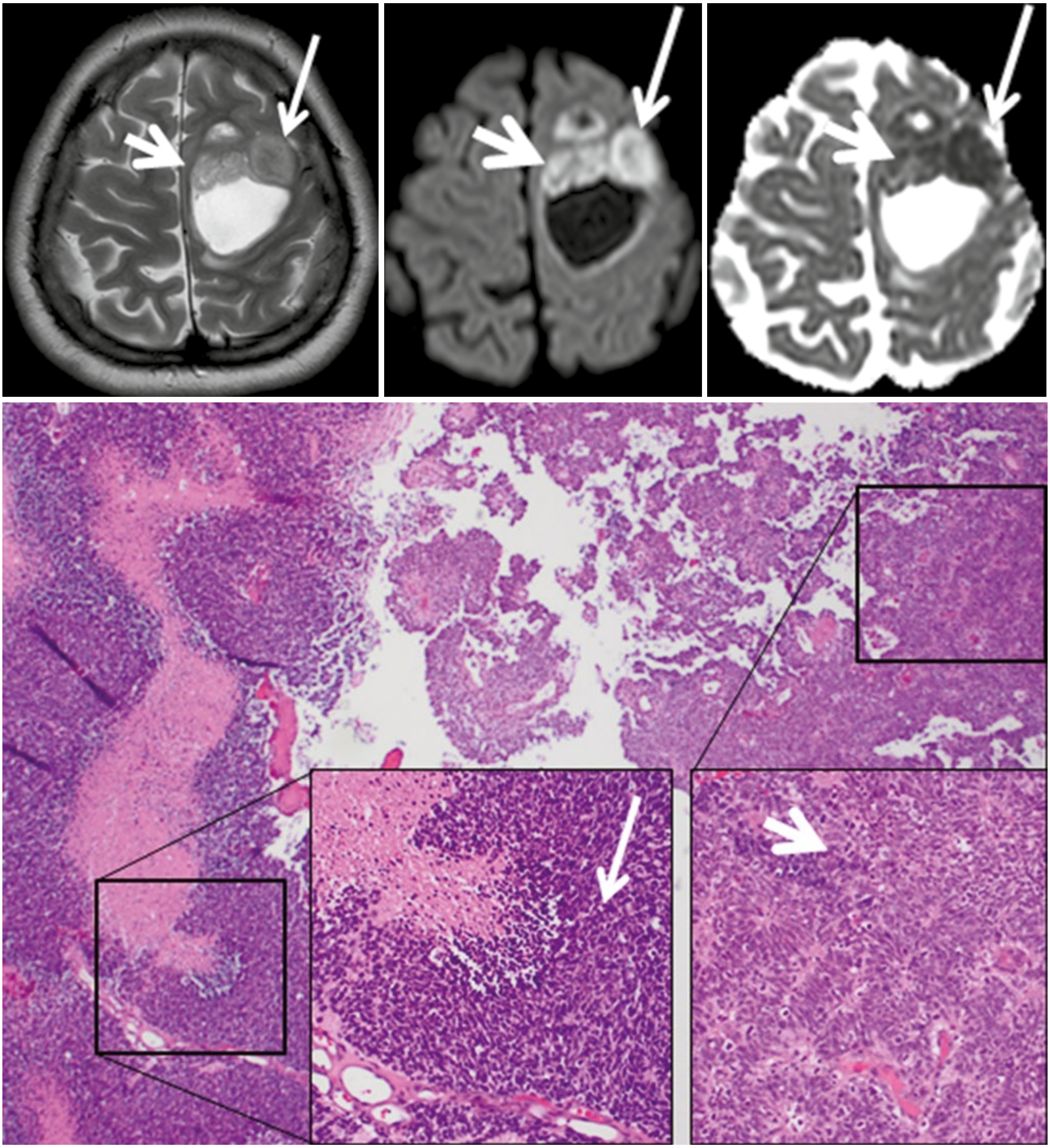

Fig. 2 This tumor was diagnosed as glioblastoma based on molecular genetic as well as histomorphological markers. Histomorphology and DWI imaging reveal the heterogeneity of this tumor. The *smaller thicker arrows* indicate a tumor part with lower cell density and architectural remnants of pseudopalisading, and this area shows almost normal ADC values combined with elevated DWI signal. The *longer thinner arrows* point at an area with very high cellularity, and the cells are positioned closely to each other without an order, and on MRI this corresponds to a nodule with lower T2w signal, strong DWI hyperintensity, and very low ADC values (Histologic images are by courtesy of Prof. F. Feuerhake, Neuropathology, Hannover Medical School, Germany; MR images by courtesy of Dr. Puschmann, Damme)

are typically located close to the foramen of Monroi, and they often show an intermediate T2w signal and may contain small cystic areas. The DWI signal is typically hyperintense with very low ADC values (see Fig. 3 (Kocaoglu et al. 2009; Tlili-Graiess et al. 2014)). Similar diffusion characteristics are found in *medulloblastomas*. This tumor

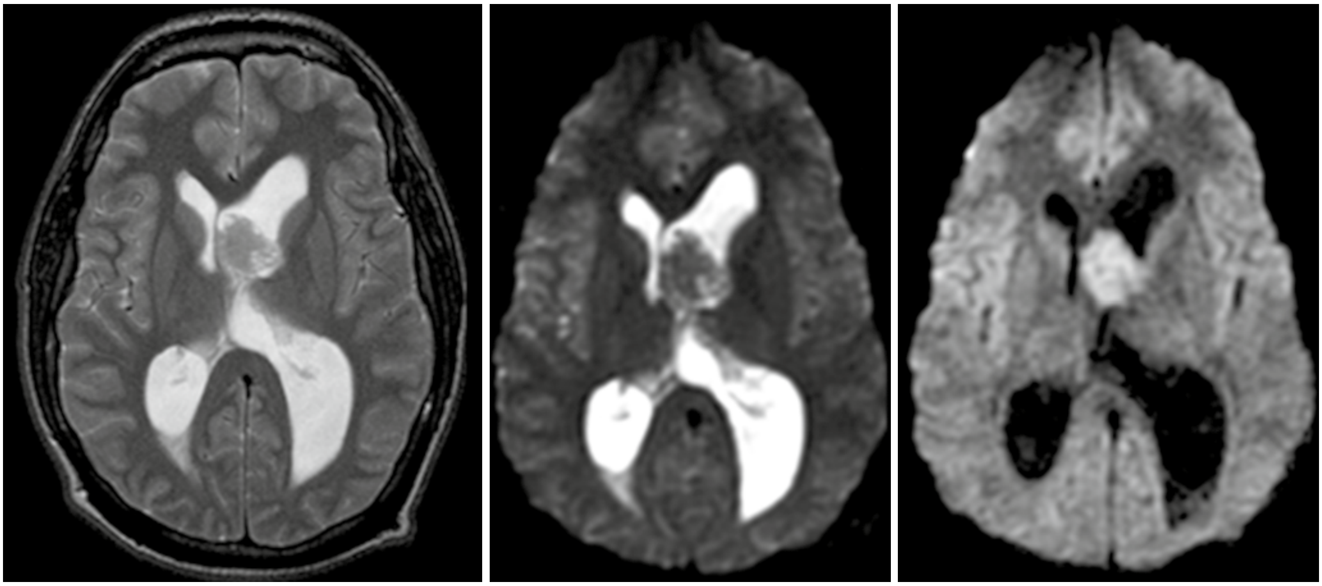

Fig. 3 Central neurocytoma with typical T2w appearance, location, and restricted diffusion

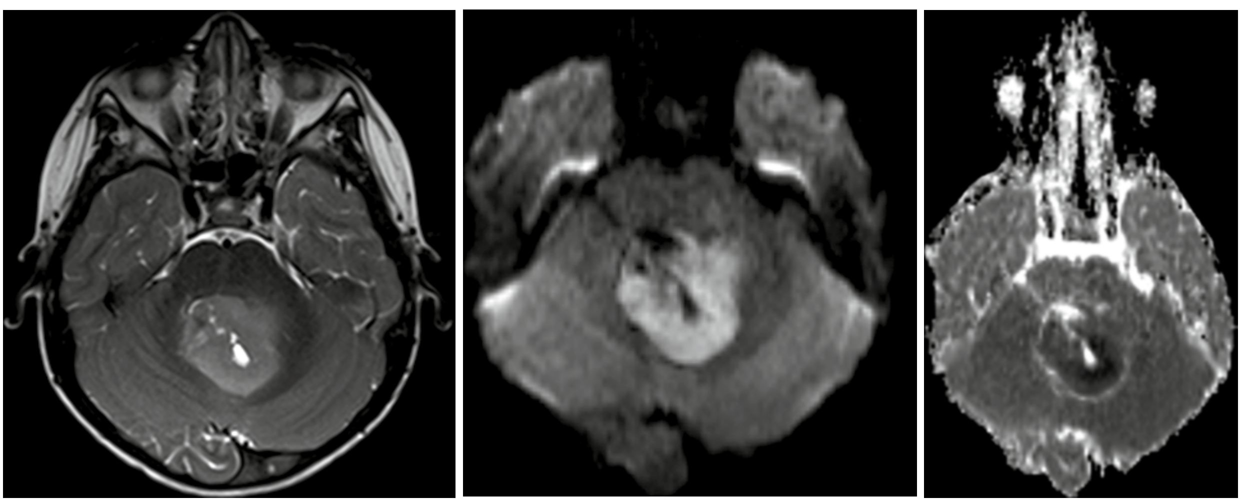

Fig. 4 Typical medulloblastoma of the 4th ventricle with slightly hyperintense T2w signal, strongly elevated DWI signal and very low ADC values in the solid tumor parts (from left to right)

shows the lowest ADC values of pediatric brain tumors in the posterior fossa (Hattingen et al. 2008; Koral et al. 2013; Pierce et al. 2014) (see Fig. 4). Due to this feature, diffusion-weighted imaging is important for follow-up examinations, since even small metastases or recurrent tumors can be recognized by their high diffusion signal. Only the very rare atypical teratoid rhabdoid tumor (*ATRT*) can show the same increased diffusion signal intensity with low ADC values also in the posterior fossa (Koral et al. 2008). The other posterior fossa tumor types show higher ADC values than medulloblastomas, although, for instance, ependymomas might have smaller areas with low ADC values also.

A very typical DWI signal pattern is found in *epidermoid tumors*. They show a very hyperintense diffusion signal combined with CSF-like (cerebrospinal fluid) T2w signal intensity and almost normal parenchymal ADC values (see Fig. 5).

Tumefactive or *tumorlike demyelinating lesions* (TDLs) represent a differential diagnosis to gliomas. Compared to low-grade gliomas that show a homogenous ADC elevation, these TDLs have centrally elevated ADC values surrounded by a rim of low ADC values (see Fig. 6). This rim represents the area of active inflammation, which is surrounded by elevated ADC values due to the surrounding edema (Hyland et al. 2013; Miron et al. 2013; Saini et al. 2011; Yacoub et al. 2011).

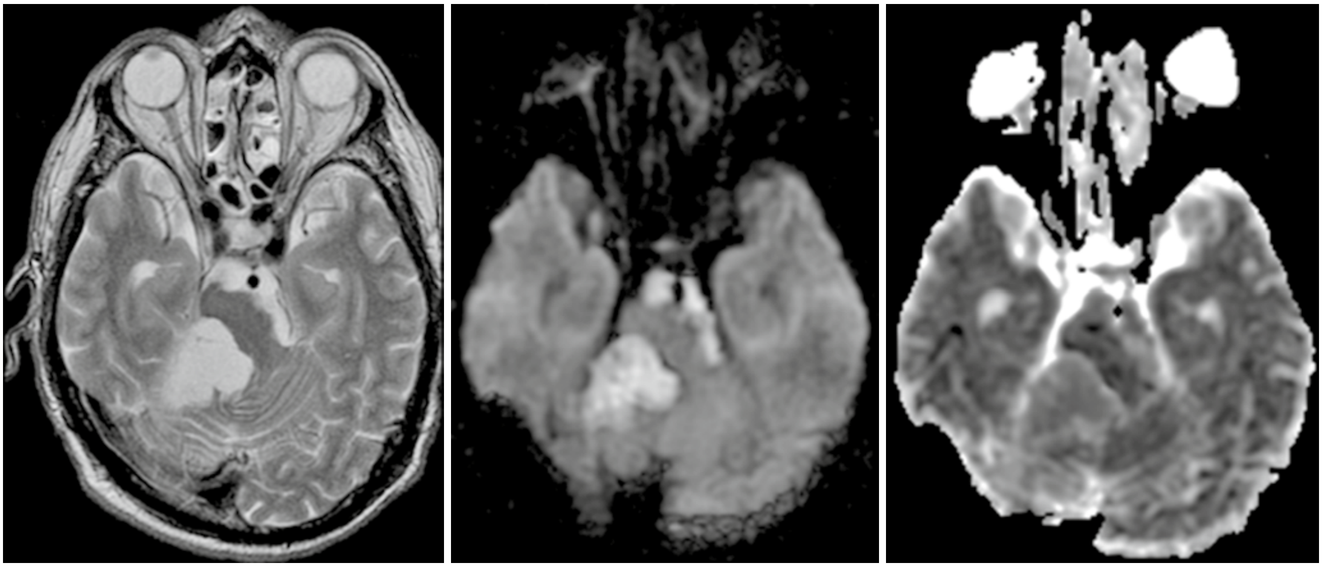

Fig. 5 Infratentorial epidermoid with typical DWI hyperintensity, CSF-like T2w signal, and ADC values almost normal compared with the normal brain

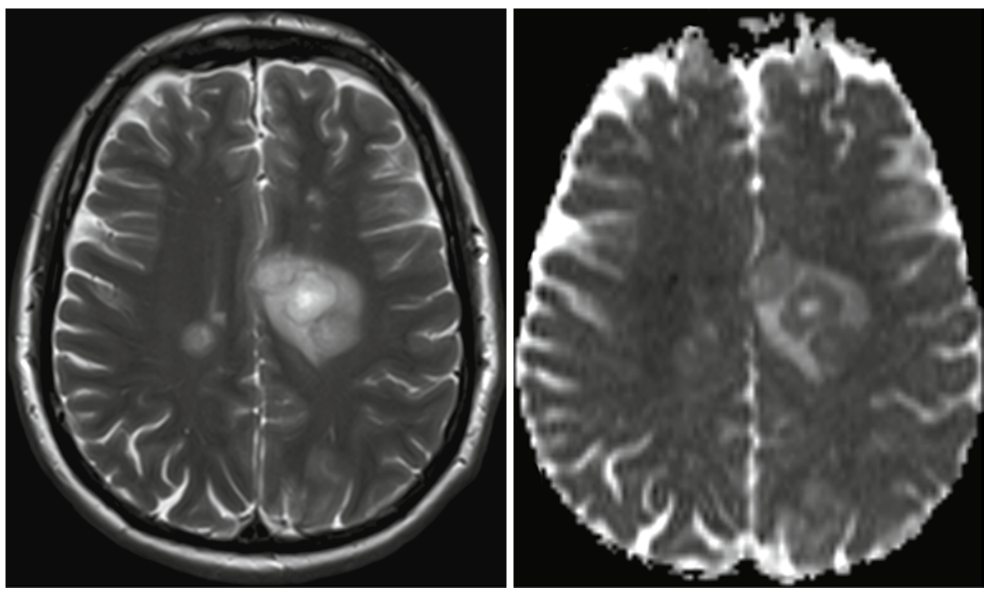

Fig. 6 Tumefactive demyelinating lesion (T2-weighted image on the *left*, ADC on the *right*). These lesions characteristically tend to have a T2w-hyperintense center and a rim with low T2w signal surrounded by edema. The T2w dark rim of these lesions has typically a bright diffusion-weighted signal with low ADC values, and often the ADC values of the center are higher compared to the surrounding edema

4 Prognostic Marker

In 2013 Zulfigar et al. (2013) presented a meta-analysis regarding ADC values and prognosis of *malignant astrocytomas*. They identified four studies reporting ADC values and survival data, covering overall 181 cases. Although therapy regimes differed among those four studies, ADC values showed an inverse relation with survival. Glioblastomas and anaplastic gliomas with minimum ADC values from solid tumor parts below cutoff values (range from 0.6–1.0×10^{-3} mm^2/s) showed poorer survival than glioblastomas with minimum ADC values above the threshold. They concluded that low ADC values in malignant gliomas correlate with poor survival, independent from tumor grade. Gupta et al. (2011) indicated that areas with restricted diffusion and without contrast enhancement in or adjacent to glioblastomas will turn into contrast-enhancing lesions a couple of months later (median 3.0 months, range 2.6–4.1 months).

In case of recurrent glioblastomas, ADC values were evaluated for their prognostic importance. In 2009 Pope et al. (2009) reported that ADC histogram analysis of the enhancing tumor volume predicts the response of *recurrent glioblastomas* to bevacizumab treatment. They compared histogram ADC values fitted with a two-compartment normal mixture model and means for the upper and lower ADC curve. Patients with lower ADC > $1{,}201 \times 10^{-6}$ mm²/s showed a longer time of survival after bevacizumab treatment. In a following study this group could link glioblastoma patients after treatment with external beam radiation and bevacizumab with low ADC means to a methylated MGMT promotor status and a better prognosis (Pope et al. 2011). Sunwoo et al. analyzed ADC values of enhancing tumor volumes and the MGMT promotor status in glioblastoma patients prior to therapy. They found a positive correlation of mean ADC and the methylated MGMT promotor status as well as longer progression-free survival.

Mostly low ADC values in untreated gliomas correspond to high cellular regions tending to be more aggressive, which might be different in *optic pathway gliomas* (OPG). Yeom et al. could follow up on OPG patients, and at the time of necessary treatment, these tumors showed higher mean ADC values than the stable tumors within their cohort. In their discussion the authors attributed this finding based on a publication by Hoyt and Baghdassarian (1969) to the certain mechanisms of growth, expansion through collateral hyperplasia of adjacent glia and connective tissue or by production of extracellular matrix. Grech-Sollars and colleagues analyzed diffusion data and survival in children with *embryonal brain tumors* (Grech-Sollars et al. 2012). They used the apparent transient diffusion coefficient in tumor (ATCT), which describes the gradient of ADC change from the last voxel outside of the tumor to the first three voxels within the tumor, calculated by the slope of the measured ADC values. Patients with a more negative ATCT had a poorer prognosis compared to patients with a less negative ATCT.

Pontine gliomas are diffusely infiltrating tumors, which were studied by Lober et al. (2014) with respect to prognostic subgroups by diffusion-weighted imaging. In 20 consecutive patients, they found a median ADC of 1.295×10^{-6} mm²/s, and the group with mean ADC below this median showed a lower median survival of 6 months compared to 12 months in the high ADC group.

Zakaria et al. studied the prognostic value of diffusion parameters in patients with *metastases* and found that minimum ADC values within the solid enhancing tumors of greater than 919.4×10^{-6} mm²/s, which was the median, indicated longer survival regardless of adjuvant therapies (Zakaria et al. 2014). An even better indicator was the ADC transition coefficient from the tumor across the border into the surrounding tissue (1 ROI inside the tumor, 3 ROIs in line outside of the tumor, slope calculation of the linear regression line of ADC values) – tumors with a sharp ADC change across the border (ATC >0.279) correlated with shorter overall survival. The authors also found different minimum ADC values in metastases from different primary cancers, also correlating with tumor cellularity. In contrast, Berghoff et al. found no correlation between cellularity and mean ADC values in their group of metastases, although semiquantitative DWI signal intensity and mean ADC values correlated with patient survival times (Berghoff et al. 2013). High DWI signal correlated with the amount of *reticulin deposition* between the tumor cells; the prognostic relevance of the diffusion data was even independent from other known prognostic factors like the primary tumor type, the KPS, and the adjuvant postsurgical therapies.

Diffusion-weighted imaging is used for prognosis estimations for different brain neoplasms; mostly low ADC values in treatment-naïve tumors correlate with poorer survival or shorter time to progression.

5 Treatment Monitoring

Besides standard MR imaging with morphological oriented sequences, nowadays physiologic MR imaging including diffusion-weighted imaging is often used for monitoring of therapy-induced tissue changes in brain tumors.

Early postsurgical MR imaging is important for the detection of residual neoplastic tissue, but also for the detection of surgically induced tissue alterations like an infarction. The detection of such a lesion is important since the enhancement of a subacute brain infarction should not be misinterpreted as progressive tumor.

Therapy-induced changes of the tumor cells have to occur prior to gross total volume changes of the whole tumor, which then are measurable by standard imaging methods. Changes in cell sizes, tumor architecture, development of necrosis, and edema should be detectable by diffusion-weighted imaging during longitudinal examinations.

Most studies on primary brain tumors were done on glioblastomas. Ellingson et al. used *functional diffusion maps* (Ellingson et al. 2011, 2012a, b, 2013), which are calculated by coregistering pre-therapy and post-therapy DWI images and ADC maps to each other and comparing the two on a voxel-by-voxel basis. The quality of coregistration is crucial for the quality of the results. This approach can be used either for different types of therapy and has been shown to be able to predict overall survival depending of the amount of ADC changes. ADC changes within enhancing tumor areas compared to areas of FLAIR hyperintensity were better predictive of overall survival (Ellingson et al. 2011), and bigger volumes of decreasing ADC in pretreatment FLAIR-hyperintense or contrast-enhancing areas indicate earlier progression after radiotherapy (Ellingson et al. 2012b). Hiramatsu et al. also used functional diffusion maps for the estimation of treatment effects after boron neutron capture therapy in glioblastomas (Hiramatsu et al. 2013). By using this technique, the authors could detect response patterns as early as 2 days after treatment prior to standard imaging techniques. An increase of the number of ADC decreased voxels compared to pretreatment data was a good predictor. This ADC decrease is often interpreted as a progressing tumor, but also cellular swelling like in ischemic stroke can lead to low ADC values which the authors confirmed by histological examination. Low ADC areas after therapy can also be seen after antiangiogenic therapy with bevacizumab, as it was reported by Hattingen et al. and Mong et al. (2011; 2012), indicating response to therapy likely due to energy depletion.

Conclusion

Diffusion-weighted imaging has shown its potential to contribute to individual tumor characterization. ADC values in solid parts of untreated gliomas tend to correlate inversely with cellularity and grade and therefore also with prognosis. Special ADC patterns with importance to the differential diagnosis are found in medulloblastomas, central neurocytomas, epidermoids, brain abscesses, and tumorlike demyelinating lesions. Diffusion data can also be helpful to differentiate between glioblastomas and metastases. During therapy ADC can be a possible marker for response or therapy failure, but ADC changes have to be interpreted with respect to the therapy used – destruction of cells likely increases ADC, whereas cytotoxic effects might lead to cell swelling and thereby restricted diffusion and lower ADC values.

For the interpretation of ADC values, one has to keep in mind that this parameter is not only influenced by microstructural determinants like cellular membranes, but it also depends on physiological changes like cell swelling or changes in viscosity; also hemorrhages, calcifications, and necrosis can have a confounding effect on ADC values. Recent sequence developments to reduce distortions and to get better SNR, methodological developments like diffusion kurtosis imaging, or analysis methods like functional response maps together with improved coregistration methods will further improve the contribution of DWI to individualized therapy.

References

Alvarez-Linera J, Benito-Leon J, Escribano J et al (2008) Predicting the histopathological grade of cerebral gliomas using high b value MR DW imaging at 3-tesla. J Neuroimaging 18:276–281

Arvinda HR, Kesavadas C, Sarma PS et al (2009) Glioma grading: sensitivity, specificity, positive and negative predictive values of diffusion and perfusion imaging. J Neurooncol 94:87–96

Atlas SW, DuBois P, Singer MB et al (2000) Diffusion measurements in intracranial hematomas: implications for MR imaging of acute stroke. AJNR Am J Neuroradiol 21:1190–1194

Bai X, Zhang Y, Liu Y et al (2011) Grading of supratentorial astrocytic tumors by using the difference of ADC value. Neuroradiology 53:533–539

Bammer R (2003) Basic principles of diffusion-weighted imaging. Eur J Radiol 45:169–184

Basser PJ (1995) Inferring microstructural features and the physiological state of tissues from diffusion-weighted images. NMR Biomed 8:333–344

Basser PJ, Özarslan E (2009) Introduction to diffusion MR. In: Johansen-Berg H, Behrens TEJ (eds) Diffusion MRI: from quantitative measurement to in vivo neuroanatomy. Academic Press, Elsevier, London/Burlington/San Diego

Basser PJ, Pierpaoli C (1996) Microstructural and physiological features of tissues elucidated by quantitative-diffusion-tensor MRI. J Magn Reson B 111:209–219

Basser PJ, Mattiello J, LeBihan D (1994) MR diffusion tensor spectroscopy and imaging. Biophys J 66:259–267

Beaulieu C (2009) The biological basis of diffusion anisotropy. In: Johansen-Berg H, Behrens TEJ (eds) Diffusion MRI: from quantitative measurement to in vivo neuroanatomy. Academic Press, Elsevier, London/Burlington/San Diego, pp 106–126

Beaulieu C, Allen PS (1994a) Water diffusion in the giant axon of the squid: implications for diffusion-weighted MRI of the nervous system. Magn Reson Med 32:579–583

Beaulieu C, Allen PS (1994b) Determinants of anisotropic water diffusion in nerves. Magn Reson Med 31:394–400

Berghoff AS, Spanberger T, Ilhan-Mutlu A et al (2013) Preoperative diffusion-weighted imaging of single brain metastases correlates with patient survival times. PLoS One 8:e55464

Brown R (1828) A brief account of microscopical observations made in the months of June, July and August, 1827, on the particles contained in the pollen of plants; and on the general existence of active molecules in organic and inorganic bodies. Philos Mag 4:161–173

Bulakbasi N, Guvenc I, Onguru O et al (2004) The added value of the apparent diffusion coefficient calculation to magnetic resonance imaging in the differentiation and grading of malignant brain tumors. J Comput Assist Tomogr 28:735–746

Busch E, Beaulieu C, de Crespigny A et al (1998) Diffusion MR imaging during acute subarachnoid hemorrhage in rats. Stroke 29:2155–2161

Byrnes TJ, Barrick TR, Bell BA et al (2011) Diffusion tensor imaging discriminates between glioblastoma and cerebral metastases in vivo. NMR Biomed 24:54–60

Carr HY, Purcell EM (1954) Effects of diffusion on free precession in nuclear magnetic resonance experiments. Phys Rev 94:630–638

Chenevert TL, Brunberg JA, Pipe JG (1990) Anisotropic diffusion in human white matter: demonstration with MR techniques in vivo. Radiology 177:401–405

Chenevert TL, Sundgren PC, Ross BD (2006) Diffusion imaging: insight to cell status and cytoarchitecture. Neuroimaging Clin N Am 16:619–632

Desprechins B, Stadnik T, Koerts G et al (1999) Use of diffusion-weighted MR imaging in differential diagnosis between intracerebral necrotic tumors and cerebral abscesses [see comments]. AJNR Am J Neuroradiol 20:1252–1257

Ebisu T, Tanaka C, Umeda M et al (1996) Discrimination of brain abscess from necrotic or cystic tumors by diffusion-weighted echo planar imaging. Magn Reson Imaging 14:1113–1116

Ebisu T, Tanaka C, Umeda M et al (1997) Hemorrhagic and nonhemorrhagic stroke: diagnosis with diffusion-weighted and T2-weighted echo-planar MR imaging. Radiology 203:823–828

Ellingson BM, Cloughesy TF, Lai A et al (2011) Graded functional diffusion map-defined characteristics of apparent diffusion coefficients predict overall survival in recurrent glioblastoma treated with bevacizumab. Neuro Oncol 13:1151–1161

Ellingson BM, Cloughesy TF, Lai A et al (2012a) Nonlinear registration of diffusion-weighted images improves clinical sensitivity of functional diffusion maps in recurrent glioblastoma treated with bevacizumab. Magn Reson Med 67:237–245

Ellingson BM, Cloughesy TF, Zaw T et al (2012b) Functional diffusion maps (fDMs) evaluated before and after radiochemotherapy predict progression-free and overall survival in newly diagnosed glioblastoma. Neuro Oncol 14:333–343

Ellingson BM, Cloughesy TF, Lai A et al (2013) Quantitative probabilistic functional diffusion mapping in newly diagnosed glioblastoma treated with radiochemotherapy. Neuro Oncol 15:382–390

Federau C, O'Brien K (2015) Increased brain perfusion contrast with T2 -prepared intravoxel incoherent motion (T2prep IVIM) MRI. NMR Biomed 28:9–16

Fick A (1855) Ueber diffusion. Ann Phys Lpz 170:59–86

Field AS, Alexander AL (2004) Diffusion tensor imaging in cerebral tumor diagnosis and therapy. Top Magn Reson Imaging 15:315–324

Grech-Sollars M, Saunders DE, Phipps KP et al (2012) Survival analysis for apparent diffusion coefficient measures in children with embryonal brain tumours. Neuro Oncol 14:1285–1293

Guo AC, Cummings TJ, Dash RC et al (2002) Lymphomas and high-grade astrocytomas: comparison of water diffusibility and histologic characteristics. Radiology 224:177–183

Gupta A, Young RJ, Karimi S et al (2011) Isolated diffusion restriction precedes the development of enhancing tumor in a subset of patients with glioblastoma. AJNR Am J Neuroradiol 32:1301–1306

Hahn EL (1950) Spin echoes. Phys Rev 80:580–594

Hattingen E, Franz K, du Mesnil de Rochemont R (2008) Medulloblastoma of the cerebellopontile angle. Rofo 180:834–835

Hattingen E, Jurcoane A, Bahr O et al (2011) Bevacizumab impairs oxidative energy metabolism and shows antitumoral effects in recurrent glioblastomas: a 31P/1H MRSI and quantitative magnetic resonance imaging study. Neuro Oncol. doi:10.1093/neuonc/nor132

Helenius J, Soinne L, Perkio J et al (2002) Diffusion-weighted MR imaging in normal human brains in various age groups. AJNR Am J Neuroradiol 23:194–199

Hiramatsu R, Kawabata S, Furuse M et al (2013) Identification of early and distinct glioblastoma response patterns treated by boron neutron capture therapy not predicted by standard radiographic assessment using functional diffusion map. Radiat Oncol 8:192

Hoyt WF, Baghdassarian SA (1969) Optic glioma of childhood. Natural history and rationale for conservative management. Br J Ophthalmol 53:793–798

Hyland M, Bermel RA, Cohen JA (2013) Restricted diffusion preceding gadolinium enhancement in large or tumefactive demyelinating lesions. Neurol Clin Pract 3:15–21

Jensen JH, Helpern JA (2003) Quantifying Non-Gaussian water diffusion by means of pulsed-field-gradient MRI. In: 11th annual meeting of ISMRM, Toronto. p 2154

Jensen JH, Helpern JA (2010) MRI quantification of non-Gaussian water diffusion by kurtosis analysis. NMR Biomed 23:698–710

Jensen JH, Helpern JA, Ramani A et al (2005) Diffusional kurtosis imaging: the quantification of non-gaussian water diffusion by means of magnetic resonance imaging. Magn Reson Med 53:1432–1440

Jones DK (2009) Gaussian modeling of the diffusion signal. In: Johansen-Berg H, Behrens TEJ (eds) Diffusion MRI: from quantitative measurement to in vivo neuroanatomy. Academic Press, Elsevier, London/Burlington/San Diego, pp 38–52

Jones DK, Cercignani M (2010) Twenty-five pitfalls in the analysis of diffusion MRI data. NMR Biomed 23:803–820

Kocaoglu M, Ors F, Bulakbasi N et al (2009) Central neurocytoma: proton MR spectroscopy and diffusion weighted MR imaging findings. Magn Reson Imaging 27:434–440

Kono K, Inoue Y, Nakayama K et al (2001) The role of diffusion-weighted imaging in patients with brain tumors. AJNR Am J Neuroradiol 22:1081–1088

Koral K, Gargan L, Bowers DC et al (2008) Imaging characteristics of atypical teratoid-rhabdoid tumor in children compared with medulloblastoma. AJR Am J Roentgenol 190:809–814

Koral K, Zhang S, Gargan L et al (2013) Diffusion MRI improves the accuracy of preoperative diagnosis of common pediatric cerebellar tumors among reviewers with different experience levels. AJNR Am J Neuroradiol 34:2360–2365

Lazar M (2010) Mapping brain anatomical connectivity using white matter tractography. NMR Biomed 23:821–835

Le Bihan D (1995) Molecular diffusion, tissue microdynamics and microstructure. NMR Biomed 8:375–386

Le Bihan D (2012) Diffusion, confusion and functional MRI. Neuroimage 62:1131–1136

Le Bihan D, Johansen-Berg H (2012) Diffusion MRI at 25: exploring brain tissue structure and function. Neuroimage 61:324–341

Le Bihan D, van Zijl P (2002) From the diffusion coefficient to the diffusion tensor. NMR Biomed 15:431–434

Le Bihan D, Breton E, Lallemand D et al (1986) MR imaging of intravoxel incoherent motions: application to diffusion and perfusion in neurologic disorders. Radiology 161:401–407

Lee EJ, terBrugge K, Mikulis D et al (2011) Diagnostic value of peritumoral minimum apparent diffusion coefficient for differentiation of glioblastoma multiforme from solitary metastatic lesions. AJR Am J Roentgenol 196:71–76

Lober RM, Cho YJ, Tang Y et al (2014) Diffusion-weighted MRI derived apparent diffusion coefficient identifies prognostically distinct subgroups of pediatric diffuse intrinsic pontine glioma. J Neurooncol 117:175–182

Lu S, Ahn D, Johnson G et al (2003) Peritumoral diffusion tensor imaging of high-grade gliomas and metastatic brain tumors. AJNR Am J Neuroradiol 24:937–941

Lu S, Ahn D, Johnson G et al (2004) Diffusion-tensor MR imaging of intracranial neoplasia and associated peritumoral edema: introduction of the tumor infiltration index. Radiology 232:221–228

Lu H, Jensen JH, Ramani A et al (2006) Three-dimensional characterization of non-gaussian water diffusion in humans using diffusion kurtosis imaging. NMR Biomed 19:236–247

Maier SE, Gudbjartsson H, Patz S et al (1998) Line scan diffusion imaging: characterization in healthy subjects and stroke patients. AJR Am J Roentgenol 171:85–93

Maier SE, Sun Y, Mulkern RV (2010) Diffusion imaging of brain tumors. NMR Biomed 23:849–864

Miron S, Tal S, Achiron A (2013) Diffusion tensor imaging analysis of tumefactive giant brain lesions in multiple sclerosis. J Neuroimaging 23:453–459

Mong S, Ellingson BM, Nghiemphu PL et al (2012) Persistent diffusion-restricted lesions in bevacizumab-treated malignant gliomas are associated with improved survival compared with matched controls. AJNR Am J Neuroradiol 33:1763–1770

Mulkern RV, Haker SJ, Maier SE (2009) On high b diffusion imaging in the human brain: ruminations and experimental insights. Magn Reson Imaging 27:1151–1162

Padhani AR, Liu G, Koh DM et al (2009) Diffusion-weighted magnetic resonance imaging as a cancer biomarker: consensus and recommendations. Neoplasia (New York NY) 11:102–125

Pavlisa G, Rados M, Pavic L et al (2009) The differences of water diffusion between brain tissue infiltrated by tumor and peritumoral vasogenic edema. Clin Imaging 33:96–101

Pierce T, Kranz PG, Roth C et al (2014) Use of apparent diffusion coefficient values for diagnosis of pediatric posterior fossa tumors. Neuroradiol J 27:233–244

Pierpaoli C, Jezzard P, Basser PJ et al (1996) Diffusion tensor MR imaging of the human brain. Radiology 201:637–648

Pipe J (2009) Pulse sequences for diffusion-weighted MRI. In: Johansen-Berg H, Behrens TEJ (eds) Diffusion MRI: from quantitative measurement to in vivo neuroanatomy. Academic Press, Elsevier, London/Burlington/San Diego, pp 11–35

Pope WB, Kim HJ, Huo J et al (2009) Recurrent glioblastoma multiforme: ADC histogram analysis predicts response to bevacizumab treatment. Radiology 252:182–189

Pope WB, Lai A, Mehta R et al (2011) Apparent diffusion coefficient histogram analysis stratifies progression-free survival in newly diagnosed bevacizumab-treated glioblastoma. AJNR Am J Neuroradiol 32: 882–889

Poretti A, Meoded A, Cohen KJ et al (2013) Apparent diffusion coefficient of pediatric cerebellar tumors: a biomarker of tumor grade? Pediatr Blood Cancer 60:2036–2041

Price SJ, Jena R, Burnet NG et al (2006) Improved delineation of glioma margins and regions of infiltration with the use of diffusion tensor imaging: an image-guided biopsy study. AJNR Am J Neuroradiol 27:1969–1974

Provenzale JM, McGraw P, Mhatre P et al (2004) Peritumoral brain regions in gliomas and meningiomas: investigation with isotropic diffusion-weighted MR imaging and diffusion-tensor MR imaging. Radiology 232:451–460

Purcell EM, Torrey HC, Pound RV (1946) Resonance absorption by nuclear magnetic moments in a solid. Phys Rev 69:37–38

Raab P, Hattingen E, Franz K et al (2010) Cerebral gliomas: diffusional kurtosis imaging analysis of microstructural differences. Radiology 254:876–881

Saini J, Chatterjee S, Thomas B et al (2011) Conventional and advanced magnetic resonance imaging in tumefactive demyelination. Acta Radiol 52:1159–1168

Stejskal E, Tanner J (1965) Spin diffusion measurements: spin echoes in the presence of a time-dependent field gradient. J Chem Phys 42: 288–292

Tabesh A, Jensen JH, Ardekani BA et al (2010) Robust estimation of kurtosis and diffusion tensors in diffusional kurtosis imaging. In: Annual meeting of ISMRM, Stockholm

Takahashi M, Hackney DB, Zhang G et al (2002) Magnetic resonance microimaging of intraaxonal water diffusion in live excised lamprey spinal cord. Proc Natl Acad Sci U S A 99:16192–16196

Tlili-Graiess K, Mama N, Arifa N et al (2014) Diffusion weighted MR imaging and proton MR spectroscopy findings of central neurocytoma with pathological correlation. J Neuroradiol 41:243–250

Toh CH, Wei KC, Ng SH et al (2011) Differentiation of brain abscesses from necrotic glioblastomas and cystic metastatic brain tumors with diffusion tensor imaging. AJNR Am J Neuroradiol. doi:10.3174/ajnr.A2581

Tsuchiya K, Fujikawa A, Nakajima M et al (2005) Differentiation between solitary brain metastasis and high-grade glioma by diffusion tensor imaging. Br J Radiol 78:533–537

Van Cauter S, Veraart J, Sijbers J et al (2012) Gliomas: diffusion kurtosis MR imaging in grading. Radiology 263:492–501

Yacoub HA, Al-Qudahl ZA, Lee HJ et al (2011) Tumefactive multiple sclerosis presenting as acute ischemic stroke. J Vasc Interv Neurol4:21–23

Yamasaki F, Kurisu K, Satoh K et al (2005) Apparent diffusion coefficient of human brain tumors at MR imaging. Radiology 235:985–991

Zakaria R, Das K, Radon M et al (2014) Diffusion-weighted MRI characteristics of the cerebral metastasis to brain boundary predicts patient outcomes. BMC Med Imaging 14:26

Zulfiqar M, Yousem DM, Lai H (2013) ADC values and prognosis of malignant astrocytomas: does lower ADC predict a worse prognosis independent of grade of tumor?–a meta-analysis. AJR Am J Roentgenol 200:624–629

Advanced MR Methods in Differential Diagnosis of Brain Tumors

Elke Hattingen, Ulrike Nöth, and Ulrich Pilatus

Contents

E. Hattingen
Neuroradiology, Clinic of Rheinische, Friedrich-Wilhelms-University, Sigmund-Freud Straße 6, 53127 Bonn, Germany
e-mail: elke.hattingen@ukb.uni-bonn.de

U. Nöth
Brain Imaging Center (BIC), Goethe University Frankfurt, Schleusenweg 2-16, 60528 Frankfurt/Main, Germany

U. Pilatus
Neuroradiology, Goethe University Frankfurt, Schleusenweg 2-16, 60528 Frankfurt/Main, Germany

Conventional MRI may considerably improve the differential diagnosis of space-occupying brain lesions. However, the specificity for providing a definite diagnosis remains limited. Given the fact that final diagnosis should be based on histopathology and immunohistochemistry, imaging diagnosis seems to be of minor significance. However, some decisions must be met prior to surgical tissue sampling, e.g., the avoidance of steroids if CNS lymphoma is suspected or the definition of the target area for biopsy in inhomogeneous gliomas (see Chap. MR Imaging of Brain Tumors).

Therefore, improving differential diagnosis of brain tumors may have decisive influence on further therapy and on surgical strategy.

Advanced MR imaging methods are more specific compared to conventional MRI and may thus provide additional information on tumor biology and tumor morphology. Methods mainly exploring tumor biology, as e.g., tumor vasculature and metabolism, are described elsewhere (see Chaps. MR Spectroscopic Imaging and MR Perfusion Imaging). While standard MRI is optimized for showing tumor morphology, more advanced MR methods can help with tissue characterization. The best known technique in this respect is diffusion-weighted imaging and its further developments (see Chap. Diffusion-Weighted Methods). Further techniques for the characterization of tumor tissue are the MR relaxometry and the susceptibility-weighted imaging, both detailed in this chapter.

We also describe experimental methods based on chemical exchange, which have high potential to uncover tumor biology but are yet to be evaluated in large patient cohorts.

1 MR Relaxometry Techniques

Standard MRI sequences provide images that may display different weightings, such as T2 (transverse relaxation time) weighted images, T1 (longitudinal relaxation time) weighted images, images with a combination of both weightings (as in fluid-attenuated inversion recovery, FLAIR), or images

E. Hattingen, U. Pilatus (eds.), *Brain Tumor Imaging*,
Med Radiol Diagn Imaging (2016)
DOI 10.1007/174_2016_1038, © Springer Berlin Heidelberg

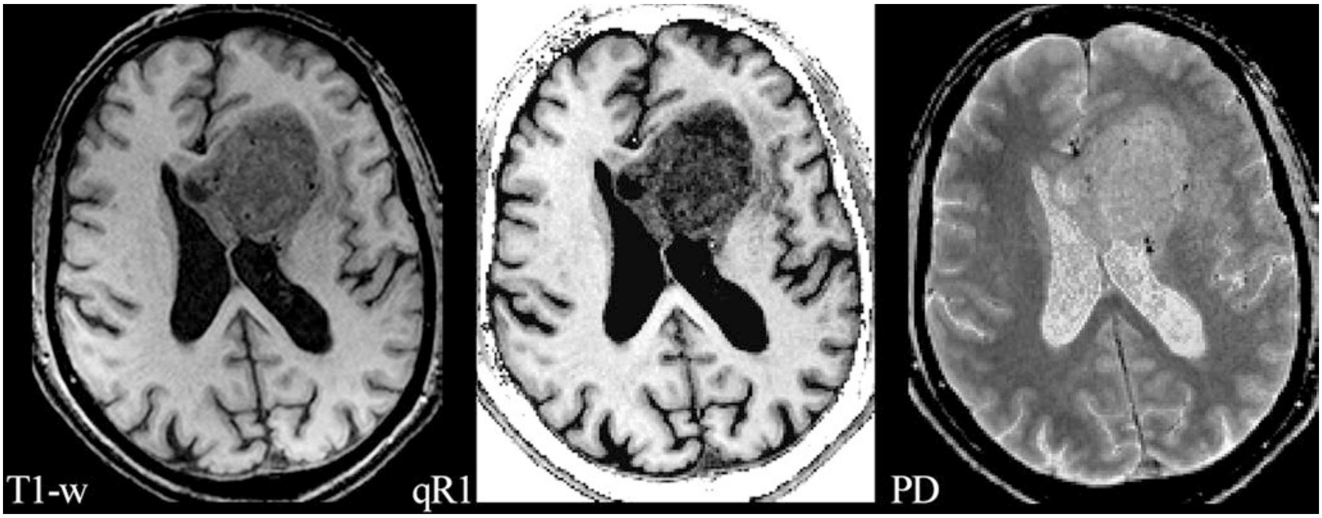

Fig. 1 A left frontal glioblastoma is shown in a conventional T1-w axial image (*T1-w*) without a contrast agent, in a map of quantitative R1 relaxation rate (*qR1*) with R1 = 1/T1, and in a map of proton density (*PD*). The qR1 map is gray scaled, showing the increasing T1 relaxation time from *white to black*; the PD map shows increasing PD values from *black to white*. The tumor is hypointense compared to white matter in the T1-w image due to the longer T1 relaxation time of tumor tissue (*dark gray* in qR1). However, the PD is increased in the tumor, increasing the signal in all weighted images of the standard MRI including T1-w images. This may attenuate the hypointense signal in T1-w images

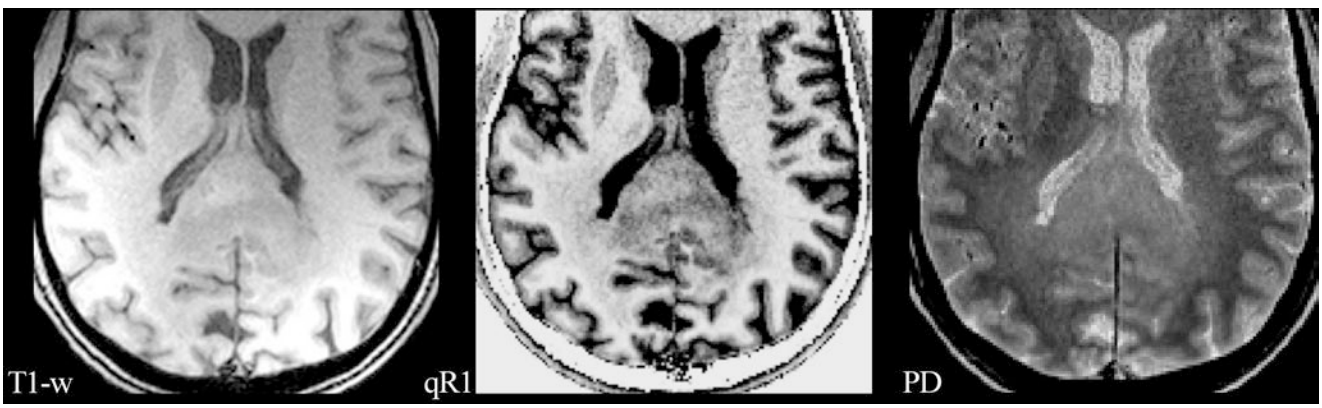

Fig. 2 A glioblastoma of the splenium of the corpus callosum with adjacent subtle white matter changes which extended into both hemispheres and were suspicious for gliomatosis. Images from standard MRI (*T1-w*) and quantitative maps (*qR1* and *PD*) are shown as in Fig. 1. T1 relaxation times of this infiltrative tumor are shorter compared to the glioblastoma in Fig. 1, resulting in a less hypointense appearance in qR1, while the PD is comparable. Thus, the tumor is hardly seen on standard T1-w images. Also note the bright signal in T1-w of the dorsal brain which is due to RF coil inhomogeneities. Quantitative mapping of theT1 relaxation time or its inverse, the R1 relaxation rate, eliminates the RF coil inhomogeneities and the PD contrast, thus showing the tumor much clearer in qR1. Even subtle changes of the adjacent white matter may be depicted

where both weightings are suppressed (proton density (PD) weighted). In fact, signal intensities and image contrast provided by standard MR sequences are influenced to some degree by all parameters (T2, T1, PD) described so far. In addition, inhomogeneities of the static magnetic field and MR hardware-related effects have an influence on image quality too. The relaxation times (T2, T1) and proton density vary between different tissues and fluids, and their influence on image contrast is difficult to estimate in standard MRI. Different parameters (T1, PD) exhibit opposite signal behavior (Fig. 1), resulting in a partial masking of their respective weightings. This effect may reduce the detectability of pathological structures (Fig. 2).

These ambiguous contrast phenomena can be avoided by acquiring a series of MR images with different T1 or T2 weighting which allows calculating the respective relaxation time. The resulting parameter maps provide quantitative values of the relaxation times (T1, T2) and thus offer more unequivocal information on tissue characteristics Schad et al. 1993. The following sections deal with the diagnostic value of these parameters.

However, the systematic approach to obtain these parameter maps is challenging. Current advances in MR imaging, hardware and post-processing techniques prepare the way to resolve these problems. The description of these quantitative methods is beyond the scope of this book and reference is made to some reviews (Cheng et al. 2012; Tofts 2003). Apart from their diagnostic value, these quantitative parameter maps are free from magnetic field inhomogeneities, RF coil characteristics and the specific choice of imaging parameters (e.g., TR, TE), thus allowing the quantification of pathological tissue changes. The diagnostic advantages of quantitative and semiquantitative MR parameter evaluation have been shown in MS patients (Cheng et al. 2012; Hasan et al. 2012; Tofts).

Unfortunately, most quantitative MR studies on brain tumors date from decades ago, i.e., the early stages of methodical development restricted by less developed hardware and low computational power. Damadian was the first to report prolonged T2- and T1-relaxation times in neoplastic tissue (Damadian 1971). Although the benefit of quantitative MR methods in differential diagnosis of brain tumors has yet to be shown, it should be considered as one of the most challenging responsibilities for radiologists to establish standardization and reliable MR parameter quantification in tumor imaging, especially in the context of tumor monitoring.

2 Transverse Relaxation Time T2

The spin-spin or transverse relaxation time T2 describes the exponential decay of the component of the tilted magnetization, which is perpendicular to the static magnetic field. Local inhomogeneities of the static magnetic field (e.g., due to magnetic susceptibility differences or chemical shifts) lead to an acceleration of this decay, which is described by the effective transverse relaxation time T2*.

The transverse relaxation rate (R2) experienced by a spin, which is the inverse of T2, depends on the energy transfer between two spins, yielding fluctuations of their respective Larmor frequencies. The T2 relaxation time is long in tissues with freely moving water molecules, such as those in pure water and aqueous solutions. Macromolecules (e.g., myelin, proteins) interacting with the water molecules influence the T2 relaxation time, which decreases as the concentration of macromolecules increases. Most brain pathologies (e.g., tumor infiltration, edema, gliosis) result in an accumulation of abnormal fluids and/or in a decrease of macromolecules within the brain tissue. Therefore, T2-weighted MR images (T2-weighted sequences in the strict sense and also FLAIR which displays a T1 contrast in addition to the T2 weighting) are used to detect brain pathologies as most of them appear bright against the darker normal tissue. Mapping of the relaxation time T2 in the brain quantifies changes of the normal and pathological tissue in an objective and reproducible manner.

Experimental animal studies as well as human studies demonstrated that glioma tissue has significantly longer T2 relaxation times compared to normal brain tissue (Englund et al. 1986; Hoehn-Berlage et al. 1992; Oh et al. 2005) and even compared to non-glial tumors (Englund et al. 1986; Oh et al. 2005). Positive correlation of T2 with ADC values in brain tumors implies that T2 values are related to the water content of the tumor. Therefore, higher T2 values indicate more necrotic tumors with lower tumor cell density, whereas a high cell density or a high amount of interstitial reticulin deposition lowers the T2 values of tumor tissue (Englund et al. 1986; Berghoff et al. 2012; Oh et al. 2005). Furthermore, a higher T2 relaxation time was observed in peritumoral edema as compared to normal tissue. It is well known from stereotactic surgery that the so-called peritumoral edema of gliomas is a mixture of vasogenic edema and tumor cell infiltration. The T2 value of the edema adjacent to the enhancing tumor (i.e., the tumor signal enhances in a T1-weighted image after application of a contrast agent) may help to differentiate metastases from gliomas: T2 values in the pure vasogenic edema of metastases and meningiomas were longer than those in the immediate peritumoral edema of gliomas (Oh et al. 2005). Despite these promising results, it should be emphasized that the characterization of neoplastic tissue changes such as necrosis, tumor cell accumulations, edema, and vasculature may not be determined by quantitative MRI alone, but also requires visual scrutiny of structural patterns.

This approach also helps to monitor tissue changes such as increasing tumor infiltration over time by using subtraction maps. For this purpose, consecutive follow-up maps of the relaxation time T2 of an individual patient are co-registered and subtracted voxel-wise from a reference map of the same patient. This allows the detection even of subtle tumor infiltration which might not be detectable by visual inspection (Hattingen et al. 2013).

Apart from tumor infiltration, acute therapeutic reactions like radiation necrosis may also increase the T2 relaxation time (Larocque et al. 2009). However, T2 values can also decrease under radiation, possibly due to the presence of paramagnetic substances such as blood products. Our own experience from T2 mapping of glioblastomas is that differences in T2 relaxation times are highest between edema and normal brain tissue, whereas the tumor tissue demonstrates a wider range of T2 values sometimes even similar to normal brain tissue. In particular, antiangiogenic therapy of patients with progressive glioblastomas resulted in a significant decrease of the T2 value in tumor tissue approaching T2 values similar to normal brain tissue (Hattingen et al. 2013). Tumor tissue with a low T2 relaxation time exhibits a reduced signal on T2-weighted images, reducing the perceptibility of these "darker" tumors which might thus be visually missed. This could explain why progression-free survival – but not the overall survival – is longer under antiangiogenic therapy compared to other treatment modalities: real progression of non-enhancing tumors may be visually missed under antiangiogenic therapy. The lower T2 values seem to reflect a normalization of the blood-brain barrier (BBB) under antiangiogenic therapy, which reduces edema and therefore tumor water content.

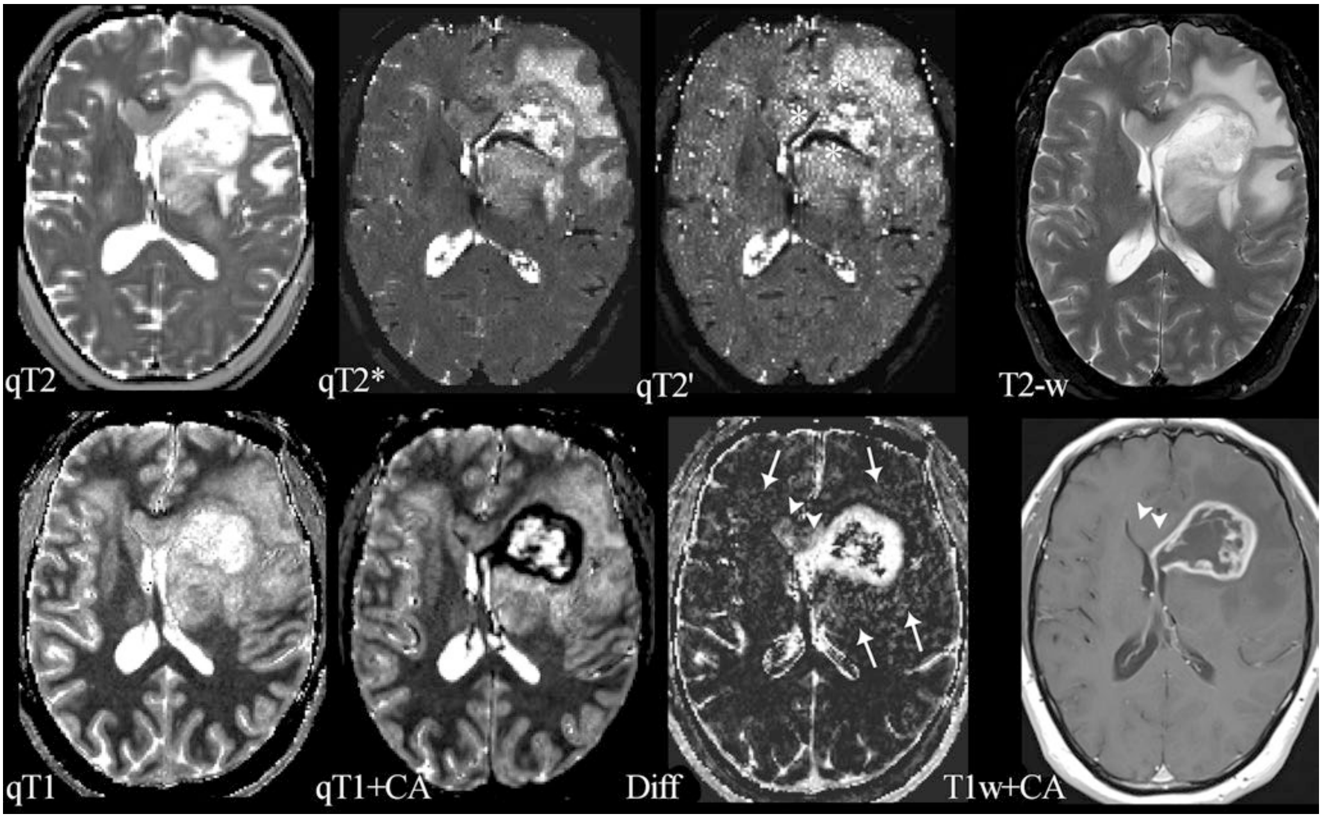

Fig. 3 Compilation of different parameter maps from quantitative MRI in a patient with left frontal glioblastoma: the *upper row* shows maps of the transverse relaxation times T2, T2*, and T2′ (qT2, qT2*, and qT2′) and a conventional T2-weighted image (*T2-w*); the *lower row* shows maps of the longitudinal relaxation time before (*qT1*) and after application of a contrast agent (qT1+CA), the difference map (*Diff*) resulting from voxel-wise subtraction of (qT1+CA) from qT1, and a conventional T1-weighted image after application of a contrast agent (T1w+CA). The standard MR images (T2-w and T1w+CA) show the tumor's central necrosis, which is surrounded by solid tumor tissue enhancing after CA application, and a large edema. The images also show that the non-enhancing part of the tumor infiltrates the corpus callosum and the basal ganglia and that there is a small area of edema in the contralateral frontal lobe. However, the maps of the different relaxation times reveal further biological information: The T2′ map (which is T2* without T2 effects) reveals some dark areas which might represent hypoxia and/or tumor bleedings (*white stars*). The qT1 map depicts the whole tumor extension and its relation to the anatomical structures showing high gray-white matter contrast (please note the inverse contrast compared to the qR1 map in Figs. 1 and 2; in qT1 the T1 relaxation time increases from *black to white*). The CA shortens the T1 relaxation time (*dark areas* in qT1+CA). However, voxel-wise subtraction of qT1+CA from qT1 yields a T1 difference map (*Diff*) additionally depicting tumor enhancement in the corpus callosum and basal ganglia which is missed on T1-weigthed images after application of a CA (T1w+CA) (*white arrow heads*). Additional slight enhancement is also seen in the "edema" region (*white arrows*), suggesting angiogenetic reactions from invisible tumor infiltrations

In summary, T2 relaxation time mapping of brain tumors seems to be sensitive to the detection of tumor-related tissue changes and might be an excellent tool for longitudinal tumor monitoring (T2 difference maps), whereas the specificity of the changes is limited.

3 Effective Transverse Relaxation Time T2* and Susceptibility-Weighted Imaging (SWI)

The effective transverse relaxation time T2* reflects the dephasing of the transverse magnetization in gradient echo sequences which is due to the spin-spin relaxation and local field inhomogeneities. Therefore, T2* is influenced by local microscopic and macroscopic magnetic field inhomogeneities due to susceptibility differences between tissue types and chemical shifts. Macroscopic field inhomogeneities (B0) are found near the skull base and may also be induced by metallic devices. Microscopic field inhomogeneities result from physiological iron depositions in the deep nuclei of the brain and deoxyhemoglobin (deoxyHb) in blood. The relation of diamagnetic oxyHb to paramagnetic deoxyHb mainly influences the T2* relaxation time in brain tissue, which is also known as "blood oxygenation level-dependent" (BOLD) effect. In summary, T2* is influenced both by spin-spin relaxation (which is described by T2) and susceptibility effects (which are described by the relaxation time T2′). The mathematical correlation of these three relaxation times is $1/T2' = 1/T2^* - 1/T2$ or alternatively when using the relaxivities $R' = R2^* - R2$. Measuring T2* and T2 relaxation times, B0 field inhomogeneities and blood volume fraction yield reliable information on the oxygenation of brain tumors (Fig. 3), so that T2′ mapping in combination with an MR perfusion measurement may be considered as "hypoxia imaging" (Tóth et al. 2013). Tumor hypoxia is considered as an important motor of malignant transformation and, therefore, increases the tumor's aggressiveness. It also causes resistance of the tumor to chemotherapy and radiation mediated by the activation of HIF-1α and carbonic anhydrase IX and XII (Harguindey et al. 2009). The indirect measurement of hypoxia by T2′ quantification might provide insight into the pathophysiology of brain tumors and into the effects of therapy (Hattingen et al. 2013; Hoskin et al. 2007). Saitta et al. could show that high-grade tumors revealed lower T2′ values, suggesting a higher degree of hypoxia in these fast growing and proliferating tumors (Saitta et al. 2011). However, it is not possible to differentiate deoxyHb from other microscopic sources of susceptibility effects like tumor microbleeds. This might result in confounding results in glioblastomas, since microbleeds are a very typical characteristic of this type of brain tumor. It has turned out that the detection of microbleeds in high-grade gliomas is very helpful for discriminating them from other space-occupying pathologies such as demyelinating lesions, lymphomas, and metastases (see below).

Since microbleeds are best detected with high-resolution susceptibility-weighted imaging (SWI), this method plays an important role in tumor diagnosis. Since field inhomogeneities and thus susceptibility effects increase with the field strength, this relatively new MR technique benefits from higher field strengths which become increasingly available in the clinic. In SWI, filtered phase and magnitude information are combined to create a new susceptibility-weighted image contrast (Haacke et al. 2004). SWI visualizes normal or pathological venous structures and microbleeds that are not visible on conventional MR images. Pronounced intratumoral susceptibility signals (ITSS) are found in almost all glioblastomas but not in CNS lymphomas, demyelinating diseases, and low-grade gliomas (Mittal et al. 2009; Park et al. 2010; Peters et al. 2012). In most cases, microbleeds in metastases are less pronounced compared to microbleeds in glioblastomas (Park et al. 2010). Furthermore, intralesional venous structures differ considerably between different space-occupying brain lesions. The perivenous inflammation in multiple sclerosis (MS) lesions shows a typical SWI pattern revealing normal venous structures which are the lead structures for the MS plaques (Mittal et al. 2009). In contrast, high-grade gliomas not only show prominent microbleeds, but also a distorted and irregular neovasculature (Kim et al. 2009; Mittal et al. 2009).

4 Longitudinal Relaxation Time T1

Several studies showed a positive correlation between the brain water content and the T1 relaxation time (MacDonald et al. 1986; Fatouros et al. 1991). The positive correlation of the mean diffusivity of water (Bastin 2002) and the T1 relaxation time and a significant T1 reduction under antiedematous therapy support the hypothesis that the T1 relaxation time reflects the tissue water content (Andersen et al. 1993). Longer T1 values were found in enhancing lesions of MS patients compared to non-enhancing lesions, indicating a disruption of the BBB and hence a higher water content in the adjacent brain tissue prolonging T1 (Jurcoane et al. 2013). Human and animal studies showed prolonged T1 relaxation times in glioblastomas and their peritumoral edema compared to normal brain tissue (Englund et al. 1986; Hoehn-Berlage and Bockhorst 1994) and other tumors such as meningiomas and schwannomas. In contrast, necrotic tumor tissue might display a shortened T1 relaxation time which might be due to the presence of methemoglobin or mineralization (Bähr et al. 2011; Boyko et al. 1992). It should be mentioned that T1 shortening might also be a prognostic marker for the survival time of patients with recurrent glioblastomas under antiangiogenic therapy (Bähr et al. 2011, 2014).

The presence of contrast agents containing gadolinium (Gd) or manganese (Mn) shortens the T1 relaxation time considerably. Furthermore, co-registered maps of the longitudinal relaxation time before (qT1) and after application of a contrast agent (qT1+CA) allow for voxel-wise subtraction of (qT1+CA) from qT1 (Fig. 3). This approach enables the quantification of an even subtle contrast agent enhancement independent of visual detectability (Jurcoane et al. 2013), yielding sensitive quantification of the BBB damage (Jurcoane et al. 2013).

However, further studies are required to answer the question if T1 mapping, alone or in combination with T2 mapping, histograms of T1 and T2 relaxation times in the tumor tissue and edema, and more sophisticated three-dimensional tumor segmentation methods are valuable tools to delineate tumor tissue and edema and if these techniques are of help in differential diagnosis and therapy monitoring.

5 Chemical Exchange Saturation Transfer (CEST)

The CEST method is based on the magnetic transfer effects of specific protons in metabolites (and exogenous contrast agents) that are in chemical exchange with the solvent. The method for detecting CEST contrast is similar to the magnetization transfer (MT) contrast, i.e., the intensity change of the water signal is monitored in the presence of off-resonance saturation. A CEST effect is observed when the off-resonance frequency matches the MR frequency of a metabolite proton which is exchanging with the water protons at an appropriate rate. By varying the frequency, power, and timing of the saturation pulses, CEST contrast can be tuned to signals from endogenous mobile proteins and peptides (amide proton transfer, APT) (Zhou et al. 2003a, b) to amino protons of glutamate (gluCEST) (Cai et al. 2012) or to hydroxyl protons like those from glucose (glucoCEST) (Chan et al. 2012; Nasrallah et al. 2013). Since the basic principle of the contrast relies on proton exchange with the solvent and therefore depends on the concentration of solvent protons, the method allows to measure tissue pH (Zhou et al. 2003b).

Fig. 4 Chemical exchange saturation transfer (*CEST*) method (With permission from van Zijl and Yadav (2011)). Further explanation is given in the text (Method)

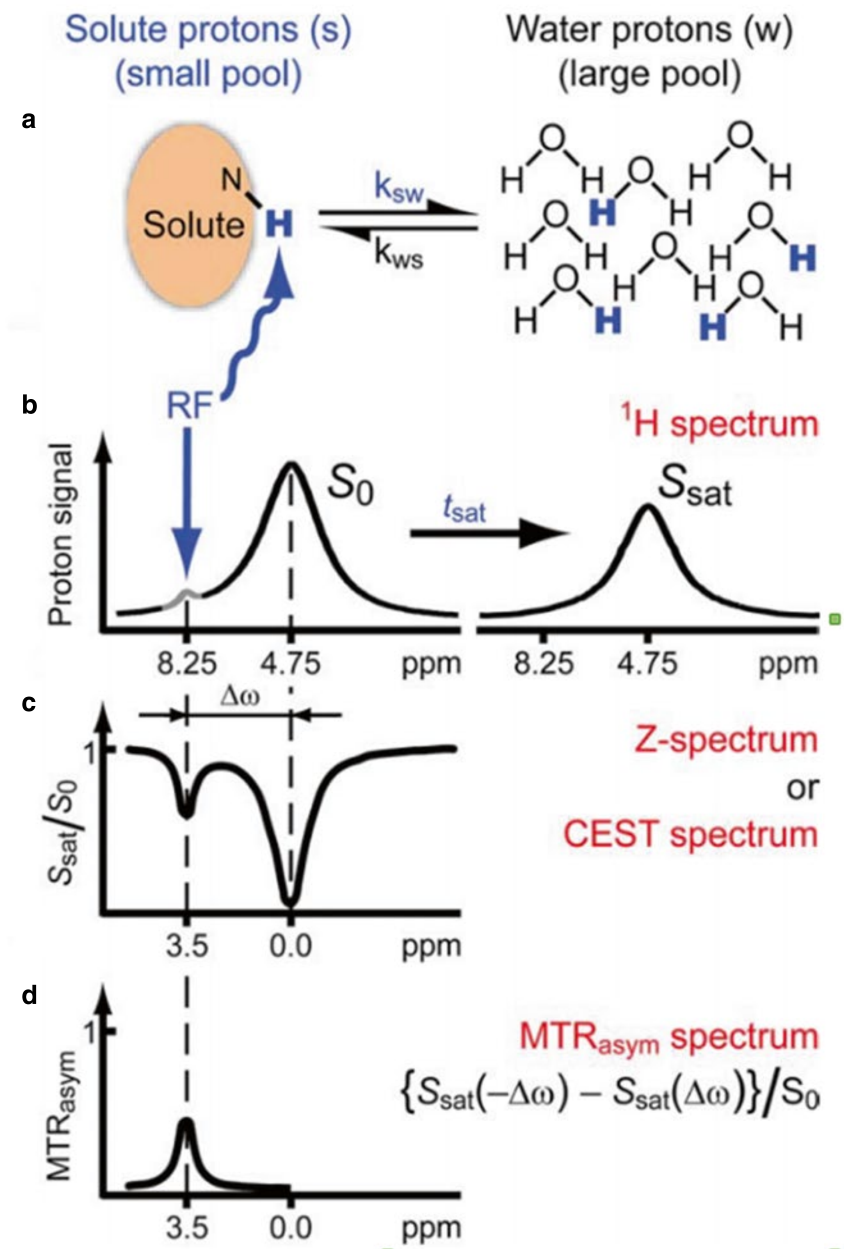

6 CEST Method

There are several articles which review the basic principles of CEST (Sherry and Woods 2008; van Zijl and Yadav 2011; van Zijl et al. 2003). Briefly, the method exploits the magnetization transfer (MT) effect which is well known from MT-MRI (Tofts 2003). In MTR contrast is generated by selectively irradiating off-resonance from the water signal, modifying the magnetization of macromolecules which are in contact with the water. By several mechanisms, this magnetization is transferred to the water protons detected with conventional MRI, causing a partial saturation and consequently a signal modification. The efficiency of the magnetization transfer is typically changed in several pathological situations providing a surrogate marker for affected tissues (Tofts 2003). Like in MTR, CEST-MRI monitors the effect (signal reduction) of an off-resonance irradiation on the water signal; however, the target molecules for irradiation are rather small (amino acids, peptides, glucose, exogenous agents with specific properties) and have a well-defined typical resonance frequency which is known from MR spectroscopy (see Chap. MR Spectroscopic Imaging). Some of the protons in these molecules are exchanged with the solvent (water). Selective saturation of these protons will transfer their magnetization to the MRI-detectable water signal, enabling the quantification of the exchange partner by measuring the signal changes of the solvent.

The effect is shown in Fig. 4.

The upper row (a) shows a scheme of the exchange mechanism, while the left part of row b depicts the MR spectrum of a sample with an aqueous solution containing a solute with amide protons (e.g., from polypeptides). On the left of the huge water signal at 4.75 ppm (S_0), a weak signal at 8.25 ppm from exchangeable amide protons is visible. Saturation of these protons by RF irradiation at 8.25 ppm not only removes this signal but also causes a significant decrease of the water signal (S_{sat}, right). The decrease of S_{sat} can be detected as contrast in MRI. Performing a series of measurements with different offset frequencies for saturation provides a so-called Z-spectrum or CEST spectrum which is shown in row c. In the CEST spectrum, the normalized water signal (S_{sat}/S_o) in the presence of saturation is plotted versus the frequency difference between the water and the offset irradiation frequency ($\Delta\omega$). Obviously, irradiation at the water signal frequency will saturate the water protons causing a minimal S_{sat} (direct saturation, DS). In addition to DS, there is also the MT effect which reduces the water signal intensity in the presence of off-resonance irradiation. In a first approximation, DS and MT can be considered as independent of the sign of $\Delta\omega$ causing a symmetric Z-spectrum around the water frequency. In contrast, saturation of the water protons via exchange with saturated amide protons only appears when the saturation frequency matches the position of the amide protons (3.5 ppm to the left of water), resulting in an additional dip in S_{sat}/S_o at this frequency.

Defining the term MTR_{asym}

$$\left\{S_{sat}\left(-\Delta\omega\right)-S_{sat}\left(\Delta\omega\right)\right\}/\,S_0$$

which determines the asymmetry of the MTR effect correcting for DS and symmetric MT provides the MTR_{asym} spectrum which is shown in row d. Chemical exchange is evident as signal at the position of the exchanging amide protons. This signal reflects a change in water proton intensity and can be detected with methods known from MT-MRI. Compared to conventional MRSI, the methods have a huge potential for signal enhancement which increases with the exchange rate k_{exchange} but is counteracted by the T1 relaxation of tissue water. Also, the efficiency of saturation of solute protons by continuous RF irradiation depends on the ratio $\Delta\omega/k_{\text{exchange}}$. Ideally $\Delta\omega/k_{\text{exchange}} >> 1$ (slow exchange regime) is required to allow sufficient saturation with reasonable RF power (van Zijl and Yadav 2011), a condition which, at clinical field strength of 3 T, is only fulfilled for amide protons. Consequently, most applications on human brain tumors are focused on mobile proteins and polypeptides, measuring either their concentrations or tumor environmental changes which can modify the exchange rate (Zhou et al. 2003a; Togao et al. 2014). Amino and hydroxyl protons usually fall in the slow to medium exchange regime ($\Delta\omega/k_{\text{exchange}} \sim 1$), but it has been shown that glucose and glycogen can be detected with CEST in animal models at high magnetic field strengths (>9 T, (Chan et al. 2012; Nasrallah et al. 2013; van Zijl et al. 2007)). Recently it was proposed that spin-locking (SL) techniques are more suited for the intermediate exchange regime (Lin et al. 2011; Jin et al. 2012) and pilot studies could detect myoinositol (Haris et al. 2011) and glutamate (Cai et al. 2012) using this method. However, no applications in oncology are published yet; thus, a description of these methods would be beyond the scope of this short overview.

In summary, for a metabolite with protons that are in exchange with the water, CEST provides a contrast which is specific to their concentration (like parameter images in MRSI) but with a signal intensity comparable to MT contrast. The following metabolites were detected via magnetization transfer mediated by chemical exchange of protons with the water:

- Amide protons in peptide bonds (endogenous mobile proteins and peptides) (APT-CEST)
- Glutamate (gluCEST)
- Glucose, glycogen, and myoinositol (glucoCEST)

Also, exogenous CEST agents have been introduced (Ward et al. 2000), and their function as pH marker has been tested as proof of principle (Ward and Balaban 2000)

While the concept of CEST imaging is very intriguing, there are various pitfalls which might render the method as too complicated and up to now not very robust for routine clinical use:

- Like MT-MRS, the method requires a rather quantitative approach to correct for many competing mechanisms which can cause a decrease in signal intensity.
- Many parameters are affecting the exchange rate. Thus, the CEST-induced contrast might be ambiguous.
- Long measurement time and SAR problems.

7 CEST Imaging in Brain Tumors

There is an increasing number of publications dealing with CEST in brain tumors. APT was introduced by Zhou et al. (2003b). First in vivo data from brain tumors were published by the same group 3 years later (Jones et al. 2006). A 3–4 % increased APT signal was found in brain tumors compared to peritumoral brain tissue or in animal models comparing glioma with radiation necrosis in rats (Zhou et al. 2008, 2011). Amide protons in the cytoplasm are thought to be the major source of the APT signal intensity. As known from FET-PET (Chap. Advanced MR Methods in Differential Diagnosis of Brain Tumors), glial brain tumors have an increased amino acid uptake compared to normal brain. Furthermore, an increased APT signal intensity was also found in necrotic high-grade gliomas, indicating that highly concentrated mobile proteins and peptides in the microcystic extracellular space might also increase APT signal intensity in tumors. In contrast to PET, the APT measures the endogenous content of amide protons without requiring external contrast agents.

Apart from the costs, this might be an advantage concerning repetitive follow-up examinations especially in young tumor patients. Recently, a study of thirty-six patients showed that APT signal intensity did not only differentiate between gliomas WHO grade II and IV, but also between gliomas WHO grade II and III and between gliomas WHO grade III and IV (Togao et al. 2014). Thus, APT seems to be a promising method for tumor grading and for depicting tumor heterogeneity. Referring to the experiences in FET-PET (Chap. Advanced MR Methods in Differential Diagnosis of Brain Tumors), APT might even be a promising method to differentiate between therapy-induced changes and tumor progression in brain tumor patients. As mentioned above, the exchange rate depends on the pH; thus, the tumor pH (Chap. MR Spectroscopic Imaging) also affects the APT signal intensity. On the other hand, pH can be measured with CEST, providing another parameter which could be exploited in tumor diagnosis. This requires to eliminate ambiguous influences between the pH and amide proton content, e.g., by combination with an independent pH measurement using phosphorus MR spectroscopy (Chap. MR Imaging of Brain Tumors).

Glycolysis, either anaerobic or aerobic, is enhanced in high-grade brain tumors, and an overexpression of glucose transporter (GLUT) proteins has been found in glioblastoma. An increased uptake of glucose in PET is a typical finding in malignant brain tumors. First results indicate that glucose concentrations can be detected by CEST via the hydroxyl protons (glucoCEST) (Nasrallah et al. 2013). Significant enhancement of the glucoCEST signal has been found upon systemic glucose infusion in an experimental study with breast cancer cells (Chan et al. 2012). However, to our knowledge, this method has not been evaluated for in vivo gliomas. It might be an interesting tool to evaluate alternative glioma therapies such as the low-carbohydrate, ketogenic diet (Rieger et al. 2014).

Although not yet applied in oncological systems, another variation of CEST with great potential is the depiction of chemical exchange saturation transfer effect between the amine group of glutamate and bulk water, also named gluCEST (Cai et al. 2012). Here, the CEST effect depends on the pH and glutamate concentration. Glutamate is released from glioma cells, possibly as by-product of GSH synthesis, an antioxidant which enhances the resistance to oxidative stress (Sontheimer 2008). In addition, glutamate is an important anaplerotic substrate which delivers α-ketoglutarate to the citrate cycle. It substitutes the intermediates of the citrate cycle which are used for protein biosynthesis in proliferating tumor cells. Glutamate can be transformed to glutamine through the glutamate-glutamine cycle of reactive astrocytes. Glutamine is a major metabolic fuel for both brain tumor cells and tumor-associated macrophages, which may create a microenvironment that facilitates aggressive growth of tumor cells. Using MR spectroscopy, increasing glutamate concentrations were found in brain tumors (Kimura et al. 2007; Rijpkema et al. 2003). However, a reliable quantification of glutamate concentrations in tumor spectra is frequently hampered by the modulated baseline due to higher concentrations of lipids and macromolecules. Therefore, future investigations have to show whether gluCEST can provide reliable values for glutamate in tumors.

The methods based on chemical exchange contrast have a high potential to provide essential information on tumor biology, however, apart from CEST with amide protons (APT), these methods are still experimental. APT can be performed on clinical scanners and has been applied to human brain tumors providing promising results for diagnostic purposes. Since the CEST mechanism depends on metabolite concentration and pH, the reliability and robustness of the results have to be evaluated in studies with larger patient cohorts at different medical centers. In contrast, quantitative relaxometry and related methods are well suitable for standardized tumor diagnosis and monitoring, but their biological significance has to be validated in the future.

References

Andersen C, Haselgrove JC, Doenstrup S, Astrup J, Gyldensted C (1993) Resorption of peritumoural oedema in cerebral gliomas during dexamethasone treatment evaluated by NMR relaxation time imaging. Acta Neurochir (Wien) 122:218–224

Bähr O, Hattingen E, Rieger J, Steinbach JP (2011) Bevacizumab-induced tumor calcifications as a surrogate marker of outcome in patients with glioblastoma. Neuro Oncol 13:1020–1029

Bähr O, Harter PN, Weise LM, You SJ, Mittelbronn M, Ronellenfitsch MW, Rieger J, Steinbach JP, Hattingen E (2014) Sustained focal antitumor activity of bevacizumab in recurrent glioblastoma. Neurology 83:227–234

Bastin ME, Sinha S, Whittle IR, Wardlaw JM (2002) Measurements of water diffusion and T1 values in peritumoural oedematous brain. Neuroreport 13:1335–1340

Berghoff AS, Spanberger T, Ilhan-Mutlu A, Magerle M, Hutterer M, Woehrer A, Hackl M, Widhalm G, Christen T, Lemasson B, Pannetier N, Farion R, Remy C, Zaharchuk G, Barbier EL (2012) Is T2* enough to assess oxygenation? Quantitative blood oxygen level-dependent analysis in brain tumor. Radiology 262:495–502

Boyko OB, Burger PC, Shelburne JD, Ingram P (1992) Non-heme mechanisms for T1 shortening: pathologic, CT, and MR elucidation. AJNR Am J Neuroradiol 13:1439–1445

Cai K, Haris M, Singh A, Kogan F, Greenberg JH, Hariharan H, Detre JA, Reddy R (2012) Magnetic resonance imaging of glutamate. Nat Med 18:302–306

Chan KW, McMahon MT, Kato Y, Liu G, Bulte JW, Bhujwalla ZM, Artemov D, van Zijl PC (2012) Natural D-glucose as a biodegradable MRI contrast agent for detecting cancer. Magn Reson Med 68:1764–1773

Cheng HL, Stikov N, Ghugre NR, Wright GA (2012) Practical medical applications of quantitative MR relaxometry. J Magn Reson Imaging 36:805–824

Damadian R (1971) Tumor detection by nuclear magnetic resonance. Science 171(3976):1151–1153

Englund E, Brun A, Larsson EM, Györffy-Wagner Z, Persson B (1986) Tumours of the central nervous system. Proton magnetic resonance relaxation times T1 and T2 and histopathologic correlates. Acta Radiol Diagn (Stockh) 27:653–659

Fatouros PP, Marmarou A, Kraft KA, Inao S, Schwarz FP (1991) In vivo brain water determination by T1 measurements: effect of total water content, hydration fraction, and field strength. Magn Reson Med 17:402–413

Haacke EM, Xu Y, Cheng YC, Reichenbach JR (2004) Susceptibility weighted imaging (SWI). Magn Reson Med 52:612–618

Harguindey S, Arranz JL, Wahl ML, Orive G, Reshkin SJ (2009) Proton transport inhibitors as potentially selective anticancer drugs. Anticancer Res 29:2127–2136. Review

Haris M, Cai K, Singh A, Hariharan H, Reddy R (2011) In vivo mapping of brain myo-inositol. Neuroimage 54:2079–2085

Hasan KM, Walimuni IS, Abid H, Datta S, Wolinsky JS, Narayana PA (2012) Human brain atlas-based multimodal MRI analysis of volumetry, diffusimetry, relaxometry and lesion distribution in multiple sclerosis patients and healthy adult controls: implications for understanding the pathogenesis of multiple sclerosis and consolidation of quantitative MRI results in MS. J Neurol Sci 313:99–109

Hattingen E, Jurcoane A, Daneshvar K, Pilatus U, Mittelbronn M, Steinbach JP, Bähr O (2013) Quantitative T2 mapping of recurrent glioblastoma under bevacizumab improves monitoring for non-enhancing tumor progression and predicts overall survival. Neuro Oncol 15:1395–1404

Hoehn-Berlage M, Bockhorst K (1994) Quantitative magnetic resonance imaging of rat brain tumors: in vivo NMR relaxometry for the discrimination of normal and pathological tissues. Technol Health Care 2:247–254

Hoehn-Berlage M, Tolxdorff T, Bockhorst K, Okada Y, Ernestus RI (1992) In vivo NMR T2 relaxation of experimental brain tumors in the cat: a multiparameter tissue characterization. Magn Reson Imaging 10:935–947

Hoskin PJ, Carnell DM, Taylor NJ, Smith RE, Stirling JJ, Daley FM, Saunders MI, Bentzen SM, Collins DJ, d'Arcy JA, Padhani AP (2007) Hypoxia in prostate cancer: correlation of BOLD-MRI with pimonidazole immunohistochemistry-initial observations. Int J Radiat Oncol Biol Phys 68:1065–1071

Jin T, Wang P, Zong X, Kim S-G (2012) Magnetic resonance imaging of the Amine–Proton EXchange (APEX) dependent contrast. Neuroimage 59:1218–1227

Jones CK, Schlosser MJ, van Zijl PC, Pomper MG, Golay X, Zhou J (2006) Amide proton transfer imaging of human brain tumors at 3 T. Magn Reson Med 56:585–592

Jurcoane A, Wagner M, Schmidt C, Mayer C, Gracien RM, Hirschmann M, Deichmann R, Volz S, Ziemann U, Hattingen E (2013) Within-lesion differences in quantitative MRI parameters predict contrast enhancement in multiple sclerosis. J Magn Reson Imaging 38:1454–1461

Kim HS, Jahng GH, Ryu CW, Kim SY (2009) Added value and diagnostic performance of intratumoral susceptibility signals in the differential diagnosis of solitary enhancing brain lesions: preliminary study. AJNR Am J Neuroradiol 30:1574–1579

Kimura T, Ohkubo M, Igarashi H, Kwee IL, Nakada T (2007) Increase in glutamate as a sensitive indicator of extracellular matrix integrity in peritumoral edema: a 3.0-tesla proton magnetic resonance spectroscopy study. J Neurosurg 106:609–613

Larocque MP, Syme A, Yahya A, Wachowicz K, Allalunis-Turner J, Fallone BG (2009) Temporal and dose dependence of T2 and ADC at 9.4 T in a mouse model following single fraction radiation therapy. Med Phys 36:2948–2954

Lin T, Autio J, Obata T, Kim SG (2011) Spin-locking versus chemical exchange saturation transfer MRI for investigating chemical exchange process between water and labile metabolite protons. Magn Reson Med 65:1448–1460

MacDonald HL, Bell BA, Smith MA, Kean DM, Tocher JL, Douglas RH, Miller JD, Best JJ (1986) Correlation of human NMR T1 values measured in vivo and brain water content. Br J Radiol 59:355–357

Mittal S, Wu Z, Neelavalli J, Haacke EM (2009) Susceptibility-weighted imaging: technical aspects and clinical applications, part 2. AJNR Am J Neuroradiol 30:232–252

Nasrallah FA, Pagès G, Kuchel PW, Golay X, Chuang KH (2013) Imaging brain deoxyglucose uptake and metabolism by glucoCEST MRI. J Cereb Blood Flow Metab 33:1270–1278

Oh J, Cha S, Aiken AH, Han ET, Crane JC, Stainsby JA, Wright GA, Dillon WP, Nelson SJ (2005) Quantitative apparent diffusion coefficients and T2 relaxation times in characterizing contrast enhancing brain tumors and regions of peritumoral edema. J Magn Reson Imaging 21:701–708

Park SM, Kim HS, Jahng GH, Ryu CW, Kim SY (2010) Combination of high-resolution susceptibility-weighted imaging and the apparent diffusion coefficient: added value to brain tumour imaging and clinical feasibility of non-contrast MRI at 3 T. Br J Radiol 83:466–475

Peters S, Knöß N, Wodarg F, Cnyrim C, Jansen O (2012) Glioblastomas versus lymphomas: More diagnostic certainty by using susceptibility-weighted imaging (SWI). Fortschr Roentgenstr 184: 713–718

Rieger J, Bähr O, Maurer GD, Hattingen E, Franz K, Brucker D, Walenta S, Kämmerer U, Coy JF, Weller M, Steinbach JP (2014) ERGO: a pilot study of ketogenic diet in recurrent glioblastoma. Int J Oncol 44:1843–1852

Rijpkema M, Schuuring J, van der Meulen Y, van der Graaf M, Bernsen H, Boerman R, van der Kogel A, Heerschap A (2003) Characterization of oligodendrogliomas using short echo time 1H MR spectroscopic imaging. NMR Biomed 16:12–18

Saitta L, Heese O, Förster AF, Matschke J, Siemonsen S, Castellan L, Westphal M, Fiehler J, Goebell E (2011) Signal intensity in T2′ magnetic resonance imaging is related to brain glioma grade. Eur Radiol 21:1068–1076

Schad LR, Blüml S, Zuna I (1993) MR tissue characterization of intracranial tumors by means of texture analysis. Magn Reson Imaging 11:889–896

Sherry AD, Woods M (2008) Chemical exchange saturation transfer contrast agents for magnetic resonance imaging. Annu Rev Biomed Eng 10:391–411

Sontheimer H (2008) A role for glutamate in growth and invasion of primary brain tumors. J Neurochem 105:287–295

Tofts P (ed) Quantitative MRI of the brain: measuring changes caused by disease. John Wiley & Sons, Chichester, England in 2003. pp 272–298

Togao O, Yoshiura T, Keupp J, Hiwatashi A, Yamashita K, Kikuchi K, Suzuki Y, Suzuki SO, Iwaki T, Hata N, Mizoguchi M, Yoshimoto K, Sagiyama K, Takahashi M, Honda H (2014) Amide proton transfer imaging of adult diffuse gliomas: correlation with histopathological grades. Neuro Oncol 16:441–448

Tóth V, Förschler A, Hirsch NM, den Hollander J, Kooijman H, Gempt J, Ringel F, Schlegel J, Zimmer C, Preibisch C (2013) MR-based hypoxia measures in human glioma. J Neurooncol 115:197–207

van Zijl PC, Yadav NN (2011) Chemical exchange saturation transfer (CEST): what is in a name and what isn't? Magn Reson Med 65:927–948

van Zijl PC, Zhou J, Mori N, Payen JF, Wilson D, Mori S (2003) Mechanism of magnetization transfer during on-resonance water saturation. A new approach to detect mobile proteins, peptides, and lipids. Magn Reson Med 49:440–449

van Zijl PC, Jones CK, Ren J, Malloy CR, Sherry AD (2007) MRI detection of glycogen in vivo by using chemical exchange saturation transfer imaging (glycoCEST). Proc Natl Acad Sci U S A 13(104):4359–4364

Ward KM, Balaban RS (2000) Determination of pH using water protons and chemical exchange dependent saturation transfer (CEST). Magn Reson Med 44:799–802

Ward KM, Aletras AH, Balaban RS (2000) A new class of contrast agents for MRI based on proton chemical exchange dependent saturation transfer (CEST). J Magn Reson 143:79–87

Zhou J, van Zijl PC (2006) Chemical exchange saturation transfer imaging and spectroscopy. Prog Nucl Magn Reson Spectrosc 48:109–136

Zhou J, Lal B, Wilson DA, Laterra J, van Zijl PC (2003a) Amide proton transfer (APT) contrast for imaging of brain tumors. Magn Reson Med 50:1120–1126

Zhou J, Payen JF, Wilson DA, Traystman RJ, van Zijl PC (2003b) Using the amide proton signals of intracellular proteins and peptides to detect pH effects in MRI. Nat Med 9:1085–1090

Zhou J, Blakeley JO, Hua J, Kim M, Laterra J, Pomper MG, van Zijl PC (2008) Practical data acquisition method for human brain tumor amide proton transfer (APT) imaging. Magn Reson Med 60:842–849

Zhou J, Tryggestad E, Wen Z, Lal B, Zhou T, Grossman R, Wang S, Yan K, Fu DX, Ford E, Tyler B, Blakeley J, Laterra J, van Zijl PC (2011) Differentiation between glioma and radiation necrosis using molecular magnetic resonance imaging of endogenous proteins and peptides. Nat Med 17:130–134

PET Imaging of Brain Tumors

Karl-Josef Langen and Norbert Galldiks

Contents

Abstract

Routine diagnostics and treatment monitoring of brain tumors is usually based on magnetic resonance imaging (MRI), but the capacity of conventional MRI to differentiate tumor tissue from nonspecific tissue changes may be limited especially after therapeutic interventions such as neurosurgical resection, radiotherapy, and chemotherapy. Molecular imaging using positron-emission tomography (PET) may provide relevant additional information on tumor metabolism, which allows for more accurate diagnostics especially in clinically equivocal situations. In the last decades, a variety of molecular targets have been addressed by specific PET tracers, but only a few have achieved relevance in routine clinical practice. This book chapter is focussed on PET tracers that appear to be especially helpful in clinical decision-making with regard to a better delineation of brain tumors, prognosis, and grading, improved differentiation of tumor recurrence from nonspecific posttherapeutic changes, and treatment monitoring.

Abbreviations

PET	Positron-emission tomography
MRI	Magnetic resonance imaging
MET	^{11}C-methionine
FET	^{18}F-fluoroethyltyrosine
FDOPA	3,4-Dihydroxy-6-^{18}F-fluoro-L-phenylalanine
BBB	Blood-brain barrier
FLT	^{18}F-3′-deoxy-3′-fluorothymidine
FMISO	^{18}F-fluoromisonidazole
HGG	High-grade gliomas
LGG	Low-grade gliomas

K.-J. Langen (✉)
Institute of Neuroscience and Medicine, Forschungszentrum Jülich, D-52425 Jülich, Germany
e-mail: k.j.langen@fz-juelich.de

Department of Nuclear Medicine, RWTH Aachen University Hospital, Aachen, Germany

N. Galldiks
Institute of Neuroscience and Medicine, Forschungszentrum Jülich, D-52425 Jülich, Germany

Department of Neurology, University of Cologne, Cologne, Germany

E. Hattingen, U. Pilatus (eds.), *Brain Tumor Imaging*, Medical Radiology. Diagnostic Imaging, DOI: 10.1007/174_2016_937,

1 Introduction

Routine diagnostics and treatment monitoring of brain tumors is usually based on magnetic resonance imaging (MRI), but the capacity of conventional MRI to differentiate tumor tissue from nonspecific tissue changes may be limited especially after therapeutic interventions such as neurosurgical resection, radiotherapy, and chemotherapy. Molecular imaging using positron-emission tomography (PET) may provide relevant additional information on tumor metabolism, which allows for more accurate diagnostics especially in clinically equivocal situations. In the last decades, a variety of molecular targets have been addressed by specific PET tracers, but only a few have achieved relevance in routine clinical practice. This chapter is focussed on PET tracers that appear to be especially helpful in clinical decision-making with regard to a better delineation of brain tumors, prognosis, and grading, improved differentiation of tumor recurrence from nonspecific posttherapeutic changes, and treatment monitoring.

2 Methods

Positron-emission tomography (PET) is based on the use of positron-emitting radionuclides that are incorporated either into substrates normally used by the human organism, such as glucose or amino acids, or into molecules that bind to receptors or participate in specific metabolic pathways. More than 70 different PET tracers have been explored in brain tumors in the last decades. Since it is beyond the scope of this chapter to address all of these tracers, this overview is focussed on those PET tracers or tracer groups that are promising in providing valuable clinical information on the basis of the current literature.

2.1 ^{18}F-2-Fluoro-2-Deoxy-D-Glucose

^{18}F-2-fluoro-2-deoxy-D-glucose (FDG), which measures cellular glucose metabolism as a function of the enzyme hexokinase, is the most common clinically utilized PET tracer due to its high potential to detect tumors in the body based on increased energy demand of malignant tumors. In the brain, FDG exhibits high uptake in normal gray matter, reflecting the metabolic demands of neurons and glia. Regional cerebral glucose consumption can be calculated by measuring quantitative FDG uptake in brain, blood glucose concentration, an arterial input of the tracer, and a "lumped constant" which accounts for differences in enzyme affinity between FDG and glucose (Herholz et al. 2012). In clinical practice, however, FDG uptake is usually quantified by standard uptake values (SUV), which reflect regional FDG uptake normalized to body weight and injected dose. In brain neoplasms, tumor-to-brain ratios using the mean or maximal tracer uptake in the tumor region divided by the mean uptake value in the contralateral brain is the preferred method. The high and regionally variable FDG uptake in normal brain parenchyma often makes the delineation of brain tumors difficult. Thus, the localization of brain tumors with FDG PET is difficult and only co-registration of FDG uptake images with MRI may allow the rating of glucose metabolism in specific areas of a tumor. There have been studies suggesting that additional delayed imaging at 180 min or later after tracer injection may increase the contrast between malignant tumors with high FDG uptake and normal brain, but the sensitivity to detect the extent of low-grade gliomas remains poor (Spence et al. 2004; Prieto et al. 2011). Another problem of FDG is the high tracer uptake in inflammatory cells. FDG accumulates in malignant tissue but also at the sites of infection and inflammation and in autoimmune and granulomatous diseases by the overexpression of distinct facultative glucose transporter (GLUT) isotypes (mainly GLUT-1 and GLUT-3) and by overproduction of glycolytic enzymes in cancer cells and inflammatory cells (Meller et al. 2007). Therefore, FDG PET is also used as a diagnostic method in fever of unknown origin (Meller et al. 2007).

2.2 Radiolabeled Amino Acids

Besides FDG, radiolabeled amino acids are the most commonly used PET tracers for brain tumors. An advantage over FDG is the relatively low uptake of amino acids by normal brain tissue. Therefore, cerebral gliomas can be distinguished from the surrounding normal tissue with higher contrast compared with FDG. Many natural amino acids and their synthetic analogs have been labeled by positron-emitting isotopes and explored as tumor imaging agents (Jager et al. 2001; Crippa et al. 2012; Huang and McConathy 2013). Most PET studies of cerebral gliomas have been performed with the amino acid [^{11}C]methyl-L-methionine (MET) (Singhal et al. 2008; Crippa et al. 2012), although the short half-life of ^{11}C (20 min) limits the use of this tracer to the few centers that are equipped with an in-house cyclotron facility. The increasing use of ^{18}F-labeled amino acids (half-life, 109 min) such as O-(2-^{18}F-fluoroethyl)-L-tyrosine (FET) or 3,4-dihydroxy-6-[^{18}F]fluoro-L-phenylalanine (FDOPA) will probably replace MET in the future (Becherer et al. 2003; Langen et al. 2006, 2008; Chen et al. 2008; Herholz et al. 2012; Walter et al. 2012).

The increased uptake of amino acids such as MET, FET, or FDOPA by cerebral glioma tissue appears to be caused almost entirely by increased transport via specific amino acid transporters, namely, *transport system L for large neutral amino acids* (Jager et al. 2001; Bergmann et al. 2004;

Langen and Broer 2004; Langen et al. 2006; Huang and McConathy 2013). MET also shows some incorporation into proteins and participation in other metabolic pathways (Singhal et al. 2008), but comparative studies between MET, FET, and FDOPA have shown that imaging of cerebral gliomas is very similar with these amino acids (Weber et al. 2000; Becherer et al. 2003; Langen et al. 2003; Grosu et al. 2011). Therefore, the participation of MET in other metabolic pathways than transport appears to be of minor importance and the clinical results obtained with the different tracers can be considered together. Since large neutral amino acids also enter normal brain tissue, a disruption of the blood-brain barrier (BBB), i.e., enhancement of contrast agent in CT or MRI scans, is not a prerequisite for intratumoral accumulation of these amino acids. Consequently, uptake of the tracers has been reported in many low-grade gliomas without BBB leakage (Herholz et al. 1998; Ribom et al. 2001; Floeth et al. 2007; Kunz et al. 2011; Smits and Baumert 2011; Rapp et al. 2013a). The sensitivity and specificity of PET using MET and FET to differentiate between gliomas and non-neoplastic lesions is within the range of 60–90 % (Herholz et al. 1998; Pichler et al. 2010; Dunet et al. 2012; Rapp et al. 2013b), and the possibility of nonspecific enhancement in inflammatory cells or reactive glial tissue must be kept in mind. There have been reports of perifocal MET and FET uptake around hematomas and areas of ischemia, as well as of rare cases of uptake in or around ring-enhancing lesion like brain abscesses and acute inflammatory demyelination (Delbeke et al. 1995; Floeth et al. 2006; Singhal et al. 2008; Hutterer et al. 2013).

2.3 Radiolabeled Nucleoside Analogs

Another approach in molecular imaging of brain tumors is the use of radiolabeled nucleoside analogs such as [^{18}F]3′-deoxy-3′-fluorothymidine (FLT) (Shields et al. 1998; Shields 2003). Once FLT is transported into the cell, it is phosphorylated by thymidine kinase (TK-1) and trapped inside the cell (Bading and Shields 2008). TK-1 is a cytosolic enzyme that is expressed *during the DNA synthesis stage of the cell cycle*. Compared to normal proliferating tissues, tumor cells have increased levels of TK-1, resulting in increased FLT uptake (Shields et al. 1998). A high rate of cellular proliferation is a key feature of malignant tumors, and proliferation markers (e.g., Ki-67) have shown a better correlation with the grade of malignancy and prognosis of cerebral gliomas than FDG uptake (Chen et al. 2005). Uptake of FLT, however, depends on BBB damage because transport across the normal BBB is slow (Chen et al. 2005; Jacobs et al. 2005). Therefore, this method does not delineate tumor parts with intact BBB (e.g., in low-grade gliomas) and is less suited to depict the full extent of cerebral gliomas.

2.4 Imaging of Hypoxia

Furthermore, imaging of hypoxia is an interesting approach to explore the metabolic features in brain tumors. Hypoxia plays a critical role in tumor development and aggressiveness and is an important prognostic factor for resistance to antineoplastic treatments (Langen and Eschmann 2008). A number of hypoxia tracers are available for PET, of which ^{18}F-fluoromisonidazole (FMISO) today is the most frequently studied tracer (Lee and Scott 2007). FMISO enters cells by passive diffusion, where it is reduced by nitroreductase enzymes to become trapped *in cells with reduced tissue oxygen partial pressure*. When oxygen is abundant in normally oxygenated cells, the parent compound is quickly regenerated by reoxidation and metabolites do not accumulate. However, in hypoxic cells, the low oxygen partial pressure prevents reoxidation of FMISO metabolites, resulting in tracer accumulation in hypoxic cells. Because FMISO only accumulates in hypoxic cells with functional nitroreductase enzymes, FMISO only accumulates in viable cells but not in dead necrotic cells (Lee and Scott 2007).

2.5 Imaging Angiogenesis

Another target of growing interest in molecular imaging is angiogenesis. One target structure is the *$\alpha_v\beta_3$-integrin receptor*, which is highly expressed on activated endothelial cells during angiogenesis. Various ligands based on the tripeptide RGD (Arg-Gly-Asp), which binds with high affinity to the $\alpha_v\beta_3$-integrin receptor, have been developed for PET (Haubner et al. 2010). The glycosylated cyclic pentapeptide ^{18}F-galacto-RGD has been successfully applied in patients with malignant gliomas, but studies on the clinical relevance of this approach for treatment planning are still scarce (Schnell et al. 2009).

2.6 Somatostatin Receptors

Moreover, somatostatin receptors have been used as a target for molecular imaging of brain tumors, especially in meningiomas. Meningiomas demonstrate expression of a variety of receptors, including *somatostatin receptor subtype* 2 (SSTR2). The SSTR2 receptor ligand ^{68}Ga-DOTATOC demonstrates high-resolution imaging and high tumor-background contrast in meningiomas and may provide valuable additional information on the extent of meningiomas beneath osseous structures, especially at the skull base (Henze et al. 2005; Gehler et al. 2009; Nyuyki et al. 2010; Graf et al. 2013). Somatostatin receptors are also present in childhood tumors, especially in medulloblastomas.

Table 1 Important PET tracers for brain tumors

Tracer	Molecular target
^{18}F-2-fluoro-2-deoxy-D-glucose (FDG)	Glucose metabolism
^{11}C-methyl-L-methionine (MET)	Amino acid transport
O-(2-^{18}F-fluoroethyl)-L-tyrosine (FET)	Amino acid transport
3,4-Dihydroxy-6-^{18}F-fluoro-L-phenylalanine (FDOPA)	Amino acid transport
^{18}F-3′-deoxy-3′-fluorothymidine (FLT)	Proliferation
^{18}F-fluoromisonidazole (FMISO)	Hypoxia
^{18}F-fluoroethyl-choline	Phospholipid synthesis
^{68}Ga-DOTATOC	Somatostatin receptors

2.7 Radiolabeled Choline

A number of studies have also investigated the role of radiolabeled choline in brain tumor imaging (Kwee et al. 2007; Gulyas et al. 2008; Kato et al. 2008). Choline is an essential nutrient that serves as an extrinsic substrate for the *synthesis of phosphatidylcholine*, which is a major constituent of the cell membrane. Phosphorylation by choline kinase constitutes an important step in the incorporation of choline into phospholipids, which is relevant for cell viability. In cancer, there is often an increase in the cellular transport and phosphorylation of choline, as well as an increase in the expression of choline kinase enzyme (Kwee et al. 2007). Uptake of choline, however, depends on BBB damage similar to FLT. Therefore, choline uptake appears to be limited to tumors with contrast enhancement in CT or MRI and does not accumulate in nonenhancing low-grade glioma (Roelcke et al. 2012).

Finally, various *radiolabeled chemotherapeuticals* such as ^{11}C-temozolomide have been used to get information on metabolism and pharmacokinetics of the substances in brain tumors, but experiences are limited to small numbers of patients (Saleem et al. 2003).

An overview of the most important radiotracers for the diagnosis of brain tumors with PET is presented in Table 1.

3 Delineation of Tumor Extent, Biopsy Guidance, and Treatment Planning

One of the most important aspects in the initial diagnosis of gliomas is the identification of tumor extension and the metabolically most active areas of the tumor. Representative tissue samples are vital for histological tumor diagnosis, prognostication, and treatment planning. The ability of contrast-enhanced MRI to show the most rapidly proliferating portions of the usually inhomogeneous gliomas is limited, particularly when the tumor does not show contrast enhancement on MRI. Multiple studies comparing the radiological findings with the histological findings in tissue samples from biopsy or open surgery have provided evidence that PET using radiolabeled amino acids detects the solid mass of gliomas and metabolically active tumor areas more reliably than either CT or MRI (Mosskin et al. 1989; Goldman et al. 1997; Kracht et al. 2004; Pauleit et al. 2005, 2009; Pirotte et al. 2007) (Fig. 1). This helps to prevent the problem of nondiagnostic biopsies from nonspecifically altered tissue and to plan invasive procedures (e.g., tumor resection, stereotactic biopsy) (Fig. 2). Local maxima of FDG uptake in heterogeneous gliomas are usually colocalized with amino acid uptake, but MET and FET PET have been shown to be considerably more sensitive than FDG PET for biopsy guidance (Pirotte et al. 2004; Pauleit et al. 2009; Plotkin et al. 2010). (Fig. 3).

Furthermore, it has been demonstrated that integrating MET PET for resection guidance of high-grade gliomas provided a final target contour different from that obtained with MRI alone in about 80 % of the procedures (Pirotte et al. 2009). Complete resection of the tumor area with increased amino acid uptake resulted in significantly longer survival of patients, while the degree of contrast enhancement on the postoperative MRI scan did not have an impact on survival. Similarly, the amount of residual tracer uptake in FET PET had a strong prognostic influence (Piroth et al. 2011a). These data indicate that resection of malignant gliomas guided by amino acid PET may increase the amount of anaplastic tissue removal and thus patients' survival.

The improved imaging of glioma tissue using amino acid PET has also attracted interest for radiation treatment planning (Grosu and Weber 2010; Matsuo et al. 2012). A number of centers have started to integrate amino acid imaging into CT- and MRI-based radiotherapy planning, particularly when high-precision radiotherapy is performed or in the setting of dose escalation studies or for the reirradiation of recurrent tumors (Levivier et al. 2004; Grosu et al. 2005; Rickhey et al. 2008; Weber et al. 2008; Piroth et al. 2009). Improved outcome of the patients with radiotherapy planning using amino acid imaging compared with conventional radiation therapy planning, however, has not yet been proven. A recent prospective study indicated that an integrated boost intensity-modulated radiation dose escalation concept, which was based on FET PET-guided

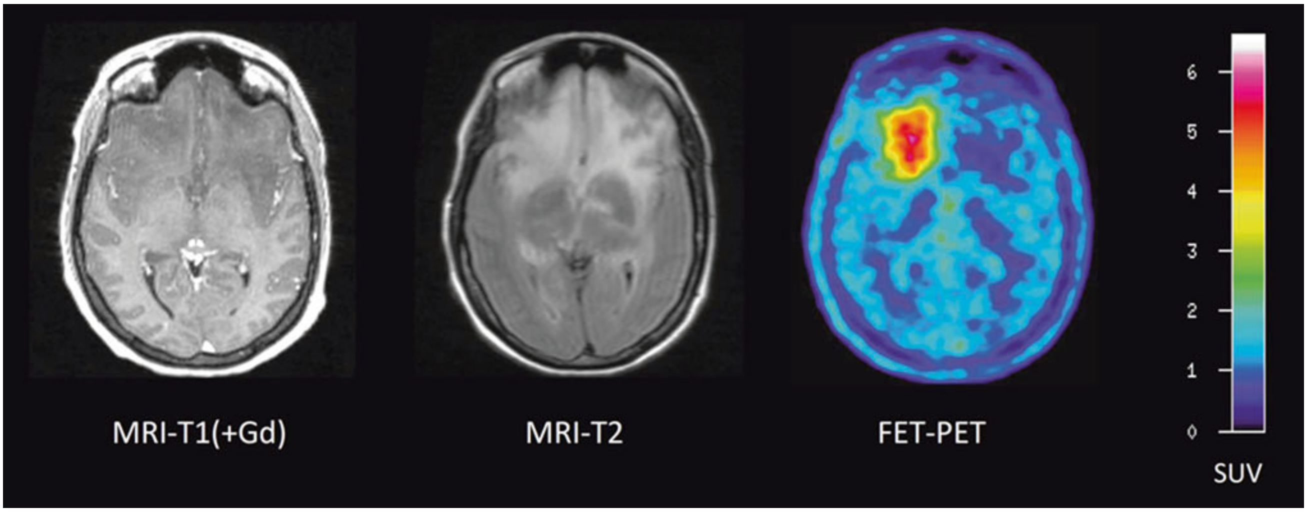

Fig. 1 Patient with an astrocytoma of WHO grade II in the frontal lobe. T1-weighted MRI after application of Gd-DTPA shows no pathological contrast enhancement and the tumor cannot be delineated. T2-weighted MRI shows widespread abnormalities in the frontal lobe and is not helpful to depict the tumor. FET PET identifies a tumor with high tracer uptake in the lower frontal lobe

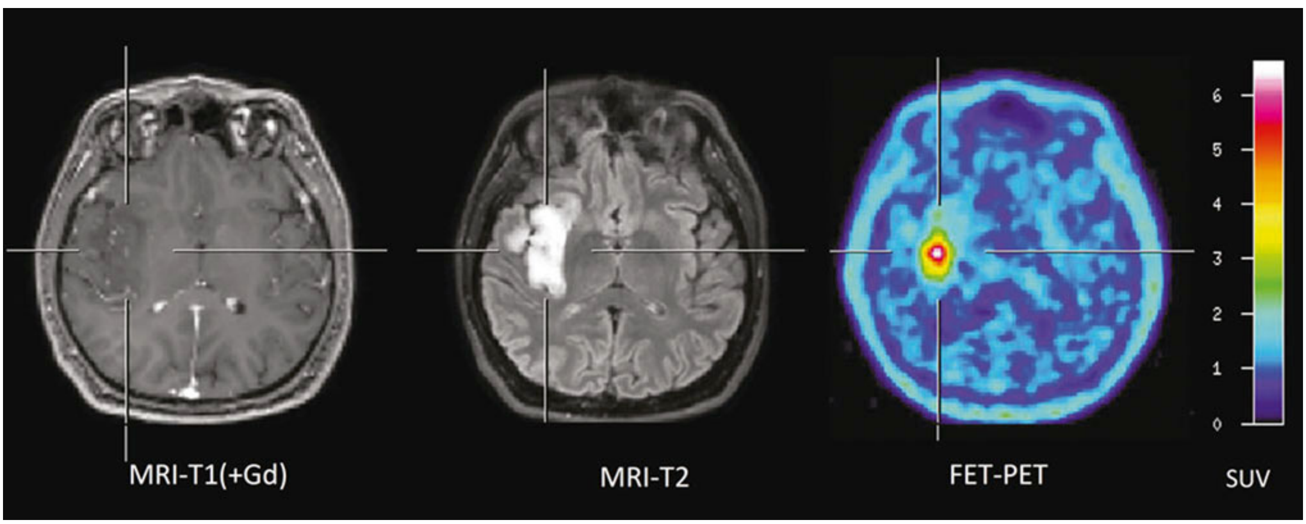

Fig. 2 Patient with a diffused astrocytoma of WHO grade II. T1-weighted MRI on the left shows no contrast enhancement and in the T2-weighted MRI (*middle*) diffused signal abnormalities. FET PET identifies a local maximum in the tumor for biopsy guidance

target volume delineation, showed no survival benefit for the patients (Piroth et al. 2012). The failure of that prospective study to improve survival time of the patients, however, does not mean that amino acid PET is an ineffective tool to plan radiotherapy in cerebral gliomas. Local relapses are usually detected within the 95 % dose-volume indicating that the local dose escalation is not able to improve local tumor control (Lee et al. 2009; Weber et al. 2009).

In meningiomas, promising results concerning imaging of tumor extent have been reported using the somatostatin receptor ligand ^{68}Ga-DOTATOC (Gehler et al. 2009; Nyuyki et al. 2010; Thorwarth et al. 2011; Afshar-Oromieh et al. 2012). All studies consistently reported that ^{68}Ga-DOTATOC PET/CT information may strongly complement anatomical data from MRI and CT in cases with complex meningioma and is thus helpful for improved target volume delineation especially for skull base manifestations and recurrent disease after surgery (Fig. 4).

4 Tumor Grading and Prognosis

FDG PET is considered as a relative accurate predictor of the World Health Organization (WHO) grading and prognosis of cerebral gliomas since the early days of PET (Di Chiro et al. 1982; Delbeke et al. 1995; Padma et al.

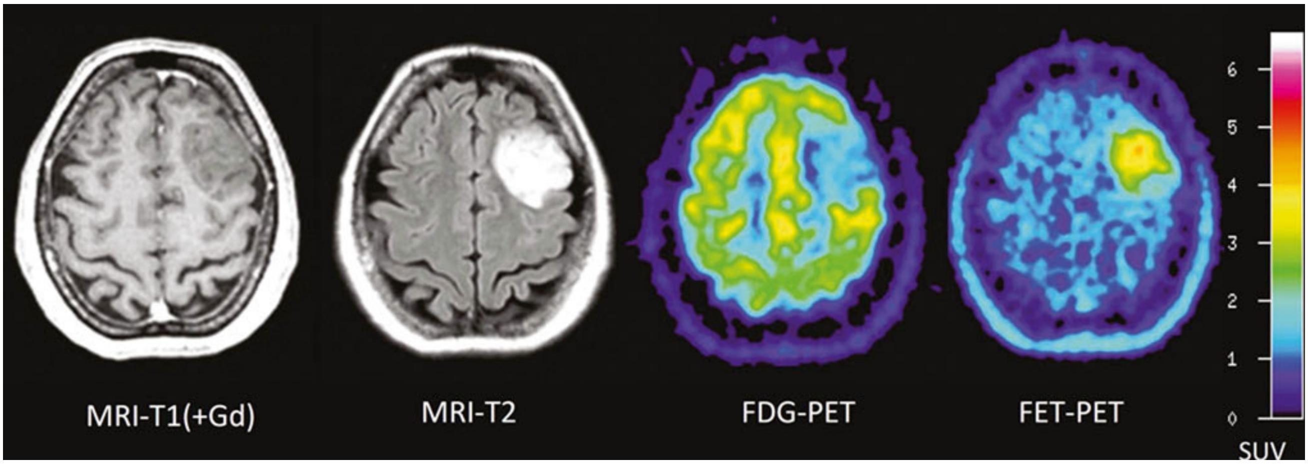

Fig. 3 Patient with a diffused astrocytoma of WHO grade II. T1-weighted MRI on the left shows no contrast enhancement in the tumor and FDG uptake is low. Again, FET PET exhibits increased tracer uptake and identifies a local maximum for biopsy guidance

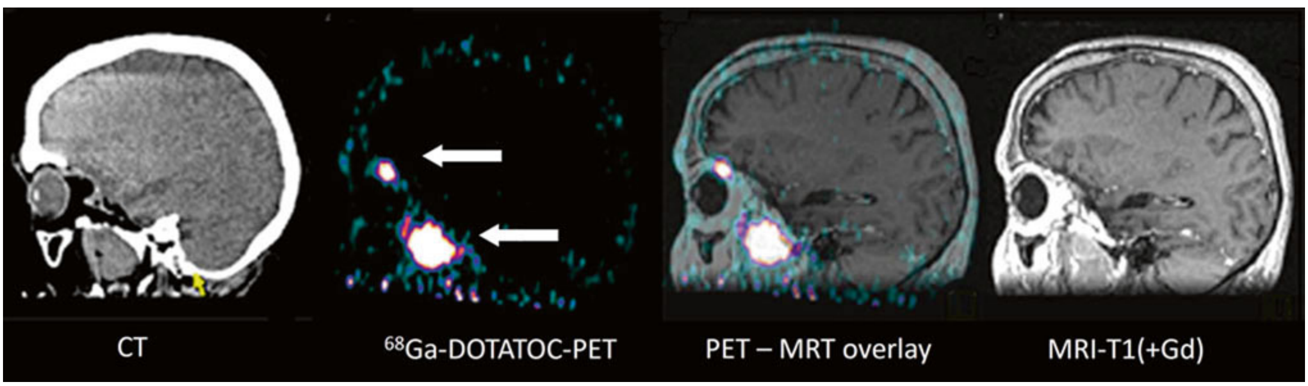

Fig. 4 Patient with a recurrent skull base meningioma 2 years after resection. Both MRI and PET/CT indicate a tumor, but ^{68}Ga-DOTATOC PET shows an additional intraorbital lesion, which is not detectable by MRI (Courtesy of Michail Plotkin, Vivantes Clinics Berlin, Germany)

2003; Chen 2007). In many studies, high-grade gliomas (HGG) could be differentiated from low-grade gliomas (LGG) (Kaschten et al. 1998; Borbely et al. 2006; Singhal et al. 2012). However, in these studies, the rate of correct identification of an HGG varies considerably. Furthermore, some studies observed no significant differences of FDG uptake in LGG and HGG (Kim et al. 2005; Miyake et al. 2012).

Some authors reported that the proliferation marker FLT may be a more powerful predictor of tumor progression and survival (Chen et al. 2005; Choi et al. 2005; Miyake et al. 2012). A relationship between in vivo derived kinetic parameters of FLT uptake and proliferation rate could be demonstrated in patients with HGG (Ullrich et al. 2008). The rate constant indicating phosphorylation k_3 had a significant correlation with proliferation index Ki-67, whereas the transport rate K_1 did not. No significant correlation was found between SUV of FLT and Ki-67 by immunostaining indicating that kinetic analysis was helpful for in vivo assessment of tumor proliferation in high-grade gliomas. Grade of malignancy and proliferation activity of primary brain tumors can be evaluated by FLT, but a limitation is high uptake in benign lesions that disrupt the blood-brain barrier and in necrotic areas (Saga et al. 2006; Miyake et al. 2012). Furthermore, some studies reported on a relationship between tumor grade and uptake of choline derivatives, but the number of studies is still too small to draw final conclusions (Kato et al. 2008; Gulyas and Halldin 2012).

Most studies employing amino acid PET have shown that gliomas of different WHO grades substantially overlap in their degree of amino acid uptake, so that the tumor grade cannot be reliably predicted with this technique (Pauleit et al. 2005; Ceyssens et al. 2006; Dunet et al. 2012; Rapp et al. 2013b). A more reliable grading, however, appears to be possible with FET PET, since this tracer exhibits differences in the time activity curves of tracer uptake depending on tumor grade (Weckesser et al. 2005). HGGs are characterized by an early peak around 10–15 min after injection followed by a decrease of FET uptake, while LGGs typically exhibit delayed and steadily increasing tracer uptake. Using dynamic FET PET, a differentiation of HGG and LGG has been reported in primary tumors as well as in recurrent tumors with an accuracy >80 % (Pöpperl et al. 2006b, 2007; Calcagni et al. 2011; Kunz et al. 2011; Jansen et al. 2012).

The prognostic significance of increased amino acid uptake in gliomas is controversial. Some studies seem to show that lower amino acid uptake especially in astrocytic glioma is associated with a better prognosis, but there may be high uptake in oligodendrogliomas of WHO grade II and III despite their apparently better prognosis (Kaschten et al. 1998; Pöpperl et al. 2007; Singhal et al. 2008). A further study suggests that the pretreatment volume of MET uptake but not the semiquantitative MET uptake ratio is a useful biologic prognostic marker in patients with anaplastic astrocytoma and glioblastoma (Galldiks et al. 2012a).

There appears, however, to be a consensus concerning the clinical role of amino acid imaging in prognostication for patients with LGG. Significant longer survival has been reported for patients with lower MET uptake in the tumors compared to those with higher uptake (cutoff of the tumor-to-brain ratio: 2.1) (Ribom et al. 2001; Smits et al. 2008; Smits and Baumert 2011; Arbizu et al. 2012). Furthermore, the patients only had a benefit from a surgical procedure if increased MET uptake was present (Ribom et al. 2001). Using FET PET, the combination with MR morphology has also been found to be a significant prognostic predictor for patients with newly diagnosed LGG (Floeth et al. 2007). Baseline FET uptake and a circumscribed versus a diffuse growth pattern on MRI were highly significant predictors for the patients' clinical course and outcome. Thus, combined assessment with amino acid PET and MRI can identify subgroups of patients with a stable course in which a "watch and wait" strategy is reasonable and patients with LGG who should receive early and aggressive treatment in order to avoid malignant transformation.

In summary, in comparison to morphological MR features, PET adds valuable information concerning grading and prognosis in patients with newly diagnosed cerebral lesions. The diagnostic accuracy, however, is not sufficient to make a final decision on the therapeutic procedure. Therefore, a histological evaluation of suspicious brain lesions by biopsy remains necessary in most of the patients with brain tumors.

5 Treatment Monitoring

The diagnostic value of MRI and CT concerning changes in tumor size or contrast enhancement in response to therapy is limited since the known reactive transient BBB alterations with consecutive contrast enhancement may mimic tumor progression. This phenomenon, so-called pseudoprogression, is seen in 20–47 % of cases and can lead to an unnecessary overtreatment (Lustig et al. 2007) (Fig. 5).

FDG PET is considered not to be ideal to evaluate treatment response because of the high accumulation in nonspecific reactive changes in the tissue (Basu and Alavi 2009). The feasibility and usefulness of MET and FET PET for treatment assessment and follow-up after surgery, chemotherapy, and radiotherapy have been demonstrated in several studies. The currently available data suggest that a reduction of amino acid uptake of a glioma is a sign of a response to treatment. Recently, a prospective study evaluated the prognostic value of early changes of FET uptake after postoperative radiochemotherapy in patients with glioblastoma (RCX) (Piroth et al. 2011b; Galldiks et al. 2012c). It could be demonstrated that PET responders with a decrease of the tumor/brain ratio of more than 10 % had a significantly longer disease-free survival and overall survival than patients with stable or increasing tracer uptake after RCX. A reliable monitoring of temozolomide chemotherapy could also be demonstrated with MET in patients with recurrent HGG (Galldiks et al. 2006, 2010a) and also in some experimental therapeutic approaches like radioimmunotherapy, convection-enhanced delivery of paclitaxel, and chemotherapy with bevacizumab and irinotecan (Pöpperl et al. 2005, 2006a; Hutterer et al. 2011; Galldiks et al. 2013). Therefore, monitoring of treatment response using amino acid PET imaging is now utilized to provide an early assessment of therapy efficacy and aid oncologists to optimize therapeutic management of brain tumors.

A number of studies have examined the value of FLT PET, an imaging biomarker of cell proliferation, for treatment monitoring (Fig. 6), especially in patients with recurrent malignant glioma treated with an antiangiogenic therapy, i.e., bevacizumab, predominantly in combination with irinotecan (Chen et al. 2007; Schiepers et al. 2010; Harris et al. 2012; Schwarzenberg et al. 2012). In comparison to standard MRI, the authors found that changes of FLT uptake were highly predictive of progression-free and overall survival in patients with recurrent malignant glioma on bevacizumab therapy. FLT PET seems to be more predictive than standard MRI for early treatment response.

Furthermore, FMISO PET seems to have the potential to monitor treatment effects. In order to evaluate the tumor oxygenation status before and immediately after fractionated radiochemotherapy with temozolomide, two glioblastoma patients underwent serial FMISO PET studies (Narita et al. 2012). In comparison to the baseline FMISO scan, in both patients, the FMISO uptake in the tumor was notably decreased in the follow-up scan, supposing a reoxygenation of the tumor. These observations suggest that changes in the oxygenation status in glioblastoma may be suitable for monitoring of radiation therapy with concomitant temozolomide.

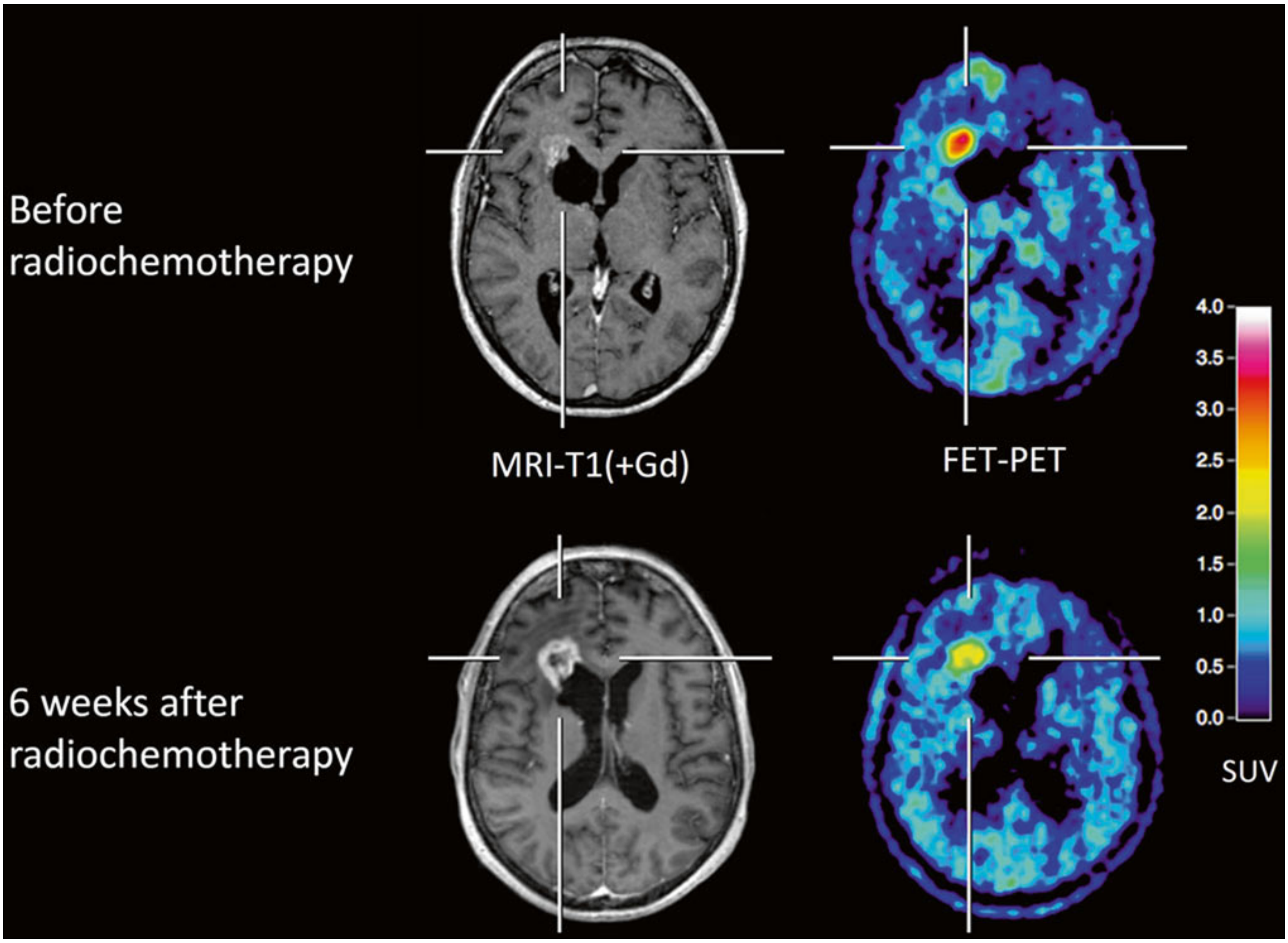

Fig. 5 Patient with a glioblastoma after resection (*upper row*) and 6 weeks after completion of radiochemotherapy (*lower* row). MRI shows enlargement of contrast enhancement after 6 weeks after completion of radiochemotherapy (*lower row*) suggesting tumor progression, whereas FET PET indicates a responder with decreasing amino acid uptake. The patient had a favorable outcome

6 The Diagnosis of Tumor Recurrence/Progression

It is difficult to distinguish tumor recurrence/progression from nonspecific posttherapeutic changes with conventional MRI alone because pathological enhancement with contrast medium may reflect either new growth of tumor or unspecific changes after radio- or chemotherapy (Brandsma et al. 2008). In addition, progressive tumor growth may miss contrast enhancement especially under antiangiogenic therapy. The role of FDG PET in such cases is limited because of the frequency of nonspecific uptake (Ricci et al. 1998; Basu and Alavi 2009). Multiple studies have shown that MET PET is highly sensitive to detect tumor recurrence/progression, but the specificity for the differentiation of vital tumor tissue from nonneoplastic changes is limited with about 70 % (Tsuyuguchi et al. 2004; Van Laere et al. 2005; Singhal et al. 2008; Crippa et al. 2012). The accuracy of FET PET to distinguish tumor recurrence/progression from nonneoplastic changes appears to be higher compared to MET PET. The lower specificity of MET may be explained by its higher affinity for macrophages compared with FET as demonstrated in animal experiments (Salber et al. 2006, 2007). A sensitivity and specificity of FET PET for the detection of tumor recurrence/progression of 100 and 93 %, respectively, has been reported compared with 93 and 50 % for MRI alone (Pöpperl et al. 2004; Rachinger et al. 2003). The additional use of dynamic FET PET allowed a differentiation of high-grade and low-grade recurrences with a sensitivity and specificity of 92 % (Pöpperl et al. 2006b).

Excellent results for the differentiation of radionecrosis and tumor recurrence in gliomas have also been reported for ^{11}C-choline and ^{18}F-fluorocholine (Kwee et al. 2007; Tan et al. 2011).

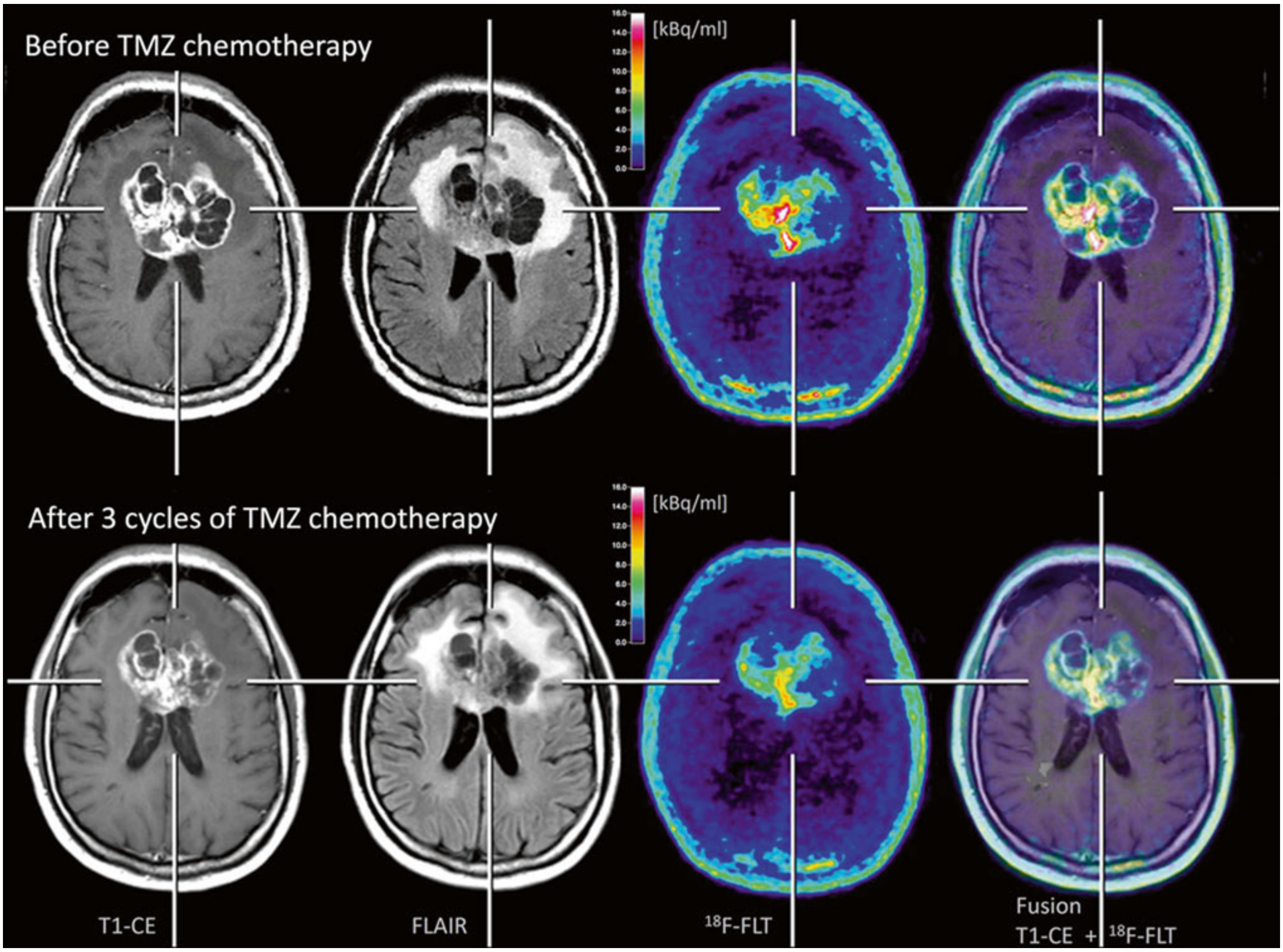

Fig. 6 Patient with a glioblastoma before (*upper row*) and after three cycles of temozolomide (TMZ) chemotherapy (*lower* row). A moderate reduction of tumor extent is observed both in the contrast-enhanced MR and FLAIR-weighted images as well as in the ^{18}F-FLT PET scans. Furthermore, it can be observed that ^{18}F-FLT uptake occurs not in areas without disruption of the blood-brain barrier (Courtesy of Lutz Kracht, Max-Planck-Institute for Neurological Research, Germany)

7 PET in Patients with Brain Metastasis

The improvement in the treatment of solid tumors has led to an increasing number of patients who experience brain metastases during the course of the disease. Stereotactic radiosurgery, brachytherapy, and whole-brain radiation therapy are commonly used to treat brain metastases and a growing percentage of patients live long enough to experience a local relapse of these metastases. Thus, the number of patients suffering local recurrence of previously irradiated brain metastases can be expected to increase. Contrast-enhanced MR imaging is the method of choice for the evaluation of metastatic brain tumors. However, in a considerable number of patients, the differentiation of local recurrent brain metastasis from radiation necrosis after radiotherapy using contrast-enhanced MRI is difficult (Dooms et al. 1986). FDG has been considered for evaluation of metastatic brain tumors, but the high physiological glucose consumption of the brain and the variable glucose uptake of metastatic brain lesions limit its use (Belohlavek et al. 2003; Lee et al. 2008). A recent study indicated that dual-phase imaging may improve the diagnostic accuracy of FDG PET for differentiation of recurrent brain metastasis from radiation necrosis (Horky et al. 2011). A limitation of that approach is the long time interval between the PET scans (range of duration, 2–5.7 h). PET using MET may be effective in differentiating recurrent metastatic brain tumor from radiation-induced changes with sensitivity and specificity of 70–80 % (Tsuyuguchi et al. 2004; Terakawa et al. 2008). The clinical usefulness of FET PET for the differentiation of local recurrent brain metastasis from radiation necrosis could be described recently in 31 patients with 40 metastases (Galldiks et al. 2012b). Using the tumor/brain ratios and results of kinetic studies, FET PET could differentiate local recurrent brain metastasis from radiation necrosis with a high sensitivity (95 %) and specificity (91 %). A first comparison of MET and ^{11}C-choline in patients with brain metastasis indicated slightly better results for choline than for MET (Rottenburger et al. 2011).

8 Imaging of Brain Tumors in Children

The histological subtypes of brain tumors in children differ considerably from that in adults. Only few mainly retrospective studies have been performed in children with brain tumors. It is, however, evident that the assessment of glucose metabolism with FDG is less suitable for the evaluation of tumor malignancy than it is the case in adults (Weckesser et al. 2001). The main reason for this is the high glucose metabolism in pilocytic astrocytomas. These low-grade tumors may exhibit metabolic rates with the intensity of gray matter; an association of the metabolic activity of the tumor and clinical presentation or outcome is not evident.

Previous studies revealed that the use of amino acid PET with the tracer MET may improve the management in this patient population (Utriainen et al. 2002; Pirotte et al. 2003; Galldiks et al. 2010b). Results of these studies suggest that MET PET might be a useful tool to differentiate tumorous from nontumorous lesions in children and young adults when a decision for further therapy is difficult or impossible from routine structural imaging procedures alone.

However, it should be noted that the differentiation between high- and low-grade gliomas using amino acid PET may be difficult. A considerable overlap of amino acid uptake has been observed in low-grade and high-grade tumors (Utriainen et al. 2002). Similar to glucose metabolism, amino acid uptake may be high in low-grade tumors like pilocytic astrocytomas and gangliogliomas, and uptake may be relatively low in highly aggressive medulloblastomas (WHO IV).

9 Perspectives

Molecular imaging of cerebral gliomas with PET is becoming more and more available for clinical use. While most of the techniques cited in this review have limited influence on diagnostic practice, the use of radiolabeled amino acids is promising and permits a more specific representation of the spatial extent of solid and diffuse glioma tissue than is possible by conventional MRI alone. This is very advantageous for the planning of biopsies, resections, and radiotherapy. Furthermore, tumor recurrence/progression can be differentiated from posttherapeutic changes with a high degree of specificity, valuable prognostic information can be obtained for low-grade gliomas, and the treatment response can probably be judged early in the course of treatment. The scientifically documented impact of PET in brain tumors seems to justify its use as a routine diagnostic technique for certain indications, but it remains to be confirmed that this will improve the overall quality of care (e.g., improvement of survival). The logistical prerequisites especially for amino acid imaging have become markedly less difficult to achieve in recent years. The costs of these diagnostic techniques would appear to be well justified by their clinical utility, not least because their timely application in a larger number of patients can be expected to save the costs incurred today by the use of other, less diagnostically reliable techniques (Heinzel et al. 2012a, b, 2013).

References

Afshar-Oromieh A, Giesel FL, Linhart HG, Haberkorn U, Haufe S, Combs SE, Podlesek D, Eisenhut M, Kratochwil C (2012) Detection of cranial meningiomas: comparison of (6)(8)Ga-DOTATOC PET/CT and contrast-enhanced MRI. Eur J Nucl Med Mol Imaging 39:1409–1415

Arbizu J, Tejada S, Marti-Climent JM, Diez-Valle R, Prieto E, Quincoces G, Vigil C, Idoate MA, Zubieta JL, Penuelas I, Richter JA (2012) Quantitative volumetric analysis of gliomas with sequential MRI and (11)C-methionine PET assessment: patterns of integration in therapy planning. Eur J Nucl Med Mol Imaging 5:771–781

Bading JR, Shields AF (2008) Imaging of cell proliferation: status and prospects. J Nucl Med (official publication) 49(Suppl 2):64S–80S

Basu S, Alavi A (2009) Molecular imaging (PET) of brain tumors. Neuroimaging Clin N Am 19:625–646

Becherer A, Karanikas G, Szabo M, Zettinig G, Asenbaum S, Marosi C, Henk C, Wunderbaldinger P, Czech T, Wadsak W, Kletter K (2003) Brain tumour imaging with PET: a comparison between [18F]fluorodopa and [11C]methionine. Eur J Nucl Med Mol Imaging 30:1561–1567

Belohlavek O, Simonova G, Kantorova I, Novotny J Jr, Liscak R (2003) Brain metastases after stereotactic radiosurgery using the Leksell gamma knife: can FDG PET help to differentiate radionecrosis from tumour progression? Eur J Nucl Med Mol Imaging 30:96–100

Bergmann R, Pietzsch J, Fuechtner F, Pawelke B, Beuthien-Baumann B, Johannsen B, Kotzerke J (2004) 3-O–methyl-6-18F-fluoro-Ldopa, a new tumor imaging agent: investigation of transport mechanism in vitro. J Nucl Med (official publication) 45:2116–2122

Borbely K, Nyary I, Toth M, Ericson K, Gulyas B (2006) Optimization of semi-quantification in metabolic PET studies with 18F-fluorodeoxyglucose and 11C-methionine in the determination of malignancy of gliomas. J Neurol Sci 246:85–94

Brandsma D, Stalpers L, Taal W, Sminia P, van den Bent MJ (2008) Clinical features, mechanisms, and management of pseudoprogression in malignant gliomas. Lancet Oncol 9:453–461

Calcagni ML, Galli G, Giordano A, Taralli S, Anile C, Niesen A, Baum RP (2011) Dynamic O–(2-[18F]fluoroethyl)-L-tyrosine (F-18 FET) PET for glioma grading: assessment of individual probability of malignancy. Clin Nucl Med 36:841–847

Ceyssens S, Van Laere K, de Groot T, Goffin J, Bormans G, Mortelmans L (2006) [11C]methionine PET, histopathology, and survival in primary brain tumors and recurrence. AJNR Am J Neuroradiology 27:1432–1437

Chen W (2007) Clinical applications of PET in brain tumors. J Nucl Med (official publication) 48:1468–1481
Chen W, Geist C, Czernin J, Silverman D, Satyamurthy N, Delaloye S, Lai A, Phelps M, Cloughesy T (2008) Assess treatment response using FDOPA PET in patients with recurrent malignant gliomas treated with bevacizumab and irinotecan. J Nucl Med (official publication) 49(Supplement):78
Chen W, Cloughesy T, Kamdar N, Satyamurthy N, Bergsneider M, Liau L, Mischel P, Czernin J, Phelps ME, Silverman DH (2005) Imaging proliferation in brain tumors with 18F-FLT PET: comparison with 18F-FDG. J Nucl Med (official publication) 46:945–952
Chen W, Delaloye S, Silverman DH, Geist C, Czernin J, Sayre J, Satyamurthy N, Pope W, Lai A, Phelps ME, Cloughesy T (2007) Predicting treatment response of malignant gliomas to bevacizumab and irinotecan by imaging proliferation with [18F] fluorothymidine positron emission tomography: a pilot study. J Clin Oncol 25:4714–4721
Choi SJ, Kim JS, Kim JH, Oh SJ, Lee JG, Kim CJ, Ra YS, Yeo JS, Ryu JS, Moon DH (2005) [18F]30-deoxy-30-fluorothymidine PET for the diagnosis and grading of brain tumors. Eur J Nucl Med Mol Imaging 32:653–659
Crippa F, Alessi A, Serafini GL (2012) PET with radiolabeled aminoacid. Q J Nucl Med Mol Imaging 56:151–162
Delbeke D, Meyerowitz C, Lapidus RL, Maciunas RJ, Jennings MT, Moots PL, Kessler RM (1995) Optimal cutoff levels of F-18 fluorodeoxyglucose uptake in the differentiation of low-grade from high-grade brain tumors with PET. Radiology 195:47–52
Di Chiro G, DeLaPaz RL, Brooks RA, Sokoloff L, Kornblith PL, Smith BH, Patronas NJ, Kufta CV, Kessler RM, Johnston GS, Manning RG, Wolf AP (1982) Glucose utilization of cerebral gliomas measured by [18F] fluorodeoxyglucose and positron emission tomography. Neurology 32:1323–1329
Dooms GC, Hecht S, Brant-Zawadzki M, Berthiaume Y, Norman D, Newton TH (1986) Brain radiation lesions: MR imaging. Radiology 158:149–155
Dunet V, Rossier C, Buck A, Stupp R, Prior JO (2012) Performance of 18F-fluoro-ethyL-tyrosine (18F-FET) PET for the differential diagnosis of primary brain tumor: a systematic review and Metaanalysis. J Nucl Med (official publication) 53:207–214
Floeth FW, Pauleit D, Sabel M, Reifenberger G, Stoffels G, Stummer W, Rommel F, Hamacher K, Langen KJ (2006) 18F-FET PET differentiation of ring-enhancing brain lesions. J Nucl Med (official publication) 47:776–782
Floeth FW, Pauleit D, Sabel M, Stoffels G, Reifenberger G, Riemenschneider MJ, Jansen P, Coenen HH, Steiger HJ, Langen KJ (2007) Prognostic value of O–(2-18F-fluoroethyl)-L-tyrosine PET and MRI in low-grade glioma. J Nucl Med (official publication) 48:519–527
Galldiks N, Kracht LW, Burghaus L, Thomas A, Jacobs AH, Heiss WD, Herholz K (2006) Use of 11C-methionine PET to monitor the effects of temozolomide chemotherapy in malignant gliomas. Eur J Nucl Med Mol Imaging 33:516–524
Galldiks N, Kracht LW, Burghaus L, Ullrich RT, Backes H, Brunn A, Heiss WD, Jacobs AH (2010a) Patient-tailored, imaging-guided, long-term temozolomide chemotherapy in patients with glioblastoma. Mol Imaging 9:40–46
Galldiks N, Kracht LW, Berthold F, Miletic H, Klein JC, Herholz K, Jacobs AH, Heiss WD (2010b) [11C]-L-methionine positron emission tomography in the management of children and young adults with brain tumors. J Neurooncol 96:231–239
Galldiks N, Rapp M, Stoffels G, Fink GR, Shah NJ, Coenen HH, Sabel M, Langen KJ (2013) Response assessment of bevacizumab in patients with recurrent malignant glioma using [18F]Fluoroethyl-Ltyrosine PET in comparison to MRI. Eur J Nucl Med Mol Imaging 40:22–33
Galldiks N, von Tempelhoff W, Kahraman D, Kracht LW, Vollmar S, Fink GR, Schroeter M, Goldbrunner R, Schmidt M, Maarouf M (2012a) 11C-methionine positron emission tomographic imaging of biologic activity of a recurrent glioblastoma treated with stereotaxy-guided laser-induced interstitial thermotherapy. Mol Imaging 11:265–271
Galldiks N, Stoffels G, Filss CP, Piroth MD, Sabel M, Ruge MI, Herzog H, Shah NJ, Fink GR, Coenen HH, Langen KJ (2012b) Role of O–(2-(18)F-fluoroethyl)-L-tyrosine PET for differentiation of local recurrent brain metastasis from radiation necrosis. J Nucl Med (official publication) 53:1367–1374
Galldiks N, Langen K, Holy R, Pinkawa M, Stoffels G, Nolte K, Kaiser H, Filss C, Fink G, Coenen H, Eble M, Piroth M (2012c) Assessment of treatment response in patients with glioblastoma using [18F] Fluoroethyl-L-Tyrosine PET in comparison to MRI. J Nucl Med (official publication) 53:1048–1057
Gehler B, Paulsen F, Oksuz MO, Hauser TK, Eschmann SM, Bares R, Pfannenberg C, Bamberg M, Bartenstein P, Belka C, Ganswindt U (2009) [68 Ga]-DOTATOC-PET/CT for meningioma IMRT treatment planning. Radiat Oncol 4:56
Goldman S, Levivier M, Pirotte B, Brucher JM, Wikler D, Damhaut P, Dethy S, Brotchi J, Hildebrand J (1997) Regional methionine and glucose uptake in high-grade gliomas: a comparative study on PET-guided stereotactic biopsy. J Nucl Med (official publication) 38:1459–1462
Graf R, Nyuyki F, Steffen IG, Michel R, Fahdt D, Wust P, Brenner W, Budach V, Wurm R, Plotkin M (2013) Contribution of 68 Ga-DOTATOC PET/CT to target volume delineation of skull base meningiomas treated with stereotactic radiation therapy. Int J Radiat Oncol Biol Phys 85:68–73
Grosu AL, Weber WA (2010) PET for radiation treatment planning of brain tumours. Radiother Oncol J Eur Soc Ther Radiol Oncol 96:325–327
Grosu AL, Weber WA, Franz M, Stark S, Piert M, Thamm R, Gumprecht H, Schwaiger M, Molls M, Nieder C (2005) Reirradiation of recurrent high-grade gliomas using amino acid PET (SPECT)/CT/MRI image fusion to determine gross tumor volume for stereotactic fractionated radiotherapy. Int J Radiat Oncol Biol Phys 63: 511–519
Grosu AL, Astner ST, Riedel E, Nieder C, Wiedenmann N, Heinemann F, Schwaiger M, Molls M, Wester HJ, Weber WA (2011) An Interindividual Comparison of O–(2- [(18)F]Fluoroethyl)-L-Tyrosine (FET)- and L-[Methyl-(11)C]Methionine (MET)-PET in Patients With Brain Gliomas and Metastases. Int J Radiat Oncol Biol Phys 81:1049–1058
Gulyas B, Halldin C (2012) New PET radiopharmaceuticals beyond FDG for brain tumor imaging. Q J Nucl Med Mol Imaging 56:173–190
Gulyas B, Nyary I, Borbely K (2008) FDG, MET or CHO? The quest for the optimal PET tracer for glioma imaging continues. Nat clin pract Neurol 4:470–471
Harris RJ, Cloughesy TF, Pope WB, Nghiemphu PL, Lai A, Zaw T, Czernin J, Phelps ME, Chen W, Ellingson BM (2012) 18F-FDOPA and 18F-FLT positron emission tomography parametric response maps predict response in recurrent malignant gliomas treated with bevacizumab. Neurooncol 14:1079–1089
Haubner R, Beer AJ, Wang H, Chen X (2010) Positron emission tomography tracers for imaging angiogenesis. Eur J Nucl Med Mol Imaging 37(Suppl 1):S86–S103
Heinzel A, Stock S, Langen KJ, Muller D (2012a) Cost-effectiveness analysis of FET PET-guided target selection for the diagnosis of gliomas. Eur J Nucl Med Mol Imaging 39:1089–1096
Heinzel A, Stock S, Langen KJ, Muller D (2012b) Cost-effectiveness analysis of amino acid PET-guided surgery for supratentorial high-grade gliomas. J Nucl Med (official publication) 53:552–558

Heinzel A, Muller D, Langen KJ, Blaum M, Verburg FA, Mottaghy FM, Galldiks N (2013) The use of O–(2-18F-Fluoroethyl)-Ltyrosine PET for treatment management of bevacizumab and irinotecan in patients with recurrent high-grade glioma: a costeffectiveness analysis. J Nucl Med (official publication) 54: 1217–1222

Henze M, Dimitrakopoulou-Strauss A, Milker-Zabel S, Schuhmacher J, Strauss LG, Doll J, Macke HR, Eisenhut M, Debus J, Haberkorn U (2005) Characterization of 68 Ga-DOTA-D-Phe1-Tyr3-octreotide kinetics in patients with meningiomas. J Nucl Med (official publication) 46:763–769

Herholz K, Langen KJ, Schiepers C, Mountz JM (2012) Brain tumors. Semin Nucl Med 42:356–370

Herholz K, Holzer T, Bauer B, Schroder R, Voges J, Ernestus RI, Mendoza G, Weber-Luxenburger G, Lottgen J, Thiel A, Wienhard K, Heiss WD (1998) 11C-methionine PET for differential diagnosis of low-grade gliomas. Neurology 50:1316–1322

Horky LL, Hsiao EM, Weiss SE, Drappatz J, Gerbaudo VH (2011) Dual phase FDG-PET imaging of brain metastases provides superior assessment of recurrence versus post-treatment necrosis. J Neurooncol 103:137–146

Huang C, McConathy J (2013) Radiolabeled amino acids for oncologic imaging. J Nucl Med (official publication) 54:1007–1010

Hutterer M, Nowosielski M, Putzer D, Waitz D, Tinkhauser G, Kostron H, Muigg A, Virgolini IJ, Staffen W, Trinka E, Gotwald T, Jacobs AH, Stockhammer G (2011) O–(2-18F-fluoroethyl)-L-tyrosine PET predicts failure of antiangiogenic treatment in patients with recurrent high-grade glioma. J Nucl Med (official publication) 52:856–864

Hutterer M, Nowosielski M, Putzer D, Jansen NL, Seiz M, Schocke M, McCoy M, Gobel G, la Fougere C, Virgolini IJ, Trinka E, Jacobs AH, Stockhammer G (2013) [18F]-fluoro-ethyl-L-tyrosine PET: a valuable diagnostic tool in neuro-oncology, but not all that glitters is glioma. Neurooncol 15:341–351

Jacobs AH, Thomas A, Kracht LW, Li H, Dittmar C, Garlip G, Galldiks N, Klein JC, Sobesky J, Hilker R, Vollmar S, Herholz K, Wienhard K, Heiss WD (2005) 18F-fluoro-L-thymidine and 11C-methylmethionine as markers of increased transport and proliferation in brain tumors. J Nucl Med (official publication) 46:1948–1958

Jager PL, Vaalburg W, Pruim J, de Vries EG, Langen KJ, Piers DA (2001) Radiolabeled amino acids: basic aspects and clinical applications in oncology. J Nucl Med (official publication) 42:432–445

Jansen NL, Graute V, Armbruster L, Suchorska B, Lutz J, Eigenbrod S, Cumming P, Bartenstein P, Tonn JC, Kreth FW, la Fougere C (2012) MRI-suspected low-grade glioma: is there a need to perform dynamic FET PET? Eur J Nucl Med Mol Imaging 39:1021–1029

Kaschten B, Stevenaert A, Sadzot B, Deprez M, Degueldre C, Del Fiore G, Luxen A, Reznik M (1998) Preoperative evaluation of 54 gliomas by PET with fluorine-18-fluorodeoxyglucose and/or carbon-11-methionine. J Nucl Med (official publication) 39:778–785

Kato T, Shinoda J, Nakayama N, Miwa K, Okumura A, Yano H, Yoshimura S, Maruyama T, Muragaki Y, Iwama T (2008) Metabolic assessment of gliomas using 11C-methionine, [18F] fluorodeoxyglucose, and 11C-choline positron-emission tomography. AJNR Am J Neuroradiology 29:1176–1182

Kim S, Chung JK, Im SH, Jeong JM, Lee DS, Kim DG, Jung HW, Lee MC (2005) 11C-methionine PET as a prognostic marker in patients with glioma: comparison with 18F-FDG PET. Eur J Nucl Med Mol Imaging 32:52–59

Kracht LW, Miletic H, Busch S, Jacobs AH, Voges J, Hoevels M, Klein JC, Herholz K, Heiss WD (2004) Delineation of brain tumor extent with [11C]L-methionine positron emission tomography: local comparison with stereotactic histopathology. Clin Cancer Res J Am Assoc Cancer Res (official) 10:7163–7170

Kunz M, Thon N, Eigenbrod S, Hartmann C, Egensperger R, Herms J, Geisler J, la Fougere C, Lutz J, Linn J, Kreth S, von Deimling A, Tonn JC, Kretzschmar HA, Pöpperl G, Kreth FW (2011a) Hot spots in dynamic (18)FET-PET delineate malignant tumor parts within suspected WHO grade II gliomas. Neurooncol 13:307–316

Kunz M, Thon N, Eigenbrod S, Hartmann C, Egensperger R, Herms J, Geisler J, la Fougere C, Lutz J, Linn J, Kreth S, von Deimling A, Tonn JC, Kretzschmar HA, Pöpperl G, Kreth FW (2011b) Hot spots in dynamic (18)FET-PET delineate malignant tumor parts within suspected WHO grade II gliomas. Neurooncol 13:307–316

Kwee SA, Ko JP, Jiang CS, Watters MR, Coel MN (2007) Solitary brain lesions enhancing at MR imaging: evaluation with fluorine 18 fluorocholine PET. Radiology 244:557–565

Langen KJ, Broer S (2004) Molecular transport mechanisms of radiolabeled amino acids for PET and SPECT. J Nucl Med (official publication) 45:1435–1436

Langen KJ, Eschmann SM (2008) Correlative imaging of hypoxia and angiogenesis in oncology. J Nucl Med (official publication) 49:515–516

Langen KJ, Tatsch K, Grosu AL, Jacobs AH, Weckesser M, Sabri O (2008) Diagnostics of cerebral gliomas with radiolabeled amino acids. Dtsch Arztebl Int 105:55–61

Langen KJ, Jarosch M, Muhlensiepen H, Hamacher K, Broer S, Jansen P, Zilles K, Coenen HH (2003) Comparison of fluorotyrosines and methionine uptake in F98 rat gliomas. Nucl Med Biol 30:501–508

Langen KJ, Hamacher K, Weckesser M, Floeth F, Stoffels G, Bauer D, Coenen HH, Pauleit D (2006) O–(2-[18F]fluoroethyl)-L-tyrosine: uptake mechanisms and clinical applications. Nucl Med Biol 33:287–294

Lee HY, Chung JK, Jeong JM, Lee DS, Kim DG, Jung HW, Lee MC (2008) Comparison of FDG-PET findings of brain metastasis from non-small-cell lung cancer and small-cell lung cancer. Ann Nucl Med 22:281–286

Lee IH, Piert M, Gomez-Hassan D, Junck L, Rogers L, Hayman J, Ten Haken RK, Lawrence TS, Cao Y, Tsien C (2009) Association of 11C-methionine PET uptake with site of failure after concurrent temozolomide and radiation for primary glioblastoma multiforme. Int J Radiat Oncol Biol Phys 73:479–485

Lee ST, Scott AM (2007) Hypoxia positron emission tomography imaging with 18f-fluoromisonidazole. Semin Nucl Med 37:451–461

Levivier M, Massager N, Wikler D, Lorenzoni J, Ruiz S, Devriendt D, David P, Desmedt F, Simon S, Van Houtte P, Brotchi J, Goldman S (2004) Use of stereotactic PET images in dosimetry planning of radiosurgery for brain tumors: clinical experience and proposed classification. J Nucl Med (official publication) 45:1146–1154

Lustig RA, Seiferheld W, Berkey B, Yung AW, Scarantino C, Movsas B, Jones CU, Simpson JR, Fishbach J, Curran WJ Jr (2007) Imaging response in malignant glioma, RTOG 90–06. Am J ClinOncol 30:32–37

Matsuo M, Miwa K, Tanaka O, Shinoda J, Nishibori H, Tsuge Y, Yano H, Iwama T, Hayashi S, Hoshi H, Yamada J, Kanematsu M, Aoyama H (2012) Impact of [11C]methionine positron emission tomography for target definition of glioblastoma multiforme in radiation therapy planning. Int J Radiat Oncol Biol Phys 82:83–89

Meller J, Sahlmann CO, Scheel AK (2007) 18F-FDG PET and PET/CT in fever of unknown origin. J Nucl Med (official publication) 48:35–45

Miyake K, Shinomiya A, Okada M, Hatakeyama T, Kawai N, Tamiya T (2012) Usefulness of FDG, MET and FLT-PET studies for the management of human gliomas. J Biomed Biotechnol 2012:205818

Mosskin M, Ericson K, Hindmarsh T, von Holst H, Collins VP, Bergstrom M, Eriksson L, Johnstrom P (1989) Positron emission tomography compared with magnetic resonance imaging and computed tomography in supratentorial gliomas using multiple stereotactic biopsies as reference. Acta Radiol 30:225–232

Narita T, Aoyama H, Hirata K, Onodera S, Shiga T, Kobayashi H, Murata J, Terasaka S, Tanaka S, Houkin K (2012) Reoxygenation of glioblastoma multiforme treated with fractionated radiotherapy concomitant with temozolomide: changes defined by 18F-fluoromisonidazole positron emission tomography: two case reports. Jpn J Clin Oncol 42:120–123

Nyuyki F, Plotkin M, Graf R, Michel R, Steffen I, Denecke T, Geworski L, Fahdt D, Brenner W, Wurm R (2010) Potential impact of (68) Ga-DOTATOC PET/CT on stereotactic radiotherapy planning of meningiomas. Eur J Nucl Med Mol Imaging 37:310–318

Padma MV, Said S, Jacobs M, Hwang DR, Dunigan K, Satter M, Christian B, Ruppert J, Bernstein T, Kraus G, Mantil JC (2003) Prediction of pathology and survival by FDG PET in gliomas. J Neurooncol 64:227–237

Pauleit D, Floeth F, Hamacher K, Riemenschneider MJ, Reifenberger G, Muller HW, Zilles K, Coenen HH, Langen KJ (2005) O–(2-[18F] fluoroethyl)-L-tyrosine PET combined with MRI improves the diagnostic assessment of cerebral gliomas. Brain J Neurol 128:678–687

Pauleit D, Stoffels G, Bachofner A, Floeth FW, Sabel M, Herzog H, Tellmann L, Jansen P, Reifenberger G, Hamacher K, Coenen HH, Langen KJ (2009) Comparison of (18)F-FET and (18)F-FDG PET in brain tumors. Nucl Med Biol 36:779–787

Pichler R, Dunzinger A, Wurm G, Pichler J, Weis S, Nussbaumer K, Topakian R, Aigner RM (2010) Is there a place for FET PET in the initial evaluation of brain lesions with unknown significance? Eur J Nucl Med Mol Imaging 37:1521–1528

Piroth MD, Pinkawa M, Holy R, Stoffels G, Demirel C, Attieh C, Kaiser HJ, Langen KJ, Eble MJ (2009) Integrated-boost IMRT or 3-D-CRT using FET-PET based auto-contoured target volume delineation for glioblastoma multiforme–a dosimetric comparison. Radiat Oncol 4:57

Piroth MD, Holy R, Pinkawa M, Stoffels G, Kaiser HJ, Galldiks N, Herzog H, Coenen HH, Eble MJ, Langen KJ (2011a) Prognostic impact of postoperative, pre-irradiation (18)F-fluoroethyl-L-tyrosine uptake in glioblastoma patients treated with radiochemotherapy. Radiother Oncol J Eur Soc Ther Radiol Oncol 99:218–224

Piroth MD, Pinkawa M, Holy R, Klotz J, Nussen S, Stoffels G, Coenen HH, Kaiser HJ, Langen KJ, Eble MJ (2011b) Prognostic value of early [18F]fluoroethyltyrosine positron emission tomography after radiochemotherapy in glioblastoma multiforme. Int J Radiat Oncol Biol Phys 80:176–184

Piroth MD, Pinkawa M, Holy R, Klotz J, Schaar S, Stoffels G, Galldiks N, Coenen HH, Kaiser HJ, Langen KJ, Eble MJ (2012) Integrated boost IMRT with FET-PET-adapted local dose escalation in glioblastomas. results of a prospective phase II study. Strahlentherapie und Onkologie: Organ der Deutschen Rontgengesellschaft [et al] 188:334–339

Pirotte B, Goldman S, Massager N, David P, Wikler D, Lipszyc M, Salmon I, Brotchi J, Levivier M (2004) Combined use of 18Ffluorodeoxyglucose and 11C-methionine in 45 positron emission tomography-guided stereotactic brain biopsies. J Neurosurg 101:476–483

Pirotte B, Goldman S, Salzberg S, Wikler D, David P, Vandesteene A, Van Bogaert P, Salmon I, Brotchi J, Levivier M (2003) Combined positron emission tomography and magnetic resonance imaging for the planning of stereotactic brain biopsies in children: experience in 9 cases. Pediatr Neurosurg 38:146–155

Pirotte BJ, Lubansu A, Massager N, Wikler D, Goldman S, Levivier M (2007) Results of positron emission tomography guidance and reassessment of the utility of and indications for stereotactic biopsy in children with infiltrative brainstem tumors. J Neurosurg 107:392–399

Pirotte BJ, Levivier M, Goldman S, Massager N, Wikler D, Dewitte O, Bruneau M, Rorive S, David P, Brotchi J (2009) Positron emission tomography-guided volumetric resection of supratentorial high-grade gliomas: a survival analysis in 66 consecutive patients. Neurosurgery 64:471–481; discussion 481

Plotkin M, Blechschmidt C, Auf G, Nyuyki F, Geworski L, Denecke T, Brenner W, Stockhammer F (2010) Comparison of F-18 FETPET with F-18 FDG-PET for biopsy planning of non-contrastenhancing gliomas. Eur Radiol 20:2496–2502

Pöpperl G, Gotz C, Rachinger W, Gildehaus FJ, Tonn JC, Tatsch K (2004) Value of O–(2-[18F]fluoroethyl)- L-tyrosine PET for the diagnosis of recurrent glioma. Eur J Nucl Med Mol Imaging 31:1464–1470

Pöpperl G, Gotz C, Rachinger W, Schnell O, Gildehaus FJ, Tonn JC, Tatsch K (2006a) Serial O–(2-[(18)F]fluoroethyl)-L: –tyrosine PET for monitoring the effects of intracavitary radioimmunotherapy in patients with malignant glioma. Eur J Nucl Med Mol Imaging 33:792–800

Pöpperl G, Goldbrunner R, Gildehaus FJ, Kreth FW, Tanner P, Holtmannspotter M, Tonn JC, Tatsch K (2005) O–(2-[18F] fluoroethyl)-L-tyrosine PET for monitoring the effects of convectionenhanced delivery of paclitaxel in patients with recurrent glioblastoma. Eur J Nucl Med Mol Imaging 32:1018–1025

Pöpperl G, Kreth FW, Herms J, Koch W, Mehrkens JH, Gildehaus FJ, Kretzschmar HA, Tonn JC, Tatsch K (2006b) Analysis of 18F-FET PET for grading of recurrent gliomas: is evaluation of uptake kinetics superior to standard methods? J Nucl Med (official publication) 47:393–403

Pöpperl G, Kreth FW, Herms J, Koch W, Mehrkens JH, Gildehaus FJ, Kretzschmar HA, Tonn JC, Tatsch K (2006c) Analysis of 18F-FET PET for grading of recurrent gliomas: is evaluation of uptake kinetics superior to standard methods? J Nucl Med 47:393–403

Pöpperl G, Kreth FW, Mehrkens JH, Herms J, Seelos K, Koch W, Gildehaus FJ, Kretzschmar HA, Tonn JC, Tatsch K (2007) FET PET for the evaluation of untreated gliomas: correlation of FET uptake and uptake kinetics with tumour grading. Eur J Nucl Med Mol Imaging 34:1933–1942

Prieto E, Marti-Climent JM, Dominguez-Prado I, Garrastachu P, Diez-Valle R, Tejada S, Aristu JJ, Penuelas I, Arbizu J (2011) Voxelbased analysis of dual-time-point 18F-FDG PET images for brain tumor identification and delineation. J Nucl Med (official publication) 52:865–872

Rachinger W, Goetz C, Pöpperl G, Gildehaus FJ, Kreth FW, Holtmannspotter M, Herms J, Koch W, Tatsch K, Tonn JC (2005) Positron emission tomography with O–(2-[18F]fluoroethyl)-L-tyrosine versus magnetic resonance imaging in the diagnosis of recurrent gliomas. Neurosurgery 57:505–511; discussion 505–511

Rapp M, Floeth FW, Felsberg J, Steiger HJ, Sabel M, Langen KJ, Galldiks N (2013a) Clinical value of O–(2-[(18)F]-fluoroethyl)-Ltyrosine positron emission tomography in patients with low-grade glioma. Neurosurg Focus 34:E3

Rapp M, Heinzel A, Galldiks N, Stoffels G, Felsberg J, Ewelt C, Sabel M, Steiger HJ, Reifenberger G, Beez T, Coenen HH, Floeth FW, Langen KJ (2013b) Diagnostic performance of 18F-FET PET in newly diagnosed cerebral lesions suggestive of glioma. J Nucl Med (official publication) 54:229–235

Ribom D, Eriksson A, Hartman M, Engler H, Nilsson A, Langstrom B, Bolander H, Bergstrom M, Smits A (2001) Positron emission tomography (11)C-methionine and survival in patients with low-grade gliomas. Cancer 92:1541–1549

Ricci PE, Karis JP, Heiserman JE, Fram EK, Bice AN, Drayer BP (1998) Differentiating recurrent tumor from radiation necrosis: time for re-evaluation of positron emission tomography? AJNR Am J Neuroradiol 19:407–413

Rickhey M, Koelbl O, Eilles C, Bogner L (2008) A biologically adapted dose-escalation approach, demonstrated for 18F-FET-PET in brain tumors. Strahlentherapie und Onkologie: Organ der Deutschen Rontgengesellschaft [et al] 184:536–542

Roelcke U, Bruehlmeier M, Hefti M, Hundsberger T, Nitzsche EU (2012) F-18 choline PET does not detect increased metabolism in F-18 fluoroethyltyrosine-negative low-grade gliomas. Clin Nucl Med 37:e1–e3

Rottenburger C, Hentschel M, Kelly T, Trippel M, Brink I, Reithmeier T, Meyer PT, Nikkhah G (2011) Comparison of C-11 methionine and C-11 choline for PET imaging of brain metastases: a prospective pilot study. Clin Nucl Med 36:639–642

Saga T, Kawashima H, Araki N, Takahashi JA, Nakashima Y, Higashi T, Oya N, Mukai T, Hojo M, Hashimoto N, Manabe T, Hiraoka M, Togashi K (2006) Evaluation of primary brain tumors with FLTPET: usefulness and limitations. Clin Nucl Med 31:774–780

Salber D, Stoffels G, Pauleit D, Reifenberger G, Sabel M, Shah NJ, Hamacher K, Coenen HH, Langen KJ (2006) Differential uptake of [18F]FET and [3H]L-methionine in focal cortical ischemia. Nucl Med Biol 33:1029–1035

Salber D, Stoffels G, Pauleit D, Oros-Peusquens AM, Shah NJ, Klauth P, Hamacher K, Coenen HH, Langen KJ (2007) Differential uptake of O–(2-18F-fluoroethyl)-L-tyrosine, L-3H-methionine, and 3Hdeoxyglucose in brain abscesses. J Nucl Med (official publication) 48:2056–2062

Saleem A, Brown GD, Brady F, Aboagye EO, Osman S, Luthra SK, Ranicar AS, Brock CS, Stevens MF, Newlands E, Jones T, Price P (2003) Metabolic activation of temozolomide measured in vivo using positron emission tomography. Cancer Res 63:2409–2415

Schiepers C, Dahlbom M, Chen W, Cloughesy T, Czernin J, Phelps ME, Huang SC (2010) Kinetics of 30-deoxy-30-18F-fluorothymidine during treatment monitoring of recurrent high-grade glioma. J Nucl Med (official publication) 51:720–727

Schnell O, Krebs B, Carlsen J, Miederer I, Goetz C, Goldbrunner RH, Wester HJ, Haubner R, Pöpperl G, Holtmannspotter M, Kretzschmar HA, Kessler H, Tonn JC, Schwaiger M, Beer AJ (2009) Imaging of integrin alpha(v)beta(3) expression in patients with malignant glioma by [18F] Galacto-RGD positron emission tomography. Neurooncol 11:861–870

Schwarzenberg J, Czernin J, Cloughesy TF, Ellingson BM, Pope WB, Geist C, Dahlbom M, Silverman DH, Satyamurthy N, Phelps ME, Chen W (2012) 30-deoxy-30-18F-fluorothymidine PET and MRI for early survival predictions in patients with recurrent malignant glioma treated with bevacizumab. J Nucl Med (official publication) 53:29–36

Shields AF (2003) PET imaging with 18F-FLT and thymidine analogs: promise and pitfalls. J Nucl Med (official publication) 44:1432–1434

Shields AF, Grierson JR, Dohmen BM, Machulla HJ, Stayanoff JC, Lawhorn-Crews JM, Obradovich JE, Muzik O, Mangner TJ (1998) Imaging proliferation in vivo with [F-18]FLT and positron emission tomography. Nat Med 4:1334–1336

Singhal T, Narayanan TK, Jain V, Mukherjee J, Mantil J (2008) 11C-L-methionine positron emission tomography in the clinical management of cerebral gliomas. Mol Imaging Biol Official Publ Acad Mol Imaging 10:1–18

Singhal T, Narayanan TK, Jacobs MP, Bal C, Mantil JC (2012) 11C-methionine PET for grading and prognostication in gliomas: a comparison study with 18F-FDG PET and contrast enhancement on MRI. J Nucl Med (official publication) 53:1709–1715

Smits A, Baumert BG (2011) The Clinical Value of PET with Amino Acid Tracers for Gliomas WHO Grade II. Int J Mol Imaging 2011:372509

Smits A, Westerberg E, Ribom D (2008) Adding 11C-methionine PET to the EORTC prognostic factors in grade 2 gliomas. Eur J Nucl Med Mol Imaging 35:65–71

Spence AM, Muzi M, Mankoff DA, O'Sullivan SF, Link JM, Lewellen TK, Lewellen B, Pham P, Minoshima S, Swanson K, Krohn KA (2004) 18F-FDG PET of gliomas at delayed intervals: improved distinction between tumor and normal gray matter. J.Nucl Med 45:1653–1659

Tan H, Chen L, Guan Y, Lin X (2011) Comparison of MRI, F-18 FDG, and 11C-choline PET/CT for their potentials in differentiating brain tumor recurrence from brain tumor necrosis following radiotherapy. Clin Nucl Med 36:978–981

Terakawa Y, Tsuyuguchi N, Iwai Y, Yamanaka K, Higashiyama S, Takami T, Ohata K (2008) Diagnostic accuracy of 11C-methionine PET for differentiation of recurrent brain tumors from radiation necrosis after radiotherapy. J Nucl Med (official publication) 49:694–699

Thorwarth D, Henke G, Muller AC, Reimold M, Beyer T, Boss A, Kolb A, Pichler B, Pfannenberg C (2011) Simultaneous 68 Ga-DOTATOC-PET/MRI for IMRT treatment planning for meningioma: first experience. Int J Radiat Oncol Biol Phys 81:277–283

Tsuyuguchi N, Takami T, Sunada I, Iwai Y, Yamanaka K, Tanaka K, Nishikawa M, Ohata K, Torii K, Morino M, Nishio A, Hara M (2004) Methionine positron emission tomography for differentiation of recurrent brain tumor and radiation necrosis after stereotactic radiosurgery—in malignant glioma. Ann Nucl Med 18:291–296

Ullrich R, Backes H, Li H, Kracht L, Miletic H, Kesper K, Neumaier B, Heiss WD, Wienhard K, Jacobs AH (2008) Glioma proliferation as assessed by 30-fluoro-30-deoxy-L-thymidine positron emission tomography in patients with newly diagnosed high-grade glioma. Clin Cancer Res Official J Am Assoc Cancer Res 14:2049–2055

Utriainen M, Metsahonkala L, Salmi TT, Utriainen T, Kalimo H, Pihko H, Makipernaa A, Harila-Saari A, Jyrkkio S, Laine J, Nagren K, Minn H (2002) Metabolic characterization of childhood brain tumors: comparison of 18F-fluorodeoxyglucose and 11C-methionine positron emission tomography. Cancer 95:1376–1386

Van Laere K, Ceyssens S, Van Calenbergh F, de Groot T, Menten J, Flamen P, Bormans G, Mortelmans L (2005) Direct comparison of 18F-FDG and 11C-methionine PET in suspected recurrence of glioma: sensitivity, inter-observer variability and prognostic value. Eur J Nucl Med Mol Imaging 32:39–51

Walter F, Cloughesy T, Walter MA, Lai A, Nghiemphu P, Wagle N, Fueger B, Satyamurthy N, Phelps ME, Czernin J (2012) Impact of 3,4-dihydroxy-6-18F-fluoro-L-phenylalanine PET/CT on managing patients with brain tumors: the referring physician's perspective. J Nucl Med (official publication) 53:393–398

Weber DC, Casanova N, Zilli T, Buchegger F, Rouzaud M, Nouet P, Vees H, Ratib O, Dipasquale G, Miralbell R (2009) Recurrence pattern after [(18)F]fluoroethyltyrosine-positron emission tomography-guided radiotherapy for high-grade glioma: a prospective study. Radiother Oncol J Eur Soc Ther Radiol Oncol 93:586–592

Weber DC, Zilli T, Buchegger F, Casanova N, Haller G, Rouzaud M, Nouet P, Dipasquale G, Ratib O, Zaidi H, Vees H, Miralbell R (2008) [(18)F]Fluoroethyltyrosine- positron emission tomographyguided radiotherapy for high-grade glioma. Radiat Oncol 3:44

Weber WA, Wester HJ, Grosu AL, Herz M, Dzewas B, Feldmann HJ, Molls M, Stocklin G, Schwaiger M (2000) O–(2-[18F]fluoroethyl)-L-tyrosine and L-[methyl-11C]methionine uptake in brain tumours: initial results of a comparative study. Eur J Nucl Med 27:542–549

Weckesser M, Matheja P, Rickert CH, Strater R, Palkovic S, Lottgen J, Kurlemann G, Paulus W, Wassmann H, Schober O (2001) High uptake of L-3-[123I]iodo-alpha-methyl tyrosine in pilocytic astrocytomas. Eur J Nucl Med 28:273–281

Weckesser M, Langen KJ, Rickert CH, Kloska S, Straeter R, Hamacher K, Kurlemann G, Wassmann H, Coenen HH, Schober O (2005) O-(2-[18F]fluorethyl)-L-tyrosine PET in the clinical evaluation of primary brain tumours. Eur J Nucl Med Mol Imaging 32:422–429

Advanced Imaging Modalities and Treatment of Gliomas: Radiation Therapy

Irina Goetz and Anca-Ligia Grosu

Contents

I. Goetz • A.-L. Grosu (✉)
Department of Radiation Oncology,
University Medical Center Freiburg,
Robert-Koch-Straße 3, 79106 Freiburg, Germany
e-mail: irina.goetz@uniklinik-freiburg.de;
anca.grosu@uniklinik-freiburg.de

Abstract

This chapter deals with radiation therapy techniques used for treatment of malignant glioma. It shows how they have become more and more sophisticated over the past decades. Due to this achievement in the planning procedure an exact definition of the target volume has become indispensable and increased the role of imaging in radiotherapy. The pros and cons of various imaging modalities are discussed from the view of a radiation oncologist.

1 Treatment of Gliomas and Radiation Therapy Techniques

Radiotherapy (RT) has played a major role in the treatment of malignant glioma since the 1970s. Adjuvant RT significantly improves local control and survival after resection. The positive effect of postoperative RT was initially demonstrated in patients treated with whole brain RT (WBRT). Three randomized trials documented the efficacy of adjuvant whole brain radiotherapy with significantly increased median survival (Walker et al. 1978, 1980; Andersen 1978). The efficacy of RT improved as advanced imaging techniques enabled more precise radiotherapy planning which focused the treatment on the tumor while minimizing the irradiation of normal brain tissue. Involved field RT (IFRT) superseded WBRT and was subsequently augmented by 3D conformal RT (3D-CRT), intensity-modulated RT (IMRT), and stereotactic radiotherapy.

Despite numerous attempts to combine radiotherapy and chemotherapy, no significant benefit was shown for adjuvant chemotherapy until the advent of temozolomide (Stupp et al. 2005), which remains the current standard therapy for glioblastoma multiforme (GBM).

A large phase III study of the Radiation Therapy Oncology Group (RTOG) and Eastern Cooperative Oncology Group (ECOG) investigated the treatment of malignant gliomas in the 1970s (Chang et al. 1983). The efficacy of four postsurgical treatment options was compared: (1) control radiation of 60 Gy/6–7 weeks to whole brain, (2) control radiation dose plus a booster

E. Hattingen, U. Pilatus (eds.), *Brain Tumor Imaging*,
Med Radiol Diagn Imaging (2016)
DOI 10.1007/174_2016_1022,

dose of 10 Gy/1–2 weeks to the tumor, (3) control radiation dose plus 1,3-bis(2-chloroethyl)-l-nitrosourea (BCNU, carbazine), and (4) control radiation dose plus combination methyl-chloroethyl-cyclohexyl-nitrosourea (CCNU, lomustine) and DTIC (dacarbazine). No treatment option was found to be significantly better than the control. At least several important prognostic factors have been identified: age, histologic type (astrocytoma with anaplastic foci versus GBM), initial performance status, time since first symptoms, and presence or absence of seizure.

2 Modern Methods and Strategies

2.1 Whole Brain Radiation Therapy (WBRT) Versus Involved Field Radiation Therapy (IFRT)

WBRT initially used opposed lateral cranial portals with 50–60 Gy. The major complications following WBRT included progressive and irreversible radiation necrosis, small blood vessel injury, vascular occlusion, and demyelination (Shapiro 1986). Other late sequelae included asymptomatic narrowing of large vessels, delayed RT-induced leukoencephalopathy, and secondary neoplasia.

The severe effects of high-dose WBRT led to the adoption of IFRT as standard therapy. Up to 80–90 % of recurrent malignant gliomas develop within 2 cm of the original tumor (Wallner et al. 1989). Thus, radiation treatment of the tumor bed plus margin could reduce the recurrence rate with far less toxicity. Initially, this concept was imperfectly realized, with external beam RT coarsely focused using individually formed lead cutouts to protect the surrounding healthy brain tissue.

2.2 3D Conformal Radiation Therapy

The use of 3D CRT radiotherapy planning improved the distribution of radiation to the tumor and surrounding tissue. Treatment plans with clearly delineated target volumes are based on tissue density measurements in Hounsfield units of computer tomography (CT). Additional imaging modalities such as magnetic resonance imaging (MRI) or positron emission tomography (PET) can be fused with the planning CT to further define target areas (Glatstein et al. 1985). Considerations in treatment planning include beam sequelae energy, field size and shape, beam modifiers, irradiated tissue density and heterogeneity, and radiation tolerance of surrounding normal tissues. With 3D treatment planning, the target is typically encompassed by multiple treatment beams. Since RT beams deliver a relative homogeneous dose to the target, wedges can be added to modify the intensity profile of the beam. Nevertheless, a significant RT dose is delivered to all tissues in the shadow of the target (Grosu et al. 1998).

2.3 Intensity-Modulated Radiotherapy (IMRT)

Further advances in computer technology enabled the application of nonhomogeneous beams, known as intensity-modulated RT (IMRT). The dose flounce is modified. Such nonuniform doses from several beam orientations are combined to deliver the highly customized dose distributions to the target, optimizing the dose to tumor while sparing normal tissue (Fig. 1). After the physician defines the desired dose distribution to tumor and organs at risk, a reiterative computer algorithm is used to generate an optimized set of beam intensity profiles. This so-called inverse planning is particularly advantageous when the target is adjacent to radiation-sensitive structures, where a steep falloff of dose can be attained. The decreased dose to organs at risk may minimize radiation-related adverse events (Narayana et al. 2006). This treatment modality depends on a clear delineation of target volumes and of structures that are to spare by the treating physician. The overall complexity of this technologically advanced radiation planning requires sophisticated computer software and hardware, skilled physicist support, and increased delivery time for treatment. Delivery of treatment depends on linear accelerators which can administer radiation through a rapid succession

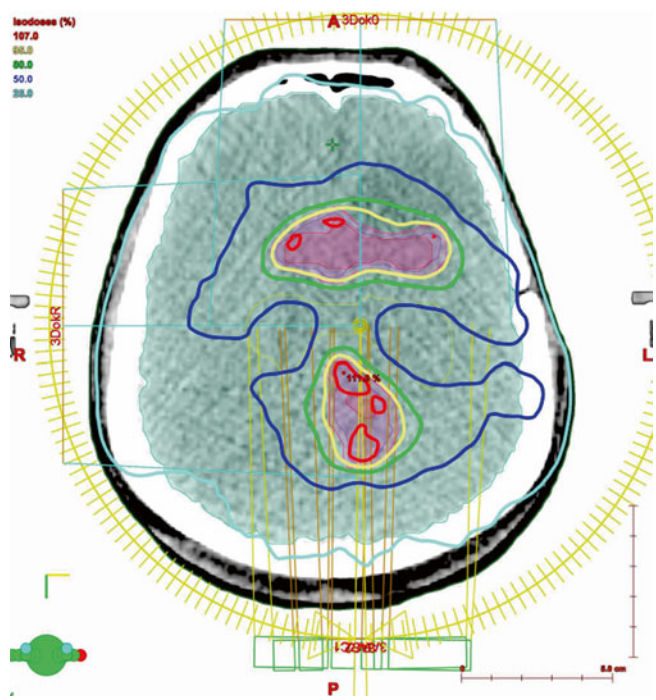

Fig. 1 Intensity-modulated radiotherapy (IMRT). The IMRT treatment plan for re-irradiation based on the FET uptake of the patient imaged in this figure. This plan of 39 Gy in 13 fractions consists of two arcs of gantry movement. One arc composed of more than 150 fields, indicated by the *yellow circle*. The concave and convex dose distribution is best visualized in the blue 50 % isodose line

of apertures, either static or moving, known as "step-and-shoot" and "sliding-window," respectively.

A nonuniform dose distribution can be intentionally prescribed in *dose painting* to target tumor areas that are markedly radiation resistant. These areas can be visualized on PET (e.g., hypoxia PET, proliferation PET, etc.) or functional MRI. Alternatively, a more conformal dosage can be obtained by a simultaneous integrated boost in which all target volumes such as viable tumor and residual tumor plus margins are treated concurrently (Piroth et al. 2012). These complex plans are evaluated on the basis of dose-volume tables and histograms that show minimum, mean, and maximum dose to a given structure. Presently there is no proven benefit to delivering doses beyond 60 Gy with IMRT in glioblastoma patients (Chan et al. 2002).

2.4 Stereotactic Radiosurgery (SRS) and Radiotherapy

Stereotactic radiosurgery (SRS) and radiotherapy are delivered using a linear accelerator or Gamma Knife with cobalt-60. Stereotactic radiosurgery is performed in a single high-dose fraction to small (<4 cm) targets, whereas fractionated stereotactic radiosurgery is delivered in several fractions. Stereotactic radiotherapy can also be delivered over multiple fractions.

The Gamma Knife contains a helmet with circular apertures ranging from 4 to 18 mm that collimates cobalt-60 rays onto a single target point. In a linear accelerator, circular collimators ranging from 4 to 40 mm diameter generate a circular pencil beam. The treatment is delivered using multiple non-coplanar arcs that intersect at a single point. The ideal target is spherical in shape. Irregularly formed lesions are treated using multiple circular collimators or collimator helmets placed on different nearby target points to minimize the exposure of normal brain. RTOG study 90–05 recommended the maximum tolerated dose of single fraction SRS to be 24 Gy to a target ≤20 mm, 18 Gy to a target of 21–30 mm, and 15 Gy to a target of 31–40 mm (Shaw et al. 2000).

LINAC radiosurgery is performed by linear accelerators incorporating improved guiding techniques and methods like micromultileaf collimators or intensity modulation for improved accuracy.

CyberKnife is a LINAC-based commercially available system mounted on an industrial robot. The robotic arm can be manipulated in six axes. The LINAC system provides energy of 6 MeV and uses circular collimators. Two orthogonal X-ray apparatus are used for target tracking leading to frameless positioning of the patient. According to the manufacturer, an accuracy of 0.2 mm can be achieved.

RTOG 93–05 trail was unable to demonstrate a benefit from adjuvant SRS in a phase III trial, in which 203 patients were randomly assigned to stereotactic radiosurgery followed by involved field RT plus carmustine (BCNU) to immediate involved field RT plus carmustine. Median survival was similar on both arms of the study (13.6 and 13.5 months, respectively), as was survival at 2 and 3 years (21 versus 19 % and 9 versus 13 %, respectively) (Souhami et al. 2004). Conversely, stereotactic radiosurgery has also been used to boost fractionated RT for the treatment of newly diagnosed GBM following either biopsy or resection. Results from observational studies have been mixed and are difficult to interpret due to patient selection bias.

Stereotactic radiotherapy is also used in recurrent gliomas for re-irradiation (Shepherd et al. 1997; Grosu et al. 2005b).

2.5 Interstitial Brachytherapy

For interstitial brachytherapy, radioisotope seeds are placed intraoperatively within the tumor or resection cavity. Iodine-125, a low-dose rate irradiator, is commonly used. The high-dose isotope iridium-192 has also been tested for selected patients. Although interstitial brachytherapy is frequently used in treatment of other disease entities, such as prostate cancer, its role is limited in the treatment of gliomas.

Brachytherapy enables the delivery of a large radiation dose to the tumor volume, with rapid falloff in surrounding tissues. Despite these theoretical dosimetric and radiobiological advantages, randomized clinical trials have shown marginal or negligible benefit in the treatment of malignant gliomas. In the largest study, 299 patients with malignant gliomas were randomly assigned postoperatively to IFRT plus carmustine with or without interstitial brachytherapy. The difference in median survival with the addition of brachytherapy was not statistically significant, 68 versus 59 weeks without brachytherapy (Selker et al. 2002).

2.6 Dose Prescription

An RT dose of 50–60 Gy has been shown to maximize postoperative survival, independent of the extent of resection (Coffey et al. 1998). Dose escalation above 60 Gy did not improve survival and was associated with severe white matter changes which correlate with the total dose of cranial irradiation (Piroth et al. 2012; Corn et al. 1994; Tsien et al. 2009).

Typically, WHO grade III gliomas are treated with a dose of 59.4 Gy in 1.8 Gy fractions versus 60 Gy in 2 Gy fractions for grade IV. This 10 % dose reduction per fraction is postulated to reduce the extent of normal tissue complications in patients with protracted survival, but there is no data comparing these regimens.

2.7 Particle Radiation Therapy

Particles used for radiation therapy include atomic particles such as electrons, neutrons, and protons (hydrogen), as well as nuclei of atoms such as helium, carbon, and neon. Heavy ion particles such as helium and neon directly damage cellular targets, rather than working through a free radical intermediary that is oxygen dependent, such as with electrons and photons. This may enhance the efficacy of treatment in the hypoxic conditions present in certain tumors such as malignant gliomas. In addition, these heavy ion particles release energy at a certain depth, known as a Bragg peak, which allows the dose to be precisely aimed within the target tissue and provide an increased relative biological effectiveness. They have been used alone and as a boost to conventional photon EBRT (Combs et al. 2010).

Prospective randomized phase III trials comparing protons or carbon ions with precision photon RT have never been conducted. There are limited data on the usage of proton beam RT in GBMs. A study of 15 patients with GBM treated with neon ion irradiation showed median survival of 13–14 months (Castro et al. 1997). In one series of 23 patients, proton RT resulted in a median survival of 20 months following surgery (Fitzek et al. 1999). In the later study a dose equivalent to 90 Gy was prescribed. The authors reported a high rate of tissue necrosis causing progressive neurological symptoms and need for surgical intervention.

Whereas the highly conformal radiation delivery with the use of protons can permit dose escalation, its potential application in treating GBM may be better suited to simply limiting RT-related side effects. Radiation therapy using protons can limit RT-related side effects due to its conformal dose delivery. However, a convincing benefit from dose escalation was not demonstrated so far. These data do not appear to be better than can be achieved with standard photon RT.

Indications for heavy particle include skull base chordomas and chondrosarcomas (Schulz-Ertner and Tsujii 2007). In a retrospective analysis of nonrandomized treatment groups, chordoma patients treated with protons had a significantly higher local control probability in comparison to patients treated with photons (Colli and Al-Mefty 2001).

3 Role of Imaging and Treatment Planning

In radiation oncology, imaging is used for clinical staging and treatment planning. Following a course of treatment, imaging is performed at regular intervals to assess for recurrence or, in case of long-term survivors, for second primary malignancies. Radiation oncologists must be familiar with imaging modalities and understand the accuracy and limitations of each. Considering the abovementioned improvements and changes of radiation therapy, the role of imaging becomes more and more important in treatment planning.

An important part of the radiation therapy is the delineation of the gross tumor volume (GTV), clinical target volume (CTV), and planning target volume (PTV). The macroscopic apparent tumor volume is referred to as GTV. The CTV encompasses suspected tumor invasion to the adjusted tissue, lymph vessels, or the draining lymph node stations, which cannot be identified by imaging. Radiation oncologists need expertise in anatomy and knowledge of the different malignancies in order to generate a rational and individual CTV. For example, glioblastoma spread along the white matter does not infiltrate the dura. The planning target volume (PTV) takes into account the accuracy of administration of the radiation therapy. A safety margin is added to the CTV in all directions depending on the accuracy of the treatment facility, the radiotherapy technique, the reproducibility of the daily patient positioning, or the patient movement during treatment.

Standard morphological imaging methods like CT (computed tomography) and MRI (magnetic resonance imaging) enhanced with contrast agents are employed.

In the treatment of GBM, the RT dose is usually delivered to the tumor or resection cavity plus a margin of apparently normal brain tissue. The EORTC guidelines (European Organization for Research and Treatment of Cancer) recommend a margin of 2 cm. The current guidelines of RTOG recommend a 2 cm margin around the resection cavity and the postoperative edema. In a recent study, patterns of failure were similar between the different treatment plans; however the median volume percent of brain irradiated to high doses was significantly smaller for EORTC plans than for RTOG plans (Minniti et al. 2010).

Margins from CTV to PTV became smaller over the years because of improvement of patient positioning using stereotactic cranial masks (STX) or STX whole body mat. Image guidance during RT not only controls the positioning of the patient but also the positioning or filling of inner organs. For this purpose, X-rays, kV imaging or MV imaging, and even cone beam CT are integrated in the linear accelerator.

Advanced imaging modalities for the RT treatment planning require sophisticated software tools to co-register multiple imaging scans. The automatic segmentation of structures can be done according to density information like Hounsfield units or by generating iso-contours by defining thresholds. Some programs can also generate structures like organs at risk from a stored database.

3.1 Computed Tomography (CT)

CT plays a primary role in RT treatment planning. Compared with conventional simulation, CT-based planning allows for more accurate target delineation, tighter margins, and less normal tissue irradiation. CT dose calculation is based on tissue density (Hounsfield units).

3.2 Magnetic Resonance Imaging (MRI)

Due to excellent soft tissue contrast and ability to image directly in multiple planes, MRI is the preferred imaging modality for intracranial and spinal tumors. Using modern software, MRI is co-registered to the planning CT.

The contrast enhancement on MRI represents the breakdown of the blood–brain barrier (BBB) (Conventional MR imaging). A disruption of the BBB can also occur from recent operations or radiation therapy (Taal et al. 2008; Clarke and Chang 2009; Wen et al. 2010). Thereby, it is not tumor specific. Additionally, there are sometimes large tumor parts where the BBB is not yet affected and that show no secondary tumor features like enhancement, cerebral edema, and/or compression of other brain structures. These tumor parts as well as non-enhancing low-grade gliomas are only seen as a hyperintense signal on FLAIR or T2 sequences (Conventional MR imaging). In these cases, the contrast enhancement in T1-weighted MRI sequences underestimates the tumor mass, and consequently, these parts are insufficiently treated.

In addition, as bevacizumab reverses the breakdown of the BBB, it leads to decrease of the contrast enhancement on MRI, pseudo-response, and alteration in tumor behavior. There is evidence that bevacizumab may alter the recurrence pattern of malignant gliomas by suppressing enhancing tumor recurrence more effectively than it suppresses nonenhancing, infiltrative tumor growth (Norden et al. 2008).

Consequently, as mentioned in Conventional MR imaging, certain treatment-related changes after surgery, radiation, and/or chemotherapy, known as pseudo-progression and pseudo-response, cannot be differentiated from tumor tissue (Clarke and Chang 2009; Wen et al. 2010; Brandsma and van den Bent 2009). Because it is self-limiting, it is necessary to separate this phenomenon from radionecrosis, which is a late and progressive radiation injury. It can develop months or even years after the treatment (Giglio and Gilbert 2003).

3.3 Positron Emission Tomography (PET)

Imaging methods like positron emission tomography (PET) and single-photon emission computed tomography (SPECT) detect metabolic activity of tumor tissue.

As described in Chap. 7, current diagnostic efforts focus on the use of radiolabeled amino acids (AA) as tracers for brain tumors. Increased AA uptake in gliomas is related to an overexpression of amino acid transporters in the cell membrane. It has been demonstrated that AA uptake in tumor tissue is almost entirely mediated by type L-AA carriers (Langen et al. 2000).

FET and MET were shown to be equally sensitive and specific in clinical practice (Weber et al. 2000; Grosu et al. 2011).

PET and MRI scans of gliomas show considerable differences in tumor volume and position (Fig. 2). In 39 resected GBM patients ^{11}C-MET uptake extended beyond the tumor identified by magnetic resonance imaging in 74 % (Grosu et al. 2005a). In a study of 41 glioma patients, integrating FET uptake into the delineation of GTVs yielded significantly larger volumes in high-grade patients. The congruence of MRI and FET signals was poor with mean uniformity indices of 0.39. MRI-based PTVs missed 17 % of FET PET-/CT-based GTVs (Rieken et al. 2013). Thus, the choice of imaging technique can affect the success of the radiotherapy.

A trial of 44 patients with re-irradiation of recurrent malignant glioma revealed a significantly longer survival time in patients irradiated using MET-PET or IMT SPECT/CT/MRI image fusion in the treatment planning, in comparison to patients treated based on MRI/CT alone. The median tumor volume was larger in the group with PET/SPECT in comparison to the MRI/CT group, 19 and 14 cm^3, respectively (Grosu et al. 2005a, b). The size and location of residual tumor after surgery seen on MET-PET scan differ considerably from abnormalities found on postoperative MRI. In another study of 39 patients, methionine uptake and contrast enhancement on MRI corresponded only in 13 % of the cases (5/39 patients), while in 74 % of the cases, the region of MET uptake was larger than the region of contrast enhancement. Otherwise, the contrast enhancement area extended beyond the MET uptake in 69 % of the 39 patients (Grosu et al. 2005a, b).

Imaging with MRI and FET PEt allowed better distinction between cellular glioma tissue and peritumoral brain tissue than MRI alone. In a study of 31 patients correlating imaging findings with histological specimens, MRI yielded a sensitivity of 96 % for the detection of tumor tissue but a specificity of only 53 %, and combined use of MRI and FET PET yielded a sensitivity of 93 % and a specificity of 94 % (Pauleit et al. 2005).

Low- and high-grade gliomas can be discriminated by using time activity curves from dynamic FET PET (see Chap. 7, Pöpperl et al. 2007). Such diagnostic advantages can be used by radiation oncologist to create IMRT plans with integrated simultaneous boost to the aggressive tumor parts. Preclinical studies even demonstrated that it is possible to detect tumor stem cells by PET using antibody-based tracer (Gaedicke et al. 2014).

PET with radiolabeled AA can be used to visualize the infiltrative growth of gliomas for radiation treatment planning and response monitoring (Götz et al. 2012; Götz and

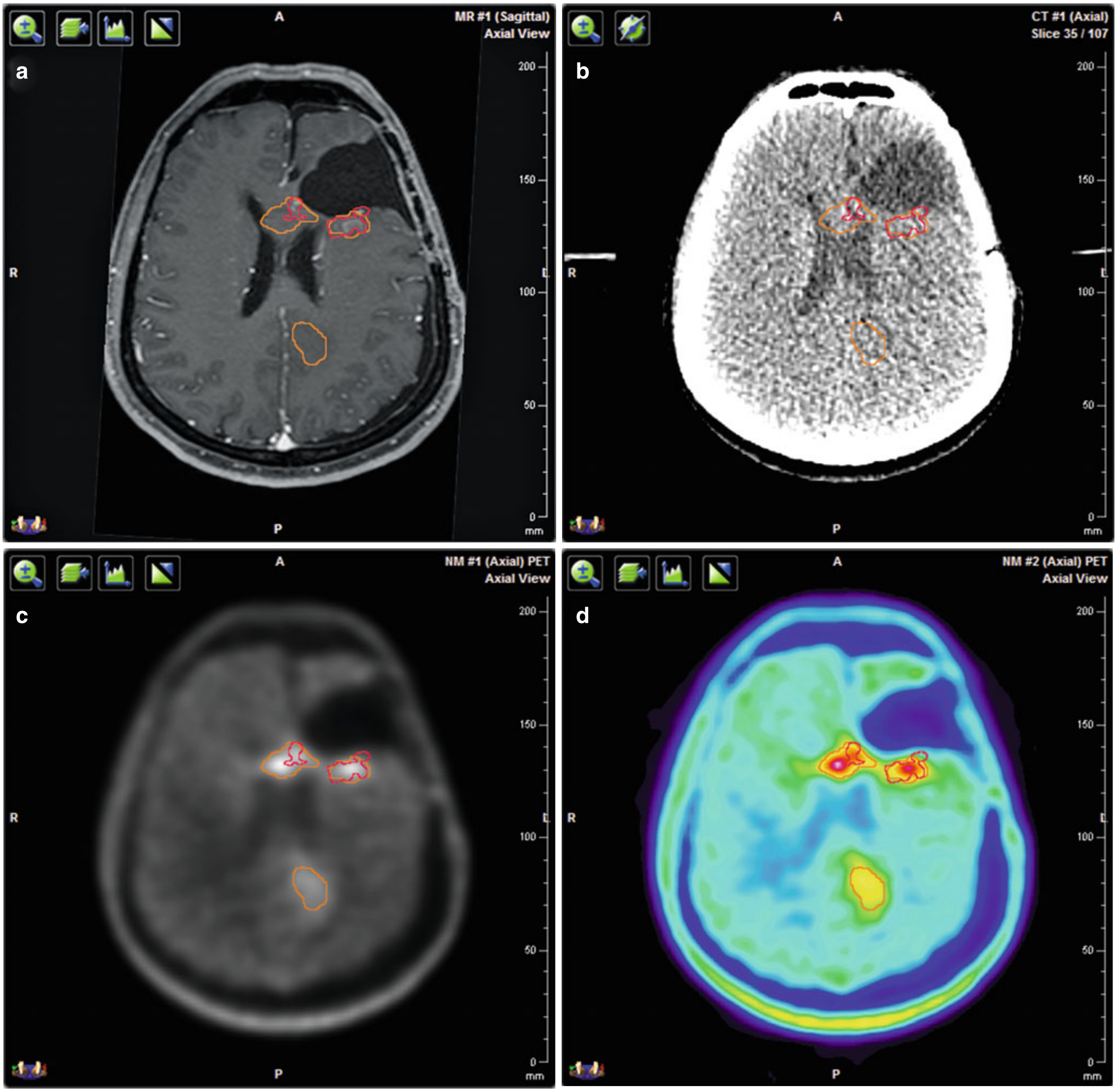

Fig. 2 Multimodal imaging for target volume delineation in a patient with recurrent glioblastoma. (**a**) Three-dimensional T1-weighted contrast enhanced MRI. (**b**) Planning CT. (**c**) 18F-FET PET/CT with CT-based attenuation correction in gray scale. (**d**) 18F-FET PET/CT with CT-based attenuation correction in rainbow scale. All images are co-registered with the planning CT. The red contour corresponds to the contrast enhancement on MRI and the orange contour to the FET uptake on PET. The volume and position of the detected tumor vary depending on the imaging method

Grosu 2013). Patients showing decrease of tracer uptake early after completion of radiochemotherapy had a significant longer progression-free survival and overall survival (Galldiks et al. 2012).

Other tracers like [^{18}F] 3′-deoxy-3′-fluorothymidine (FLT) that visualize cell proliferation are currently under research and might prove to be a valuable tool in response assessment, but are not yet used in clinical practice.

3.4 Image-Guided Radiation Therapy (IGRT)

Radiation therapy has essentially always been guided by images. However, today this term defines not only the use of modern imaging modalities incorporating functional or biological information but also the use of imaging to adjust for target motion or positional uncertainty. The RT field of the

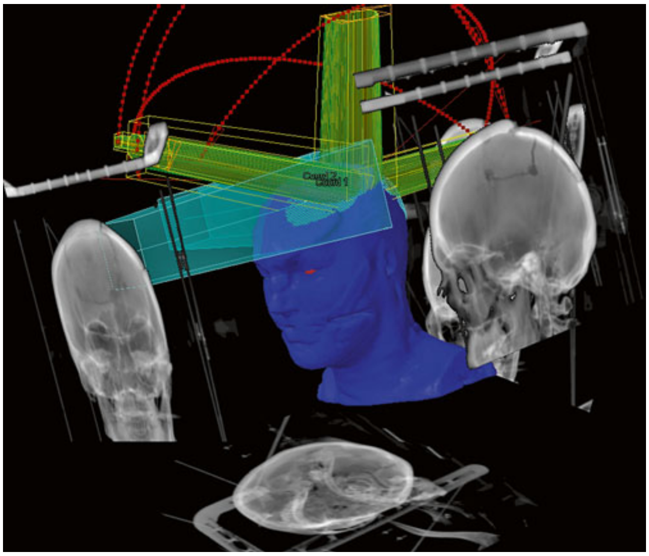

Fig. 3 Image-guided radiation therapy (IGRT). Patient positioning is verified by X-ray images taken directly before treatment. Treatment images are matched to reconstructed images from the planning CT (shown in *gray*) by using sophisticated software to adjust the treatment table in 6 rotation axes. This guarantees a high precision in dose application. The *blue* figure represents a patient's head in a stereotactic RT mask. The *yellow and green* beams represent the stereotactic photon beams

linear accelerator is monitored by X-rays using formerly with radiographic films and currently electronic portal imaging. Features of IGRT include daily online imaging, X-rays, cone beam CT, and megavolt CT to four-dimensional (4D) target localization. For brain tumors the combination of gantry and a planar kV imaging system leads to high-resolution diagnostic quality images of the patient in treatment position. The target tracking is by orthogonal X-ray images matched using bone or implanted markers (Fig. 3). The exposure to radiation is considerably less than using electronic portal imaging device (EPID).

IGRT has taken on greater importance with the introduction of IMRT including prolonged treatment time and the presence of steep dose gradients. The use of high fraction size in stereotactic radiation therapy requires an optimal target definition patient positioning to limit complication risk.

A cone beam CT can be made before and even during the radiation treatment in the treatment position to check the position of the patient (Jaffray et al. 2002).

3.5 Recurrence and Re-irradiation

Diagnostic challenge arises in cases of recurrence in high-grade brain tumors. Often, there are post-therapeutic changes visible on MRI and CT that can develop over a long time span. In cases of contrast enhancement, it is often impossible to differentiate between post-therapeutic changes and true tumor recurrence.

During follow-up ^{18}F-FET PET contributes important additional information for clinical management over and above the information obtained by MRI response assessment based on RANO criteria. More accuracy is needed in cases of re-irradiation, because of the exposure of organs at risk.

4 Prognosis

For the future we will pay more attention to tumor heterogeneity. We know that tumor stem cells are radioresistant while differentiated cells are more radiosensitive. It is worthwhile to learn more about these stem cells in order to optimize the treatment, for example, by modifying the fractionation scheme (Leder et al. 2014).

Conclusion

Radiation therapy plays an important role in the treatment of gliomas and prolongs the survival of the patients. The most effective and widely used technique is LINAC percutaneous radiation therapy with photons.

Radiation techniques have improved during the past decades, starting with opposed fields for whole brain irradiation leading to sophisticated intensity-modulated radiotherapy using more than 150 fields with modified fluency. By upgrading the precision of the beam, imaging modalities became increasingly important in treatment planning and in treatment application. Advanced imaging techniques will stay irreplaceable in the further progress of radiation therapy.

References

Andersen AP (1978) Postoperative irradiation of glioblastomas: results in a randomized series. Acta Oncol 17(6):475–484

Brandsma D, van den Bent MJ (2009) Pseudoprogression and pseudoresponse in the treatment of gliomas. Curr Opin Neurol 22(6): 633–638

Castro JR, Phillips TL, Prados M et al (1997) Neon heavy charged particle radiotherapy of glioblastoma of the brain. Int J Radiat Oncol Biol Phys 38(2):257–261

Chan JL, Lee SW, Fraass BA et al (2002) Survival and failure patterns of high-grade gliomas after three-dimensional conformal radiotherapy. J Clin Oncol 20(6):1635–1642

Chang CH, Horton J, Schoenfeld D et al (1983) Comparison of postoperative radiotherapy and combined postoperative radiotherapy and chemotherapy in the multidisciplinary management of malignant gliomas. A Joint Radiation Therapy Oncology Group and Eastern Cooperative Oncology Group study. Cancer 52(6):997–1007

Clarke JL, Chang S (2009) Pseudoprogression and pseudoresponse: challenges in brain tumor imaging. Curr Neurol Neurosci Rep 9(3):241–246

Coffey RJ, Lunsford LD, Taylor FH (1998) Survival after stereotactic biopsy of malignant gliomas. Neurosurgery 22(3):465

Colli B, Al-Mefty O (2001) Chordomas of the craniocervical junction: follow-up review and prognostic factors. J Neurosurg 95(6): 933–943

Combs SE, Kieser M, Rieken S et al (2010) Randomized phase II study evaluating a carbon ion boost applied after combined radiochemotherapy with temozolomide versus a proton boost after radiochemotherapy with temozolomide in patients with primary glioblastoma: the CLEOPATRA trial. BMC Cancer 10:478

Corn BW, Yousem DM, Scott CB et al (1994) White matter changes are correlated significantly with radiation dose. Observations from a randomized dose-escalation trial for malignant glioma (Radiation Therapy Oncology Group 83–02). Cancer 74(10):2828–2835

Fitzek MM, Thornton AF, Rabinov JD et al (1999) Accelerated fractionated proton/photon irradiation to 90 cobalt gray equivalent for glioblastoma multiforme: results of a phase II prospective trial. J Neurosurg 91(2):251–260

Gaedicke S, Braun F, Prasad S et al (2014) Noninvasive positron emission tomography and fluorescence imaging of CD133+ tumor stem cells. Proc Natl Acad Sci U S A 111(6):E692–E701

Galldiks N, Langen KJ, Holy R et al (2012) Assessment of treatment response in patients with glioblastoma using O-(2-18F-fluoroethyl)-L-tyrosine PET in comparison to MRI. J Nucl Med 53(7): 1048–1057

Giglio P, Gilbert MR (2003) Cerebral radiation necrosis. Neurologist 9(4):180–188

Glatstein E, Lichter AS, Fraass BA et al (1985) The imaging revolution and radiation oncology: use of CT, ultrasound, and NMR for localization, treatment planning and treatment delivery. Int J Radiat Oncol Biol Phys 11(2):299–314

Götz I, Grosu AL (2013) [(18)F]FET-PET imaging for treatment and response monitoring of radiation therapy in malignant glioma patients – a review. Front Oncol 3:104

Götz L, Spehl TS, Weber WA, Grosu AL (2012) PET and SPECT for radiation treatment planning. Q J Nucl Med Mol Imaging 56(2): 163–172, Review

Grosu AL, Feldmann HJ, Albrecht C et al (1998) 3-Dimensional irradiation planning in brain tumors. The advantages of the method and the clinical results. Strahlenther Onkol 174(1):7–13, German

Grosu AL, Weber WA, Riedel E et al (2005a) L-(methyl-11C) methionine positron emission tomography for target delineation in resected high-grade gliomas before radiotherapy. Int J Radiat Oncol Biol Phys 63(1):64–74

Grosu AL, Weber WA, Franz M et al (2005b) Reirradiation of recurrent high-grade gliomas using amino acid PET (SPECT)/CT/MRI image fusion to determine gross tumor volume for stereotactic fractionated radiotherapy. Int J Radiat Oncol Biol Phys 63(2):511–519

Grosu AL, Astner ST, Riedel E et al (2011) An interindividual comparison of O-(2-[18F]fluoroethyl)-L-tyrosine (FET)- and L-[methyl-11C]methionine (MET)-PET in patients with brain gliomas and metastases. Int J Radiat Oncol Biol Phys 81(4):1049–1058

Jaffray DA, Siewerdsen JH, Wong JW, Martinez AA (2002) Flat-panel cone-beam computed tomography for image-guided radiation therapy. Int J Radiat Oncol Biol Phys 53(5):1337–1349

Langen KJ, Muhlensiepen H, Holschbach M et al (2000) Transport mechanisms of 3-[123I]iodo-alpha-methyl-L-tyrosine in a human glioma cell line: comparison with [3H]methyl]-L-methionine. J Nucl Med 41(7):1250–1255

Leder K, Pitter K, Laplant Q et al (2014) Mathematical modeling of PDGF-driven glioblastoma reveals optimized radiation dosing schedules. Cell 156(3):603–616

Minniti G, Amelio D, Amichetti M et al (2010) Patterns of failure and comparison of different target volume delineations in patients with glioblastoma treated with conformal radiotherapy plus concomitant and adjuvant temozolomide. Radiother Oncol 97(3):377–381

Narayana A, Yamada J, Berry S et al (2006) Intensity-modulated radiotherapy in high-grade gliomas: clinical and dosimetric results. Int J Radiat Oncol Biol Phys 64(3):892–897

Norden AD, Young GS, Setayesh K et al (2008) Bevacizumab for recurrent malignant gliomas Efficacy, toxicity, and patterns of recurrence. Neurology 70(10):779–787

Pauleit D, Floeth F, Hamacher K et al (2005) O-(2-[18F] fluoroethyl)-L-tyrosine PET combined with MRI improves the diagnostic assessment of cerebral gliomas. Brain 128(Pt 3):678–687

Piroth MD, Pinkawa M, Holy R et al (2012) Integrated boost IMRT with FET-PET-adapted local dose escalation in glioblastomas. Strahlenther Onkol 188(4):334–339

Pöpperl G, Kreth FW, Mehrkens JH et al (2007) FET PET for the evaluation of untreated gliomas: correlation of FET uptake and uptake kinetics with tumour grading. Eur J Nucl Med Mol Imaging 34(12):1933–1942

Rieken S, Habermehl D, Giesel FL et al (2013) Analysis of FET-PET imaging for target volume definition in patients with gliomas treated with conformal radiotherapy. Radiother Oncol 109(3):487–492

Schulz-Ertner D, Tsujii H (2007) Particle radiation therapy using proton and heavier ion beams. J Clin Oncol 25(8):953–964, Review

Selker RG, Shapiro WR, Burger P et al (2002) The Brain Tumor Cooperative Group NIH Trial 87–01: a randomized comparison of surgery, external radiotherapy, and carmustine versus surgery, interstitial radiotherapy boost, external radiation therapy, and carmustine. Neurosurgery 51(2):343–355

Shapiro WR (1986) Therapy of adult malignant brain tumors: what have the clinical trials taught us? Semin Oncol 13(1):38–45

Shaw E, Scott C, Souhami L et al (2000) Single dose radiosurgical treatment of recurrent previously irradiated primary brain tumors and brain metastases: final report of RTOG protocol 90–05. Int J Radiat Oncol Biol Phys 47(2):291–298

Shepherd SF, Laing RW, Cosgrove VP et al (1997) Hypofractionated stereotactic radiotherapy in the management of recurrent glioma. Int J Radiat Oncol Biol Phys 37(2):393–398

Souhami L, Seiferheld W, Brachman D et al (2004) Randomized comparison of stereotactic radiosurgery followed by conventional radiotherapy with carmustine to conventional radiotherapy with carmustine for patients with glioblastoma multiforme: report of Radiation Therapy Oncology Group 93–05 protocol. Int J Radiat Oncol Biol Phys 60(3):853–860

Stupp R, Mason WP (2005) Radiotherapy plus concomitant and adjuvant temozolomide for glioblastoma. N Engl J Med 352(10): 987–996

Taal W, Brandsma D, de Bruin HG et al (2008) Incidence of early pseudo-progression in a cohort of malignant glioma patients treated with chemoirradiation with temozolomide. Cancer 113(2):405–410

Tsien C, Moughan J, Michalski JM et al (2009) Phase I three-dimensional conformal radiation dose escalation study in newly diagnosed glioblastoma: Radiation Therapy Oncology Group Trial 98–03. Int J Radiat Oncol Biol Phys 73(3):699–708

Walker MD, Alexander E Jr, Hunt WE et al (1978) Evaluation of BCNU and/or radiotherapy in the treatment of anaplastic gliomas: a cooperative clinical trial. J Neurosurg 49(3):333–343

Walker MD, Green SB, Byar DP et al (1980) Randomized comparisons of radiotherapy and nitrosoureas for the treatment of malignant glioma after surgery. N Engl J Med 303(23):1323–1329

Wallner KE, Galicich JH, Krol G et al (1989) Patterns of failure following treatment for glioblastoma multiforme and anaplastic astrocytoma. Int J Radiat Oncol Biol Phys 16(6):1405–1409

Weber WA, Wester HJ, Grosu AL et al (2000) O-(2-[18F]fluoroethyl)-L-tyrosine and L-[methyl-11C]methionine uptake in brain tumours: initial results of a comparative study. Eur J Nucl Med 27(5):542–549

Wen PY, Macdonald DR, Reardon DA et al (2010) Updated response assessment criteria for high-grade gliomas: response assessment in neuro-oncology working group. J Clin Oncol 28(11):1963–1972

Advanced Imaging Modalities and Treatment of Gliomas: Neurosurgery

Johannes Wölfer and Walter Stummer

Contents

J. Wölfer • W. Stummer (✉)
Neurochirurgische Klinik, Universitätsklinikum Münster,
Albert-Schweitzer-Campus 1, Geb. A1, Münster 48149, Germany
e-mail: woelfer@uni-muenster.de; walter.stummer@ukmuenster.de

Abstract

Current data warrant cytoreductive surgical approaches in low as well as high grade gliomas. Surgical aims vary depending on histology – speed of growth and impending malignant transformation being major aspects in low grades, while surgical improvement of preconditions for adjuvant therapy gains prognostic relevance in malignant glioma. A delicate balance between the extent of resection and functional integrity has to be kept in all of these procedures. Their planning and realization thus require reliable conceptions of tumor extension with reference to functional anatomy. Radiology and nuclear medicine provide preoperative and, to a certain extent also intraoperative insights. Additional intraoperative assistance is provided by electrophysiology and – in malignant glioma – by direct tumor visualization, which uses pharmacologic agents together with specialized optics. Emerging surgical concepts like functionally guided tissue removal or so-called supramarginal resection are still waiting for their clinical validation and for new techniques which might be able to morphologically substantiate the respective rationale.

1 Why Is Advanced Imaging Indispensable for Modern Glioma Surgery?

During the last two decades, the understanding of the value of glioma resection has undergone a change. Despite a paucity of randomized studies, a number of prospective cohort studies have provided acceptable evidence that maximal cytoreduction is a meaningful treatment option which serves to improve prognosis in patients suffering from high- and low-grade gliomas alike. Nowadays, many surgeons are adapting this strategy.

Low-grade glioma (LGG) patients are frequently young and oligosymptomatic, usually presenting with focal seizures which can be easily managed by appropriate medication. In such patients the neurosurgeon's responsibility is particularly great since the purpose of surgery is not primarily

E. Hattingen, U. Pilatus (eds.), *Brain Tumor Imaging*,
Med Radiol Diagn Imaging (2016)
DOI 10.1007/174_2016_1023, © Springer International Publishing Switzerland

the amelioration of symptoms. Neurosurgeons must keep this in mind before deciding on whether to operate and to what extent this should be done. On the other hand, recent studies have demonstrated that all LGGs will grow. The rate of growth has been calculated as about 4 mm/year (95 % CI: 3.8–4.4 mm, Mandonnet et al. 2003). This observation certainly questions whether a "wait-and-see" strategy is appropriate for the management of these patients if cytoreductive surgery may be considered an option. To the least, this observation cautions against just comparing one MRI with the previous one but rather suggests to use the earliest available MRI to decide whether a tumor is more or less stable or whether it is growing or changing, especially in the light of the quoad vitam prognosis of these patients. About 75 % of LGG patients die within 5–10 years after initial diagnosis (Keles et al. 2001; McGirt et al. 2008), and the prognosis of a low-grade glioma is similar to many non-glial cancers. Overall, such considerations justify active approaches in low-grade glioma therapy including cytoreductive surgery. Even though prospectively randomized studies which would unequivocally clarify the role of cytoreductive surgery in LGG patients are difficult to envision, a number of large and prospective cohort studies afford useful data on the value of cytoreductive surgery (McGirt et al. 2008; Smith et al. 2008). One such study from Norway provided additional interesting data (Jakola et al. 2013). In Norway basically two neurosurgical departments are involved in glioma care. One department favors biopsies, the other craniotomies. Patients treated in the hospital with the more aggressive approach survived longer. Of note: Even though controlled trials are still missing (Veeravagu et al. 2013), several large cohort studies indicate that resection should extend as far as possible because only complete or nearly complete resections, as measured by MRI as the best available imaging instrument, will have an impact on prognosis (McGirt et al. 2008; Smith et al. 2008).

Similarly, data are available which underline the value of resection in *high-grade gliomas* (HGG; Laws et al. 2003). One small randomized study compared biopsies with resections in elderly (>65 years of age) HGG patients (Vuorinen et al. 2003). Patients treated by craniotomy and tumor resection survived significantly longer. Another prospectively randomized study on 5-ALA for fluorescence-guided resections (Fig. 1) was able to demonstrate that patients had prolonged progression-free survival when the extent of the resection was improved by the use of 5-ALA (Stummer et al. 2006). Similar effects were observed in a study with patients being randomized into surgery with or without intraoperative MRI (Senft et al. 2011). Authors suggest that progression-free survival was improved by the use of intraoperative MRI, albeit not significantly due to the small number of patients in this study. However, most of these studies combined resection with adjuvant radiotherapy alone, and it might be questioned whether surgery in conjunction with adjuvant radiochemotherapy according to the EORTC regime still requires maximal cytoreduction. To this end, newer studies confirm that the prognostic effect of maximum possible resection of contrast-enhancing tumor remains unmitigated or is even boosted when patients are treated by the current standard regime, concomitant radiochemotherapy, rather than radiotherapy alone (Stummer et al. 2012; Kreth et al. 2013). Similar to the results

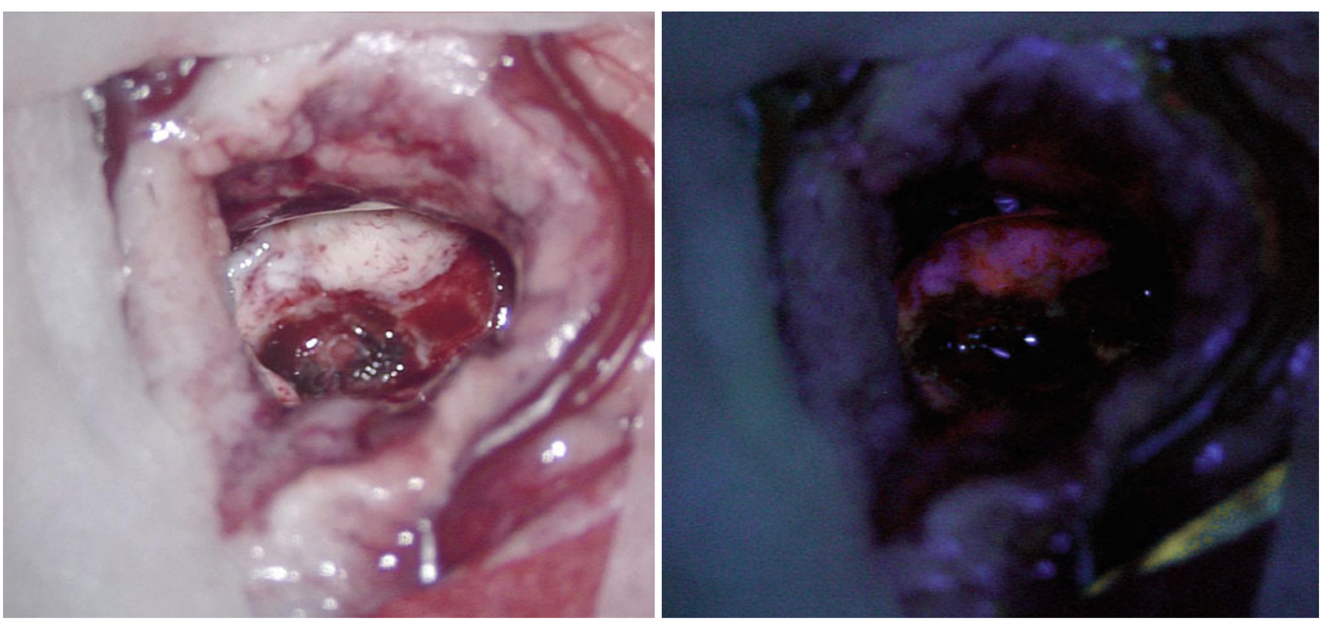

Fig. 1 View through the microscope, the *left image* shows the native surgical site of a small glioblastoma. After exogenous 5-ALA application, tumor cells will become fluorescent under ultraviolet light (red tumor on the *right image*). This feature identifies the tumor cells intraoperatively and facilitates complete resection

in LGG, these newer studies suggest that even the removal of small residual contrast-enhancing tumor volumes is a decisive element and should be strived for (Stummer et al. 2012; Kreth et al. 2013), as was the case in earlier studies conducted prior to the dawn of concomitant radiochemotherapy for glioblastomas (Stummer et al. 2008; Lacroix et al. 2001). In these studies surgery was combined with radiotherapy only, and small areas of contrast-enhancing tumor remnants significantly worsened prognosis as well.

On the other hand, it is widely accepted that major neurological deficits will have an adverse influence on prognosis (McGirt et al. 2009a, b; Stummer et al. 2012). The reasons for this have not been clarified. Possibly, patients with prolonged and marked postoperative neurological impairments are less likely to undergo intensive second-line therapies in the case of tumor progression; additionally, they might be prone to immobility-related complications.

Altogether, neurosurgeons are faced with conflicting goals, i.e., to achieve maximal resection during removal of diffuse neoplasms of the brain while maintaining neurological integrity, both for low- and high-grade gliomas. In this context, modern pre- and intraoperative imaging modalities are indispensable for state-of-the-art surgical planning and should be directly integrated into surgical decision making. Imaging, be it preoperative or intraoperative, has greatly helped the surgeon in achieving these opposing aims. Postoperative imaging is equally essential. Not only will it allow the surgeon to assess the quality of his work and whether his predetermined resection aims were achieved, but it will also allow for more differentiated decisions on adjuvant therapies. Residual tumor on postoperative imaging is closely related to prognosis in patients with low- and high-grade gliomas alike.

This chapter gives an overview on how imaging strategies currently assist in surgical decision making and how they can be used intraoperatively for improving surgical management of gliomas.

2 Preoperative Imaging Strategies

The decision of the surgeon on whether to perform debulking surgery, maximal cytoreduction, or only a biopsy, and the appropriate counseling of patients and families, depends on preoperative risk assessment. This assessment in turn relies on preoperative imaging, which gives information on the anatomical extent of tumor deemed appropriate for resection, on its potential dignity, and on the limits of resection, the latter being defined by functionally important brain structures, i.e., the cortex or deep white matter tracts that border on the tumor. Thus, preoperative imaging may be subdivided into imaging of surgical tumor morphology and imaging of functional brain anatomy.

2.1 What Is the Surgical Target in Low-Grade Gliomas?

LGGs are diffuse lesions which extend further than to be assumed from the usual MRI sequences. Nevertheless, for the sake of defining resectability[1] before, the estimated extent of resection during, and the surgical result after an operative procedure, standard MRI sequences will have to be relied upon as the modality giving the best morphological information. Among the available sequences, fluid attenuated inversion recovery (FLAIR) is the one most often used. To this end, three large studies which are frequently cited in conjunction with the value of resection in low-grade gliomas (Smith et al. 2008; McGirt et al. 2008; De Witt Hamer et al. 2012) rely on FLAIR images to define the extent of tumor and resection (Fig. 2). Apart from FLAIR images, additional sequences are considered necessary (see Conventional MR imaging), especially T2-weighted images (possibly in two orientations) and T1-weighted images before and after intravenous application of Gd-containing contrast agent, the latter intended to identify areas with possible malignant transformation. Identification of such hot spots is crucial since the surgeon has to ensure that these areas are specifically included into the histopathological analysis to avoid undergrading of tumors. Hot spots may also be found in LGG presenting as gliomatosis (Fig. 3). It has not yet been addressed in specific studies whether focal resection and treatment of such hot spots in an otherwise unresectable diffuse LGG influence prognosis.

Due to the diffuse nature of LGG with cells extending beyond what can generally be imaged by standard MRI (Sahm et al. 2012), "supratotal" resection strategies have been proposed (Duffau 2013; Yordanova et al. 2011), which consider functional rather than morphological borders of surgery. In such surgery, resection would not just be limited to the extent of the tumor as defined by the FLAIR image, but extend further up to cortex areas or deep white matter tracts which are considered functionally relevant. Such approaches are justified according to the value of maximal cytoreduction, provided they are safe. However, it remains to be established whether such surgery offers additional benefit.

[1] "Resectability" in glioma surgery is a complex concept which is determined by the surgeon's perception of possible neurological deficits related to surgical removal, which in turn is influenced by tumor location, tumor extension, and morphology, including vessels traversing or deep white matter tracts bordering to the tumor. Resectability is further influenced by the intended use of intraoperative monitoring and mapping techniques for minimizing risk while maximizing resection. Certain neurological functions are considered indispensable, such as language or motor function, while others might be considered amenable to limited sacrifice, such as visual field defects, or are simply not prioritized and therefore not monitored in the context of glioma treatment, such as elements of neurocognitive function.

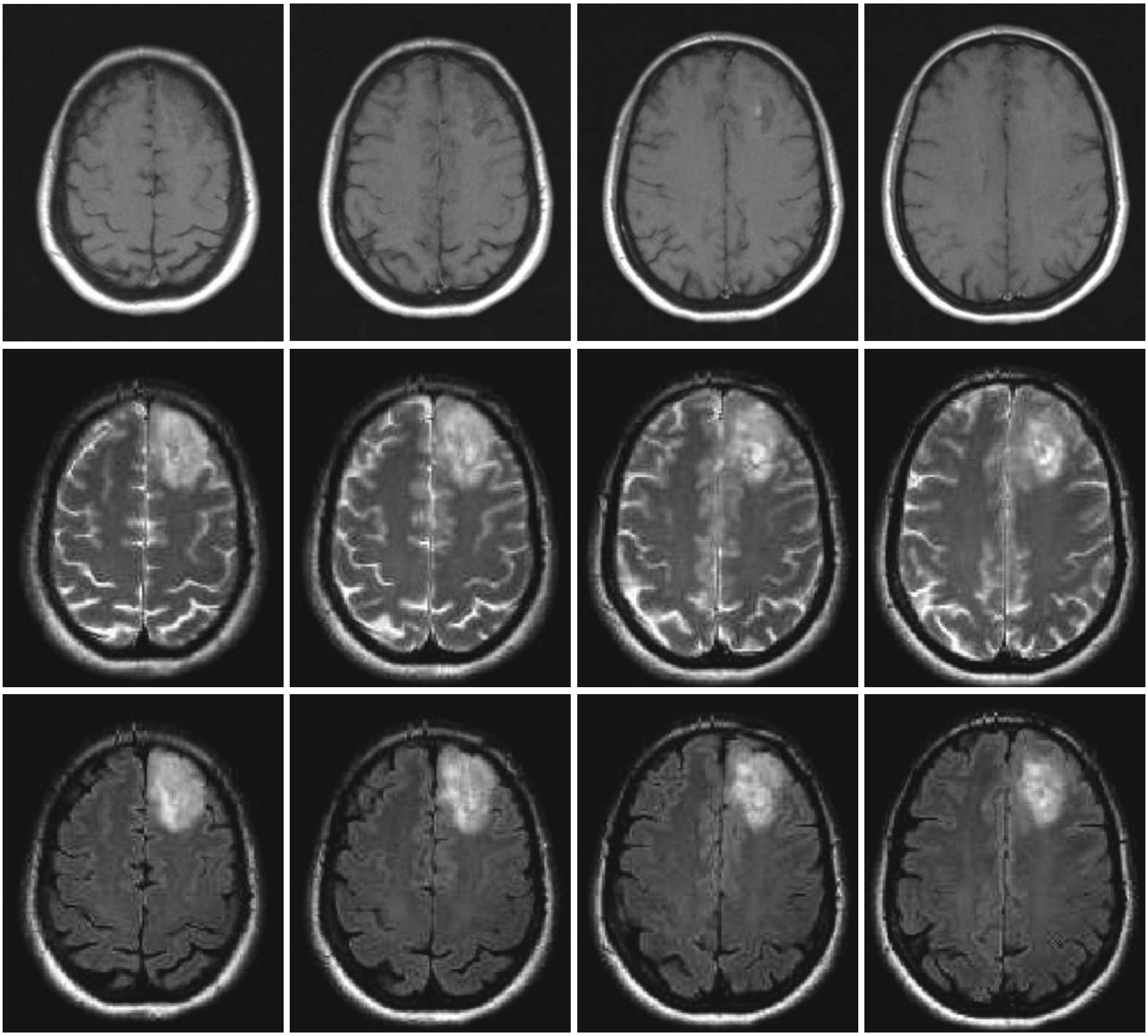

Fig. 2 Left frontal low-grade glioma in different MR sequences; female, 51 years. – native T1 (*top*), T2 (*middle*), and FLAIR (*bottom*) sequences (Courtesy of the Institute of Clinical Radiology, Münster)

2.2 The Role of Modern Imaging in Indicating Surgery in Low-Grade Gliomas

The EORTC study (Pignatti et al. 2002) has helped to define LGG patients with poor prognosis as opposed to patients with a longer survival, based on morphological criteria, histology, patient age, and neurological deficits. Higher age (>40 years), diffuse astrocytic pathology rather than oligoastrocytoma and oligodendroglioma, and neurological deficits contribute to the risk. Large tumors (>6 cm) and tumors crossing the midline were independent risk factors as well. Due to the restricted prognosis of high-risk patients, it might appear justified to treat these more aggressively, including surgical debulking or cytoreduction. Others have observed that the speed of growth, as determined from MR imaging, will also help to discern those tumors which carry a bad prognosis and possibly require a more aggressive surgical approach. Pallud et al. (2006) have demonstrated that if LGGs grow more than 8 mm per year, their prognosis is considerably worse than that of slower-growing tumors.

Amino acid positron emission tomography (PET) is a modern tool with increasing availability and acceptance for guiding the decision whether to perform surgery in appar-

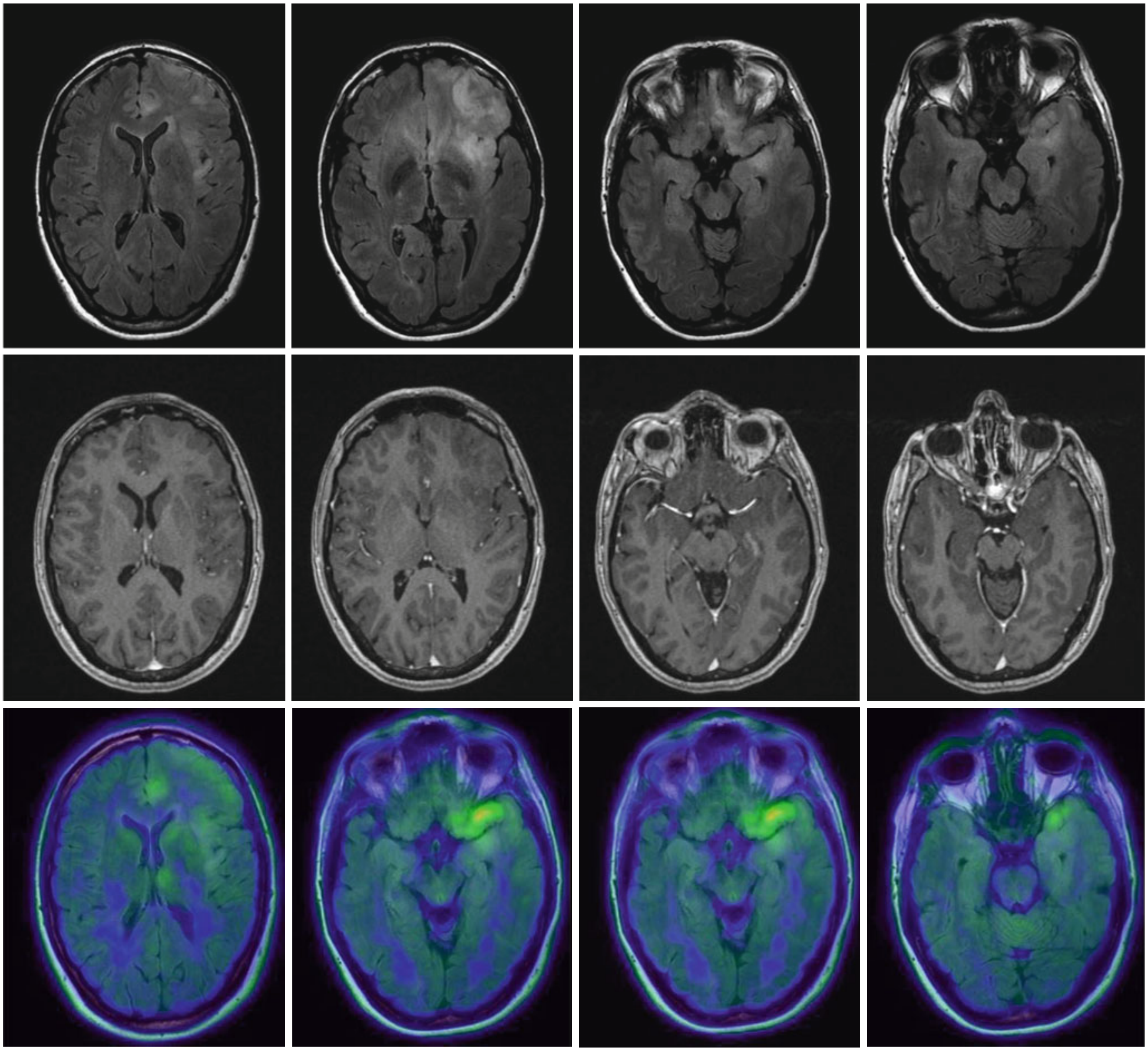

Fig. 3 Low-grade gliomatosis with metabolic hot spots demonstrated by PET; female, 45 years. – FLAIR (*top*), contrast-enhanced T1 (*middle*), and ^{18}FET-PET (*bottom*) (Courtesy of the Institute of Clinical Radiology and Clinic for Nuclear Medicine, Münster)

ently low-grade gliomas and in which areas to specifically collect biopsies. Hot spots in diffusely infiltrating tumors do not only delineate malignant tumor regions (Kunz et al. 2012; Ewelt et al. 2011) but they will also help to avoid undergrading if areas of malignant degeneration are missed (Fig. 3). It is estimated that high-grade astrocytomas are frequently undergraded if they are only biopsied instead of being resected after craniotomy, the latter with a higher likelihood of finding the anaplastic focus in up to 30 % of cases (Glantz et al. 1991; Woodworth et al. 2005; Jackson et al. 2001; Muragaki et al. 2008). Even in histologically proven LGG, increased amino acid uptake appears to signify a worse prognosis than in LGG without enhanced uptake (Floeth et al. 2007). Consequently, if a presumed LGG shows enhanced amino acid uptake, cytoreductive therapy should be considered more strongly, which can be based on the available evidence from the surgical treatment of HGG and the probability that such tumors might actually represent malignant gliomas which require adjuvant therapies.

PET (Chap. 7) and MR modalities (Chaps. 3, 4, 5, and 6) are currently being introduced into routine use, supplementing the information to be derived from standard sequences and possibly helping to identify low-grade tumors at risk for rapid progression (Guillevin et al. 2012; Geer et al. 2012; Sahin et al. 2013).

2.3 What Is the Surgical Target in High-Grade Gliomas?

In HGG a prognostic value of resection has always been associated with the removal of the contrast-enhancing parts of the tumor, as visualized by the contrast-enhanced

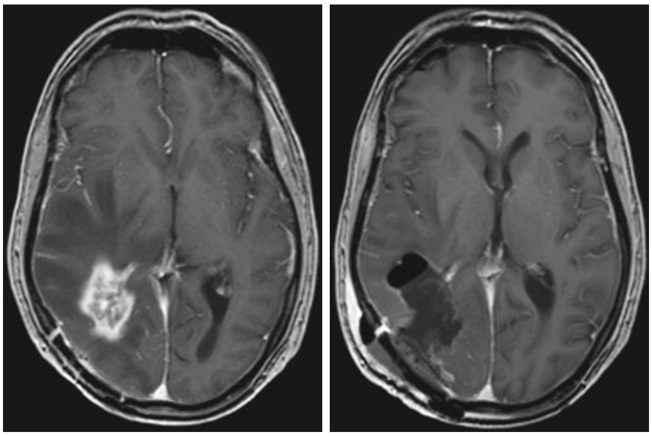

Fig. 4 Glioblastoma; male, 61 years. – contrast-enhanced T1 sequence. *Left*: Edema encasing the region of contrast enhancement. *Right*: Postoperative image after "supramarginal" resection guided by 5-ALA fluorescence (Courtesy of the Institute of Clinical Radiology, Münster)

T1-weighted sequence, although it is well known that malignant glioma cells infiltrate many centimeters beyond the contrast-enhancing tumor margins or even beyond the zone of edema (Sahm et al. 2012). This has been observed for both the anaplastic astrocytomas (Keles et al. 2006) and, with several large cohort studies and one randomized study, in glioblastoma (McGirt et al. 2009a, b; LaCroix et al. 2001; Stummer et al. 2008; Stummer et al. 2012; Kreth et al. 2013). This observation may be related to the biological characteristics of contrast-enhancing tumor. Contrast-enhancing areas are highly replete with dysfunctional vessels from uncontrolled angiogenesis, which are inefficient in supplying the tumor with oxygen, resulting in tumor hypoxia. This hypoxia, among other factors, renders the tumor resistant to radiotherapy (Stummer et al. 2011a, b).

Recent evidence, however, suggests that resections extending beyond the area of contrast enhancement might further improve prognosis in patients with glioblastomas as demonstrated by Aldave et al. (2013). This group operated glioblastoma patients guided by 5-ALA fluorescence. The zone of fluorescing tissue, which the surgeon can observe intraoperatively, is now known to extend well beyond the area of contrast enhancement as visualized by the MRI or even the ^{18}FET-PET (Fig. 4) (Schucht et al. 2014; Roessler et al. 2012). Aldave et al. (2013) analyzed all their patients without contrast-enhancing residual tumor on early postoperative MRI and stratified by whether all fluorescing tissue had been resected or not. They demonstrated that patients in whom all fluorescing tissue had been removed survived significantly longer. The MRI equivalent to this region of fluorescence extending beyond contrast enhancement is not known. Whether MR spectroscopy (see Chap. 3), diffusion-weighted imaging (Chap. 5), or MR perfusion methods (Chap. 4) will play a future role in helping to predict the extension of fluorescence beyond the region of contrast enhancement cannot yet be foreseen. In a malignant glioma, contrast enhancement will typically be encased by the zone of edema (Fig. 4).

The CT scan may also play a role in defining surgical strategies for oligodendrogliomas or oligoastrocytomas. These tumors frequently show calcifications on CT scans which are sometimes difficult to confidently diagnose on the MRI. Recognizing a possible "oligo" component on preoperative imaging will influence the surgeon's strategy regarding cytoreduction when neurological function is at stake (Fig. 5). High-grade oligodendrogliomas and oligoastrocytomas have a better prognosis in the face of cytotoxic therapies than anaplastic astrocytomas (Wick et al. 2009), and thus for such patients jeopardizing neurological function for the sake of radical tumor removal need not be an option.

2.4 Preoperative Imaging of Function and Functional Anatomy

During glioma surgery preservation of neurological function is paramount compared to radicalness, but safely achievable utmost radicalness must always remain the goal of surgery, or else the risks of surgery would not be justified. Intraoperatively, low-grade or infiltrating high-grade tumor tissue outside the region of gross necrosis is not easily distinguishable using microscopic visualization techniques, nor is function. Thus, preoperative knowledge of the anatomical localization of non-dispensable functions relative to tumor tissue aimed for resection is crucial. This knowledge will influence the surgeon's judgment of resectability in the individual case and will guide his decision on the surgical approach, the selection of technological aid for surgery (neuronavigation, fluorescence, intraoperative mapping or monitoring), and his counseling of patients and families regarding the risks and gains of surgery.

2.4.1 Imaging of Functional Cortex

Intraoperatively, apart from gross anatomical landmarks for indication of functionally important cortex and tracts, the brain offers few clues to individual functional representation on the one hand, or to the extent of resectable tumor on the other (see Conventional MR imaging).

With the exception of the primary motor cortex (Farrel et al. 2007; Shinoura et al. 2009), the classical anatomi-

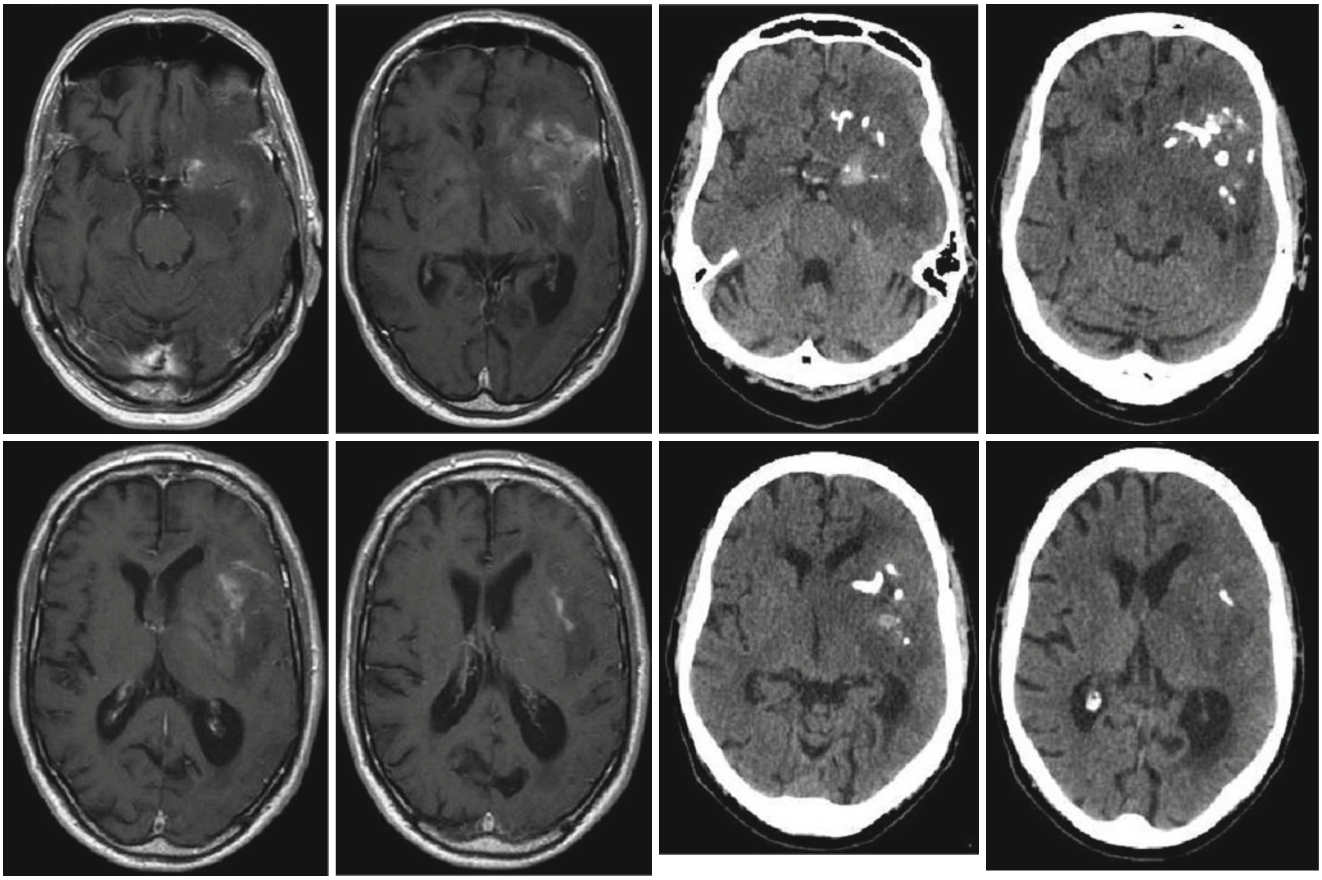

Fig. 5 Anaplastic oligoastrocytoma with calcifications; male, 72 years. – contrast-enhanced T1 (*left*), and native CT (right; courtesy of the Institute of Clinical Radiology, Münster)

cal representation of functions on the cortical surface may show considerable interindividual variability, especially with regard to the areas of language representation. The so-called "Broca" area in the inferior precentral frontal gyrus and the so-called "Wernicke" region located in the posterior third of the superior temporal gyrus are more or less statistical concentrations of cortical locations relevant for speech phonology, syntax, and semantics (Vigneau et al. 2006). Cortical regions with significant language functions may be found outside the classical regions so that simply respecting anatomical topography will not give the necessary safety for resecting tumors close to the so-called eloquent brain regions (McGirt et al. 2009a, b; Ojemann et al. 2008). Such knowledge has been derived from mapping during brain surgery under local anesthesia. Furthermore, brain tumors sometimes lead to considerable distortion of normal topography, a factor in itself obscuring efforts to maintain safety during resection close to eloquent brain regions. Further, functional rearrangement over time as an indicator of brain plasticity has been demonstrated as a response to tumor invading eloquent brain (Desmurget et al. 2007), which further confounds attempts to localize individual functions based on anatomy alone. Thus, preoperative imaging of the individual representation of function would be of utmost benefit. To this end functional MRI (fMRI) is the most commonly employed modality (see Conventional MR imaging) (Belliveau et al. 1991). Appropriate computer algorithms serve to convert this information into overlays on conventional MR imagery for the representation of "eloquent" brain regions (Fig. 6).

This information can be imported into the image base used for neuronavigation, which can then be used for locating functionally important cortex intraoperatively (Nimsky et al. 2011). However, the reliability of fMRI in precisely predicting the location of cortical locations critical for language functions is not unanimously accepted (Giussani et al. 2010). Furthermore, fMRI information suffers from brain shift, as does neuronavigation, further losing reliability during the course of surgery. Nevertheless, fMRI gives sufficient preoperative information to determine which hemisphere is dominant for language, thus allowing to determine preoperatively whether advanced neurophysiological monitoring or mapping techniques are necessary and helping to approximately predict at which locations the surgeon should test for function during surgery.

A newer development for the expansion of the potential of MRI and neuronavigation is transcranial magnetic stimula-

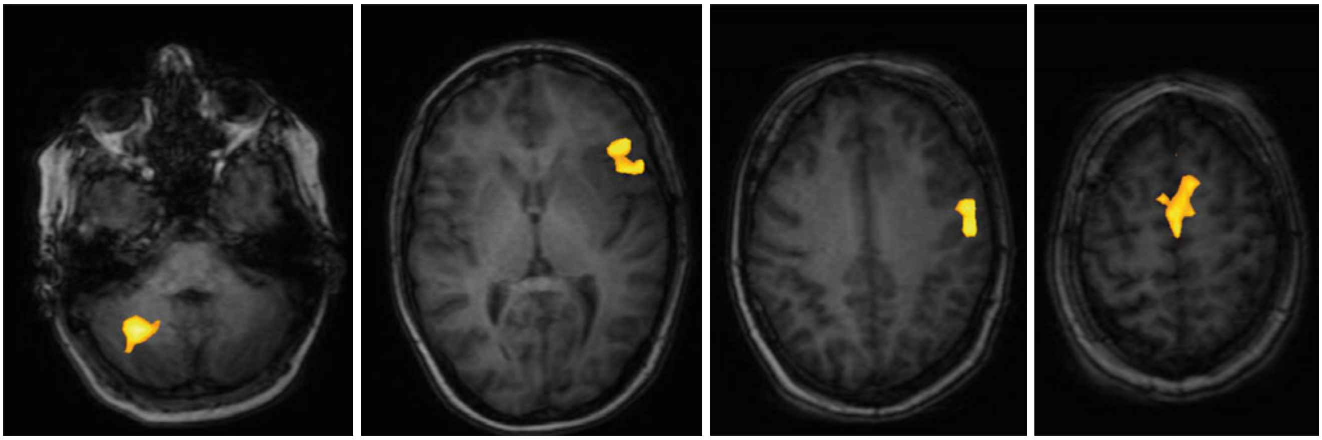

Fig. 6 Language mapping by functional MRI; female, 45 years. – BOLD data superimposed on native T1 images (Courtesy of Wolfram Schwindt, Institute of Clinical Radiology, Münster)

tion (TMS), a technique which promises greater reliability and spatial resolution than fMRI (Weiss et al. 2012). With this method a magnetic coil is used to generate highly defined electrical fields for the transcranial induction of cortical potentials which in turn elicit motor responses. These responses can be detected, quantified, and incorporated into the MRI images used for neuronavigation, a procedure referred to as navigated brain stimulation (NBS). So far, reliable data are available for the noninvasive detection of motor functions of the hands and feet (Weiss et al. 2012). The detection of the cortical representation of perioral muscles and the muscles of the tongue and the detection of regions essential for language production (by inhibitory stimulation) are presently being validated in clinical studies.

2.4.2 Imaging of Subcortical Tracts

Although fMRI and NBS have proven useful for preoperative localization of functionally relevant cortex, these methods do not give information on subcortical white matter tracts that connect functionally relevant cortex areas and are equally important for maintenance of function. Diffusor tensor imaging, which is based on the preferential diffusion of water along fiber structures in the brain (Basser et al. 1994), has provided the technological basis for imaging of deep white matter tracts (Fig. 7). This information can be integrated into the MR imaging set used for neuronavigation, providing an instrument for localizing these tracts intraoperatively and reducing surgical risk (Wu et al. 2007). However, surgeons must bear in mind that these data rely on preoperative imaging and are distorted during the course of surgery by tissue shifts due to the loss of CSF and tumor resection ("brain shift"). Thus, this technique only gives an estimate of the true location of functional tracts (Zolal et al. 2012; Maesawa et al. 2010; Prabhu et al. 2011).

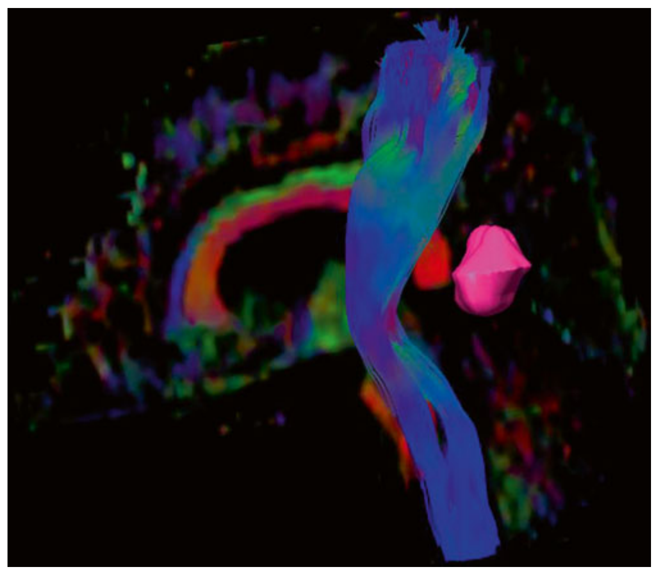

Fig. 7 3D reconstruction of the pyramid tract from a diffusion tensor data set, tumor marked lilac; male, 62 years (DTI data courtesy of the Institute of Clinical Radiology, Münster)

Recently, NBS has been combined with tractography, providing seeding points for reconstructing functionally relevant white matter tracts using DTI and carrying the potential for maps of fiber tracts for individual brain function, for instance, within the pyramidal tract (Frey et al. 2012).

3 Intraoperative Allocation of Relevant Anatomy

The main confounder involved in neuronavigation is a phenomenon called brain shift, i.e., the distortion of anatomy as a result of mass resection, puncture of cysts, or loss of

CSF during surgery (Hartkens et al. 2003; Spetzger et al. 2002), compared to the image data set obtained preoperatively on which neuronavigation is usually based. This markedly reduces the accuracy of neuronavigation as surgery progresses, especially in the late stages of surgery where accuracy is crucial for identifying eloquent cortex, critical tracts, or residual tumor. For this reason intraoperative MRI or CT is frequently used where such devices are available, with the possibility of obtaining a new image data set for updating neuronavigation in an iterative fashion (Nabavi et al. 2001; Ferrant et al. 2002; Uhl et al. 2009). Intraoperative MRI by itself or in conjunction with navigation has been demonstrated to be a useful tool for identifying residual tumor in glioma surgery. Studies indicate efficacy of intraoperative MRI in increasing the radicality of glioma surgery (Senft et al. 2011; Kubben et al. 2011) or in the localization of relevant tracts or cortex. Navigated 3D ultrasound, which is far less expensive and logistically simpler in its use, fulfills a similar purpose (Rygh et al. 2008) but may be less beneficial for HGG due to the confounding influence of edema on ultrasound images (Solheim et al. 2010).

In principle, however, identification of eloquent brain or cortex based on imaging modalities will rely on the aptitude of these modalities to truthfully detect structures that are surgically relevant. At the end of the day, these methods provide two-dimensional indirect pictures derived from tissue biology which are susceptible to artifacts and require mental reconstruction and interpretation by the surgeon regarding the tissue he is confronted with in a three-dimensional space. Navigation as an aid for orientation in this space is helpful but can only be as good as the underlying imaging. Due to these limitations, many dedicated neuro-oncological surgeons resort to additional, direct, and biologically oriented methods to define function and tumor margins during surgery.

To this end, direct cortical stimulation (DCS), which was introduced during the 1960s of the last century, is experiencing increasing popularity especially for localizing language functions in the awake patient under local anesthesia. This method relies on the application of electrical currents for interrupting critical functions during language testing. For detecting deep matter tracts, subcortical stimulation is employed (Seidel et al. 2013). For the mapping of motor functions, surgery may also be performed under anesthesia. Surgery in patients using local anesthesia is complex, requiring dedicated anesthesiology and neurophysiology. Due the refinements of modern-day management, this technique need not be restricted to language mapping in monitoring, but can be extended to many types of neurocognitive functions, e.g., reading, writing, mathematics, different languages, spatial cognition, working memory, etc. (Ilmberger et al. 2008; Fernández Coello et al. 2013).

A large meta-analysis recently established intraoperative mapping and monitoring techniques to allow a high frequency of maximal tumor resections while reducing the probability of long-term neurological deficits (De Witt Hamer et al. 2012). Thus, this methodology allowing for direct surveillance of function must currently be considered standard for the surgery of gliomas in contrast to the indirect method of navigation based on preoperative imaging.

Direct methods for the visualization of malignant gliomas are also currently available. Intraoperatively, the contrast-enhancing margins of malignant gliomas are difficult to identify as such. This results in a high incidence of residual contrast-enhancing tumor, if the surgeon relies on his visual impression only (Albert et al. 1994; Stummer et al. 2006; Senft et al. 2011). Neuronavigation alone could not be shown to increase the rate of complete resections of contrast-enhancing tumor (Willems et al. 2006).

One such intraoperative visual method, which was introduced by our group after a randomized trial (Stummer et al. 2006), is based on the propensity of malignant glioma tissue to accumulate fluorescent porphyrins in response to external administration of the heme metabolite 5-aminolevulinic acid (Gliolan®). Accumulation is based on the metabolic particularities of malignant glioma tissue. Ensuing fluorescence can be visualized using commercially available operating microscopes and provides real-time information to the surgeon useful for resection on a macroscopic basis (Stummer et al. 1998, 2000, 2014). In addition, the method allows direct detection and biopsy of anaplastic foci in otherwise low-grade gliomas, which is not confounded by the limitations of neuronavigation (Widhalm et al. 2010; Stummer et al. 1998). Such foci are preoperatively identifiable by the amino acid PET, and close correlations between hot spots on the amino acid PET and visible intraoperative porphyrin fluorescence have been demonstrated (Ewelt et al. 2011; Widhalm et al. 2010; Stockhammer et al. 2009). Unfortunately, there are no similar methods available for LGG as yet.

Conclusions

Perioperative and intraoperative imaging in conjunction with neuronavigation is crucial for planning, risk assessment, and implementation of modern glioma surgery. However, direct, biologically oriented methods such as cortical and subcortical mapping and monitoring, as well as biological intraoperative visualization of tumors, are valuable methods expanding the armamentarium of the neuro-oncological neurosurgeon for rendering this surgery as safe and effective as possible.

Acknowledgements We thankfully acknowledge the provision of images by the Institute of Clinical Radiology (W.-L. Heindel, T. Niederstadt, W. Schwindt) and the Clinic of Nuclear Medicine (M. Schäfers).

References

Albert FK, Forsting M, Sartor K, Adams HP, Kunze S (1994) Early postoperative magnetic resonance imaging after resection of malignant glioma: objective evaluation of residual tumor and its influence on regrowth and prognosis. Neurosurgery 34(1):45–60; discussion 60–61

Aldave G, Tejada S, Pay E, Marigil M, Bejarano B, Idoate MA, Díez-Valle R (2013) Prognostic value of residual fluorescent tissue in glioblastoma patients after gross total resection in 5-aminolevulinic Acid-guided surgery. Neurosurgery 72(6):915–920; discussion 920–921

Basser PJ, Mattiello J, LeBihan D (1994) Estimation of the effective self-diffusion tensor from the NMR spin echo. J Magn Reson B 103(3):247–254

Belliveau JW, Kennedy DN Jr, McKinstry RC, Buchbinder BR, Weisskoff RM, Cohen MS, Vevea JM, Brady TJ, Rosen BR (1991) Functional mapping of the human visual cortex by magnetic resonance imaging. Science 254(5032):716–719

De Witt Hamer PC, Robles SG, Zwinderman AH, Duffau H, Berger MS (2012) Impact of intraoperative stimulation brain mapping on glioma surgery outcome: a meta-analysis. J Clin Oncol 30(20):2559–2565

Desmurget M, Bonnetblanc F, Duffau H (2007) Contrasting acute and slow-growing lesions: a new door to brain plasticity. Brain 130(Pt 4):898–914

Duffau H (2013) A new philosophy in surgery for diffuse low-grade glioma (DLGG): oncological and functional outcomes. Neurochirurgie 59(1):2–8

Ewelt C, Floeth FW, Felsberg J et al (2011) Finding the anaplastic focus in diffuse gliomas: the value of Gd-DTPA enhanced MRI, FET-PET, and intraoperative, ALA-derived tissue fluorescence. Clin Neurol Neurosurg 113:541–547

Farrel DF, Burbank N, Lettich E, Ojemann G (2007) Individual variation in human motor-sensory (rolandic) cortex. J Clin Neurophysiol 24(3):286–293

Fernández Coello A, Moritz-Gasser S, Martino J, Martinoni M, Matsuda R, Duffau H (2013) Selection of intraoperative tasks for awake mapping based on relationships between tumor location and functional networks. J Neurosurg 119(6):1380–1394

Ferrant M, Nabavi A, Macq B, Black PM, Jolesz FA, Kikinis R, Warfield SK (2002) Serial registration of intraoperative MR images of the brain. Med Image Anal 6(4):337–359

Floeth FW, Pauleit D, Sabel M et al (2007) Prognostic value of O-(2-18F-fluoroethyl)-L-tyrosine PET and MRI in low-grade glioma. J Nucl Med 48:519–527

Frey D, Strack V, Wiener E, Jussen D, Vajkoczy P, Picht T (2012) A new approach for corticospinal tract reconstruction based on navigated transcranial stimulation and standardized fractional anisotropy values. Neuroimage 62:1600–1609

Geer CP, Simonds J, Anvery A, Chen MY, Burdette JH, Zapadka ME, Ellis TL, Tatter SB, Lesser GJ, Chan MD, McMullen KP, Johnson AJ (2012) Does MR perfusion imaging impact management decisions for patients with brain tumors? A prospective study. AJNR Am J Neuroradiol 33(3):556–562

Giussani C, Roux FE, Ojemann J, Sganzerla EP, Pirillo D, Papagno C (2010) Is preoperative functional magnetic resonance imaging reliable for language areas mapping in brain tumor surgery? Review of language functional magnetic resonance imaging and direct cortical stimulation correlation studies. Neurosurgery 66(1):113–120

Glantz MJ, Burger PC, Herndon JE 2nd, Friedman AH, Cairncross JG, Vick NA, Schold SC Jr. (1991) Influence of the type of surgery on the histologic diagnosis in patients with anaplastic gliomas. Neurology 41(11):1741–1744

Guillevin R, Menuel C, Abud L et al (2012) Proton MR spectroscopy in predicting the increase of perfusion MR imaging for WHO grade II gliomas. J Magn Reson Imaging 35:543–550

Hartkens T, Hill DL, Castellano-Smith AD, Hawkes DJ, Maurer CR Jr, Martin AJ, Hall WA, Liu H, Truwit CL (2003) Measurement and analysis of brain deformation during neurosurgery. IEEE Trans Med Imaging 22(1):82–92

Ilmberger J, Ruge M, Kreth FW, Briegel J, Reulen HJ, Tonn JC (2008) Intraoperative mapping of language functions: a longitudinal neurolinguistic analysis. J Neurosurg 109:583–592

Jackson RJ, Fuller GN, Abi-Said D, Lang FF, Gokaslan ZL, Shi WM, Wildrick DM, Sawaya R (2001) Limitations of stereotactic biopsy in the initial management of gliomas. Neuro Oncol 3(3): 193–200

Jakola AS, Myrmel KS, Kloster R, Torp SH, Lindal S, Geirmund U, Solheim O (2013) Comparison of a strategy favoring early surgical resection vs. a strategy favoring watchful waiting in low-grade gliomas. JAMA 308:1881–1888

Keles GE, Lamborn KR, Berger MS (2001) Low-grade hemispheric gliomas in adults: A critical review of extent of resection as a factor influencing outcome. J Neurosurg 95:735–745

Keles GE, Chang EF, Lamborn KR, Tihan T, Chang CJ, Chang SM, Berger MS (2006) Volumetric extent of resection and residual contrast enhancement on initial surgery as predictors of outcome in adult patients with hemispheric anaplastic astrocytoma. J Neurosurg 105(1):34–40

Kreth FW, Thon N, Simon M, Westphal M, Schackert G, Nikkhah G, Hentschel B, Reifenberger G, Pietsch T, Weller M, Tonn JC, German Glioma Network (2013) Gross total but not incomplete resection of glioblastoma prolongs survival in the era of radiochemotherapy. Ann Oncol 24:3117–3123

Kubben PL, ter Meulen KJ, Schijns OE, ter Laak-Poort MP, van Overbeeke JJ, van Santbrink H (2011) Intraoperative MRI-guided resection of glioblastoma multiforme: a systematic review. Lancet Oncol 12(11):1062–1070

Kunz M, Thon N, Eigenbrod S, Hartmann C, Egensperger R, Herms J, Geisler J, la Fougere C, Lutz J, Linn J, Kreth S, von Deimling A, Tonn JC, Kretzschmar HA, Pöpperl G, Kreth FW (2012) Hotspots in dynamic (18)-Fet PET delineate malignant tumor parts within suspected grade II gliomas. Neuro Oncol 13(3):307–316

Lacroix M, Abi-Said D, Fourney DR, Gokaslan ZL, Shi W, DeMonte F, Lang FF, McCutcheon IE, Hassenbusch SJ, Holland E, Hess K, Michael C, Miller D, Sawaya R (2001) A multivariate analysis of 416 patients with glioblastoma multiforme: prognosis, extent of resection, and survival. J Neurosurg 95(2):190–198

Laws ER, Parney IF, Huang W et al. and the Glioma Outcomes Investigators (2003) Survival following surgery and prognostic factors for recently diagnosed malignant glioma: data from the Glioma Outcomes Project. J Neurosurg 99:467–473

Maesawa S, Fujii M, Nakahara N, Watanabe T, Wakabayashi T, Yoshida J (2010) Intraoperative tractography and motor evoked potential (MEP) monitoring in surgery for gliomas around the corticospinal tract. World Neurosurg 74(1):153–161

Mandonnet E, Delattre JY, Tanguy ML et al (2003) Continuous growth of mean tumor diameter in a subset of grade II gliomas. Ann Neurol 53:524–528

McGirt MJ, Chaichana KL, Attenello FJ et al (2008) Extent of surgical resection is independently associated with survival in patients with hemispheric infiltrating low-grade gliomas. Neurosurgery 63:700–707

McGirt MJ, Chaichana KL, Gathinji M et al (2009a) Independent association of extent of resection with survival in patients with malignant brain astrocytoma. J Neurosurg 110:156–162

McGirt MJ, Mukherjee D, Chaichana KL, Than KD, Weingart JD, Quinones-Hinojosa A (2009b) Association of surgically acquired motor and language deficits on overall survival after resection of glioblastoma multiforme. Neurosurgery 65:463–469

Muragaki Y, Chernov M, Maruyama T, Ochiai T, Taira T, Kubo O, Nakamura R, Iseki H, Hori T, Takakura K (2008) Low-grade glioma

on stereotactic biopsy: how often is the diagnosis accurate? Minim Invasive Neurosurg 51(5):275–279
Nabavi A, Black PM, Gering DT, Westin CF, Mehta V, Pergolizzi RS Jr, Ferrant M, Warfield SK, Hata N, Schwartz RB, Wells WM 3rd, Kikinis R, Jolesz FA (2001) Serial intraoperative magnetic resonance imaging of brain shift. Neurosurgery 48(4):787–797; discussion 797
Nimsky C, Kuhnt D, Ganslandt O, Buchfelder M (2011) Multimodal navigation integrated with imaging. Acta Neurochir Suppl 109:207–214
Ojemann G, Ojemann J, Lettich E, Berger M (2008) Cortical language localization in left, dominant hemisphere. An electrical stimulation mapping investigation in 117 patients. J Neurosurg 108(2):411–421
Pallud J, Mandonnet E, Duffau H, Kujas M, Guillevin R, Galanaud D, Taillandier L, Capelle L (2006) Prognostic value of initial magnetic resonance imaging growth rates for World Health Organization grade II gliomas. Ann Neurol 60(3):380–383
Pignatti F, van den Bent M, Curran D, Debruyne C, Sylvester R, Therasse P, Afra D, Cornu P, Bolla M, Vecht C, Karim AB, European Organization for Research and Treatment of Cancer Brain Tumor Cooperative Group; European Organization for Research and Treatment of Cancer Radiotherapy Cooperative Group (2002) Prognostic factors for survival in adult patients with cerebral low-grade glioma. J Clin Oncol 20(8):2076–2084
Prabhu SS, Gasco J, Tummala S, Weinberg JS, Rao G (2011) Intraoperative magnetic resonance imaging-guided tractography with integrated monopolar subcortical functional mapping for resection of brain tumors. J Neurosurg 114(3):719–726
Roessler K, Becherer A, Donat M, Cejna M, Zachenhofer I (2012) Intraoperative tissue fluorescence using 5-aminolevolinic acid (5-ALA) is more sensitive than contrast MRI or amino acid positron emission tomography ((18)F-FET-PET) in glioblastoma surgery. Neurol Res 34(3):314–317
Rygh OM, Selbekk T, Torp SH, Lydersen S, Hernes TA, Unsgaard G (2008) Comparison of navigated 3D ultrasound findings with histopathology in subsequent phases of glioblastoma resection. Acta Neurochir 150(10):1033–1041; discussion 1042
Sahin N, Melhem ER, Wang S, Krejza J, Poptani H, Chawla S, Verma G (2013) Advanced MR imaging techniques in the evaluation of nonenhancing gliomas: perfusion-weighted imaging compared with proton magnetic resonance spectroscopy and tumor grade. Neuroradiol J 26(5):531–541
Sahm F, Capper D, Jeibmann A, Habel A, Paulus W, Troost D, von Deimling A (2012) Addressing diffuse glioma as a systemic brain disease with single-cell analysis. Arch Neurol 69(4):523–526
Schucht P, Knittel S, Slotboom J, Seidel K, Murek M, Jilch A, Raabe A, Beck J (2014) 5-ALA complete resections go beyond MR contrast enhancement: shift corrected volumetric analysis of the extent of resection in surgery for glioblastoma. Acta Neurochir 156(2):305–312; discussion 312
Seidel K, Beck J, Stieglitz L, Schucht P, Raabe A (2013) The warning-sign hierarchy between quantitative subcortical motor mapping and continuous motor evoked potential monitoring during resection of supratentorial brain tumors. J Neurosurg 118:287–296
Senft C, Bink A, Franz K, Vatter H, Gasser T, Seifert V (2011) Intraoperative MRI guidance and extent of resection in glioma surgery: a randomised, controlled trial. Lancet Oncol 12(11):997–1003
Shinoura N, Suzuki Y, Yamada R, Tabei Y, Saito K, Yagi K (2009) Precentral knob corresponds to the primary motor and premotor area. Can J Neurol Sci 36(2):227–233
Smith JS, Chang EF, Lamborn KR et al (2008) Role of extent of resection in the long-term outcome of low-grade hemispheric gliomas. J Clin Oncol 26:1338–1345
Solheim O, Selbekk T, Jakola AS, Unsgård G (2010) Ultrasound-guided operations in unselected high-grade gliomas – overall results, impact of image quality and patient selection. Acta Neurochir 152(11):1873–1886
Spetzger U, Hubbe U, Struffert T, Reinges MH, Krings T, Krombach GA, Zentner J, Gilsbach JM, Stiehl HS (2002) Error analysis in cranial neuronavigation. Minim Invasive Neurosurg 45(1):6–10
Stockhammer F, Misch M, Horn P, Koch A, Fonyuy N, Plotkin M (2009) Association of F18-fluoro-ethyl-tyrosin uptake and 5-aminolevulinic acid-induced fluorescence in gliomas. Acta Neurochir 151(11):1377–1383
Stummer W, Stocker S, Wagner S, Stepp H, Fritsch C, Goetz C, Goetz AE, Kiefmann R, Reulen HJ (1998) Intraoperative detection of malignant gliomas by 5-aminolevulinic acid-induced porphyrin fluorescence. Neurosurgery 42:518–525
Stummer W, Novotny A, Stepp H, Goetz C, Bise K, Reulen HJ (2000) Fluorescence-guided resection of glioblastoma multiforme by using 5-aminolevulinic acid-induced porphyrins: a prospective study in 52 consecutive patients. J Neurosurg 93(6):1003–1013
Stummer W, Pichlmeier U, Meinel T et al (2006) Fluorescence-guided surgery with 5-aminolevulinic acid for resection of malignant glioma: a randomised controlled multicentre phase III trial. Lancet Oncol 7:392–401
Stummer W, Reulen HJ, Meinel T, Pichlmeier U, Schumacher W, Tonn JC, Rohde V, Oppel F, Turowski B, Woiciechowsky C, Franz K, Pietsch T, ALA-Glioma Study Group (2008) Extent of resection and survival in glioblastoma multiforme: identification of and adjustment for bias. Neurosurgery 62(3):564–576; discussion 564–576
Stummer W, Nestler U, Stockhammer F et al (2011a) Favorable outcome in the elderly cohort treated by concomitant temozolomide radiochemotherapy in a multicentric phase II safety study of 5-ALA. J Neurooncol 103:361–370
Stummer W, van den Bent MJ, Westphal M (2011b) Cytoreductive surgery of glioblastoma as the key to successful adjuvant therapies: new arguments in an old discussion. Acta Neurochir 153(6):1211–1218
Stummer W, Meinel T, Ewelt C, Martus P, Jakobs O, Felsberg J, Reifenberger G (2012) Prospective cohort study of radiotherapy with concomitant and adjuvant temozolomide chemotherapy for glioblastoma patients with no or minimal residual enhancing tumor load after surgery. J Neurooncol 108:89–97
Stummer W, Tonn JC, Goetz C, Ullrich W, Stepp H, Bink A, Pietsch T, Pichlmeier U (2014) 5-aminolevulinic acid-derived tumor fluorescence: the diagnostic accuracy of visible fluorescence qualities as corroborated by spectrometry and histology and postoperative imaging. Neurosurgery 74(3):310–320
Uhl E, Zausinger S, Morhard D, Heigl T, Scheder B, Rachinger W, Schichor C, Tonn JC (2009) Intraoperative computed tomography with integrated navigation system in a multidisciplinary operating suite. Neurosurgery 64(5 Suppl 2):231–239; discussion 239
Veeravagu A, Jiang B, Ludwig C, Chang SD, Black KL, Patil CG (2013) Biopsy versus resection for the management of low-grade gliomas. Cochrane Database Syst Rev doi: 10.1002/14651858.CD009319.pub2
Vigneau M, Beaucousin V, Hervé PY, Duffau H, Crivello F, Houdé O, Mazoyer B, Tzourio-Mazoyer N (2006) Meta-analyzing left hemisphere language areas: phonology, semantics, and sentence processing. Neuroimage 30(4):1414–1432
Vuorinen V, Hinkka S, Farkkila M et al (2003) Debulking or biopsy of malignant glioma in elderly people – a randomised study. Acta Neurochir (Wien) 145:5–10
Weiss C, Nettekoven C, Rehme AK, Neuschmelting V, Eisenbeis A, Goldbrunner R, Grefkes C (2012) Mapping the hand, foot and face representations in the primary motor cortex – retest reliability of neuronavigated TMS versus functional MRI. Neuroimage 66:531–542
Wick W, Hartmann C, Engel C, Stoffels M, Felsberg J, Stockhammer F, Sabel MC, Koeppen S, Ketter R, Meyermann R, Rapp M, Meisner C, Kortmann RD, Pietsch T, Wiestler OD, Ernemann U, Bamberg M, Reifenberger G, von Deimling A, Weller M (2009) NOA-04 randomized phase III trial of sequential radiochemotherapy of

anaplastic glioma with procarbazine, lomustine, and vincristine or temozolomide. J Clin Oncol 27(35):5874–5880. Erratum (2010) in: J Clin Oncol 28(4):708
Widhalm G, Wolfsberger S, Minchev G et al (2010) 5-Aminolevulinic acid is a promising marker for detection of anaplastic foci in diffusely infiltrating gliomas with non-significant contrast enhancement. Cancer 116:1545–1552
Willems PW, Taphoorn MJ, Burger H et al (2006) Effectiveness of neuronavigation in resecting solitary intracerebral contrast-enhancing tumors: a randomized controlled trial. J Neurosurg 104:361–368
Woodworth G, McGirt MJ, Samdani A, Garonzik I, Olivi A, Weingart JD (2005) Accuracy of frameless and frame-based image-guided stereotactic brain biopsy in the diagnosis of glioma: comparison of biopsy and open resection specimen. Neurol Res 27(4):358–362
Wu JS, Zhou LF, Tang WJ, Mao Y, Hu J, Song YY, Hong XN, Du GH (2007) Clinical evaluation and follow-up outcome of diffusion tensor imaging-based functional neuronavigation: a prospective, controlled study in patients with gliomas involving pyramidal tracts. Neurosurgery 61(5):935–948; discussion 948
Yordanova YN, Moritz-Gasser S, Duffau H (2011) Awake surgery for WHO Grade II gliomas within "noneloquent" areas in the left dominant hemisphere: toward a "supratotal" resection. J Neurosurg 115(2):232–239
Zolal A, Hejčl A, Vachata P, Bartoš R, Humhej I, Malucelli A, Nováková M, Hrach K, Derner M, Sameš M (2012) The use of diffusion tensor images of the corticospinal tract in intrinsic brain tumor surgery: a comparison with direct subcortical stimulation. Neurosurgery 71(2):331–340

Future Methods in Tumor Imaging

Ulrich Pilatus and Elke Hattingen

Contents

Abstract

Chapter Advanced MR Methods in Differential Diagnosis of Brain Tumors deals with advanced and future MR imaging methods in brain tumors. In this chapter, we will discuss future MR spectroscopic methods that are promising regarding the tumor diagnosis and the research of tumor biology. Whereas Chap. MR Spectroscopic Imaging focuses on diagnostic significance of ^{1}H and ^{31}P MRS, we herein put more emphasis on methodical issues of MRS. First, we deal with special editing methods to detect special "tumor" metabolites (glycine, 2-hydroxyglutarate). In the second part, we discuss methods and biological implications of x-nucleus spectroscopy, focusing on the nuclei ^{31}P and ^{13}C. Here, we point out that a considerable proportion of advanced spectroscopic studies dealing with brain tumors come from animal studies.

Abbreviations

2-HG	2-hydroxyglutarate
ATP	Adenosine triphosphate
Gly	Glycine
GPC	Glycerophosphocholine
MI	Myo-inositol
PCho	Phosphocholine
PCr	Phosphocreatine
Pi	Inorganic phosphate
TCA cycle	Tricarboxylic acid cycle or Krebs cycle
tCho	Total choline
tCr	Total creatine
tNAA	Total N-acetylaspartate

U. Pilatus (✉)
Department of Neuroradiology, Goethe University Frankfurt, Schleusenweg 2-16, Frankfurt 60528, Germany
e-mail: u.pilatus@em.uni-frankfurt.de

E. Hattingen
Neuroradiology, Clinic of Rheinische Friedrich-Wilhelms-University, Sigmund-Freud Straße 6, 53127 Bonn, Germany
e-mail: elke.hattingen@ukb.uni-bonn.de

1 Special Editing Methods in ^{1}H MRS

In Chap. MR Spectroscopic Imaging, spectroscopic methods were described which provide biochemical information. In addition to the easily detectable main metabolites (creatine,

E. Hattingen, U. Pilatus (eds.), *Brain Tumor Imaging*,
Med Radiol Diagn Imaging (2016),
DOI 10.1007/174_2016_1055, © Springer Berlin Heidelberg

choline, tNAA), other compounds can be detected using more sophisticated technique markers, which may serve as biomarkers for specific questions in tumor diagnosis. These are glycine and 2-hydroxyglutarate (2-HG), which require nonstandard techniques like specific spacing of the refocusing pulses in PRESS or additional RF pulses in the sequence like MEGA PRESS.

1.1 Measuring Glycine

At short echo time (TE) of about 30 ms, the glycine (Gly) signal, a singlet at 3.56 ppm, is masked by the main peak of myo-inositol (MI). Since MI represents a strongly coupled spin system (Govindaraju et al. 1998), its pattern is significantly changing with TE, exhibiting a signal reduction at TE of 135–44, which is far beyond the signal decay due to typical T2 relaxation of singlets. This effect can be exploited for differentiation between MI and Gly as has been shown in several studies on brain tumors using either both TE (Hattingen et al. 2009; Davies et al. 2010) or performing a single spectroscopic measurement with an optimized TE and refocusing pulse spacing in addition to dedicated spectral analysis (Choi et al. 2011; Maudsley et al. 2014). Figure 1 shows the efficiency of using the long and short TE, comparing tumor spectra for TE at 30 ms to those obtained at 144 ms. It is obvious that there is no significant decrease in the 3.56 ppm signal between the tumor spectra (b, d). In contrast, rather small signal at TE of 144 ms in normal-appearing tissue (c) indicates the rather low concentration of MI here.

1.2 Measuring 2-hydroxyglutarate

About 70 % of WHO grade II and III gliomas have a mutation of isocitrate dehydrogenase (IDH1 and IDH2). These mutations cause an increased formation of 2-hydroxyglutarate (2-HG) from isocitrate, offering the obvious approach to consider increased 2-HG as a tumor marker visible in vivo

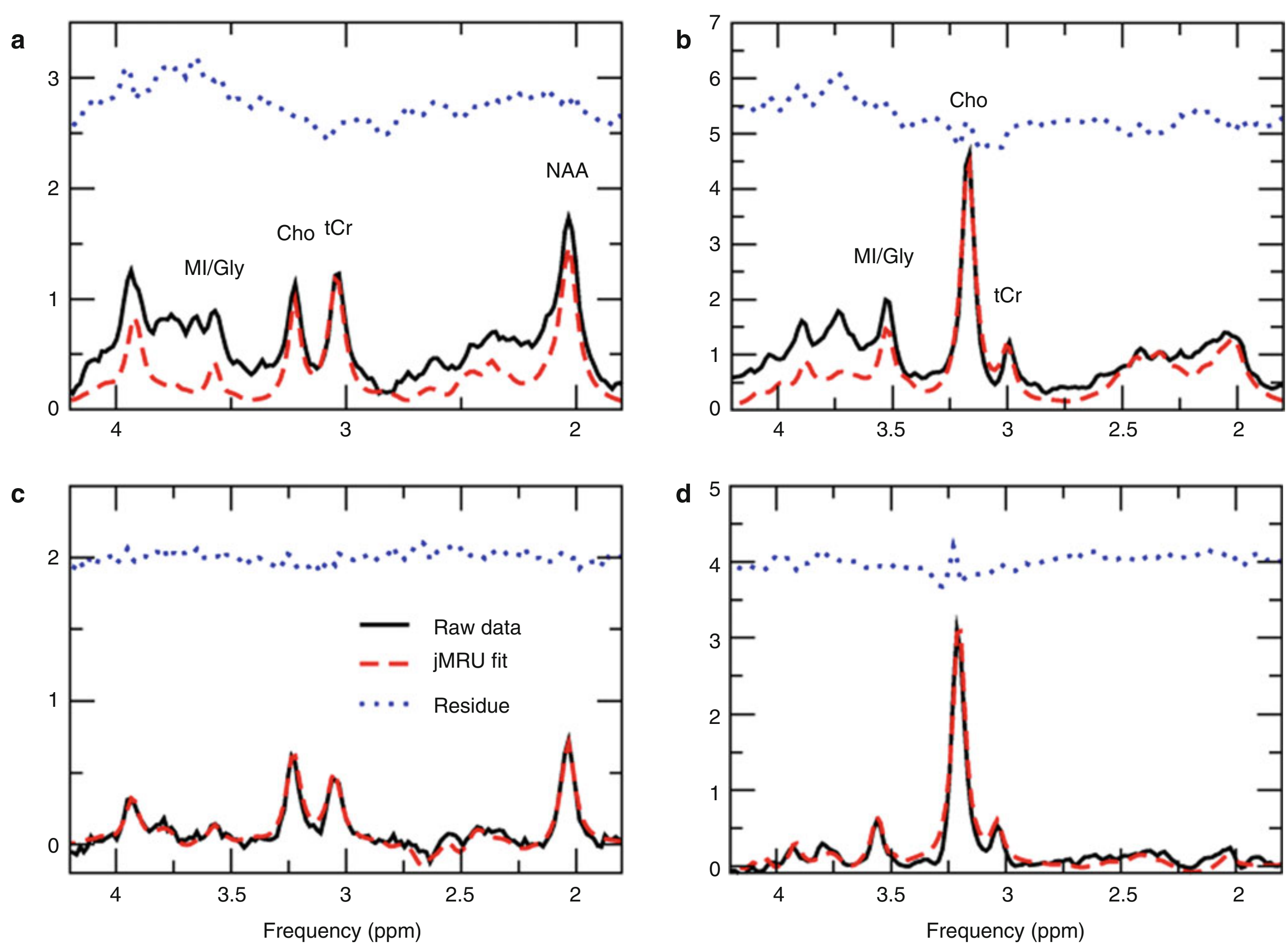

Fig. 1 Discriminating glycine from myo-inositol by comparing short and long TE spectra. **a** shows a spectrum from normal tissue and **b** from tumor tissue at TE of 30 ms. The signal at 3.56 ppm could be Gly or MI. **c** shows the normal tissue at a TE of 144 ms, while **d** shows the repective tumor voxel. Normal tissue is known to contain MI but rather low concentrations of glycine. The lack of the 3.56 signal in **c** indicates the sufficient suppression of MI at long TE. (*Black* raw data, *red* signal estimated by data analyisis, *blue* residual)

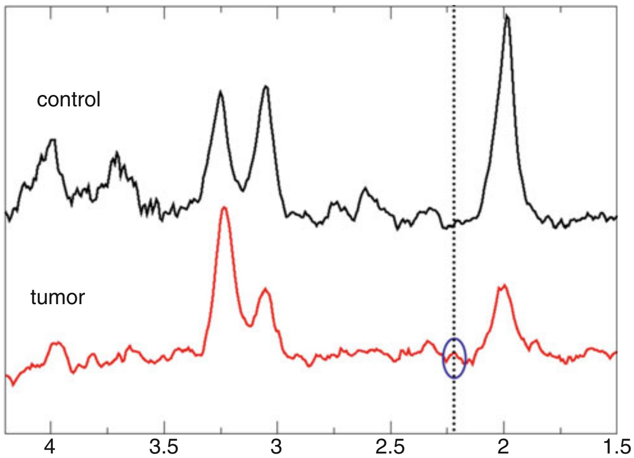

Fig. 2 PRESS spectra obtained at a TE optimized for detection of 2-HG. The dotted vertical line marks the position of the 2-HG signal. The tumor spectrum (*lower trace*, *red*) shows a small signal at this position while nothing can be detected in control tissue (*upper trace*, *black*)

by ^{1}H MRS. Increased 2-HG has been observed in vivo in mutated tumors (Andronesi et al. 2012; Choi et al. 2012; Pope et al. 2012), but as for glycine, it cannot be detected easily in standard short TE spectra. Difficulties and potential solutions were recently reviewed (Andronesi et al. 2013) and can be summarized as follows:

- Many false positives in standard spectra
- Reasonable at optimized TE and adjusted spacing of refocusing pulse followed by dedicated data fitting
- Good but clinically not feasible detection using spectral editing either by MEGA-PRESS or 2D methods sensitive to spin–spin coupling

Figure 2 shows data for optimized TE PRESS.

A recent study hints to a metabolic profile related to the mutation (Esmaeili et al. 2014). This might offer an alternative approach using changes in the phospholipid profile for detection of 2-HG.

2 Other Nuclei

All nuclei with odd mass number do have a spin and a related magnetic moment, i.e., they should be visible with MR spectroscopy. Nuclei other than ^{1}H are also called x-nuclei. Table 1 lists the gyromagnetic ratio γ for nuclei with potential interest in tumor diagnosis. It determines the Larmor frequency ωo for each nucleus in the magnetic field B_0 according to $\omega_o = \gamma B_o$. Keeping in mind that the sensitivity of MR decreases with decreasing Larmor frequency, the bottom row in Table 1 compares the frequency of the x-nuclei to ^{1}H indicating their inferior sensitivity in MR.

Phosphorous (^{31}P) is of special interest since with almost half the Larmor frequency of ^{1}H it still has a reasonable sensitivity. Actually, ^{31}P MRS was the first method to study tissue metabolism in vivo with MR spectroscopy (see Chap. MR Spectroscopic Imaging).

Table 1 Values of the gyromagnetic ratios for nuclei of biochemical interest and their ratios to the proton gyromagnetic ratio. Smaller numbers indicate decreased sensitivity in MR

Isotope	^{1}H	^{31}P	^{13}C	^{23}NA	^{15}N
γ	26.7	10.8	6.73	7.08	−2.7
γ/γ_H	1	0.40	0.25	0.27	0.10

Further, there is a carbon isotope (^{13}C), which has a natural abundance of 1 % and can also be monitored with MRS. The carbohydrate metabolism can be followed using substances which are enriched (labeled) at specific positions with ^{13}C like [1-^{13}C]glucose, monitoring the fate of the labeled atoms during metabolism. Unfortunately, due to the rather low frequency, the sensitivity of ^{13}C MRS is low. However, there is a method for increasing the amount of MR-sensitive nuclei by hyperpolarization (Ardenkjaer-Larsen et al. 2003), which artificially increases the magnetization for the nuclei of interest by several orders of magnitude compared to the thermodynamic equilibrium. Using this method, imaging of ^{13}C-labeled pyruvate was achieved in several experimental tumor models.

Although not a metabolite, the sodium (^{23}Na) can be monitored with MR as well. The rather high Na concentration in part compensates the low sensitivity. Just for completeness, we added the nitrogen isotope ^{15}N to the table since it has been used for measuring the pathological metabolism by analyzing body fluids in high-resolution NMR spectroscopy.

We will focus on ^{31}P MRS as an easy-to-monitor nucleus with intriguing capabilities to provide information on lipid metabolism which is complementary to ^{1}H MRS. ^{31}P MRS can also be used to measure the intracellular pH and energy metabolism in tissue. In a second part, we will focus on ^{13}C since this nucleus offers a unique field of applications that may become realistic with a broad availability of hyperpolarization. In addition, conventional MRS using ^{13}C-enriched compounds will profit from the potential sensitivity increase due to higher magnetic fields of 7 T and beyond.

2.1 ^{31}P MRS

Chapter MR Spectroscopic Imaging already outlined an introduction into the basic principle of ^{31}P MRS and elaborated on the physiological and biochemical information on tumor metabolism. As has already been outlined in this Chapter, its main advantage to ^{1}H MRS is the ability to discriminate between glycerophosphocholine (GPC) and phosphocholine (PCho), adding detailed information to the so-called total choline signal (tCh) obtained from ^{1}H MRS. Also, the signal of the respective ethanolamine compounds can be detected. In addition, ^{31}P MRS measures signals from adenosine triphosphate (ATP) and phosphocreatine (PCr), two important metabolites in energy metabolism. Finally, the position of the signal of inorganic phosphate (Pi), which occurs between 4.6 and 5.5 ppm, is sensitive to pH. With the assumptions that tumor tissue represents densely packed cells, the position of the Pi signal offers an intracellular pH marker. Tissue pH has been discussed as sensitive indicator for treatment effects. These advantages are confronted with the lower sensitivity compared to ^{1}H. Roughly, a factor of 1/2 results from the lower gyromagnetic ratio. Furthermore, an additional factor of 1/3 occurs for creatine and 1/9 for choline compounds, since the main singlet signals in ^{1}H MRS originate from three or nine protons per molecule. Measurements at ultrahigh B_0 fields (≥7 T) may compensate for the lower gyromagnetic ratio. Thus, except for the main metabolites, the sensitivity becomes comparable to the sensitivity of ^{1}H MRS. On the other hand, there is the big advantage that no unwanted water and fat signals have to be suppressed during measurement or in data processing. This leads to a well-defined baseline, which considerably improves the accuracy of spectral analysis routines. Since we already stressed the pathophysiological significance of ^{31}P MRS detectable parameters in Chap. MR Spectroscopic Imaging, we will rather concentrate on methodological challenges and potential solutions in the following paragraphs.

2.1.1 Spatial Resolution

Considering the lower gyromagnetic ratio and the lower number of nuclei in a distinct chemical bonding for metabolites (see above), the inherent sensitivity for a compound like PCr, which is visible in ^{1}H and ^{31}P MRS, should be about 20 % of its ^{1}H sensitivity. This simply requires a ^{31}P voxel volume of five times the ^{1}H-voxel volume or, assuming isotropic resolution, an increase in matrix grid size by almost 75 %. When ^{1}H MRSI and ^{31}P MRSI are obtained with the intention to combine data, a reasonable geometry would match the slice thickness and fit four ^{1}H voxels into one ^{31}P voxel. On top of the larger voxel size, an increased spreading of signal into adjacent voxels caused by the point spread function, which describes the blurring of a point due to coarse k-space sampling, has also been considered. Figure 3 demonstrates the effect: It shows a T2-weighted anatomical slice with a tumor in panel a. Panel b depicts the same slice; however, by digital filtering a blurring was implied which mimics a resolution typical to a ^{1}H MRSI data set obtained with a 16×16 matrix at 240 mm^2 FOV. Panel c shows this slice at a resolution corresponding to an 8×8×8 matrix for data acquisition followed by digital resolution enhancement. Obviously, the T2 enhancement marking the tumor is still clearly marked at the ^{1}H MRSI resolution but tends to be blurred across the entire brain at the rather poor k-space sampling employed for ^{31}P MRSI.

2.1.2 Measuring pH

The unique feature of ^{31}P MRS is the ability of the method to detect the pH values in tissue. The effect is based on the pH-dependent equilibrium between HPO_4^{2-} and $H_2PO_4^{-}$ with the signal position of inorganic phosphate providing a weighted average of both ions (Prichard et al. 1983). Many studies observed a shift of the Pi signal toward a more alkaline environment (Negendank 1992). With the assumption that this signal originates mainly from intracellular phosphate (Stubbs et al. 1992), the ^{31}P MRS data indicate a reversed pH gradient in tumor tissue (more acidic extracellular) with respective consequences for tumor metabolism and drug efficiency (Stubbs et al. 1994). Figure 4 shows typical ^{31}P MRS spectra from normal-appearing tissue (black) and the tumor (red). The insert at the upper right corner represents the extended

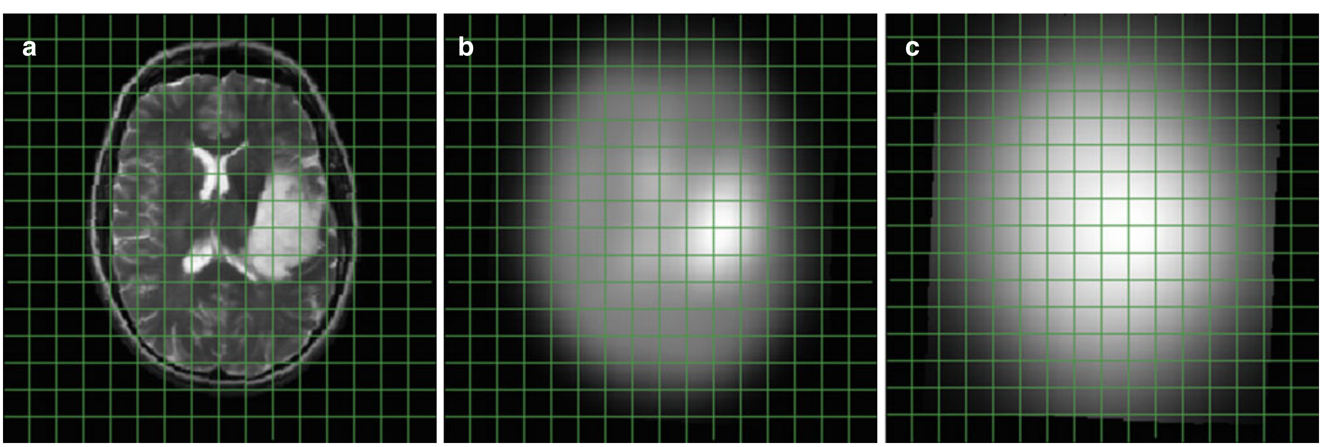

Fig. 3 Blurring of signal intensity due to poor digital sampling. **a** shows the anatomical image with the tumor in the left hemisphere. **b** represents the same slice, however, digitally filtered as if the data were obtained with 16×16 k-space sampling followed by extrapolation to the image resolution presented in **a.** **c** is similar to **b**, however, with an 8×8×8 k-space sampling, which is typical in many 31P MRSI studies

Pi region. For the tumor spectra, the Pi signal exhibits a shoulder to the left (lower frequencies or higher pH) and a shift in this direction.

We want to stress here that partial volume effects prevent from a thorough analysis of tumor pH, leaving the open question whether the lower pH fractions are due to healthy tissue adjacent to the tumor or result from extracellular Pi. A recent publication at least identifies the averaged Pi position as a sensitive marker for treatment (Hattingen et al. 2011).

2.1.3 Measuring Lipid Metabolism

While the tCho signal in ^{1}H MRS just reflects an overall concentration of choline compounds, its main components GPC and PCho can be discriminated with ^{31}P MRS. However, for MRSI data the quantitative analysis in terms of tissue concentrations is severely hampered by partial volume effects as described above. The poor point spread function related to the standard 8×8 matrix for data acquisition is causing a sensitivity profile with enhanced signal intensity in the center of the brain. Correction by dividing by tissue content obtained from anatomical MRI after appropriate filtering (see Fig. 3) may account for this, but experimental data on recurrent brain tumors show that the ratio of PCho/GPC, which provides an inherent correction for this, gives better results for comparing tumor to healthy tissue and monitoring treatment (Hattingen et al. 2011; Hattingen et al. 2013). A further advantage of ^{31}P MRS is the ability to observe the ethanolamine analogues to the choline membrane metabolism adding more variables for determining tumor-specific biochemistry.

2.1.4 Energy Metabolism

Metabolite signals from Pi, ATP, and PCr can easily be detected in the ^{31}P MRSI data allowing an estimation of changes in energy metabolism by comparing the ratio of the high-energy phosphates (ATP, PCr) to Pi. Most publications report a consistent drop in this ratio (Negendank 1992; Hattingen et al. 2011; Hubesch et al. 1990; Rutter et al. 1995; Maintz et al. 2002) indicating limited energy supply in tumor tissue.

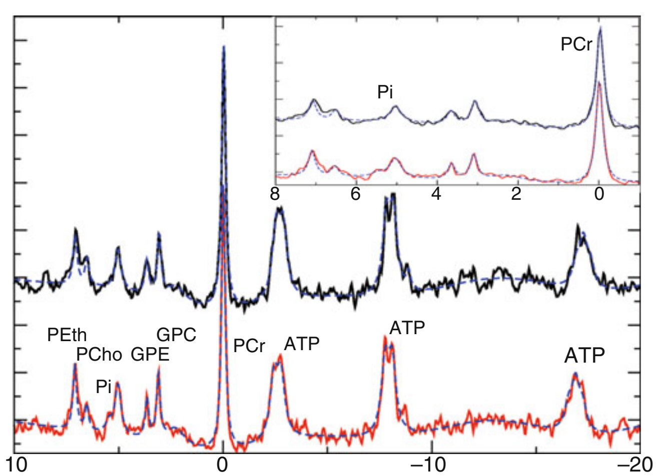

Fig. 4 31P spectra of control (*upper trace*) and tumor (*lower trace*) tissue. The insert shows the extended region downfield of PCr, with the position of the Pi signal indicating intracellular pH. *x*-axes show chemical shift in ppm; *y*-axes show laboratory units

2.2 ^{13}C MRS

2.2.1 Conventional ^{13}C MRS

De Graaf et al. reviewed the unique role of ^{13}C MRS in measuring brain metabolism in vivo (de Graaf et al. 2003) while Ross et al. described preliminary clinical experience in the same journal (Ross et al. 2003). However, due to the poor sensitivity, the in vivo application of ^{13}C MRS to focal lesions in the human brain is even more hampered by limited spatial resolution and partial volume effect than ^{31}P MRS. At least there is one case study (Wijnen et al. 2010) reporting on a malignant glioma. In this study, ^{13}C labeling of lactate and glutamate was observed during an intravenous infusion of 100 % enriched [1-^{13}C]-glucose solution (20 %, w/w). The authors compared $54 \times 32 \times 29$ mm^{3} voxels, one placed onto the tumor and the other one in the contralateral hemisphere, monitoring the increase in labeled lactate and glutamate. As expected, only glutamate labeling was observed in the normal-appearing tissue while the tumor voxel showed increased lactate labeling and diminished labeling of glutamate. Based on the glutamate labeling in the reference voxel and correcting for the partial volume effect in the tumor voxel, the authors concluded that no glutamate labeling occurs in tumor tissue, indicating no oxidative phosphorylation in tumor cells in accordance with the Warburg effect (Warburg 1956). A more recent study performed in situ ^{13}C labeling with uniformly labeled ^{13}C glucose during surgery (Maher et al. 2012). Perchloric acid extracts from excised tumor specimens were then analyzed by high-resolution NMR spectroscopy. This study enrolled 11 patients with different types of tumors (including metastasis). Despite the variability in tumor type, the authors observed some common features in carbohydrate metabolism: (1) glucose is entering the TCA cycle indicating mitochondrial oxidation of glucose; (2) formation of glycine, glutamate, and glutamine from glucose; (3) in tumor tissue, the TCA cycle oxidizes alternative carbon sources indicating anaplerosis probably due to a high demand for other cell metabolites. In summary, these data highlight the potential of ^{13}C MRS to provide tumor-specific biochemical information, but a noninvasive in vivo protocol for monitoring focal lesions is not available yet.

2.2.2 Hyperpolarized ^{13}C MRS

With the development of methods to obtain strongly polarized spins in solution based on dynamic nuclear polarization (Ardenkjaer-Larsen et al. 2003), the signal intensity of ^{13}C labeled substances are enhanced by the order of 10^5 allowing even molecular imaging with ^{13}C labeled compounds (Golman et al. 2003). However, it must be stressed that in all studies using hyperpolarized compounds, the magnetization (i.e., signal intensity) of the injected labeled substrate will decay with the T1 relaxation rate of the respective nucleus. On the one hand, this is posing the technical challenge to develop very fast MRSI while on the other hand it provides only a time window for labeling of metabolic products from the labeled substrate. In addition, not all metabolites can be hyperpolarized with the same efficiency. Pyruvate, which can be hyperpolarized, is an ideal substrate for studies on cancer metabolism, since the signal from the C-1 carbon relaxes very slowly, and it is at the entry point to the TCA cycle. In particular, it can be either converted to lactate in glycolysis, which should be the dominant pathway according to the Warburg effect (Warburg 1956), or it can enter the TCA cycle via acetyl-CoA and oxaloacetate as it is the standard pathway in regular brain tissue (see above). Consequently, one of the first applications using hyperpolarized ^{13}C compounds was monitoring the fate of ^{13}C-pyruvate in animal tumor models (Golman et al. 2006; Day et al. 2007; Albers et al. 2008). Brindle et al. summarized in a review article the unique potential of this new method including methodological challenges and constraints (Brindle et al. 2011). This article also provides a list of ^{13}C labeled compounds which can be hyperpolarized and used to address specific questions in cancer research.

Although huge efforts in this field are still engaged in developing and optimizing methods for data acquisition and data evaluation, the first results on animal models are quite promising. While the initial publications rather report the feasibility of imaging tumor lactate concentrations based on the conversion of ^{13}C labeled pyruvate to lactate (Golman et al. 2006; Day et al. 2007; Albers et al. 2008), other substrates like [1,4-$^{13}C2$]fumarate (Witney et al. 2010), [1-^{13}C] glutamate (Gallagher et al. 2011a), or [5-$^{13}C_1$]glutamine (Gallagher et al. 2008a) were also tested. Whereas these compounds are directed to monitor carbohydrate metabolism, the application of ^{13}C-labeled hyperpolarized bicarbonate provides a tool for measuring extracellular tumor pH (Gallagher et al. 2008b). Endogenous bicarbonate resulting from oxidation of ^{13}C labeled hyperpolarized pyruvate can also indicate tissue pH, but it may rather indicate the intracellular pH value (Gallagher et al. 2011b).

Park et al. performed the first applications in brain tumors by using hyperpolarized [1-^{13}C] pyruvate in rat glioma models (Park et al. 2010, 2012, 2013). As expected, lactate formation is significantly increased in tumor tissue compared to the contralateral hemisphere. Tumor models from different cell lines also showed differences in labeling, which were consistent with the inherent molecular characteristics (Park et al. 2010). Dynamic MRS data monitoring the time course of lactate labeling after bolus injection were used to characterize the kinetics of the conversion of pyruvate to lactate in the C6 rat glioma model (Park et al. 2012). According to the data, conversion rates may be a better marker than the lactate/pyruvate ration for differentiating between tumor and normal brain. Finally, the authors report on a dichloroacetate treatment study of the same tumor model (Park et al. 2013). The aim of this study was to determine the flux of the ^{13}C label from pyruvate via pyruvatedehydrogenase (PDH) to acetyl-CoA by monitoring bicarbonate labeling due to CO_2 production in the TCA cycle. In accordance with the Warburg effect (Warburg 1956), tumor tissue is characterized by decreased bicarbonate compared to normal tissue. Administering dichloroacetate, which activates PDH, causes a further increase of bicarbonate not only in the normal tissue but also in the tumor-bearing hemisphere. These experiments clearly show the potential of ^{13}C labeled hyperpolarized pyruvate to detect shifts in energy metabolism between glycolytic and oxidative pathways.

The safety and feasibility of the method for applications in humans was demonstrated in a study on 31 patients with prostate cancer (Nelson et al. 2013). No toxicities were observed at doses sufficient to detect the increased [1-^{13}C] lactate/[1-^{13}C]pyruvate ratio in the tumor in vivo.

Prostate cancer was also the focus of a recent review article on the use of hyperpolarized ^{13}C MRS for molecular imaging (Wilson and Kurhanewicz 2014).

Most of the biochemical rationales and arguments herein can be adapted to human brain tumor. Especially, working on the methodological challenges (i.e., improved fast MRSI sequences, miniaturization and optimization of the device for hyperpolarization, development of other substrates) are pivotal for transferring this promising technique into a clinical tool.

References

Albers MJ, Bok R, Chen AP, Cunningham CH, Zierhut ML, Zhang VY, Kohler SJ, Tropp J, Hurd RE, Yen Y-F, Nelson SJ, Vigneron DB, Kurhanewicz J (2008) Hyperpolarized 13C lactate, pyruvate, and alanine: noninvasive biomarkers for prostate cancer detection and grading. Cancer Res 68:8607–8615

Andronesi OC, Kim GS, Gerstner E, Batchelor T, Tzika AA, Fantin VR, Vander Heiden MG, Sorensen AG (2012) Detection of 2-hydroxyglutarate in IDH-mutated glioma patients by in vivo spectral-editing and 2D correlation magnetic resonance spectroscopy. Sci Transl Med 4:116ra4

Andronesi OC, Rapalino O, Gerstner E, Chi A, Batchelor TT, Cahill DP, Sorensen AG, Rosen BR (2013) Detection of oncogenic IDH1 mutations using magnetic resonance spectroscopy of 2-hydroxyglutarate. J Clin Invest 123:3659–3663

Ardenkjaer-Larsen JH, Fridlund B, Gram A, Hansson G, Hansson L, Lerche MH, Servin R, Thaning M, Golman K (2003) Increase in signal-to-noise ratio of >10,000 times in liquid-state NMR. Proc Natl Acad Sci U S A 100:10158–10163

Brindle KM, Bohndiek SE, Gallagher FA, Kettunen MI (2011) Tumor imaging using hyperpolarized 13C magnetic resonance spectroscopy. Magn Reson Med 66:505–519

Choi C, Ganji SK, DeBerardinis RJ, Dimitrov IE, Pascual JM, Bachoo R, Mickey BE, Malloy CR, Maher EA (2011) Measurement of glycine in the human brain in vivo by 1H-MRS at 3T: application in brain tumors. Magn Reson Med 66:609–618

Choi C, Ganji SK, DeBerardinis RJ, Hatanpaa KJ, Rakheja D, Kovacs Z, Yang X-L, Mashimo T, Raisanen JM, Marin-Valencia I, Pascual JM, Madden CJ, Mickey BE, Malloy CR, Bachoo RM, Maher EA (2012) 2-hydroxyglutarate detection by magnetic resonance spectroscopy in IDH-mutated patients with gliomas. Nat Med 18:624–629

Davies NP, Wilson M, Natarajan K, Sun Y, MacPherson L, Brundler M-A, Arvanitis TN, Grundy RG, Peet AC (2010) Non-invasive detection of glycine as a biomarker of malignancy in childhood brain tumours using in-vivo 1H MRS at 1.5 tesla confirmed by ex-vivo high-resolution magic-angle spinning NMR. NMR Biomed 23:80–87

Day SE, Kettunen MI, Gallagher FA, Hu D-E, Lerche M, Wolber J, Golman K, Ardenkjaer-Larsen JH, Brindle KM (2007) Detecting tumor response to treatment using hyperpolarized 13C magnetic resonance imaging and spectroscopy. Nat Med 13:1382–1387

de Graaf R, Mason G, Patel A, Behar K, Rothman D (2003) In vivo 1H-[13C]-NMR spectroscopy of cerebral metabolism. NMR Biomed 16:339–357

Esmaeili M, Hamans BC, Navis AC, van Horssen R, Bathen TF, Gribbestad IS, Leenders WP, Heerschap A (2014) IDH1 R132H mutation generates a distinct phospholipid metabolite profile in glioma. Cancer Res 74:4898–4907

Gallagher FA, Kettunen MI, Day SE, Lerche M, Brindle KM (2008a) 13C MR spectroscopy measurements of glutaminase activity in human hepatocellular carcinoma cells using hyperpolarized 13C-labeled glutamine. Magn Reson Med 60:253–257

Gallagher FA, Kettunen MI, Day SE, Hu D-E, Ardenkjaer-Larsen JH, Zandt RI, Jensen PR, Karlsson M, Golman K, Lerche MH, Brindle KM (2008b) Magnetic resonance imaging of pH in vivo using hyperpolarized 13C-labelled bicarbonate. Nature 453:940–943

Gallagher FA, Kettunen MI, Day SE, Hu D, Karlsson M, Gisselsson A, Lerche MH, Brindle KM (2011a) Detection of tumor glutamate metabolism in vivo using (13)C magnetic resonance spectroscopy and hyperpolarized [1-(13)C]glutamate. Magn Reson Med 66:18–23

Gallagher FA, Kettunen MI, Brindle KM (2011b) Imaging pH with hyperpolarized 13C. NMR Biomed 24:1006–1015

Golman K, Ardenkjaer-Larsen JH, Petersson JS, Mansson S, Leunbach I (2003) Molecular imaging with endogenous substances. Proc Natl Acad Sci U S A 100:10435–10439

Golman K, Zandt RI, Lerche M, Pehrson R, Ardenkjaer-Larsen JH (2006) Metabolic imaging by hyperpolarized 13C magnetic resonance imaging for in vivo tumor diagnosis. Cancer Res 66:10855–10860

Govindaraju V, Basus V, Matson G, Maudsley A (1998) Measurement of chemical shifts and coupling constants for glutamate and glutamine. Magn Reson Med 39:1011–1013

Hattingen E, Lanfermann H, Quick J, Franz K, Zanella FE, Pilatus U (2009) (1)H MR spectroscopic imaging with short and long echo time to discriminate glycine in glial tumours. MAGMA 22:33–41

Hattingen E, Jurcoane A, Bähr O, Rieger J, Magerkurth J, Anti S, Steinbach JP, Pilatus U (2011) Bevacizumab impairs oxidative energy metabolism and shows antitumoral effects in recurrent glioblastomas: a 31P/1H MRSI and quantitative magnetic resonance imaging study. Neuro Oncol 13(12):1349–1363

Hattingen E, Bähr O, Rieger J, Blasel S, Steinbach J, Pilatus U (2013) Phospholipid metabolites in recurrent glioblastoma: in vivo markers detect different tumor phenotypes before and under antiangiogenic therapy. PLoS One 8:e56439

Hubesch B, Sappey-Marinier D, Roth K, Meyerhoff DJ, Matson GB, Weiner MW (1990) P-31 MR spectroscopy of normal human brain and brain tumors. Radiology 174:401–409

Maher EA, Marin-Valencia I, Bachoo RM, Mashimo T, Raisanen J, Hatanpaa KJ, Jindal A, Jeffrey FM, Choi C, Madden C, Mathews D, Pascual JM, Mickey BE, Malloy CR, DeBerardinis RJ (2012) Metabolism of [U-13 C]glucose in human brain tumors in vivo. NMR Biomed 25:1234–1244

Maintz D, Heindel W, Kugel H, Jaeger R, Lackner KJ (2002) Phosphorus-31 MR spectroscopy of normal adult human brain and brain tumours. NMR Biomed 15:18–27

Maudsley AA, Gupta RK, Stoyanova R, Parra NA, Roy B, Sheriff S, Hussain N, Behari S (2014) Mapping of glycine distributions in gliomas. AJNR Am J Neuroradiol 35(6 Suppl):S31–S36

Negendank W (1992) Studies of human tumors by MRS: a review. NMR Biomed 5:303–324

Nelson SJ, Kurhanewicz J, Vigneron DB, Larson PEZ, Harzstark AL, Ferrone M, van Criekinge M, Chang JW, Bok R, Park I, Reed G, Carvajal L, Small EJ, Munster P, Weinberg VK, Ardenkjaer-Larsen JH, Chen AP, Hurd RE, Odegardstuen L-I, Robb FJ, Tropp J, Murray JA (2013) Metabolic imaging of patients with prostate cancer using hyperpolarized [1-^{13}C]pyruvate. Sci Transl Med 5:198ra108

Park I, Larson PEZ, Zierhut ML, Hu S, Bok R, Ozawa T, Kurhanewicz J, Vigneron DB, Vandenberg SR, James CD, Nelson SJ (2010) Hyperpolarized 13C magnetic resonance metabolic imaging: application to brain tumors. Neuro Oncol 12:133–144

Park JM, Josan S, Jang T, Merchant M, Yen Y-F, Hurd RE, Recht L, Spielman DM, Mayer D (2012) Metabolite kinetics in C6 rat glioma model using magnetic resonance spectroscopic imaging of hyperpolarized [1-(13) C]pyruvate. Magn Reson Med 68(6):1886–1893

Park JM, Recht LD, Josan S, Merchant M, Jang T, Yen Y-F, Hurd RE, Spielman DM, Mayer D (2013) Metabolic response of glioma to dichloroacetate measured in vivo by hyperpolarized (13)C magnetic resonance spectroscopic imaging. Neuro Oncol 15:433–441

Pope WB, Prins RM, Albert Thomas M, Nagarajan R, Yen KE, Bittinger MA, Salamon N, Chou AP, Yong WH, Soto H, Wilson N, Driggers E, Jang HG, Su SM, Schenkein DP, Lai A, Cloughesy TF, Kornblum HI, Wu H, Fantin VR, Liau LM (2012) Non-invasive detection of 2-hydroxyglutarate and other metabolites in IDH1 mutant glioma patients using magnetic resonance spectroscopy. J Neurooncol 107:197–205

Prichard JW, Alger JR, Behar KL, Petroff OA, Shulman RG (1983) Cerebral metabolic studies in vivo by 31P NMR. Proc Natl Acad Sci U S A 80:2748–2751

Ross B, Lin A, Harris K, Bhattacharya P, Schweinsburg B (2003) Clinical experience with 13C MRS in vivo. NMR Biomed 16:358–369

Rutter A, Hugenholtz H, Saunders JK, Smith IC (1995) One-dimensional phosphorus-31 chemical shift imaging of human brain tumors. Invest Radiol 30:359–366

Stubbs M, Bhujwalla ZM, Tozer GM, Rodrigues LM, Maxwell RJ, Morgan R, Howe FA, Griffiths JR (1992) An assessment of 31P MRS as a method of measuring pH in rat tumours. NMR Biomed 5:351–359

Stubbs M, Rodrigues L, Howe FA, Wang J, Jeong KS, Veech RL, Griffiths JR (1994) Metabolic consequences of a reversed pH gradient in rat tumors. Cancer Res 54:4011–4016

Warburg O (1956) On the origin of cancer cells. Science 123:309–314

Wijnen JP, Van der Graaf M, Scheenen TWJ, Klomp DWJ, de Galan BE, Idema AJS, Heerschap A (2010) In vivo 13C magnetic resonance spectroscopy of a human brain tumor after application of 13C-1-enriched glucose. Magn Reson Imaging 28:690–697

Wilson DM, Kurhanewicz J (2014) Hyperpolarized 13C MR for molecular imaging of prostate cancer. J Nucl Med 55:1567–1572

Witney TH, Kettunen MI, Hu DE, Gallagher FA, Bohndiek SE, Napolitano R, Brindle KM (2010) Detecting treatment response in a model of human breast adenocarcinoma using hyperpolarised [1-13C]pyruvate and [1,4-13C2]fumarate. Br J Cancer 103:1400–1406